Seismic imaging and anisotropic inversion using vertical cable data

by

Hejie Wang

Thesis submitted for the degree of Doctor of Philosophy

Department of Geology and Geophysics

University of Edinburgh

2003



I hereby declare that this thesis has been composed by myself and that the work described is entirely my own unless explicitly stated in the text.

Hejie Wang

Abstract

As an alternative method of acquiring 3-D seismic data, vertical cable seismic (VCS) uses vertical arrays of hydrophones and a conventional airgun source to obtain data with multi-azimuths while not compromising horizontal and vertical seismic resolution. This unique geometry does not allow us to directly use conventional 3-D tools to handle the data. I have designed a special processing scheme for VCS imaging and developed relevant techniques involving wavefield separation, multiple suppression, common scatter point (CSP) stack and prestack migration. A traveltime inversion technique has also been developed to investigate seismic anisotropy using VCS data. These techniques have been successfully applied to a real VCS data set from the North Sea.

The wavefield separation is achieved by a dip filtering, which is performed by using a finite-difference algorithm to solve differential equations in the time and space domain. The design of filtering parameters is quite flexible and it can also overcome the undesirable artifacts related to spatial aliasing or side effects in the $f-k$ filtering with the small number of traces. Synthetic tests show that compared to the median filtering and $f-k$ filtering approach, this method obtains the best result. Then I have proposed a demultiple filter with a Butterworth gain function to suppress water-column multiples in VCS data. This filtering is carried out in the $\tau-p$ domain for each VCS common-shot gather. It can automatically define the multiple rejection areas and tapers the rejection boundary in the $\tau-p$ domain by using the amplitude ratio of upgoing and downgoing wavefields. This filter makes no assumption on periodicity or moveout patterns of multiples, nor

does it require any knowledge of the subsurface.

The analysis of a horizontal interface reflection in VCS geometry has shown that the residual moveouts and dispersal of reflection points in vertical cable seismic data, due to the depth difference between receivers in the same cable, increase with increasing offset to depth ratios in performing the conventional CDP stack. Alternatively, a CSP-based imaging technique has been developed to replace a CDP-based one in VCS data processing. As a result, the high fold and large offsets in CSP gathers allow us to make a more accurate velocity analysis at each imaging position, and the conventional processing tools can be used in the CSP-based processing. I have also presented a prestack migration algorithm for common receiver gathers. The application of arrival angle weight in migration has much improved the imaging quality.

The existence of anisotropy causes a difference between the vertical and horizontal $P-$ and $S-$wave velocities and induces azimuthal changes. Based on the weak anisotropic approximation, I have proposed a slowness-based anisotropic inversion procedure to investigate the seismic anisotropy in a multi-layered azimuthally isotropic or anisotropic model with an assumption that the layers are parallel to each other and the symmetry axes are perpendicular or parallel to the layer surface in the presence of dip using refracted arrivals in VCS data, whilst the reflected $P-$waves in VCS data are insufficient for accurate determination of the vertical velocity and anisotropic parameters, even if the long-spread data are used. The inversion results for the synthetic $P-$wave VCS data show that this technique can provide an accurate and quantitative description of the anisotropic parameters v_{p0} and ϵ, the symmetry axis azimuth φ_a, and layer parameters β and φ_d in multi-layered azimuthally anisotropic media. The relative errors for inverted parameters v_{p0} and ϵ are less than 0.4% and 6.0%, respectively, when the $P-$wave anisotropy is up to 22%. In addition, the overburden has no effect on the inversion results for the refractor in this case. The results of inversion from

a real VCS dataset have demonstrated the existence of 5% azimuthal anisotropy in marine sediments of the exploration area. This technique can also be easily extended to orthorhombic media, since both TI media with a horizontal axis (HTI) and orthorhombic media may have the same form of the slowness approximation in the horizontal plane.

Acknowledgments

I wish to thank my supervisor Xiang-Yang Li of the British Geological Survey (BGS) for providing me with the opportunity to study with the Edinburgh Anisotropy Project (EAP), and for many stimulating discussions and suggestions throughout this study and the preparation of this thesis. I would also like to thank professor Martin Landrø of Norwegian University of Science and Technology for his kind support in the final preparation of this thesis during my stay in Norway.

I am grateful to my co-supervisor Roger Scrutton of the University of Edinburgh for his guidance and encouragements. His comments on my work were always most helpful. My special thanks are also extended to my former supervisors Colin MacBeth of Heriot-Watt University and Alexander Druzhinin in EAP for their stimulating discussions and ideas in early stages of my study.

I enjoyed my stay in EAP and I appreciate the hospitality and the facilities provided by BGS. I learned a great deal with my colleagues during seminars and informal discussions. Some of them also assisted greatly in the computer system maintenance. For both the scientific and computer system contributions, I owe special thanks to Jerry Yuan, Henchang Dai, Yi-jie Liu, Enru Liu, Peter Hanssen, Mark Chapman, Anna Droujinina, Fabien Borocin, Charles Fyfe and Ruth Addinall.

My sincere thanks go to John Lovell, who proof read the manuscript. His expertise in editing helped me enormously during the preparation of this thesis.

I would also like to thank Xiucheng Wei for his invaluable assistance during the final preparation of this thesis when I had left Edinburgh.

I acknowledge the financial support from the EAP sponsors: Agip, Amerada Hess, BP, Cheveron, Conoco, ExxonMobil, PGS, Philips, Schlumberger, Shell, Texaco, TotalFinaElf and Veritas DGC. In particular, I am grateful to Texaco for providing the data used here and for permission to publish the results.

I would like to thank my wife, Wenjuan, my daughter, Annie, for their love, patience and support during my years of study. I could not have undertaken this challenge without their encouragement. Finally, I wish to thank my parents for encouraging me in the desire to learn and to discover new things since I was a child. It is their support and encouragement that have helped me make the transition in my life from East to West.

Contents

Abstract i

Acknowledgements v

Notations and conventions 1

1 Introduction 9

1.1 Thesis objectives 9

1.2 Outline of thesis 12

1.3 Software used for this thesis 13

2 What is vertical cable seismic 15

2.1 Introduction 15

2.2 Benefits of marine VCS 17

2.3 Applications of VCS 18

2.3.1 High quality data acquisition 19

2.3.2 Time-lapse reservoir monitoring 20

2.3.3 A subsalt imaging tool 20

2.3.4 Identifying anisotropy 21

2.4 A real data set 21

3 Wave field separation **29**

3.1 Introduction 29

3.2 Wavefield separation techniques 30

3.2.1 $F-K$ velocity filtering 32

3.2.2 Median filtering 33

3.3 Differential equation-based (DEB) filter 37

3.3.1 Design of 2-D DEB filter 37

3.3.2 Determination of filter parameters 38

3.3.3 Filtering equations 41

3.3.3.1 Filtering equation $A1$ 43

3.3.3.2 Filtering equation $A2$ 44

3.3.4 Finite-difference algorithm 45

3.3.4.1 Differential equation $A1$ 45

3.3.4.2 Differential equation $A2$ 48

3.3.5 Application to VCS wavefield separation 50

3.4 Comparison of different filtering techniques for wave field separation 51

3.5 Application to real VCS data 56

3.6 Conclusions 57

4 Multiple suppression **63**

4.1 Introduction 63

4.2 Review of multiple attenuation 64

4.2.1 Categories of multiples 65

4.2.2 Multiple attenuation methods 67

4.3 New demultiple filter 69

4.3.1 The principle of filtering 70

4.3.2 Test examples 71

4.4 A case study of VCS multiple attenuation 72

4.4.1 Results of wavefield separation 72

4.4.2 Application of predictive deconvolution 76

4.4.3 Application of the new demultiple filtering 76

4.5 Conclusions 77

5 Vertical cable seismic imaging **85**

5.1 Introduction 85

5.2 Reflection of a horizontal interface 86

5.2.1 Traveltime 87

5.2.2 Residual moveout 88

5.2.3 Dispersal of reflection points 89

5.2.4 Case studies 89

5.3 Prestack migration 91
5.3.1 Wavefield extrapolation 93
5.3.2 Imaging principle 94
5.3.3 Traveltime calculation 95
5.3.4 Arrival angle weight 96
5.4 CSP stack 97
5.4.1 Initial velocity analysis 98
5.4.2 Generation of CSP gather 100
5.5 Case study 103
5.5.1 Generation of CSP gather 103
5.5.2 CSP stack 104
5.5.3 Prestack migration 104
5.6 Conclusions 105

6 Feasibility study of anisotropic traveltime inversion using VCS data **119**

6.1 Introduction 119
6.2 Common anisotropic media and parameters 120
6.2.1 Transverse isotropic with vertical axis of symmetry (VTI) 121
6.2.2 Transverse isotropic with horizontal axis of symmetry (HTI) 122
6.2.3 Transverse isotropic with tilted axis of symmetry (TTI) . 123

6.2.4 Orthorhombic 124

6.3 Analysis of slowness variations 124

6.3.1 Slowness surface 125

6.3.2 VTI medium 127

6.3.2.1 Thomsen anisotropy parameters 129

6.3.3 HTI medium 130

6.3.4 TTI medium 131

6.3.5 Orthorhombic medium 134

6.4 Anisotropic traveltime inversion methods 137

6.4.1 Walkaway VSPs 138

6.4.2 Reflection survey 139

6.4.3 Refraction survey 141

6.5 Viability of VCS traveltime inversion 142

6.5.1 Direct arrival 142

6.5.2 Reflected arrival 143

6.5.3 Refracted arrival 145

6.6 Refracted traveltime equations 145

6.6.1 Refracted traveltime equation in a single refractor 145

6.6.2 Refracted traveltime equation in multi-layered media . . . 147

6.7 Dip and ray-slowness calculations from refracted arrivals 148

6.7.1 Horizontal apparent and ray-slownesses 149

6.7.2 Vertical apparent and ray-slownesses 150

6.7.3 Determination of dip and ray-slowness 151

6.8 Conclusions 152

7 Applications of refracted traveltime inversion to VCS data 155

7.1 Introduction 155

7.2 Azimuthal variations of ray-slownesses 156

7.2.1 Ray-slowness approximation 156

7.2.2 Horizontal ray-slowness 158

7.2.3 Vertical ray-slowness 159

7.3 Inversion procedure 159

7.4 Analysis of inversion accuracy 161

7.5 Applications to synthetic data 165

7.5.1 Effects of dip 165

7.5.2 Numerical modelling 165

7.5.3 Azimuthal variations 172

7.5.4 Results of estimation for anisotropy 174

7.6 Field data example 181

7.6.1 Azimuthal variations 181

7.6.2 Inversion results 183

7.7 Conclusions 186

8 Summary **189**

8.1 VCS processing techniques 189

8.2 VCS imaging techniques 190

8.3 Anisotropic inversion 192

8.4 Suggestions for future work 194

References **195**

Appendices

A Elastic tensor for TI media with a non-vertical axis of symmetry 207

B Refracted traveltime equation in multilayered media **211**

C Ray velocities in transversely isotropic media **213**

D The LSQ solution for a cosine function **215**

E List of publications **219**

F A paper published on Geophysical Prospecting 50, 2002 **221**

Notations and conventions

In this section all the mathematical variables and abbreviations used in this thesis are explained. They are arranged by chapters in the order of their appearance.

General

Symbol	Meaning
VCS	vertical cable seismic
VSP	vertical seismic profile
CMP	common mid-point
CDP	common depth-point
CSP	common scatter-point
TI	transverse isotropic
VTI	transverse isotropic with a vertical axis of symmetry
HTI	transverse isotropic with a horizontal axis of symmetry
TTI	transverse isotropic with a tilted axis of symmetry
NMO	normal moveout
AVO	amplitude versus offset
rms	root mean square
LSQ	least squares
2-D,3-D and 4-D	two, three, and four dimensional
PGS	Petroleum Geo-Services
CGG	Compagnie Générale de Géophysique

Chapter 3

Symbol	Meaning	Unit
DEB	differential equation based	
k_z	wavenumber in z (depth) direction	$cycle/m$
ω	angular frequency	$cycle/s$
$H(k_z, \omega)$	transfer function of a dip filter	
$\theta(k_z, \omega)$	phase spectrum	
V	apparent velocity	m/s
V_c	cut-off apparent velocity	m/s
f_d	dominant frequency	H_z
f_{max}	maximum frequency	H_z
ω_{max}	maximum angular frequency	$cycle/s$
α	filtering parameter	m/s^2
z	depth	m
t	time	s
t_{max}	maximum time	s
$p(z,t)$	input data in the time-space domain	
$P(k_z, \omega)$	input data in the $f-k$ domain	
$q(z,t)$	output data in the time-space domain	
$Q(k_z, \omega)$	output data in the $f-k$ domain	
η	parameter for controlling the boundary condition	
Δz	trace spacing	m
Δt	time sampling interval	s
β	$0.25 - 1/\pi^2$	
$\mathbf{p}_m$	vector of input data in discrete form	
$\mathbf{q}_m$	vector of output data in discrete form	
L	the length of seismic traces in sample points	
M	the number of traces	
$\overrightarrow{\mathbf{A}}, \overrightarrow{\mathbf{B}}, \overrightarrow{\mathbf{C}}$	coefficient matrixes of filtering equations	
$\overrightarrow{\mathbf{A}'}, \overrightarrow{\mathbf{B}'}, \overrightarrow{\mathbf{C}'}$	coefficient matrixes of filtering equations	

Chapter 4

Symbol	Meaning	Unit
$u_U(t,z)$	upgoing wave in the time-space domain	
$u_D(t,z)$	downgoing wave in the time-space domain	
$u_U(\tau,p)$	upgoing wave in the $\tau-p$ domain	
$u_D(\tau,p)$	downgoing wave in the $\tau-p$ domain	
$A_D(\tau)$	amplitude summation of downgoing wave at each value of τ	
$A_U(\tau)$	amplitude summation of upgoing wave at each value of τ	
$g(\tau)$	Butterworth gain function	
h	depth	m
ϵ	multiple rejection parameter	
n	parameter used to control the smoothness of the filter	

Chapter 5

Symbol	Meaning	Unit
DSR	double square root	
CR	common receiver	
h_r	depth of the receiver	m
h_w	depth of the sea-floor	m
h_m	depth of the reflector	m
θ_1	angle of incidence	
θ_0	angle of transmission	
x	source-cable offset	m
v_0	$P-$wave velocity in the water layer	m/s
v_1	$P-$wave velocity in the sub-water layer	m/s
t_{SPR}	traveltime from source S to receiver R via reflection point P	s
$t_{SM'C}$	traveltime from source S to receiver C via reflection point M'	s

Symbol	Meaning	Unit
t_0	two-way vertical traveltime	s
V_{rms}	root-mean-square velocity	m/s
Δt_1	two-way vertical traveltime within the water layer	s
Δt_2	two-way vertical traveltime within the second layer	s
Δt_R	residual moveout of the receiver at the location R	s
x_{cp}	horizontal distance between cable and reflection point	m
$x_{pm'}$	horizontal distance between reflection points P and M'	m
$\mathbf{r}$, $\mathbf{r}_0$	coordinate vectors	
$S(\mathbf{r}_0)$	source at the location $\mathbf{r}_0$	
$D(\mathbf{r})$	scatter point at the location $\mathbf{r}$	
$R = \lvert\mathbf{r} - \mathbf{r}_0\rvert$	distance between $\mathbf{r}_0$ and $\mathbf{r}$	m
$U(\mathbf{r}_0, t)$	wavefield at the location $\mathbf{r}_0$	
$U(\mathbf{r}, t)$	wavefield at the location $\mathbf{r}$	
S_0	source surface	
v	$P-$wave velocity	m/s
θ	ray angle with respect to the $z-$axis	
tr	traveltime from the scatter point to the receiver	s
ts	traveltime from the source to the scatter point	s
x_s	horizontal distance between source and scatter point	m
x_r	horizontal distance between scatter point and receiver	m
t_{rv}	two-way vertical traveltime	
	from receiver level to surface datum	s
V_s	rms velocity at source side	m/s
V_r	rms velocity at source side	m/s
θ_S, θ_{S0}	arrival angle	
H	depth of the reflector	m
t_{CSP}	traveltime in CSP gather	s
x_{CSP}	offset in CSP gather	m

Chapter 6

Symbol	Meaning	Unit
C_{ij}	elastic tensor	N/m^2
k	wavenumber	
$\mathbf{u}$	particle displacement vector	m
$X_i, i = 1, 3$	Cartesian axes	m
X, Y, Z	Cartesian axes	m
Γ_{ij}	Christoffel matrix	
$\mathbf{l}$	direction cosine matrix	
$\mathbf{C}$, $[C]$	stiffness matrix	
ρ	density	kg/m^3
S	slowness	s/m
θ_p	phase angle	
qP	quasi-P wave	
qSV	quasi-SV wave	
$(S^2)_P$	square slowness of $qP-$wave	s^2/m^2
$(S^2)_{SV}$	square slowness of $qSV-$wave	s^2/m^2
v_{p0}	$P-$wave velocity along the symmetry axis	m/s
v_{s0}	$S-$wave velocity along the symmetry axis	m/s
ϵ, γ, δ	Thomsen anisotropy parameters	
A_{ij}	density-weighted stiffnesses	m^2/s^2
S_h	horizontal slowness	s/m
S_z	vertical slowness	s/m
δ'	$2\delta - \epsilon$	
V_v	average vertical velocity	m/s
V_h	horizontal velocity	m/s
V_γ	skew moveout velocity	m/s
v_0, v_{45}, v_{90}	bedding-normal, 45° azimuth and bedding-parallel	
	velocities for $P-$waves	m/s

Symbol	Meaning	Unit
η	anisotropic coefficient	
V_{nmo}	NMO velocity	m/s
V_0	$P-$wave velocity in the water layer	m/s
ϕ	source-cable azimuth	
θ_C	critical angle	
h_O	depth of the sea-floor at the cable location	m
h_R	receiver-to-sea-floor distance	m
α	apparent dip	
β	real dip	
φ_d	dip azimuth	
$V_n(\phi)$	$P-$wave ray-velocity along the top interface of layer n	m/s
$t_n(\phi)$	refracted traveltimes at the measured azimuth ϕ	
	in $n-$layered media	s
$V_k(\theta_k, \phi)$	$P-$wave ray-velocities at given ray paths (θ_k, ϕ)	m/s
$\theta_k, k = 1, n-1$	angles of incidence	
$z_k, k = 1, n-1$	vertical layer thickness at the cable location	m
$S_{nx}(\phi)$	horizontal apparent slowness	s/m
$S_{nh}(\phi)$	horizontal ray-slowness	s/m
$S_{nz}(\phi)$	vertical apparent slowness	s/m
$S_{nv}(\phi)$	vertical ray-slowness	s/m
$S_n(\phi)$	ray-slowness	s/m

Chapter 7

Symbol	Meaning	Unit
ϕ	azimuth of the observation point	
φ_a	azimuth of the horizontal axis of symmetry	
$V(\phi, \theta)$	ray velocity	m/s
θ	ray angle	
A_0, B_0, C_0	coefficients of a three-term approximation	
	for the square ray-velocity	m^2/s^2
dh_R	receiver interval in the vertical direction	m
$E_{v_{p0}}$	relative error of v_{p0}	
E_ϵ	relative error of ϵ	
S_e	relative estimation error	
N	the number of azimuths measured	
y_i	measured value	
$\widehat{y}_i$	fitting value	

CHAPTER 1

Introduction

1.1 Thesis objectives

The vertical cable seismic (VCS) represents an alternative method of acquiring and processing 3-D marine seismic data, developed by Paul Krail and Dwight Sukup of Texaco's Exploration and Production Technology Division throughout the 1980s and early 1990s (Krail 1991; Anderson et al. 1997; Leach 1997), using cables which are suspended vertically in the water column with an anchor at one end, a buoy at the other, and a recording buoy at the surface. Hydrophones are located along each of the cables. The shooting vessel fires a dense pattern of shots on the surface covering the area around and between the cables. Comparison with conventional 3-D in the deep water Gulf of Mexico and the Strathspey Field of the North Sea has shown that this technique can provide high quality seismic data with lower cost (Leach 1997; Krail 1993). The truly 3-D seismic data acquired by vertical cable seismic with a full azimuthal coverage of the target also provide a good opportunity to estimate azimuthal anisotropy in the subsurface.

However, the unique characteristic of this acquisition does not allow us to directly use conventional 3-D tools to handle the VCS data, and it also results in some new challenges in the data processing. My thesis aims to design appropriate processing schemes for VCS imaging and investigation of anisotropy in

marine sediments, and develop related key techniques which involve wave field separation, multiple suppression, CSP stack, prestack migration and anisotropic inversion of refracted waves.

As in a VSP, both upgoing and downgoing waves are present across VCS common-shot gathers. Many methods like $f-k$, $\tau-p$ and median filtering have been successfully used to perform these wave field separations for VSP data in the industry. However, major difficulties may arise when we apply these algorithms to VCS data. This is because there are long offset spreads in VCS acquisition, and the first arrivals are generally refracted waves (upgoing waves) instead of direct waves (downgoing waves) at almost all offsets. On the other hand, transform procedures may give undesirable artifacts in vertical cable seismic data processing due to the small number of receiver locations. In this thesis, a dip filter is developed to tackle these issues by using a finite-difference algorithm to solve differential equations in the time and space domain.

The presence of water-column multiples is also a serious problem in vertical cable seismic data processing. The concept of CDP or CMP gather is not effective in vertical cable seismic data processing, when we use the concept of a point receiver for this special geometry. The moveout-based methods (Ryu 1982; Yilmaz 1989; Foster and Mosher 1992) of multiple suppression could not be used to remove multiples in VCS data, nor could the wave equation-based prediction and subtraction methods (Wiggins 1988) be applied in VCS common-shot gathers to attenuate the receiver-side reverberation in VCS data. Here, a new demultiple filter has been developed to tackle this issue by using a Butterworth gain function in the $\tau-p$ domain.

Since the concept of CMP is not effective in VCS data processing, a common scatter point (CSP)-based imaging technique has been proposed to replace a CMP-based one here. CSP gathers are formed from each common-receiver gather

as the double-square-root traveltime equation. As a result, the conventional hyperbolic traveltime equation is satisfied in the CSP gather. In particular, we can make more accurate velocity analysis in CSP gathers which hold high fold and large offset data. Furthermore, I have also developed a prestack Kirchhoff time migration algorithm to perform VCS imaging in a common-receiver gather, and the arrival angle information is considered to reduce the imaging artifacts. These imaging techniques have been successfully applied to a real dataset with promising results.

The existence of anisotropy may seriously affect the seismic wave propagation in sedimentary rocks. Seismic imaging may be greatly distorted and amplitude variation with offset (AVO) effects may be incorrect if isotropy is assumed in the far-offset seismic data processing and interpretation. Past work (Fryer and Miller 1986; Fryer et al., 1989) have shown that ignoring anisotropy in marine data may lead to systematic errors in interpretation, including overestimates of depth and errors in Poisson's ratio. Here, I have discussed the slowness variations in the transverse isotropic (TI) and orthorhombic media, and investigated the feasibility of anisotropic traveltime inversion using direct, reflected and refracted arrivals in VCS data.

The multi-azimuth refracted waves in VCS data allow us to estimate the azimuthal anisotropy in marine sediments. I consider the subsurface is multilayered azimuthally isotropic or anisotropic media with the assumption that the layers are parallel to each other and the axes of symmetry are perpendicular or parallel to the dipping layer interface. Based on this consideration, I have proposed a slowness-based anisotropic inversion procedure in the presence of dip, which can be used to accurately estimate the dip, $P-$wave velocity along the direction of symmetry axis, $P-$wave anisotropy strength, and the azimuth of the symmetry axis from the measured refracted traveltimes.

1.2 Outline of the thesis

In Chapter 2, I introduce the concept of vertical cable seismic, review VCS acquisition, and summarize the benefits and applications of this technology. I also give a brief description of the data set used in this thesis.

Chapter 3 focuses on techniques of wavefield separation. Firstly I give an overview of commonly-used methods in the industry for VSP data processing, and then present a differential-equation-based filter to perform the separation of upgoing and downgoing wavefields in VCS data. The principle of filtering and the processing procedure have been discussed. Finally this technique is examined using both synthetic and real VCS data.

In Chapter 4, I discuss the type of multiples which may be present in the VCS upgoing wave fields and review the commonly-used methods for the suppression of these multiples in the surface data. A special processing scheme has been proposed and tested for VCS multiple suppression, which includes wave field separation, forward and inverse $\tau - p$ transforms, and demultiple filtering in the $\tau - p$ domain. A real case study with a selected 2-D VCS data set is also completed.

Chapter 5 shows variations of residual moveout and dispersal of reflection points in VCS data with offset to depth ratios in performing the conventional CDP stack by analyzing a horizontal interface reflection in VCS geometry. I have then presented a CSP-based technique and prestack Kirchhoff time migration algorithm for VCS imaging. A complete real case study has also been done for this processing.

Chapter 6 focuses on the feasibility study of anisotropic traveltime inversion using VCS data. I have reviewed anisotropic traveltime inversion methods using walkaway VSP, refraction and reflection survey data. A refraction method for

determining the dip and ray-slowness distributions along the layer interface of marine sediments using VCS data in the presence of dip has then been proposed.

In Chapter 7, I have presented a slowness-based anisotropic inversion procedure for TI media to estimate Thomsen anisotropy parameters and the symmetry axis azimuth of the refractor by using refracted traveltimes in VCS data. The effects of the presence of dip and anisotropy on the azimuthal variations in apparent and ray slownesses are tested with two sets of TI models. The synthetic $P-$wave VCS data analysis and application of this inversion procedure to a real VCS data set are also presented.

Chapter 8 summaries the findings of this thesis, and gives suggestions for future work.

1.3 Software used for this thesis

I have produced most diagrams in this thesis with the Seismic Unix (SU) software (Cohen and Stockwell, 2000). Other figures were made with the Unix tool Xfig and Matlab 6.0 (Hanselman and Littlefield, 2001). ProMax version 7.0 was used for all the data processing. All other calculations were done by FORTRAN programs which are written by myself. The layout of the thesis was achieved using LaTeX.

CHAPTER 2

What is vertical cable seismic

2.1 Introduction

The vertical cable seismic is a patented method for acquiring and processing prestack 3-D marine seismic data which is mainly used to enhance depth imaging in structurally complex areas (Havig and Krail 1996; Krail 1991; 1994). It is based on the technology developed by the US Navy for antisubmarine warfare. This technique had been tested in three research shoots in the Gulf of Mexico before it was applied at Texaco's Strathspey field located in the North Sea.

Figure 2.1 shows a marine vertical cable seismic acquisition system. In this acquisition method, each hydrophone cable, consisting of 16 hydrophones (in the first generation), is suspended in the water column by a floating element at the top and anchored at the sea bottom. The cables are deployed in a grid fashion with a cable separation ranging from 700 metres to 1800 metres, depending on water and target depth. A data transmission cable connects each vertical cable to a recording buoy containing the instrumentation for recording the data. The source vessel shoots a series of inlines with a regular shot spacing and line spacing covering the whole swath. The system needs a minimum water depth of 70-80 metres, but can be used as deep as 1500-2000 metres.

Land vertical cable seismic can be described as multi-survey, multi-offset walka-

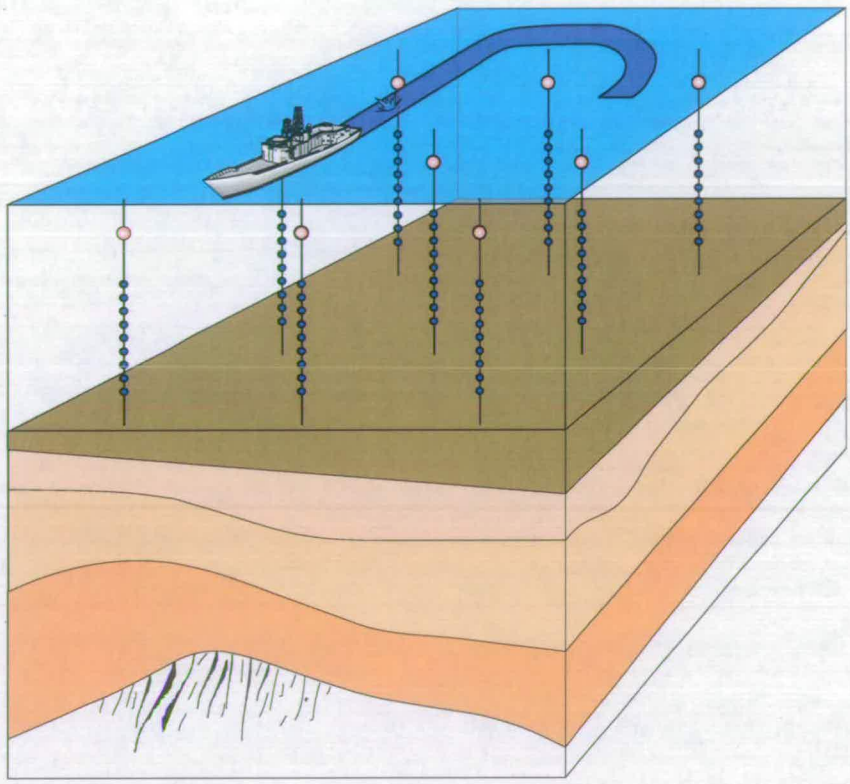


Figure 2.1: Vertical cable seismic acquisition system. Cables are suspended vertically in the water column by a floating element at the top and anchored at the sea bottom. Source boats circle around the cables.

way VSP. Vertical receiver arrays are positioned in boreholes at specified intervals, just as in VSP. The difference is that VSP experiments take place in production boreholes, but VCS surveys occur in less costly and shallower exploratory boreholes. Multi-component geophones are coupled to the borehole wall and shooting occurs at the surface. Based on the synthetic VCS data analysis, generated in a faulted earth model with undulating low-velocity layers, Ikelle and Wilson (1999) have demonstrated that VCS is able to overcome traditional land surface seismic problems like ground roll and statics. Correctly sampled VCS survey obtain equivalent or higher quality data than surface surveys and increase imaging resolution. By coupling the cable onto the walls of fluid-filled boreholes, we gain the opportunity to record four-component (pressure plus 3C geophone) data versus three-component (3C) surface data. The added pressure data can aid in the upgoing and downgoing wave separation. Also, the orientation and coupling of each receiver are guaranteed when positioned on a fixed vertical cable.

2.2 Benefits of marine VCS

Marine vertical cable seismic had its genesis in walkaway VSP, but there are important differences between them. It has no borehole, tube waves nor expensive standby rig time. VCS aims to image the entire subsurface, whilst VSP targets near-hole reflectors. It also has several advantages over a conventional towed streamer (Havig and Krail 1996; Krail 1991; Ward 1997):

(a) the motionless hydrophones are in a quiet environment compared to towed arrays so that point receivers may be used, which results in complete and accurate data analysis;

(b) it can provide high quality data for reservoir characterization because the noise level is lower at greater depths and bad weather may not affect the

vertical cables as much as a conventional streamer survey;

(c) there is sufficient distance between adjacent receivers so that up and down going waves may be separated;

(d) the vertical cables yield high resolution 3-D data which is acquired in a truly 3-D sense as opposed to conventional acquisition using a series of 2-D lines;

(e) the common mid-point assumption is never used and the data must be used in 3-D pre-stack migration; these data exhibit significant advantages to be considered as complementary information to a standard 3-D survey especially in areas that are troubled by the common mid-point and post stack migration assumption;

(f) the cable design allows complete flexibility in azimuth and offset distribution and with respect to both hydrophone spacing and cable separation. It offers virtually unlimited scope for survey planning in terms of acquisition geometry;

(g) costs of vertical cable surveys are considerably less than conventional 3-D surveys, because the seismic vessel does not have to tow a cable and can manoeuvre easily and quickly over the survey area. Thus the time taken to collect data is greatly reduced. Additionally, vertical cable seismic processing with a 3-D pre-stack depth migration is more economical than the conventional surface data processing.

2.3 Application of VCS

This technique of data acquisition reveals great potential in seismic exploration and reservoir monitoring from deep water to land surveys (Anderson et al. 1997;

Havig and Krail 1996; Krail 1993, 1994; Leach 1997; Ward 1997; Meunier and Huguet 2000). The main applications focus on high quality data acquisition, 4-D seismic monitoring, subsalt imaging and identifying anisotropy.

2.3.1 High quality data acquisition

PGS used this technology for the first time at Texaco's Strathspey field located in the North Sea. The survey objective was to get better reservoir characterization below the producing Brent group. Existing seismic data in this area, known for its high noise and strong multiples, did not permit accurate internal interpretation of this formation. The Strathspey survey comprised some 72 vertical cable positions covering about 35 sq km. Cables were positioned by anchoring them to the seafloor, with strong buoys holding them vertical, along with hydrophones attached along their length at specific locations. Bad weather experienced during the survey did not affect the VCS as much as it would have done in a conventional streamer survey.

The Strathspey vertical cable dataset is a dramatic improvement over the 1985 3-D dataset, and shows data quality comparable to the 1995 Brent Field 3-D survey, which is an optimized, state-of-the-art 3-D seismic survey. As the vertical cable seismic technology matures, more equipment is built, and additional software is developed, further improvement in data quality can be expected. In addition, vertical cable seismic acquisition becomes more cost effective in deep water, where the greater vertical spacing of the hydrophones allows for greater horizontal spacing of cables, resulting in larger swaths and reduced acquisition time.

VCS technology has been applied in marine surveys with encouraging results, and it may also significantly improve land data quality by reducing the effects of ground roll and statics, which result from the near surface low-velocity layers.

Also, vertical cable seismic, where each receiver is precisely positioned on a fixed vertical cable, has potenial to overcome problems of poor coupling and imprecise orientation of multi-component geophones, which result in low signal-to-noise ratio in multi-component land seismic acquisition.

2.3.2 Time-lapse reservoir monitoring

Vertical cables provide high-resolution seismic data with accurate positioning, virtually independent of weather conditions. This technology is also suitable for 4-D or time-lapse 3-D seismic acquisition for reservoir monitoring. Since cables are easy to deploy, and fully retrievable, this acquisition system provides an economic solution to 4-D instrumentation.

In partnership with Gaz de France and Institut Français du Pétrole, CGG has developed a continuous seismic monitoring system. It uses low-energy, stationary seismic sources operating permanently in conjunction with vertical multi-component receiver antennae. By locating the receivers in an underground environment, it is possible to distinguish the surrounding noise from reservoir-related events, i.e. to obtain an excellent signal-to-noise ratio. Because of its high degree of repeatability, the system is sensitive to changes 10 fold finer than those perceptible in a conventional 4-D survey, and thus opens the way to a new range of applications of 4-D seismic.

2.3.3 A subsalt imaging tool

In complex geological areas, like Fuji (Ward 1997), vertical cable data have shown clearer subsurface images than is possible with conventional towed-streamer data because real 3-D shot records can result in better imaging from prestack migration, especially for subsalt reflections where the CDP assumption is not valid.

In addition, VCS technology allows far offset recording out to 25 kilometres. These aerial shot records can then be efficiently pre-stack depth migrated so that the seismic reflections are correctly located before stack. This provides for the potential for much better subsalt imaging.

Recent physical modelling research (Guimarães et al. 1998) shows that the vertical cable technique is an excellent tool for obtaining a depth image of complex geological structures, and the power of stacking migrated images of different hydrophones and cables with different illumination increases tremendously the signal-to-noise ratio of the depth image resulting in more reliable subsurface information.

2.3.4 Identifying anisotropy

Since hydrophones in the vertical arrays receive seismic signals from any azimuth, full azimuthal coverage of information can be obtained. This full coverage is essential for characterizing azimuthal anisotropy in the subsurface.

Based on these multi-azimuth data, azimuthal variation of the $P-$ wave traveltime, velocity and amplitude can be estimated. These azimuthal dependencies, if they exist, reveal the direction and relative magnitude of fracture or stress-induced anisotropy, which may relate to fluid flow in the subsurface. This technology has potential applications in multi-azimuth AVO for pore-fluid estimation and in identifying fracture-induced anisotropy in subsurface strata, depending on azimuthal $P-$ wave distribution recorded at the vertical array.

2.4 A real data set

The data used in my project were acquired in the Strathspey Field of North Sea in 1995. Figure 2.2 shows the geometry of one swath, where red dots indicate the cable locations, and blue lines are the source lines. There are 12 live cables deployed in a four by three rectangle for each swath. The space between each cable is $800m$ and there are 16 hydrophones per cable with a separation of 25 feet. The source coverage in each swath is $5600 \times 5600m^2$ with a shot interval of $25m$ and a line spacing of $50m$. Six overlapping swaths were planned, giving a total subsurface coverage of 8 km (N-S) by 6.4 km (E-W), covering the whole of the Strathspey Field.

The offset-azimuth coverage is shown in Figure 2.3. The maximum offset is over $4000m$, and there is almost full azimuthal coverage at the offsets ranging from $\pm 500m$ to $\pm 2800m$. Figure 2.4 shows the CDP fold distribution for one receiver in each cable with a CDP element of $12.5m \times 12.5m$. Since there are only a few fixed receivers, the CDP distribution is not uniform for each CDP gather. Although there are 16 receivers in one cable, which could increase the CDP folds, however, the same source-cable offset for all receivers in each cable may cause only a few offsets in each CDP gather. Therefore, it is not sufficient to perform conventional velocity analysis and further data processing under the CDP assumption for vertical cable seismic data.

The depth of the sea floor in this area is about $136m$, the top hydrophone is at $14m$ under the surface, and the bottom phone is near the sea floor. Figure 2.5 shows ray paths and time-distance curves of the $P-$ wave propagation in the water column, assuming that the depth of sources is $9m$, the sea-floor is horizontal and the recording is at the top receiver. These include direct waves, reflected waves and refracted wave from the sea-floor. The velocities of $P-$wave propagation in the water and at sea-floor are $1500m/s$ and $1800m/s$, respectively.

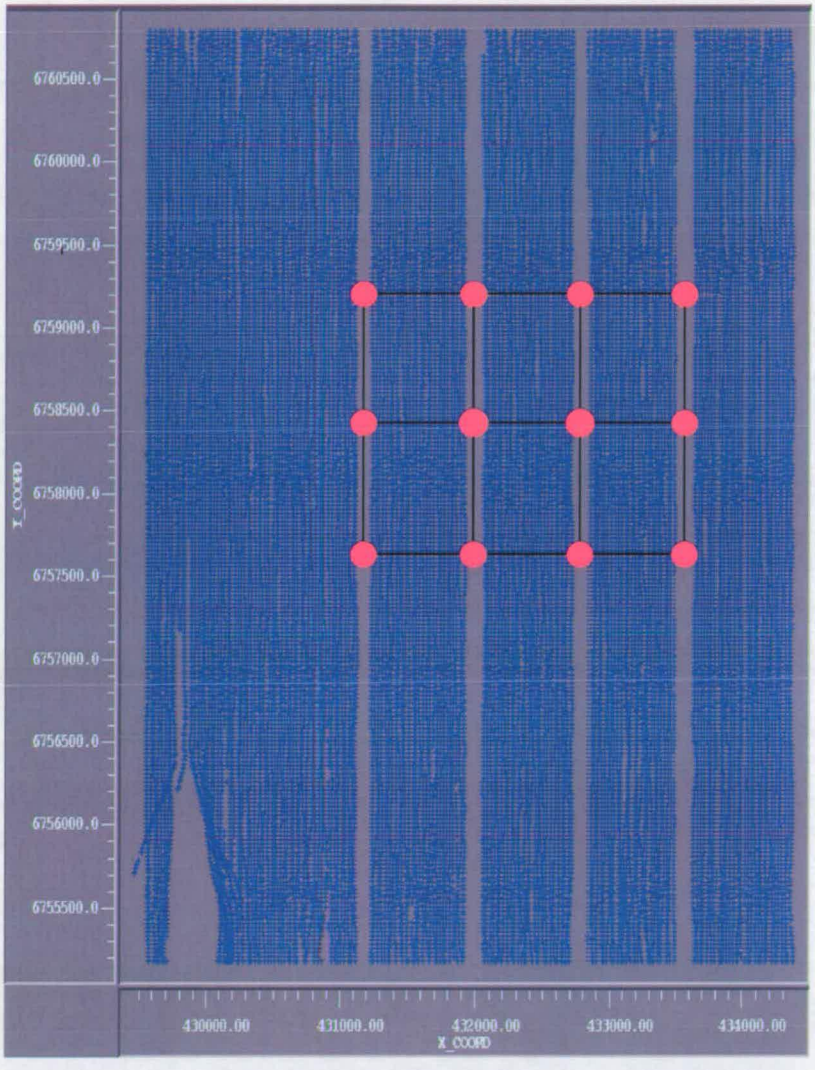


Figure 2.2: Vertical cable seismic geometry. Red dots indicate the cable locations, and blue lines are the source lines.

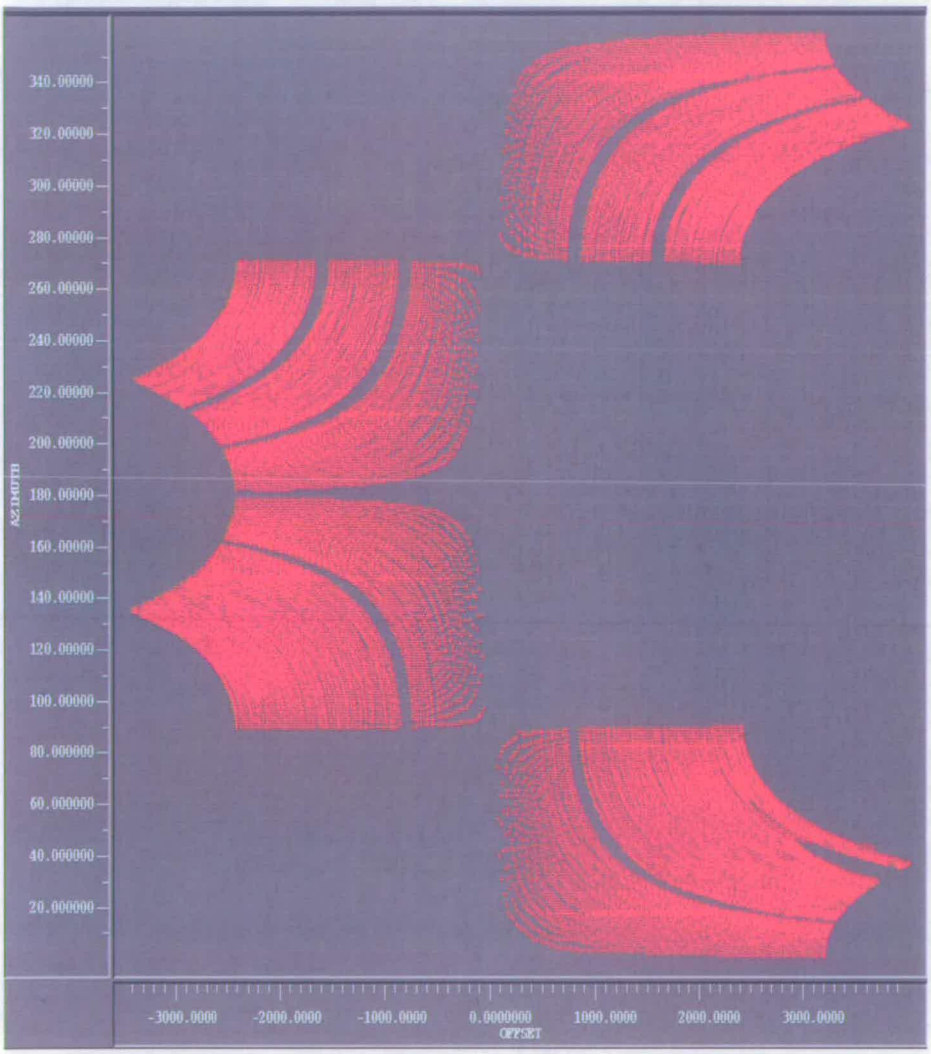


Figure 2.3: Offset-azimuth coverage.

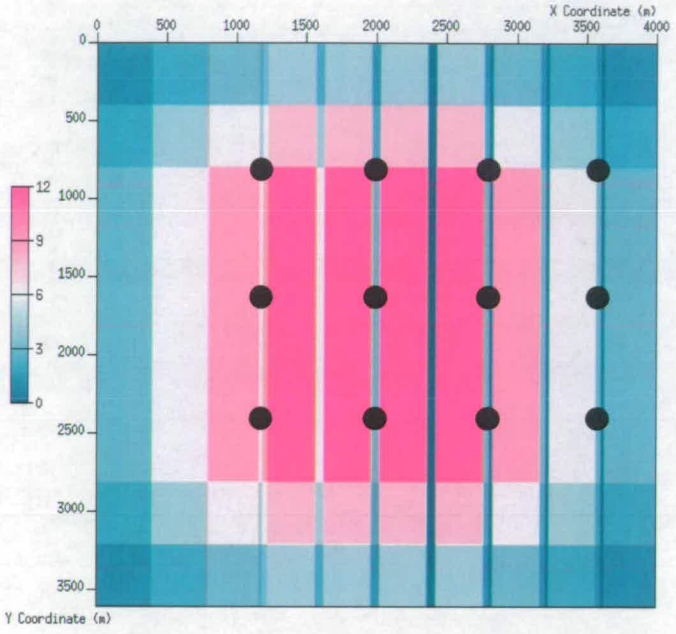
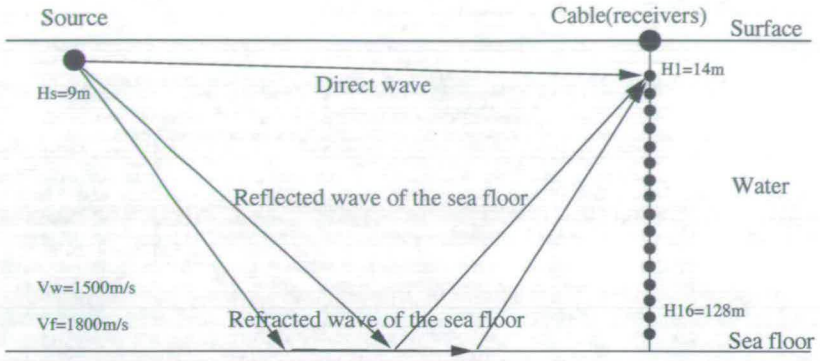


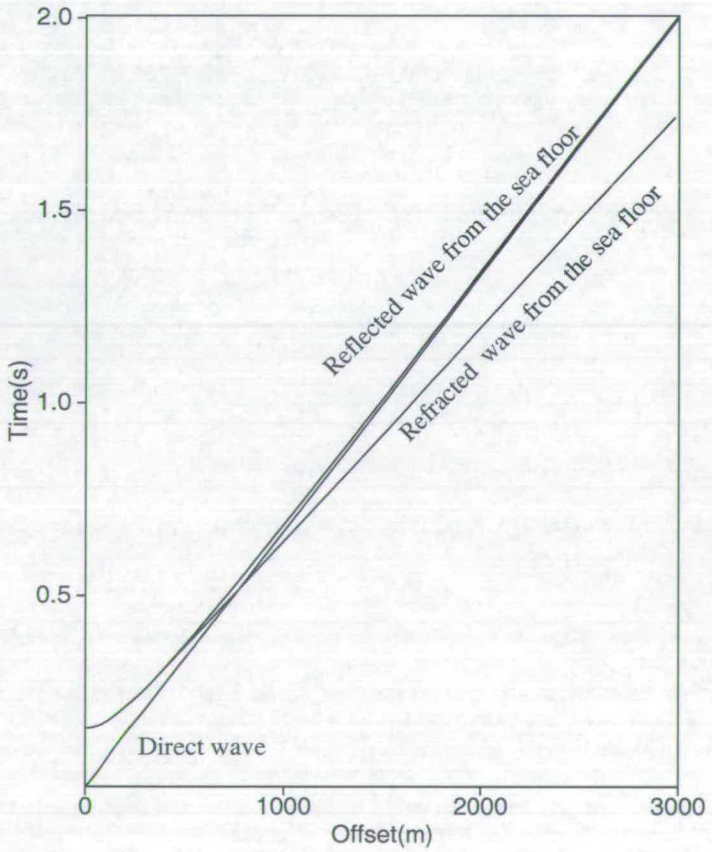
Figure 2.4: CDP fold distribution. Black dots are the locations of cables.

As the sea floor is quite shallow, the first arrivals are refracted waves when offsets are larger than 780 m.

Figures 2.6 and 2.7 show real vertical cable seismic gathers, which are taken from a selected 2-D source line of one cable. The source line is near the cable locations. As it can be seen, the common-shot gathers hold good quality upgoing and downgoing waves like VSPs, which overlay and interfere with each other. The strong water-column multiples are also shown at near offset in the common-receiver gather. The linear moveouts of direct waves and refracted waves prove that the variation of the receiver position during the survey should be very small, and in the data processing we can assume that the cable is fixed during the survey.



Ray paths



Time-distance curves

Figure 2.5: Sketch showing ray paths and time-distance curves of the $P-$wave (direct wave, reflected wave and refracted wave from the sea-floor) propagation in the water column. The source depth is $9m$, the receiver depth (choose first level) is $14m$, and the sea-floor depth is $136m$. The velocities of $P-$wave propagation in the water and at sea-floor are 1500m/s and 1800m/s, respectively.

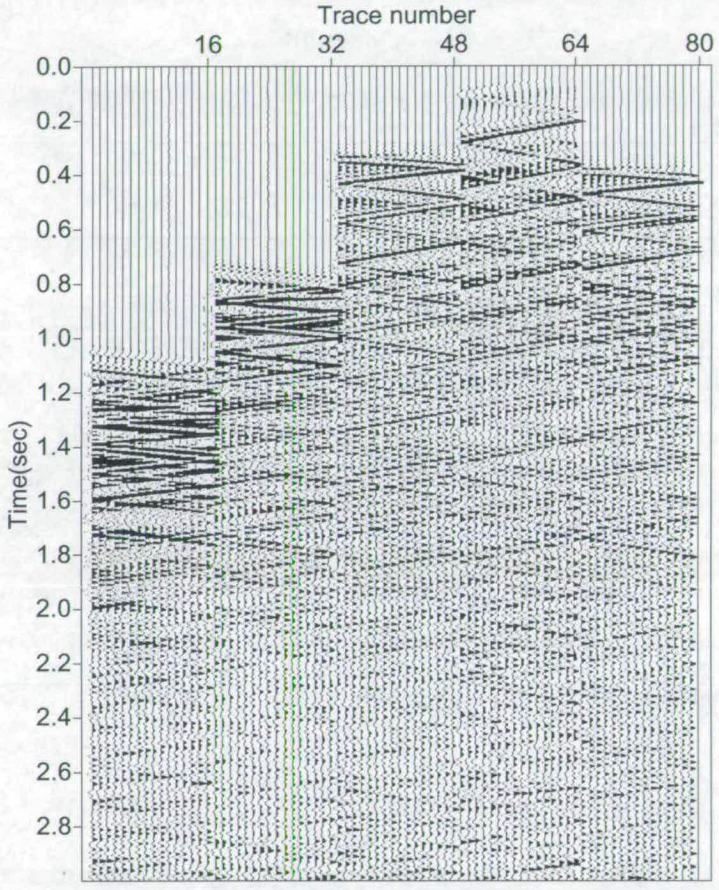


Figure 2.6: Vertical cable seismic common-shot gathers.

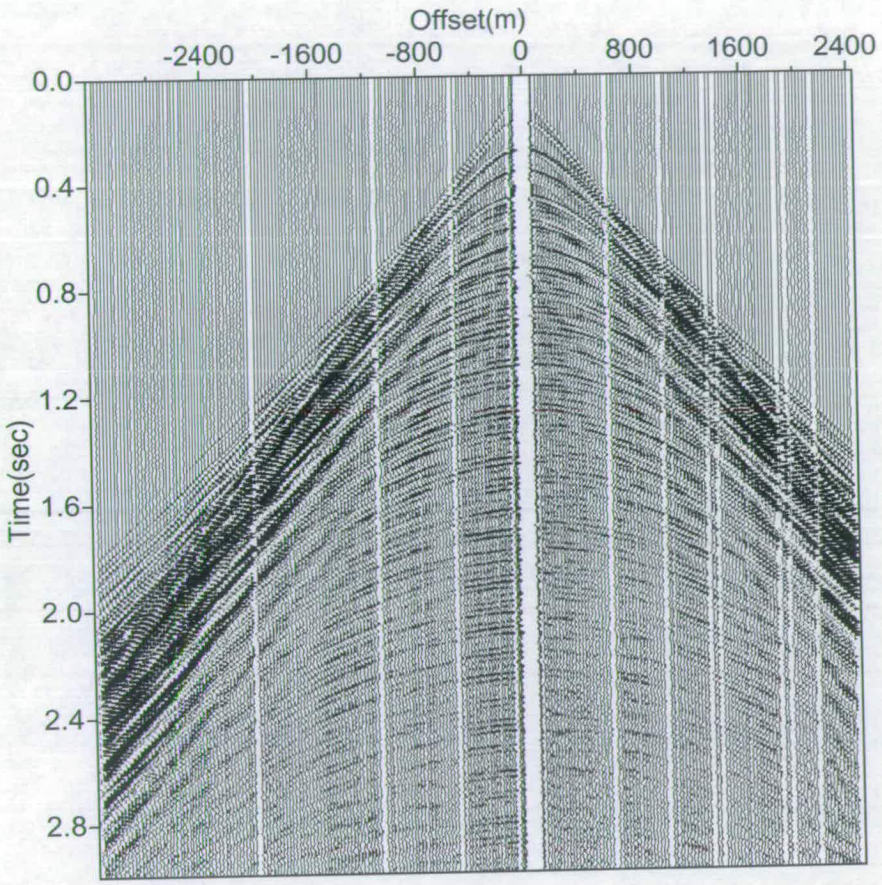


Figure 2.7: A vertical cable seismic common-receiver gather.

CHAPTER 3

Wave field separation

3.1 Introduction

The data obtained by the vertical cable seismic acquisition require unique processing before interpretation. In a similar fashion to the early processing stages of VSP, the separation of the upgoing and downgoing wavefields is an important step in VCS data processing. In this chapter, I give firstly an overview of the techniques of wavefield separation, which are commonly applied in the industry for VSP data processing, and then present a differential equation based (DEB) filter to perform the separation of upgoing and downgoing wavefields in VCS data. The principle of filtering and the processing procedure are discussed. I also examine this approach with both synthetic and real VCS data.

Although there are a lot of efficient methods to tackle this issue for zero-offset and offset VSP data processing, major difficulties may arise when achieving wavefield separation on VCS datasets. This is because there are long offset spreads in VCS acquisition, and the first arrivals are generally refracted waves (upgoing waves) instead of direct waves (downgoing waves) at almost all offsets. On the other hand, transform procedures may give undesirable artifacts in VCS data processing due to the small number of receiver locations. As a result, Sun (1997) applied an alternative, recursive approaching signal filter (RASF) to the wave

field separation problem in VCS. This filter aims to pick up the downgoing waves and suppress noise as well, when the upgoing waves are attenuated.

Unlike conventional filtering techniques, which use convolution operations or mathematical transforms, the DEB filter is actually a dip filter using a finite-difference algorithm to solve differential equations in the time and space domain. The filtering parameters are determined by a combination of user-specified dominant frequencies and apparent velocities, and can vary at every temporal and spatial point. Synthetic tests show that compared to the median filtering, or $f-k$ filtering approach, this method obtains the best result. Furthermore, application to real vertical cable seismic data indicates an encouraging performance.

3.2 Wavefield separation techniques

The concept of wavefield separation was first proposed in VSP data processing. VSP surveys record both downgoing and upgoing wavefields which overlay and interfere with each other. The analysis of upgoing waves is particularly important since these events are the ones recorded by surface seismic measurements. Thus, the wavefield separation is essential in VSP data processing, and the fact that the amplitude of an upgoing wavefield is four to five times smaller than a primary downgoing wave makes this task more difficult and complicated.

There has been much research in the area of wavefield separation for zero offset, offset and walkaway VSP data. The optimum filter technique (Seeman and Horowicz 1983; Simaan and Love 1984) is well suited for zero offset VSPs, but it requires some knowledge of the impedance structure and well-positioned data for a VSP section in which the reconstructed wavefield is placed properly, when it is applied to 2-D acquisitions, making this process time consuming and often inaccurate. Parametric decomposition of wavefields (Scott et al. 1989; Esmersoy

1990) has obtained improvement on the apparent velocity estimation by non-linear optimization instead of travel time picking, and a vectorial formation is used for multicomponent data which permits arrival angle and medium velocity estimation.

The application of 2-D Fourier transformation (Christie et al. 1983; Suprajitno and Greenhalgh 1985; Gaiser and DiSiena 1982; March and Bailey 1983), the Radon transformation (Maroof and Gravely 1984; Moon et al. 1986; Tjåland 1986; Boelle et al. 1998), multi-level median filters (Hardage 1983; Gallagher and Wise 1981; Nodes and Gallagher 1982; Arce and McLoughlin 1987), are all suggested as possible approaches to the wavefield separation problem. By comparing the application of these methods to synthetic and real data, Kommedal and Tjøstheim(1989) have shown that it is not possible to point to one particular method that will always yield the best result, particularly in multi-offset VSPs with only a few depth levels. The choice of method becomes a choice between the distortion of the waveform, if a median or an optimum array filter is applied, and the noise problem of the outer traces of the $f-k$ or $\tau-p$ filters.

Two techniques commonly used in the industry for the separation of upgoing and downgoing waves in VSP data processing are discussed in the following subsections. The first approach involves the design of velocity filters in frequency-wavenumber $(f-k)$ space. The construction of these filters requires that VSP data be recorded at uniform increments in both time and space. Both the spatial and the temporal sampling intervals must satisfy the Nyquist sampling theorem, which requires that at least two sample points be recorded within the shortest wavelength contained in the data. The second approach is a median filter technique which can be used to estimate the wave mode that is to be eliminated, and this estimate is then subtracted from each VSP trace (Hardage, 1983).

3.2.1 F-K velocity filtering

A velocity filter can attenuate unwanted signals having apparent velocities that are significantly different from those of the desired signals in the propagation directions or the magnitudes. The $f-k$ velocity filtering is an efficient way to implement the wavefield separation of VSP data since the downgoing and upgoing energy are segregated into two different half planes of $f-k$ space, depending on the propagation directions of those events.

A general procedure for the removal of VSP downgoing wave modes by using $f-k$ velocity filtering is illustrated in Figure 3.1. Data set A represents VSP data in the time-depth domain, where strong downgoing modes (heavy arrows) exhibit a down and to-the-right time stepout with depth, and upgoing modes (light arrows) have an up and to-the-right time stepout. The first processing step is a forward 2-D Fourier transform of data set A. The result is shown in data set B, where the downgoing wave modes are in the positive half plane, and upgoing wave modes are in the negative half plane of $f-k$ space. Data set C is achieved by applying a 2-D $f-k$ filter to the data set B, which results in downgoing wave modes to be rejected. Performing an inverse Fourier transform on these modified $f-k$ data generates a new data set D in the time-depth domain, in which downgoing wave modes are attenuated.

There are two problems often encountered in using the $f-k$ velocity filter (Kommedal and Tjøstheim,1989): (1) the ringing experienced when a sharp edge in the $f-k$ domain is inverted back to the $t-x$ domain; (2) the aliasing problem, where the pass- (or reject) band of the filter wraps around into the quadrant of the undesired (or desired) waves and includes (or rejects) them. Another practical problem is that a VSP data set may not always have uniform receiver sampling relative to depth, which is a prerequisite for the $f-k$ filtering.

We can design a $f-k$ velocity filter by using interactive screen processing to

compare the input and outputs of the $f-k$ filtering, evaluating the success of the single step of processing, and modifying the $f-k$ filtering parameters (accept or reject zones) until processing artifacts are minimized. The boundary between the mute window and the desired $f-k$ domain data is usually sloped to alleviate the 2-D version of Gibbs phenomena (March and Bailey 1983). As for aliasing, a narrow reject filter is suggested by Suprajitno and Greenhalgh (1985) to reduce the distortion of the spectrum of the desired signal in such cases.

3.2.2 Median filtering

The median filtering has been used extensively by the industry for smoothing data. It is a simple and robust filter, with the useful feature of preserving discontinuities in the filtered section, where upgoing waves have a discontinuity at the point they coincide with the downgoing waves in a VSP. As a non-linear filter, the output of a $2N+1$ level median filter is the statistical median of the $2N+1$ samples of a sliding window.

Applied to VSP wavefield separation, the undesired signal, after alignment of the desired signal, will appear to the median filter as a statistical outlier and be rejected or reduced. According to Hardage (1983), two properties that make median filters attractive in VSP data processing are: 1) median filters absolutely reject noise spikes, and 2) median filters pass step functions without altering them. This is because VSP data contain numerous wave modes which exhibit abrupt discontinuities or which originate and terminate at discrete depth points. These types of events can be viewed as "step functions".

A procedure for the removal of downgoing wave modes in VSP data by median filtering is shown in Figure 3.2. The main processing steps include time shifting, downgoing wave estimation and subtraction. Data set A in this figure represents the original VSP data, where the strong downgoing waves (solid arrows) exhibit

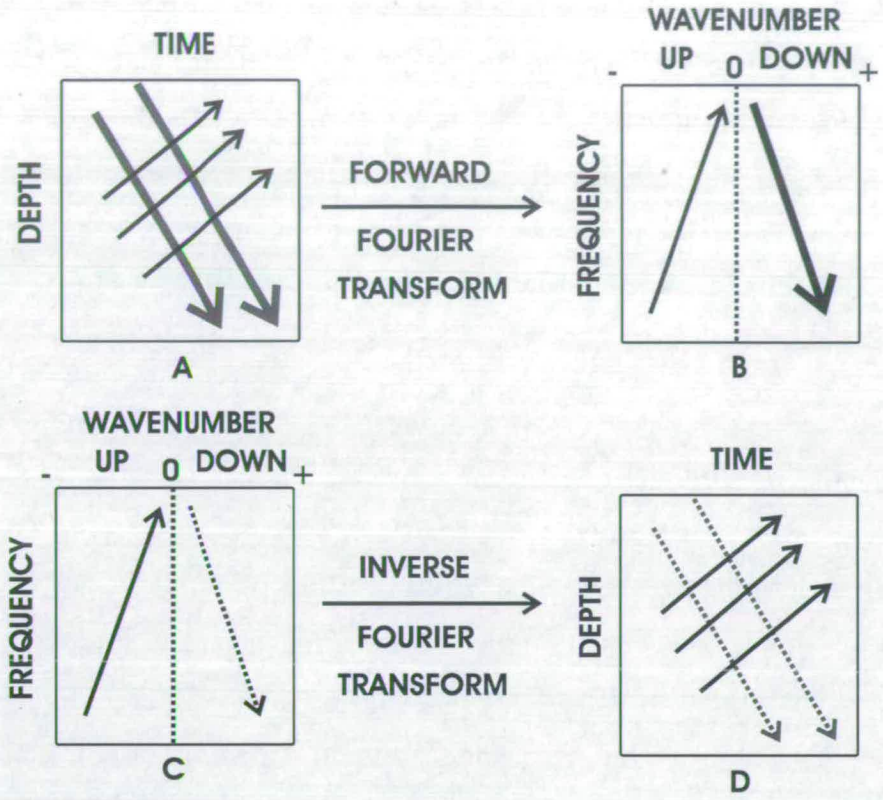


Figure 3.1: The removal of downgoing wave modes by F-K velocity filtering.

A. Original VSP data in the time-depth domain. Downgoing wave modes shown as heavy arrows. Upgoing wave modes shown by light arrows.

B. Data set A in the frequency-wavenumber domain by forward 2-D Fourier transform. Downgoing waves are in the positive half plane. Upgoing waves are in the negative half plane.

C. Data set B after applying a 2-D f-k filter. Downgoing wave modes are attenuated (dotted arrow). Upgoing wave modes are unaffected.

D. Data set C in the time-depth domain by inverse 2-D Fourier transform. Downgoing wave modes are attenuated. Upgoing wave modes are now much stronger than are the downgoing events.

a down-to-the-right time stepout with depth, and upgoing waves (dashed arrows) have an up-to-the right time stepout.

We obtain data set B where downgoing events are vertically aligned now by a negative time shift. These times are usually measured by the first-break picking in VSP data processing. A median filter is then applied to these data in the depth direction along every constant time line. The filtered section is illustrated as data set C. All upgoing modes are strongly attenuated and all downgoing events are smoothed and coherent. These objectives are achievable only if the basic seismic wavelets throughout data set B have a constant wave shape trace to trace, and the length of the filter is long enough. It is also important to measure the first-break times with extreme care, otherwise the static time shifts that create data set B in Figure 3.2 will not be precise, and downgoing events will not be aligned vertically with an optimum phase agreement. Median filtering of poorly aligned data will generate excessive noise.

The output of a median filter may exhibit some small amplitude noise spikes called "whiskers" at random locations. These spikes usually do not have a large amplitude, but they can make the output of a median filter have a slightly jagged appearance. In order to remove these whiskers, a bandpass filter may have to be applied to the median filtered data. Then, data set C is shifted back to the same time alignment as data set A. This new data set, D, is considered to only have the downgoing waves without upgoing waves and noise spikes. The last processing step is to subtract the estimated downgoing waves (data set D) trace by trace from the original VSP data (data set A). This subtraction step, shown as data set E, heavily attenuates the downgoing energy in A (the small downgoing residues are shown as weak dotted arrows), but it does not affect upgoing events since no significant upgoing energy occurs in data set D.

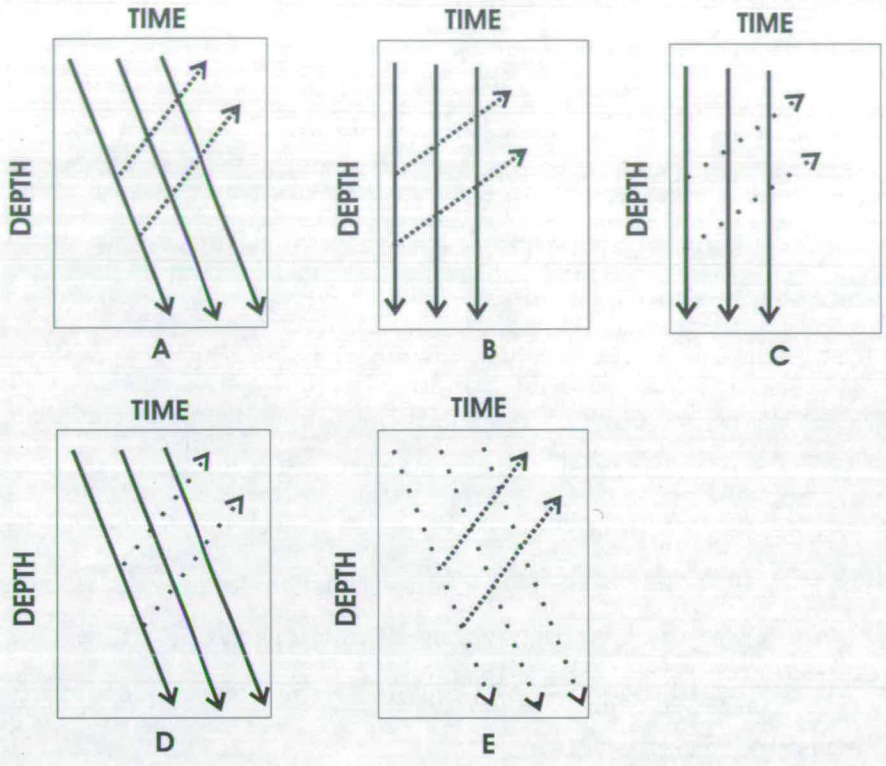


Figure 3.2: The removal of downgoing wave modes by median filtering.

A. Original VSP data. Downgoing wave modes shown as solid arrows. Upgoing wave modes shown by dashed arrows.

B. VSP data time shifted to vertically align downgoing wave modes.

C. Data set B after applying a median filter along the depth axis. Downgoing wave modes are smoothed and emphasized. Upgoing wave modes are strongly attenuated.

D. Data set C is shifted back to the same time alignment as data set A.

E. Result after subtracting data set D from data set A. Downgoing wave modes are heavily attenuated (dotted arrows). Upgoing waves are only slightly affected and are now stronger than downgoing waves.

3.3 Differential equation-based (DEB) filter

As an alternative to the conventional velocity filtering, the differential equation-based filtering method was first proposed by Li and Larner (1993) to suppress noise and enhance useful seismic signal by using a finite-difference algorithm to solve differential filtering equations. In order to achieve zero phase filtering, I design a new kind of DEB filter in performing VCS wavefield separation. The key steps of this methodology are: (1) design the filters and set up the filtering equations in the $f-k$ domain, (2) transform these equations back into the time-space domain, as variable-coefficient differential equations, and (3) use a finite-difference algorithm to solve these equations.

3.3.1 Design of 2-D DEB filter

In consideration of the simplicity of development, computational efficiency, and stability, I define transfer functions of 2-D velocity filters in the $f-k$ domain as follows, which are similar to the forms of 2-D Butterworth filters (Hale and Claerbout 1983). For a high-dip-pass filter

$$H_1(k_z,\omega)=\frac{ik_z\alpha}{ik_z\alpha+\omega^2}, \tag{3.1}$$

and for a low-dip-pass filter

$$H_2(k_z,\omega)=\frac{\omega^2}{ik_z\alpha+\omega^2}, \tag{3.2}$$

where

$$H_1(k_z,\omega)+H_2(k_z,\omega)=1. \tag{3.3}$$

Here, k_z is the wavenumber in $z-$ (depth) direction, ω denotes the angular frequency, and α is a filter parameter determined by the user-specified cut-off "dip". Based on equation (3.3), we need only discuss the high-dip-pass filter $H_1(k_z,\omega)$.

In the $f-k$ domain, a signal with a high dip means it has low apparent velocity. Thus, I also call this filter low-(apparent-velocity)-pass DEB filter, since the filtering is operated in the time-space domain by solving differential equations (discussed below). Its amplitude and phase spectra can be expressed as, respectively,

$$\begin{aligned} |H_1(k_z,\omega)| &= \frac{1}{\sqrt{1+\frac{\omega^4}{\alpha^2 k_z^2}}} \\ &= \frac{1}{\sqrt{1+4\pi^2\omega^2(\frac{V}{\alpha})^2}}, \end{aligned} \tag{3.4}$$

and

$$\begin{aligned} \theta_1(k_z,\omega) &= \tan^{-1}(\frac{\omega^2}{\alpha k_z}) \\ &= \tan^{-1}(\frac{2\pi\omega V}{\alpha}), \end{aligned} \tag{3.5}$$

where $V = f/k_z$, is the apparent velocity of a signal.

3.3.2 Determination of filter parameters

In the $f-k$ plane, the desired boundary between the pass and reject zone of an ideal dip filter can be expressed as a straight line

$$k_z = \frac{\omega}{V_c}, \tag{3.6}$$

within the range $\omega \geq 0$ and $k_z \geq 0$, where V_c is the user-specified cut-off apparent velocity. In fact, it is impossible to achieve such a desired filter with a sharp boundary in the practical seismic data processing.

Here, a special contour,

$$k_z = \pm\frac{\omega^2}{\alpha}, \tag{3.7}$$

is chosen as the approximate boundary between the pass and reject zone of the filter in the $f-k$ domain. This is the expression for the half-power contour of

$H(k_z, \omega)$ based on equation 3.4, and signals will have 45° phase shift along this contour after filtering. To accomplish desired filtered results, we should make this parabolic boundary of $H(k_z, \omega)$ as close to the straight line boundary of the ideal dip filter as possible within the range of ω and k_z of interest. Figure 3.3 shows the straight-line boundary of an ideal dip filter and the parabolic half-power contour of a low-pass DEB filter with an example of $f_d = 40Hz$ and $V_c = 2000m/s$ in the $f - k$ domain, where f_d is the user-specified dominant frequency. If we assume the intersection point of these two lines at (f_s, k_{zs}), thus

$$f_s = \frac{\alpha}{2\pi V_c}, \tag{3.8}$$

and

$$k_{zs} = \frac{\alpha}{V_c^2}. \tag{3.9}$$

The area between the straight and the parabolic line over the frequency range $(0, f_{max})$ can be expressed as

$$\begin{aligned} S &= \int_0^{\omega_s} (\frac{\omega}{V_c} - \frac{\omega^2}{\alpha}) d\omega + \int_{\omega_s}^{\omega_{max}} (\frac{\omega^2}{\alpha} - \frac{\omega}{V_c}) d\omega \\ &= \frac{\alpha^2}{3V_c^3} + \frac{\omega_{max}^3}{3\alpha} - \frac{\omega_{max}^2}{2V_c}. \end{aligned} \tag{3.10}$$

where $\omega_s = 2\pi f_s$, and $\omega_{max} = 2\pi f_{max}$. To minimize the area S, one makes

$$\begin{aligned} \frac{\partial S}{\partial \alpha} &= \frac{2\alpha}{3V_c^3} - \frac{\omega_{max}^3}{3\alpha^2}, \\ &= 0. \end{aligned} \tag{3.11}$$

This optimum gives

$$\alpha = 2^{5/3} \pi f_d V_c, \tag{3.12}$$

where the dominant frequency $f_d = 1/2 f_{max}$. As we can see, the DEB filter is a rough approximation of the ideal dip filter, with a smooth transition in amplitude from the pass to the reject zone.

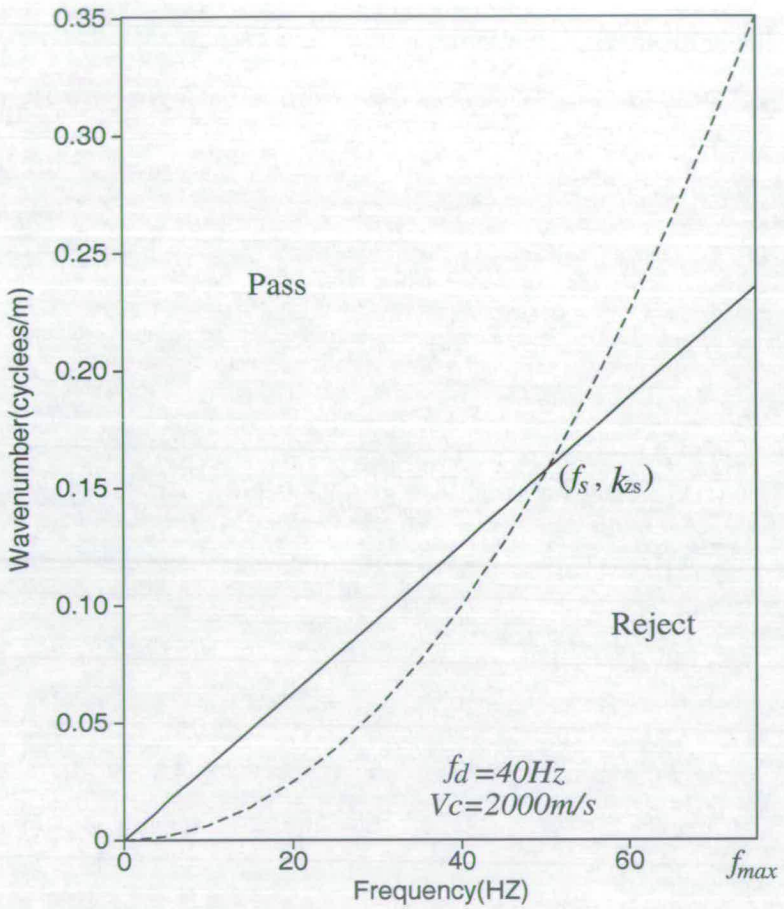


Figure 3.3: Straight-line boundary of an ideal dip filter and the parabolic half-power contour of a low-(apparent-velocity)-pass DEB filter with an example of $f_d = 40HZ$ and $V_c = 2000m/s$ in the $f - k$ domain. The intersection point of these two lines is at (f_s, k_{zs}), and the frequency range is from 0 to f_{max}.

3.3.3 Filtering equations

Since there is obvious difference in the apparent velocity between the up and down-going waves, it is possible to use a 2-D filter defined by equations (3.1) and (3.12) to perform the wavefield separation in vertical cable seismic data processing. However, this kind of filter is not a zero-phase filter. Figure 3.4 shows the phase shift versus frequency of a low-pass filter with $f_d = 30Hz$ and $V_c = 3500m/s$. The red and blue lines demonstrate phase changes of signals with apparent velocity $V = 1500m/s$ and $V = 1000m/s$, respectively, when the 2-D filter is applied to these data. As we can see, the higher the frequency, the bigger the phase shift. The phase change of the signal with apparent velocity $V = 1500m/s$ is up to 24° at the dominant frequency 30 Hz. In order to preserve the phase of signals when the filtering is carried out, I define a new low-pass filter as

$$H(k_z, \omega) = H_1(k_z, \omega) H_1'(k_z, \omega), \tag{3.13}$$

and

$$H_1'(k_z, \omega) = \frac{ik_z\alpha}{-\omega^2 + ik_z\alpha}. \tag{3.14}$$

Substitution of equations (3.1) and (3.14) into equation (3.13), gives

$$\begin{aligned} H(k_z, \omega) &= \frac{\alpha^2 k_z^2}{\omega^4 + \alpha^2 k_z^2} \\ &= |H(k_z, \omega)|. \end{aligned} \tag{3.15}$$

Thus, this is a zero phase filter.

Applying this filter to vertical cable seismic data, the filtering equation in the $f - k$ domain can be expressed as

$$\begin{aligned} Q(k_z, \omega) &= H(k_z, \omega) P(k_z, \omega) \\ &= H_1(k_z, \omega) H_1'(k_z, \omega) P(k_z, \omega) \end{aligned} \tag{3.16}$$

where $P(k_z, \omega)$ is the Fourier transformation of the input vertical cable seismic data $p(z, t)$ with respect to z and t; $Q(k_z, \omega)$ is the filtered result in the $f - k$

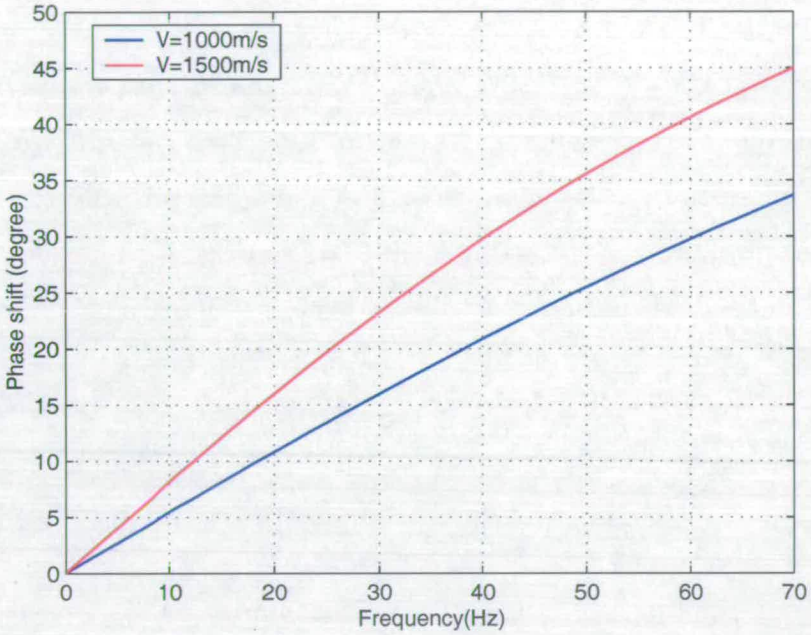


Figure 3.4: The phase shift versus frequency of a low-(apparent-velocity)-pass DEB filter with $f_d = 30HZ$ and $V_c = 3500m/s$. The red line denotes the phase shift of signals with apparent velocity $V = 1500m/s$, and the blue line is for signals with apparent velocity $V = 1000m/s$.

domain (with $q(z,t)$ in the time-space domain). The filtering based on equation (3.16) can be implemented in two steps. The filtering equations with respect to these steps are expressed as follows,

A1

$$P'(k_z,\omega) = H_1'(k_z,\omega)P(k_z,\omega), \tag{3.17}$$

A2

$$Q(k_z,\omega) = H_1(k_z,\omega)P'(k_z,\omega), \tag{3.18}$$

where $P'(k_z,\omega)$ is the filtered result of the first step based on the filtering equation **A1** in the $f-k$ domain (with $p'(z,t)$ in the time-space domain). It is also the input of the second step based on the filtering equation **A2**. These filtering equations in the time-space domain will be discussed in the following subsections.

3.3.3.1 Filtering equation A1

Substituting equation (3.14) into equation (3.17) gives

$$(-\omega^2 + ik_z\alpha)P'(k_z,\omega) = ik_z\alpha P(k_z,\omega). \tag{3.19}$$

Performing the inverse Fourier transformation of equation (3.19) into the time-space domain yields

$$\left[\alpha(z,t)\frac{\partial}{\partial z} + \frac{\partial^2}{\partial t^2}\right] p'(z,t) = \alpha(z,t)\frac{\partial p(z,t)}{\partial z}, \tag{3.20}$$

with

$$\alpha(z,t) = 2^{5/3}\pi f_d V_c(z,t), \tag{3.21}$$

where the filtering parameter $\alpha(z,t)$, determined by the dominant frequency f_d and the cut-off apparent velocity V_c, can vary in both temporal and spatial directions. To obtain equation (3.20) by inverse Fourier transformation of equation

(3.19), I have assumed that parameter $\alpha(z,t)$ varies slowly in both space and time. This is an acceptable approximation in practice only if the user-specified cut-off velocity and dominant frequency vary gradually over the effective length of the filter operator (Li and larner 1993). To solve this partial differential equation, the following conditions are used:

$$\begin{aligned} p(-\triangle z,t) &= \eta * p(0,t), \\ p'(-\triangle z,t) &= \eta * p'(0,t), \\ p'(z,0)=0, &\qquad p'(z,t_{max})=0, \end{aligned} \tag{3.22}$$

where η controls the boundary condition and is selected by trial and error ($0 \leq \eta \leq 1$), $\triangle z$ is the vertical trace spacing, and $z = 0$ is the location of the first trace in the vertical cable seismic data.

3.3.3.2 Filtering equation A2

Substituting equation (3.1) into equation (3.18) gives

$$(\omega^2 + ik_z\alpha)Q(k_z,\omega) = ik_z\alpha P'(k_z,\omega). \tag{3.23}$$

Performing the inverse Fourier transformation of equation (3.23) into the time-space domain yields

$$\left[\alpha(z,t)\frac{\partial}{\partial z} - \frac{\partial^2}{\partial t^2}\right] q(z,t) = \alpha(z,t)\frac{\partial p'(z,t)}{\partial z}, \tag{3.24}$$

where the filtering parameter $\alpha(z,t)$, defined by equation (3.21), is a function of both time and space. Similar to equation (3.20), equation (3.24) is an acceptable approximation of equation (3.23) as long as the user-specified cut-off velocity and dominant frequency vary gradually over the effective length of the filter operator, as is typically true in practice. To solve this partial differential equation, I use the following conditions:

$$p'(-\triangle z,t) = \eta * p'(0,t),$$

$$q(-\triangle z, t) = \eta * q(0,t), \qquad (3.25)$$
$$q(z,0) = 0, \qquad q(z, t_{max}) = 0,$$

where η controls the boundary condition and is selected by trial and error ($0 \leq \eta \leq 1$), $\triangle z$ is the vertical trace spacing, and $z = 0$ is the location of the first trace in the vertical cable seismic data.

3.3.4 Finite-difference algorithm

Equations (3.20) and (3.24) denote the filtering equation in the time-space domain. I develop a finite difference algorithm to solve these differential equations by using the modified Crank-Nicholson difference pattern. Instead of using ordinary central-difference pattern, I choose Claerbout's (1985) 1/6 strategy to improve the approximation accuracy of the second order of the partial differential with respect to time. The solutions for difference equations of filtering equations **A1** and **A2** are derived respectively in the next two subsections.

3.3.4.1 Differential equation A1

From Claerbout's (1985) difference approximation used in the finite difference migration, we have

$$\frac{\partial^2 p'(z,t)}{\partial t^2} \approx \frac{\delta_{tt}}{\Delta t^2(1+\beta\delta_{tt})} p'(z,t), \qquad (3.26)$$

with

$$\beta = 0.25 - 1/\pi^2, \qquad (3.27)$$

and

$$\delta_{tt} p'_m(n) = p'_m(n+1) - 2p'_m(n) + p'_m(n-1), \qquad (3.28)$$
$$n = 1, 2, 3, \cdots, L, \quad m = 1, 2, 3, \cdots, M,$$

where Δt is the time sampling interval, L is the maximum length of seismic traces in sample points and M is the maximum number of traces processed.

Using the modified Crank-Nicholson difference pattern, the difference equation **A1** with respect to filtering equation (3.20) can be expressed as

$$\frac{\alpha_m(n)}{\Delta z}\delta_z p'_m(n) + \frac{\delta_{tt}}{2\Delta t^2(1+\beta\delta_{tt})}\left[p'_m(n) + p'_{m-1}(n)\right] = \frac{\alpha_m(n)}{\Delta z}\delta_z p_m(n), \tag{3.29}$$

where Δz is the trace interval, and

$$\begin{aligned}\delta_z p'_m(n) &\equiv p'_m(n) - p'_{m-1}(n)\\ \delta_z p_m(n) &\equiv p_m(n) - p_{m-1}(n).\end{aligned}$$

The conditions for determining the solution in equation (3.22) can be written as

$$\begin{aligned}\mathbf{p}_{-1} &= \eta\mathbf{p}_0,\\ \mathbf{p}'_{-1} &= \eta\mathbf{p}'_0,\\ p'_m(0) = 0,\ p'_m(L+1) &= 0,\end{aligned} \tag{3.30}$$

where

$$\begin{aligned}\mathbf{p}_m &\equiv [p_m(1), p_m(2), p_m(3), \cdots, p_m(L)]^T,\\ \mathbf{p}'_m &\equiv [p'_m(1), p'_m(2), p'_m(3), \cdots, p'_m(L)]^T.\end{aligned}$$

We may further express equation (3.29) in matrix terms as

$$\overrightarrow{\mathbf{A}'}\mathbf{p}'_m = \overrightarrow{\mathbf{B}'}\mathbf{p}'_{m-1} + \overrightarrow{\mathbf{C}'}(\mathbf{p}_m - \mathbf{p}_{m-1}), \tag{3.31}$$

where

$$\overrightarrow{\mathbf{A}'} = \begin{bmatrix} b'_1 & a'_1 & 0 & 0 & \cdots & 0 & 0\\ a'_2 & b'_2 & a'_2 & 0 & \cdots & 0 & 0\\ 0 & a'_3 & b'_3 & a'_3 & \cdots & 0 & 0\\ \vdots & \vdots & \vdots & \vdots & \ddots & \vdots & \vdots\\ 0 & 0 & 0 & 0 & \cdots & a'_L & b'_L \end{bmatrix},$$

$$\vec{\mathbf{B}'} = \begin{bmatrix} d'_1 & c'_1 & 0 & 0 & \cdots & 0 & 0 \\ c'_2 & d'_2 & c'_2 & 0 & \cdots & 0 & 0 \\ 0 & c'_3 & d'_3 & c'_3 & \cdots & 0 & 0 \\ \vdots & \vdots & \vdots & \vdots & \ddots & \vdots & \vdots \\ 0 & 0 & 0 & 0 & \cdots & c'_L & d'_L \end{bmatrix},$$

$$\vec{\mathbf{C}'} = \begin{bmatrix} f'_1 & e'_1 & 0 & 0 & \cdots & 0 & 0 \\ e'_2 & f'_2 & e'_2 & 0 & \cdots & 0 & 0 \\ 0 & e'_3 & f'_3 & e'_3 & \cdots & 0 & 0 \\ \vdots & \vdots & \vdots & \vdots & \ddots & \vdots & \vdots \\ 0 & 0 & 0 & 0 & \cdots & e'_L & f'_L \end{bmatrix},$$

and

$$\begin{aligned} a'_n &= g_m(n)\beta + 1, \\ b'_n &= g_m(n) - 2(1 + g_m(n)\beta), \\ c'_n &= g_m(n)\beta - 1, \\ d'_n &= g_m(n) - 2(g_m(n)\beta - 1), \\ e'_n &= g_m(n)\beta, \\ f'_n &= g_m(n)(1 - 2\beta), \\ g_m(n) &= 2^{8/3}\pi\Delta t^2 f_d V_{cm}(n)/\Delta z, \\ m &= 0, 1, 2, \cdots\cdots M. \end{aligned}$$

This equation shows an implicit finite difference for the first step implementation of 2-D DEB filtering. Being a diagonally dominant tridiagonal system of equations which are explicitly recursive in the space direction, this equation can be solved by a fast algorithm. Also , one can see that it only requires two input traces to obtain one output trace in this filtering step based on equation (3.31).

3.3.4.2 Differential equation A2

In a similar way to the first filtering step, I also use the modified Crank-Nicholson difference pattern to solve the filtering equation (3.24) in the second step, the responding difference equation **A2** can be expressed as

$$\frac{\alpha_m(n)}{\Delta z}\delta_z q_m(n) - \frac{\delta_{tt}}{2\Delta t^2(1+\beta\delta_{tt})}\left[q_m(n)+q_{m-1}(n)\right] = \frac{\alpha_m(n)}{\Delta z}\delta_z p'_m(n), \tag{3.32}$$

with

$$\begin{aligned}\delta_z p'_m(n) &\equiv p'_m(n) - p'_{m-1}(n),\\ \delta_z q_m(n) &\equiv q_m(n) - q_{m-1}(n),\end{aligned}$$

and

$$\delta_{tt} q_m(n) = q_m(n+1) - 2q_m(n) + q_m(n-1),$$

$$n = 1, 2, 3, \cdots, L, \quad m = 1, 2, 3, \cdots, M,$$

where Δt and Δz are the time sampling and trace intervals, respectively, L is the maximum length of seismic traces in sample points and M is the maximum number of traces processed.

The conditions for determining the solution in equation (3.25) can be written as

$$\begin{aligned}\mathbf{p}'_{-1} &= \eta\mathbf{p}'_0,\\ \mathbf{q}_{-1} &= \eta\mathbf{q}_0,\\ q_m(0) = 0,\ q_m(L+1) &= 0,\end{aligned} \tag{3.33}$$

where

$$\begin{aligned}\mathbf{q}_m &\equiv [q_m(1), q_m(2), q_m(3), \cdots, q_m(L)]^T,\\ \mathbf{p}'_m &\equiv [p'_m(1), p'_m(2), p'_m(3), \cdots, p'_m(L)]^T.\end{aligned}$$

Finally, the difference equation **A2** can be expressed in matrix terms as

$$\vec{\mathbf{A}}\mathbf{q}_m = \vec{\mathbf{B}}\mathbf{q}_{m-1} + \vec{\mathbf{C}}(\mathbf{p}'_m - \mathbf{p}'_{m-1}) \tag{3.34}$$

where

$$\vec{\mathbf{A}} = \begin{bmatrix} b_1 & a_1 & 0 & 0 & \cdots & 0 & 0 \\ a_2 & b_2 & a_2 & 0 & \cdots & 0 & 0 \\ 0 & a_3 & b_3 & a_3 & \cdots & 0 & 0 \\ \vdots & \vdots & \vdots & \vdots & \ddots & \vdots & \vdots \\ 0 & 0 & 0 & 0 & \cdots & a_L & b_L \end{bmatrix},$$

$$\vec{\mathbf{B}} = \begin{bmatrix} d_1 & c_1 & 0 & 0 & \cdots & 0 & 0 \\ c_2 & d_2 & c_2 & 0 & \cdots & 0 & 0 \\ 0 & c_3 & d_3 & c_3 & \cdots & 0 & 0 \\ \vdots & \vdots & \vdots & \vdots & \ddots & \vdots & \vdots \\ 0 & 0 & 0 & 0 & \cdots & c_L & d_L \end{bmatrix},$$

$$\vec{\mathbf{C}} = \begin{bmatrix} f_1 & e_1 & 0 & 0 & \cdots & 0 & 0 \\ e_2 & f_2 & e_2 & 0 & \cdots & 0 & 0 \\ 0 & e_3 & f_3 & e_3 & \cdots & 0 & 0 \\ \vdots & \vdots & \vdots & \vdots & \ddots & \vdots & \vdots \\ 0 & 0 & 0 & 0 & \cdots & e_L & f_L \end{bmatrix},$$

and

$$\begin{aligned} a_n &= g_m(n)\beta - 1, \\ b_n &= g_m(n) + 2(1 - g_m(n)\beta), \\ c_n &= 1 + g_m(n)\beta, \\ d_n &= g_m(n) - 2(1 + g_m(n)\beta), \\ e_n &= g_m(n)\beta, \\ f_n &= g_m(n)(1 - 2\beta), \\ g_m(n) &= 2^{8/3}\pi\Delta t^2 f_d V_{cm}(n)/\Delta z, \end{aligned}$$

$$m = 0, 1, 2, \cdots\cdots M.$$

Equation (3.34) is a finite difference solution for the second step implementation of 2-D DEB filtering. As we can see, the difference equation **A2** has the same form as the difference equation **A1**. Performing DEB filtering with these two steps is based on solving two diagonally dominant tridiagonal systems of equations which are explicitly recursive in the space direction, and it only requires two input traces to obtain one output trace in both filtering steps. Therefore, this filtering has high computational efficiency.

3.3.5 Application to VCS wavefield separation

The flexibility of design and the simplicity of implementation make this approach attractive in velocity filtering. A processing scheme of wavefield separation for vertical cable seismic data using a DEB filter is illustrated in Figure 3.5, which includes forward time shifting, filtering, backward time shifting and subtraction steps. Data set A in this figure shows the original vertical cable seismic data, in which downgoing events (solid arrows) demonstrate a down and to-the-right time stepout with depth, and upgoing events (dashed arrows) have an up and to-the-right time stepout.

To begin, we need to pick the arrival time of one downgoing event instead of the first break time, and then shift each trace to the left by an amount equal to its picked time. This is because the first break in vertical cable seismic data is not always in downgoing waves. This step is shown as data set B, where downgoing events are vertically aligned. A low-(apparent-velocity)-pass filter is now applied to these data by using the DEB filtering technique, where the various dominant frequencies and cut-off velocities along the temporal direction may be used within filtering. This filtering step, shown as data set C, severely attenuates all downgoing events, and upgoing waves are only slightly affected

near the boundary of the filter.

The final upgoing wave section, shown as data set D, is achieved by backward time shifting of data set C to the same time alignment as data A. There are only small downgoing residues shown as weak dotted arrows in these data. Subtracting the estimated upgoing waves (data set D) trace by trace from the original vertical cable seismic data (data set A) generates the expected downgoing wave section shown as data set E, in which upgoing waves are heavily attenuated, but this subtraction does not affect downgoing modes since no significant downgoing energy occurs in data set D.

3.4 Comparison of different filtering techniques for wavefield separation

To examine the filtering performance on the wavefield separation, I compare this method to applications of the $f-k$ filter and median filter with synthetic data shown in Figure 3.6. In the original data (Figure 3.6(a)), apparent velocities are 1600m/s, 2000m/s and 2400m/s, for the first, second and third downgoing wave events, respectively, and the corresponding upgoing wave events have negative apparent velocities -1600m/s, -2000m/s and -2400m/s, respectively. The maximum of relative differences among these apparent velocities is up to 50 percent. The wavelet used is a 30-Hz zero-phase Ricker waveform with a length of 100ms. There are 16 traces with a trace interval of 8m and a time interval of 2ms in this dataset.

The first step is to horizontally align the second downgoing wave event by a negative time shift. The new dataset is shown in Figure 3.6(b), where the apparent velocities of events become 8000m/s, -889m/s, infinity, -1000m/s, 12000m/s and -1090m/s, respectively. Then I design a low-pass DEB filter with a cut-off


EX BIBL. UNIV. EDINBURGH

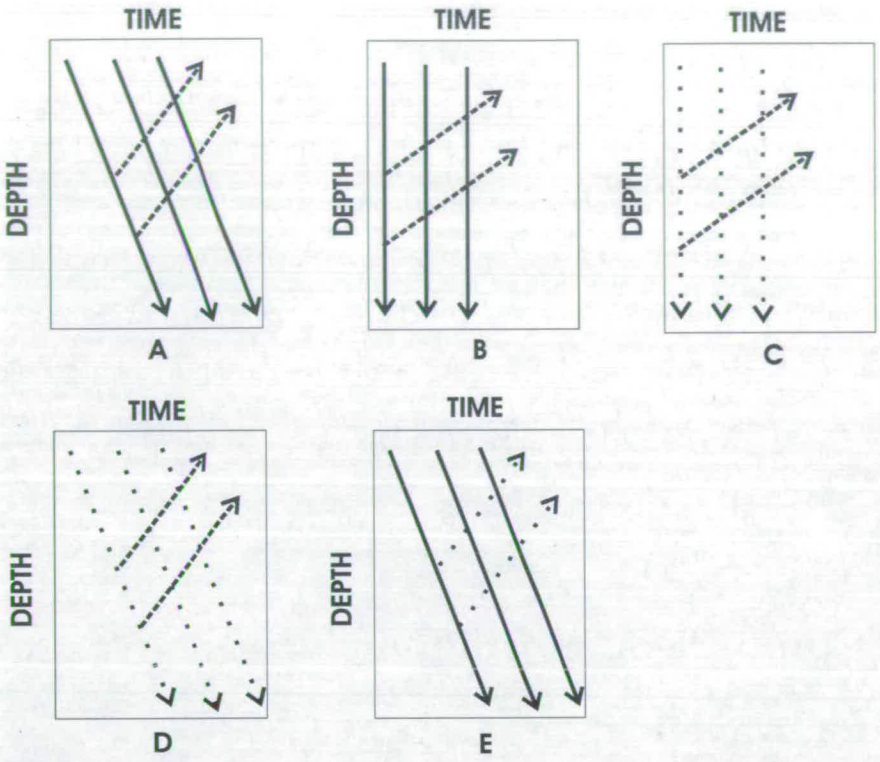


Figure 3.5: A scheme of wavefield separation in vertical cable seismic data processing using DEB filtering technique.

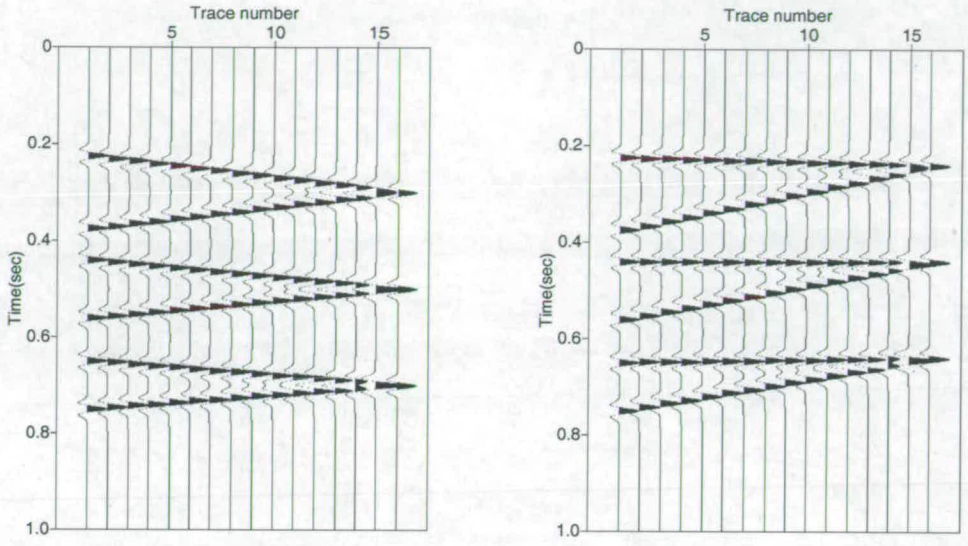
A. Original VCS data. Downgoing wave modes shown as solid arrows. Upgoing wave modes shown by dashed arrows.

B. VCS data time shifted to vertically align downgoing wave modes.

C. Data set B after applying a DEB filter along the depth axis. Downgoing wave modes are completely rejected (dotted arrows). Upgoing wave modes are slightly attenuated near the boundary of the filter.

D. Data set C is shifted back to the same time alignment as data set A.

E. Result after subtracting data set D from data set A. Upgoing wave modes are heavily attenuated (dotted arrows). Downgoing waves are only slightly affected.



(a) (b)

Figure 3.6: (a) Original synthetic data with three downgoing wave events and upgoing wave events. (b) After time shifting to horizontally align the second downgoing wave event.

velocity of 2500m/s and a dominant frequency of 30Hz.

Figures 3.7 and 3.8 show results of the wavefield separation using an $f-k$ filter with an attempt to reject downgoing wavefields, a median filter with a 9 point window moving size along the depth direction, and the DEB filter. As we can see, the DEB filtering yields the best quality on both upgoing wavefields shown in Figure 3.7(c) and downgoing wavefields shown in Figure 3.8(c), although there are still some small residues left on both sections. This is because the DEB filter uses a smooth cut-off boundary between the pass and reject zone.

The $f-k$ filter produces some artifacts on the outer traces and some residual energy is also present both on Figure 3.7(a) and Figure 3.8(a). On the median filtered sections (Figure 3.7(b) and Figure 3.8(b)), we can see that there are strong upgoing wave modes left in the downgoing wave section, and the waveforms are also distorted significantly in the outer traces.

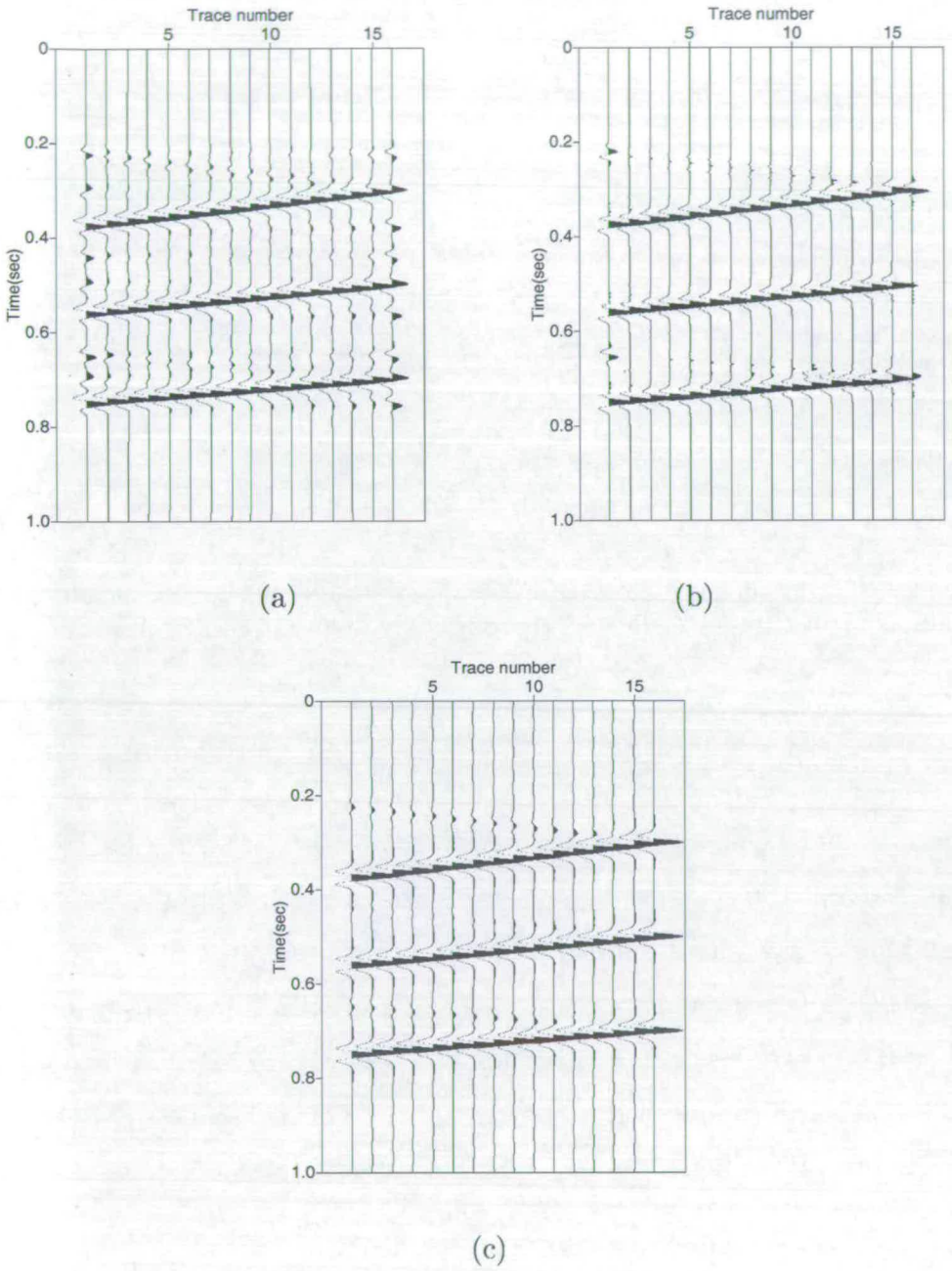


Figure 3.7: Synthetic upgoing wavefield sections obtained by (a) the $f-k$ filtering, (b) median filtering, and (c) DEB filtering from the data set shown in Figure3.6.

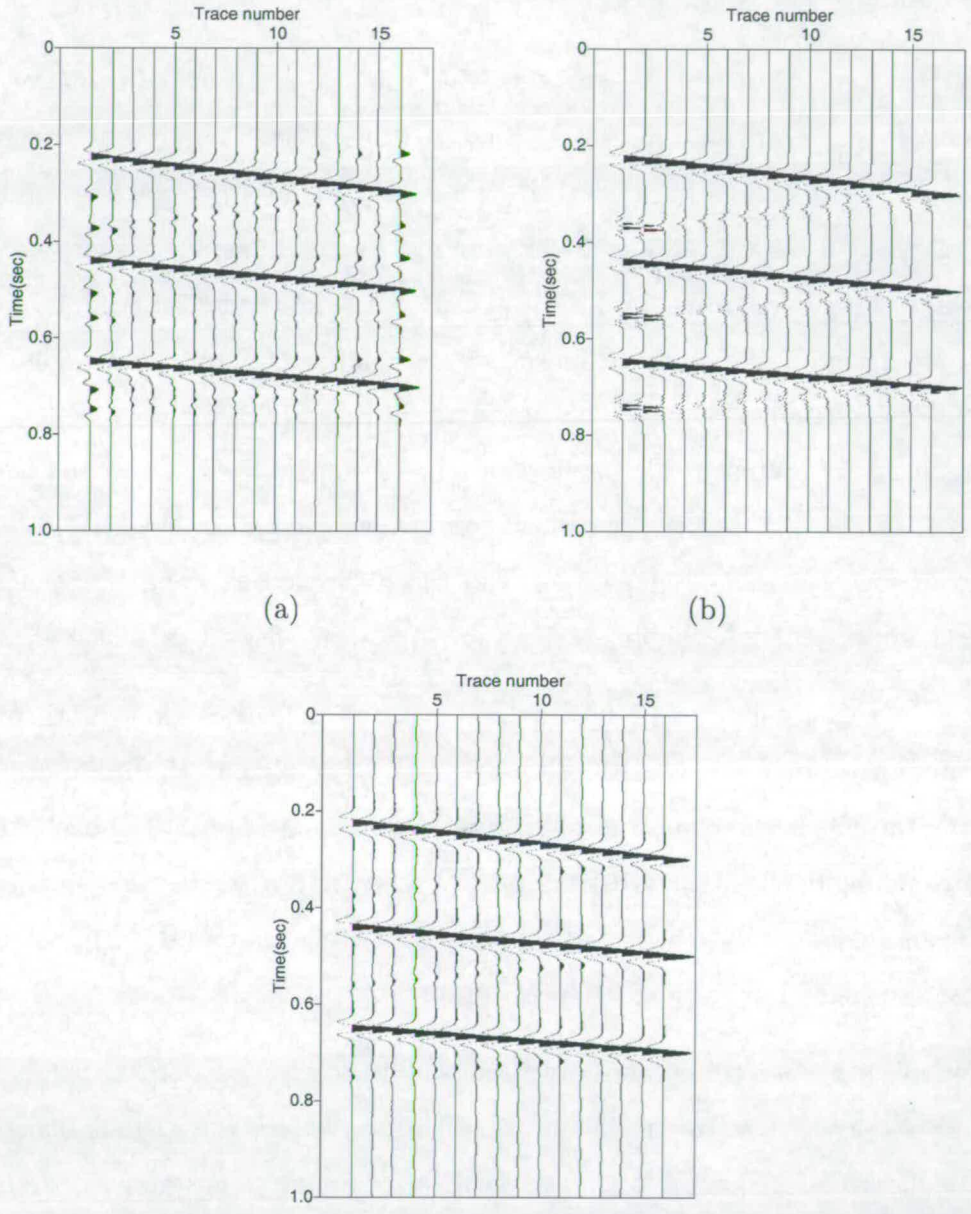


Figure 3.8: Synthetic downgoing wavefield sections obtained by (a) the $f-k$ filtering, (b) median filtering, and (c) DEB filtering from the data set shown in Figure3.6.

3.5 Application to real VCS data

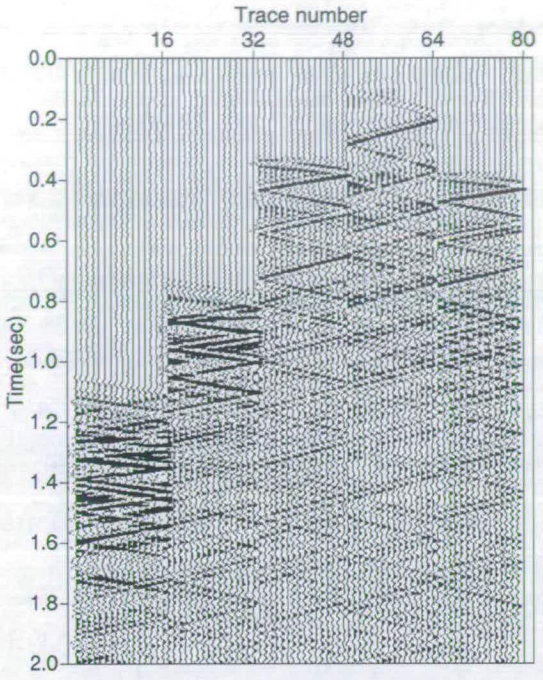
I also examine this wavefield separation algorithm on real vertical cable seismic data shown in Figures 3.9 and 3.11. In these data sets, there are 16 receivers on each cable with a depth interval of 25 feet. Figure 3.9(a) shows five common shot gathers, offsets are 1833m, 1233m, 486m, 64m and 569m for the left to right gathers, respectively. To begin, I pick up the arrivals of the first downgoing wave events in each gather, then make a negative time shifting to horizontally align this event at the location of 300ms. This new data set is shown in Figure 3.9(b), where downgoing wave events are almost horizontal at the near offset (the second gather from the right), the upgoing and downgoing wave events significantly interfere with each other at far offset gathers, and the differences of apparent velocities between upgoing and downgoing waves vary from near-offset to far-offset gathers.

A low-pass DEB filter with slowly varied cut-off velocities along both offset and time directions is applied to this data set. The output of this filtering is upgoing wavefields shown in Figure 3.10(a), where signals are shifted back to the same time alignment of the original data. Figure 3.10(b) shows the downgoing wavefields generated by subtracting the upgoing wavefields from the original data. We can see that both sections are of good quality.

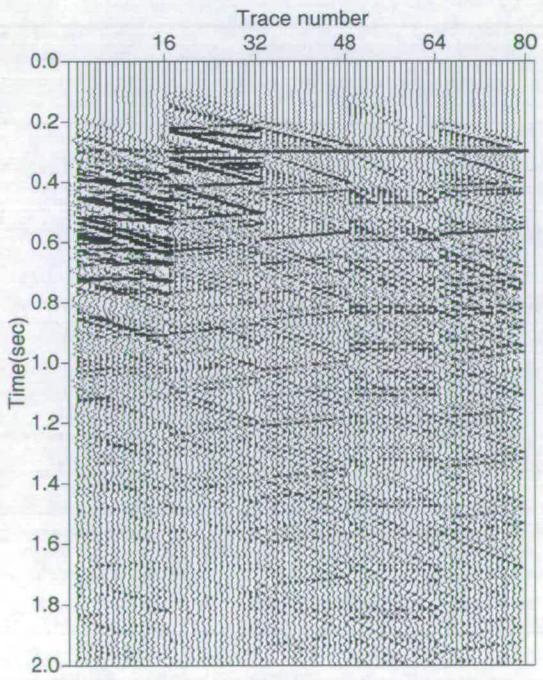
Figure 3.11 shows a common receiver (the eighth receiver) vertical cable seismic gather with a offset range of -1800m to 1800m in a selected 2-D shot line. The results of wavefield separation using a DEB filter are now shown in Figure 3.12. After this wave field separation, the direct waves and surface multiples are in the down-going wave section (Figure 3.12(a)), but the primaries and multiples of the sea bottom are moved to the up-going section (Figure 3.12(b)). It is evident that the upgoing and downgoing waves are clearly separated, and there are no artifacts on the outer traces.

3.6 Conclusions

The differential equation-based filtering approach using a finite difference algorithm, unlike the $f-k$ or $\tau-p$ filtering, does not require a large number of traces and it can also overcome the harmful artifacts related to spatial aliasing and side effects in the $f-k$ filtering. Both the synthetic and real vertical cable seismic data tests show that this technique can successfully perform the upgoing and downgoing wavefield separation in vertical cable seismic data processing. In addition, the design of filtering parameters is quite flexible and it also can be adapted to vertical cable seismic data with nonuniform spatial sampling. This filtering is accomplished in the time-space domain by solving a diagonally dominant tridiagonal system of equations, thus it has quite high computational efficiency.

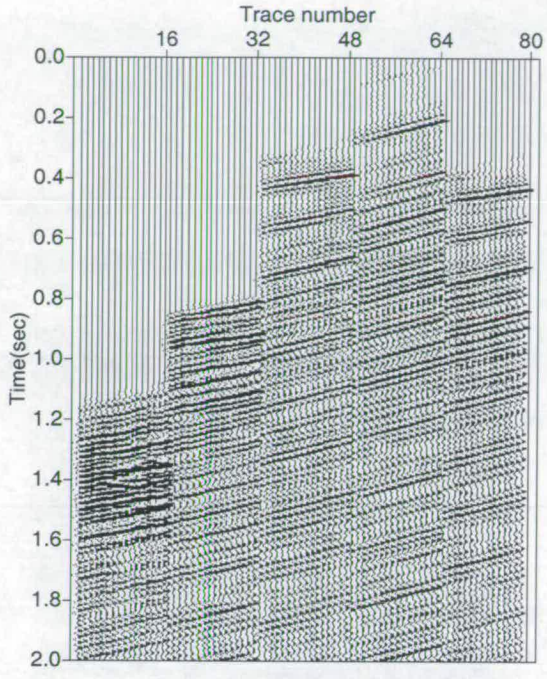


(a)

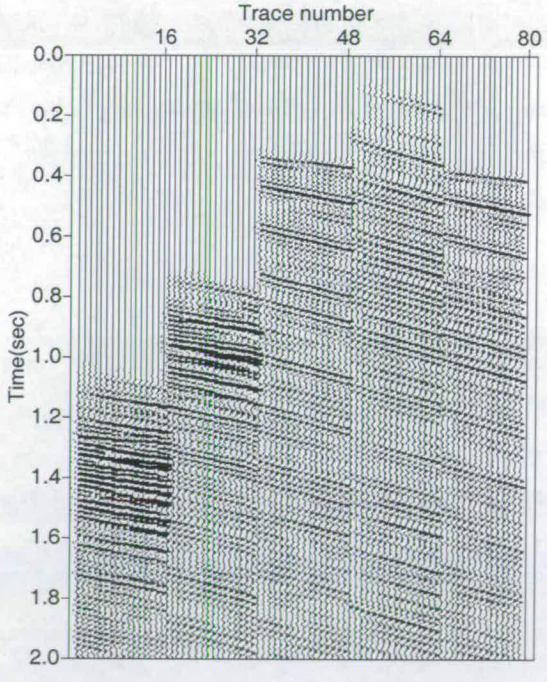


(b)

Figure 3.9: Real VCS common shot gathers: (a) Original data with five shots in different offsets, and there are 16 receivers in each gather; (b) after a negative time shifting to horizontally align the first down going wave events at 300ms.



(a)



(b)

Figure 3.10: The results of Figure 3.9 filtered by using a DEB filter with varied cut-off velocities both on offset and time directions: (a) downgoing wavefield section; (b) upgoing wavefield section.

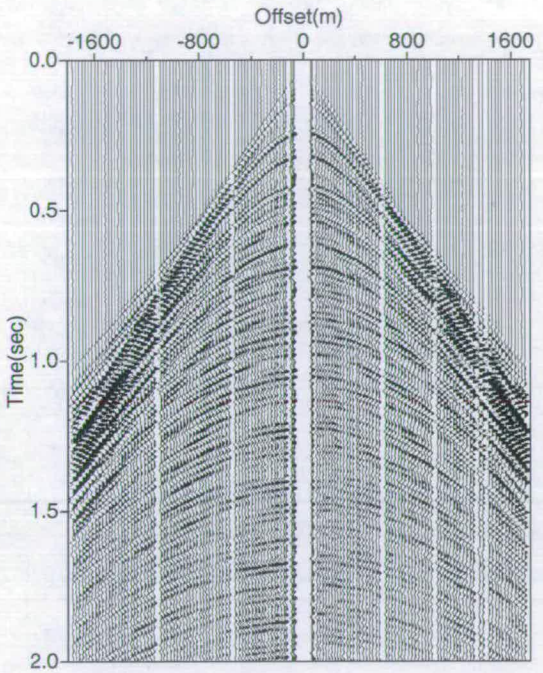
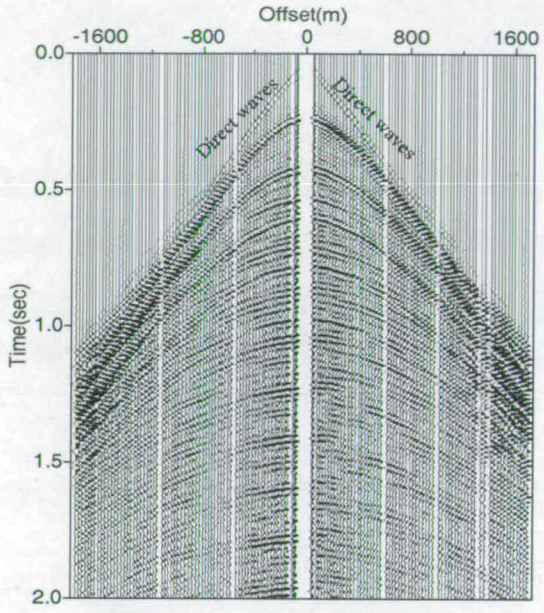
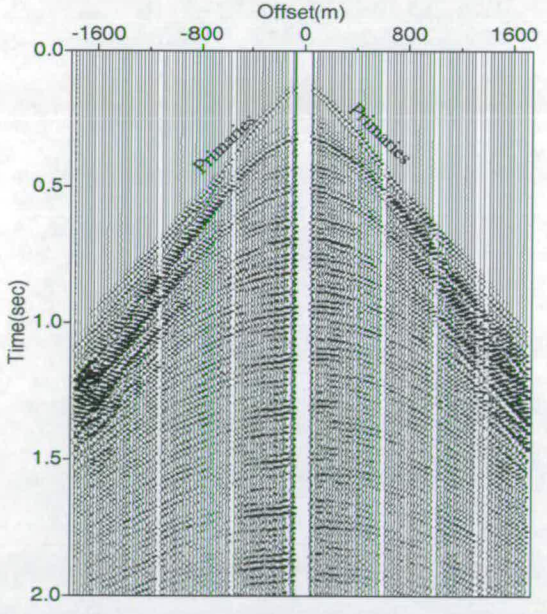


Figure 3.11: A real common-receiver VCS gather with an offset range of -1800m to 1800m.



(a)



(b)

Figure 3.12: The results of Figure 3.11 filtered by a DEB filter with varied cut-off velocities both on offset and time directions: (a) down-going wave section, (b) up-going wave section. The direct waves are present in section (a), whilst the sea bottom primaries are moved to section (b).

CHAPTER 4

Multiple Suppression

4.1 Introduction

As with other marine exploration methods, multiples are still one of the most troublesome forms of noise in the vertical cable seismic data. In this chapter, I first give the definitions of multiples that may be present in the VCS upgoing wavefields, which include water-bottom, peg-leg, surface and intra-bed multiples, and review the commonly-used methods for the suppression of these multiples in the surface data. Since the concept of CDP or CMP gather is not effective in vertical cable seismic data processing, the moveout-based methods of multiple suppression can not be applied to remove multiples in vertical cable seismic data. In the meantime, there are only a small number of traces at each common-shot gather, and these receivers have the same horizontal positions at each cable, therefore, the wave-equation-based prediction and subtraction methods can not be used for the suppression of receiver side multiples in VCS data, too. Ikelle (2001) presented an inverse scattering algorithm for attenuating primaries, free-surface multiples, and the receiver ghosts of free-surface multiples while preserving the receiver ghosts of primaries. It assumes that surface seismic data are available or that they can be computed from VCS data after the upgoing and downgoing wavefield separation at the receiver locations.

A special processing scheme has been proposed for VCS multiple suppression in this chapter. I take the advantage of the unique vertical cable seismic geometry to separate the upgoing and downgoing wavefields in vertical cable seismic data. The technique used for this separation is DEB filtering described in the previous chapter. Then a new common-shot demultiple filter is developed to attenuate water-bottom and receiver-side peg-leg multiples by using the amplitude ratio of upgoing and downgoing waves in the $\tau - p$ domain. The forward and inverse $\tau - p$ transforms are performed in the process. This filter makes no assumption on periodicity or moveout patterns of multiples, nor does it require any knowledge of the subsurface. Synthetic and field data examples demonstrate the efficiency of the procedure.

Finally, I complete a case study of VCS multiple suppression with a selected 2-D VCS data set. The effectiveness of this processing scheme is examined by the velocity analysis and imaging results for a common-receiver gather. The results of predictive deconvolution on the same data set are also provided for the purpose of comparison.

4.2 Review of multiple attenuation

A common problem in interpreting marine seismic data is that multiples can severely mask primary reflection events and contaminate AVO amplitude information. It is also important to suppress multiples at an early stage of seismic processing, since the basic model in seismic processing assumes that reflection data consist of primaries only. We know, of course, that this is not true and that the presence of multiples leaves us with spurious images and amplitudes. A water-bottom multiple may coincide with the image of the reservoir, and multiples arising from complex structure may share the same velocity as the deeper primaries. This is a longstanding and only partially solved problem in explo-

ration seismology. The suppression of multiple reflections has long been a topic of interest in geophysical exploration.

4.2.1 Categories of multiples

Based on their ray-paths, multiples in vertical cable seismic data (we only consider upgoing wavefields) are classified into one of four basic categories defined as follows.

1. Water-bottom multiples

Water-bottom multiples are those multiples whose ray-paths lie entirely within the water layer (Figure 4.1(a)). They have very large amplitude since the sea-floor has much higher reflectivity than deeper geological horizons.

2. Peg-leg multiples

Peg-leg multiples are those generated by seismic waves that have reflected once below the water-bottom and have reflected one or more times between the free-surface and water-bottom. These include source-side peg-leg (Figure 4.1(b)) and receiver-side peg-leg (Figure 4.1(c)) multiples.

3. Surface multiples

Surface multiples are multiples whose downward reflections occur at the free-surface, and their upcoming rays are the reflections of deeper geological horizons rather than the reflections of the water-bottom (Figure 4.1(d)). This definition aims to discriminate between surface multiples and water-bottom and peg-leg multiples. As a general definition, surface multiples also include both water-bottom and peg-leg multiples.

4. Intra-bed multiples

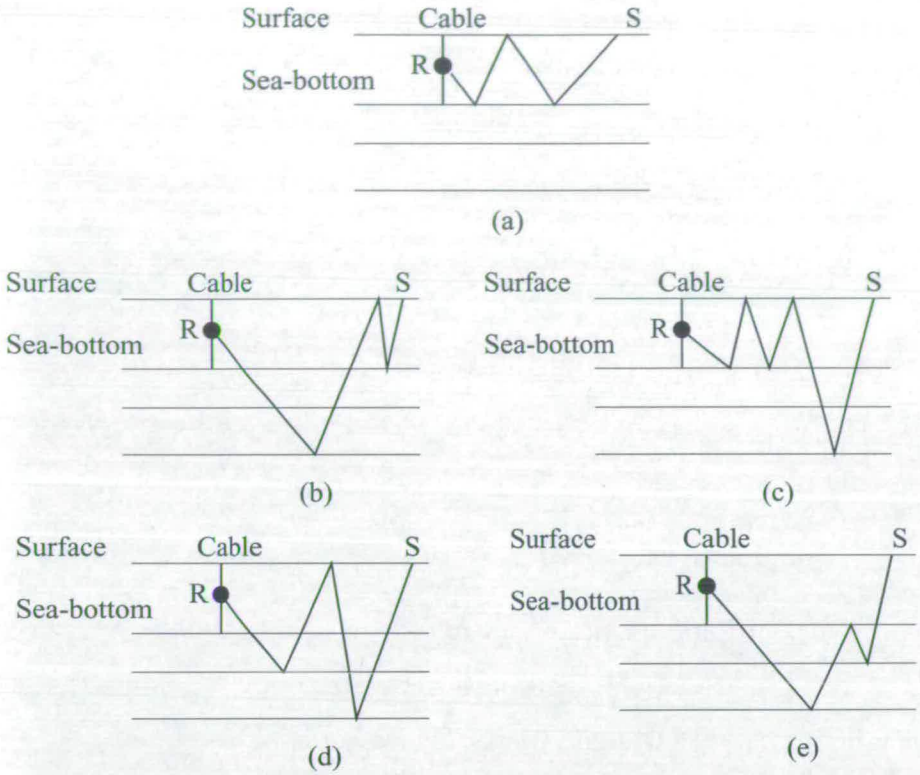


Figure 4.1: Ray-path diagrams for (a) water-bottom multiple, (b) source-side peg-leg multiple, (c) receiver-side peg-leg multiple, (d) surface multiple and (e) intra-bed multiple. S and R indicate the source and receiver locations, respectively.

Intra-bed multiples are multiples that have all of their downward reflections below the free-surface. A ray-path is shown in Figure 4.1(e). Intra-bed multiples have experienced reflections that are in general more remote and harder to precisely define (in comparison with the last three classes of multiples), hence these multiples are more difficult to predict and attenuate.

According to the time between successive reverberations at zero offset, multiples can also be classified into either short-period or long-period multiples.

The short-period multiples are taken to be those whose repeat interval at zero offset is only a few times the length of the source wavelet. The short-period multiples are approximately periodic and often suppressed by the predictive deconvolution techniques.

The long-period multiples are taken to be those whose repeat interval at zero offset is greater than three times the length of the source wavelet. The long-period multiples are commonly attenuated by methods based on the difference in moveout between primary and multiple reflections.

4.2.2 Multiple attenuation methods

The multiples can be selectively removed only if we can use some identifying characteristic to discriminate them from the primaries. Yilmaz(1987) identified four characteristics of multiples: 1) the moveout difference between primaries and multiples (velocity discrimination); 2) the dip difference between primaries and multiples on the CMP stack ($f-k$ discrimination); 3) the difference in frequency content between primaries and multiples; and 4) the periodicity of multiples (predictability). Over the years, many approaches have been developed to suppress water-bottom and surface multiples. Predictive deconvolution techniques are commonly used to suppress short-period multiples at near-offset traces where periodicity could be assumed (Backus, 1959; Peacock and Treitel, 1969; Yilmaz, 1987). This method is often more effective on the stacked traces as these approximate the zero-offset section. The periodicity of multiples along the radial direction was first noted by Taner (1980), who designed a multichannel predictive deconvolution along different radial directions to suppress the deep water-bottom multiples. Yilmaz (1987) used an autocorrelogram to display the periodicity, and described a method to design the predictive deconvolution operator for each p (slant-stack) trace and suppress multiples at nonzero offsets.

A second means of multiple suppression suitable for long-period multiples or the multiples at far-offset traces is based on the differential moveout between primary and multiple reflections. The simplest method is common midpoint (CMP) stack. Some modified stack procedures have been introduced (Buttkus, 1979;

Haldorsen and Farmer, 1989). To exploit the differential moveout, some appropriate transform procedures are used to maximize the separation of primaries and multiples in the transform domains. The $f-k$ dip filtering of Ryu (1982) is a popular approach for multiple suppression. Radon transform methods have also been proposed to distinguish multiples from primaries and then subtract them (Thorson and Claerbout, 1985; Hampson, 1986; Yilmaz, 1989; Foster and Mosher, 1992).

The multiple-generation process can be simulated by using wavefield modelling. The wave-equation-based, and inverse-scattering prediction and subtraction methods have attracted much attention in recent years (Wiggins, 1988; Fokkema and Van den Berg, 1990; Verschuur et al., 1992; Weglein et al., 1997; Araujo et al., 1994; Dragoset and Jericevic, 1998; Zhou and Greenhalgh, 1991; 1996; Landa et al., 1999; Ikelle and Yoo, 2000). The wave-equation-based method models wave propagation in the water column. It takes the data one round trip through the water column, and then adaptively subtracts these up- and downward continued data from the original. This method requires: (1) a priori estimate of the water depth and, (2) a posteriori estimate of a set of parameters for an adaptive matching and subtraction process. The inverse-scattering technique is based on a free-surface and point-scatter model. It models primaries and multiples in terms of reference medium propagation (propagation in water) and scattering at every point where the properties of the earth differ from water. The practical prerequisites include: (1) estimating the source signature and (2) missing near-trace compensation. Ziolkowski et al. (1999) proposed a new wave-theoretical method for removing free surface multiples from marine 3-D seismic data in which the reflection response of the earth, referred to a plane just above the sea-floor, is computed as the ratio of the plane-wave components of the upgoing and the downgoing wave. Using source measurements of the wavefield made during data acquisition, three problems associated with earlier work are solved: (i) the method

accommodates source arrays, rather than point sources; (ii) the incident field is removed without simultaneously removing part of the scattered field; and (iii) the minimum-energy criterion to find a wavelet is eliminated. However, this technique requires sources and receivers with full sampling.

It has been found that most of the methods for multiple suppression are data-dependent, there is no optimum method applied to all data sets. Hardy and Hobbs (1991) compared commonly used approaches of multiple suppression and proposed a formalized strategy for multiple suppression. Weglein (1999) gave an overview of recent advances and the road ahead in multiple attenuation. Many methods exist to remove multiples, and they are useful when their assumptions and prerequisites are satisfied. However, there are also many instances when these assumptions are violated or where the prerequisites are difficult or impossible to attain. This motivates the search for new demultiple concepts, algorithms, and acquisition techniques in the research and petroleum industry.

4.3 New demultiple filter

In order to attenuate receiver reverberations including water-bottom and receiver-side peg-leg multiples in the upgoing waves, I design a demultiple filter in the $\tau - p$ domain which is performed in a common-shot VCS gather after wavefield separation. The multiple rejecting areas are determined automatically by comparing the energy of the multiple model and the original input data in the $\tau - p$ domain. The analogous multiple suppression filter was proposed by Zhou and Greenhalgh (1991; 1996) to attenuate multiples in the surface data. In this work, however, I do not need to construct the multiple model since the downgoing waves in vertical cable seismic data can be considered as a multiple model for upgoing wave multiple attenuation.

4.3.1 The principle of filtering

In marine VCS acquisition, hydrophone cables are deployed vertically in the water column. Each hydrophone can receive both downgoing multiples from the sea surface and upgoing multiples from the sea bottom. If a receiver is located at the sea bottom ($z = h$), it can record the downgoing wavefields $u_D(t, h)$ and upgoing wavefields $u_U(t, h)$ produced at the sea-bottom with the same arrival time, where h is the depth of the sea bottom. To measure and use this traveltime, we construct two linear $\tau - p$ transform pairs $u_D(t, z) \leftrightarrow u_D(\tau, p)$ and ($u_U(t, z) \leftrightarrow u_U(\tau, p)$ by stacking along the slant line $t = \tau + p(z - h)$. Using an $2N+1$ sample time window of M traces in the $\tau - p$ domain, we define the following simple summation measure at each value of τ for downgoing and upgoing wavefields, respectively,

$$A_D(\tau) = \sum_{i=-N}^{N} \sum_{j=1}^{M} |u_D(\tau + i\Delta\tau, p_j)|, \tag{4.1}$$

and

$$A_U(\tau) = \sum_{i=-N}^{N} \sum_{j=1}^{M} |u_U(\tau + i\Delta\tau, p_j)|, \tag{4.2}$$

where $\Delta\tau$ is the time sampling interval. Since the receiver reverberation in the upgoing wave is the reflection of the down-going wave at the sea-bottom shown in Figure (4.1(c)), the ratio of amplitude summation described in equations (4.1) and (4.2) between downgoing and upgoing wavefields can be used as a key parameter for multiple attenuation.

To achieve this, we design a nonlinear filter using the Butterworth gain function in the $\tau - p$ domain. The gain function of this filter takes the following form:

$$g(\tau) = \frac{1}{\sqrt{1 + \left(\frac{A_D(\tau)}{\epsilon A_U(\tau)}\right)^n}}, \tag{4.3}$$

where ϵ (≥ 1)is the multiple rejection parameter, and n is the parameter used to control the smoothness of the filter with a value between 6 and 8. The function (4.3) is applied on a pixel by pixel basis to the data $u_U(\tau, p)$. This demultiple

filter automatically defines the multiple rejection areas and tapers the rejection boundary in the $\tau - p$ domain. If $g(\tau) \ll 1$ where high-amplitude events (multiples) are present in the data $u_D(\tau, p)$, the corresponding upgoing events at the same value of τ in the data $u_U(\tau, p)$ will be severely attenuated after applying this demultiple filtering. On the other hand, the condition $A_D(\tau)/A_U(\tau) \ll \epsilon$ produces a flat response $g(\tau) \to 1$, and no multiples are rejected. Then performing the inverse Radon transform $u_U(\tau, p)g(\tau) \to \tilde{u}_U(t, z)$ yields the upgoing wavefield $\tilde{u}_U(t, z)$ without receiver reverberations.

4.3.2 Test examples

To begin, we examine this demultiple filter on a synthetic vertical cable seismic data set shown in Figure 4.2. The original shot gather (Figure 4.2a) is produced from a horizontal three-layer model by using a finite difference algorithm. The $P-$wave velocities for the three layers are designed as $V_1 = 1500m/s$ (water),$V_2 = 2200m/s$ and $V_3 = 3000m/s$, respectively. The thicknesses of two upper-layers are $h_1 = 140m$ and $h_2 = 360m$, the third layer is half-space. There are 16 receivers deployed vertically in the first layer with $8m$ interval, the first receiver level is $8m$ below the free-surface, and the source-cable offset is $300m$.

The first processing step is to perform wavefield separation, and results are shown in Figures 4.2 (b) and (c). We can see that each section has five events within the time window $0 \sim 1.0s$. For upgoing waves (Figure 4.2c), there are two primary events from the two layer-interfaces and three multiples. Then a demultiple filtering is carried out to remove these multiples. The filtered result is shown in Figure 4.2(d). Figure 4.3 shows these wavefields in the $\tau - p$ domain. The $p-$values range from $-667ms/m$ to $0s/m$ for upgoing waves (Figures 4.3(b) and (c)), and from $0s/m$ to $667ms/m$ for down-going waves (Figure 4.3(a)). We find that multiples can be suppressed effectively where the amplitude ratios of

downgoing and upgoing waves are relatively large.

Following successful experiments with synthetic vertical cable seismic data, we apply this demultiple filter to a field vertical cable seismic data set from the North Sea. Figure 4.4 shows an original common shot-gather with 16 receivers (Figure 4.4(a)), and the upgoing waves by wavefield separation before and after multiple attenuation (Figures 4.4(b) and 4.4(c)). We can see that the water-bottom multiples are obscuring primaries shown in Figure 4.4(b). Comparison of Figures 4.4(b) and (c) shows that multiples are, to a great extent, removed by applying this demultiple filter.

4.4 A case study of VCS multiple attenuation

The single shot gather examples have shown the effectiveness of this demultiple filtering for the multiple attenuation. In this case study, we apply this technique to a selected 2-D vertical cable seismic data set from the North Sea (courtesy of Texaco). The comparison of this processing scheme to the predictive deconvolution method on multiple suppression with a common-receiver gather has been given as well.

4.4.1 Results of wavefield separation

Figure 4.5 shows the result of wavefield separation for a common-receiver gather along a selected 2-D source line near the cable location at a window of $1.8s$ to $3.6s$. The whole data set was recorded by 12 live cables in a four by three rectangle with $800m$ interval between each cable. There are 16 hydrophones in each cable with a separation of 25 feet. This 2-D line includes 213 shots with $25m$ shot spacing.

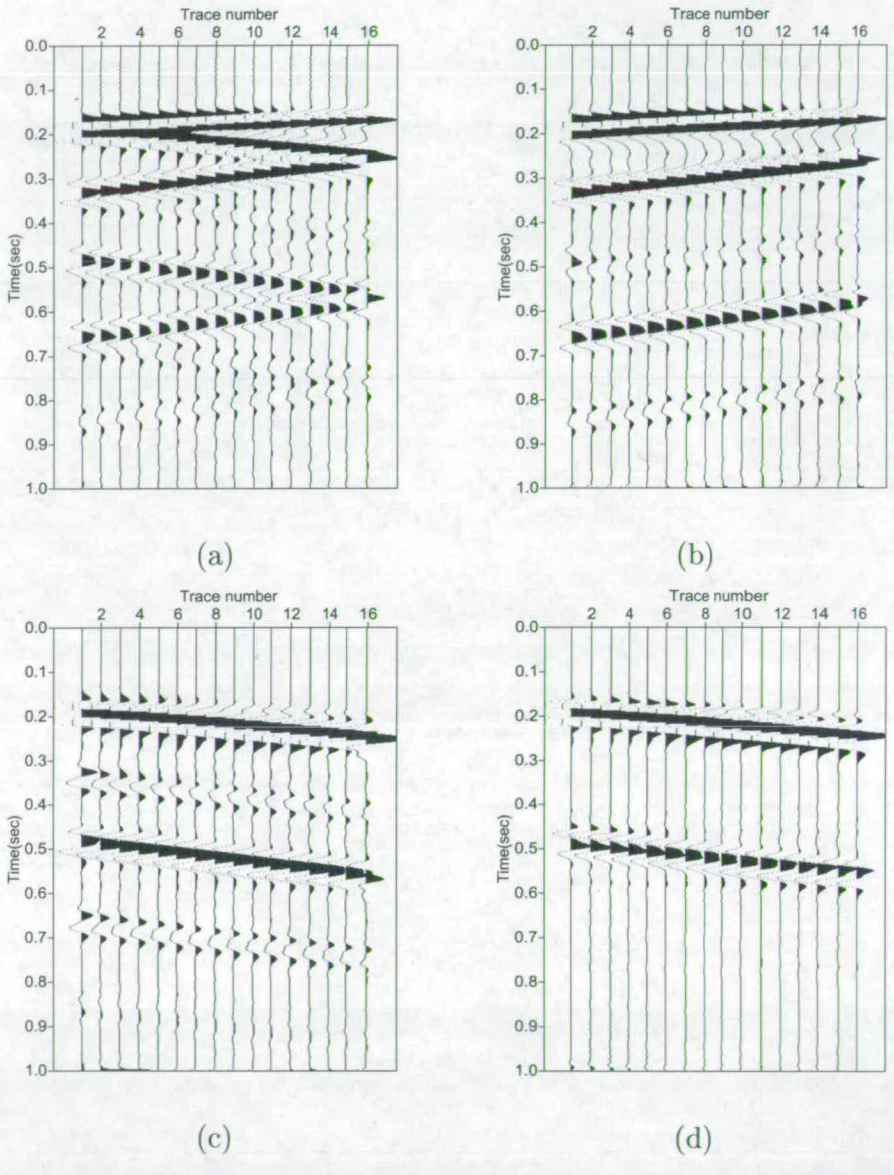


Figure 4.2: Synthetic VCS data: (a) original data (full wavefields), (b) down-going waves, (c) up-going waves, and (d) up-going waves with application of the demultiple filter.

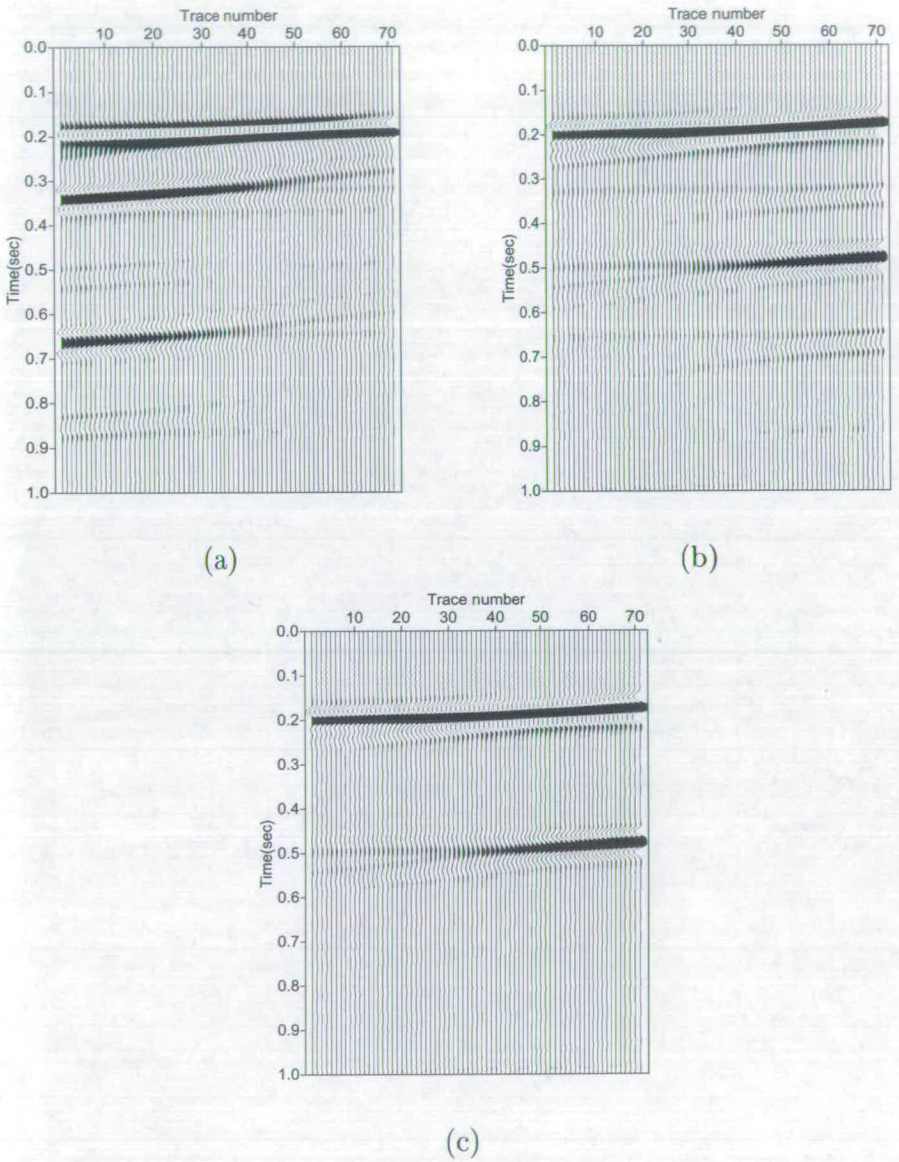


Figure 4.3: $\tau - p$ Transforms of synthetic VCS data shown in Figure 4.2: (a) down-going waves, (b) up-going waves, and (c) up-going waves with application of the de-multiple filter.

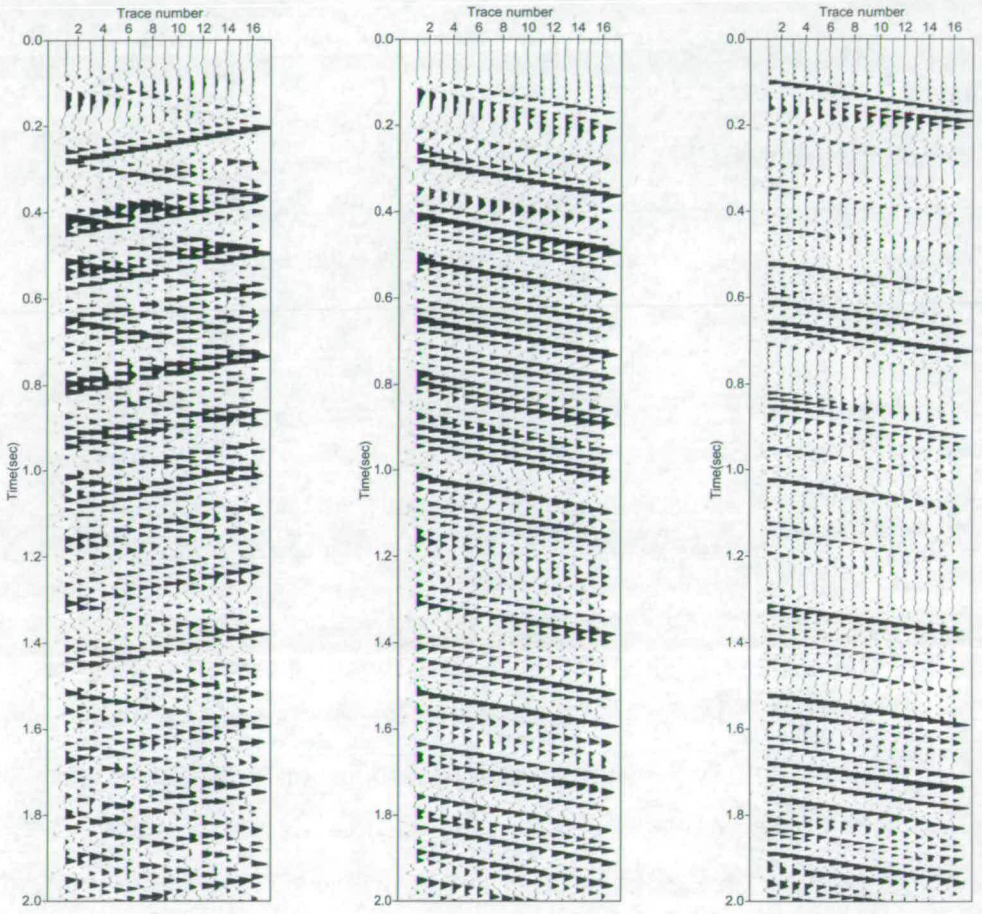


Figure 4.4: Real VCS shot gathers: (a) original data (full wave fields), (b) up-going waves before multiple removal, and (c) up-going waves after applying the demultiple filter.

It appears that multiples are so strong that we can not distinguish any primaries in these sections (Figure 4.5 (a) and (b)) although all downgoing multiples are removed by wave field separation. To identify multiples, we perform stack velocity analysis in these two common-receiver gathers. The velocity semblance plots are shown in Figure 4.6. We can see that there are strong water column multiples with a velocity of near $1500m/s$, which present before $1.5s$ in this common-receiver gather, and peg-leg multiples presenting between $2.0s$ to $4.0s$. For the raw data, the multiples are obscuring primaries which degrades both the vertical and horizontal resolution of the velocity semblance plot.

4.4.2 Application of predictive deconvolution

To suppress these water bottom and peg-leg multiples, we have applied the predictive deconvolution to the upgoing wave section shown in Figure 4.5(b). The water depth in this area is about $136m$. The periods of these multiples at near offsets are about $180ms$. The deconvolution result is shown in Figure 4.7(a) in a window of $1.8s$ to $3.6s$, and we display the velocity semblance plot shown in Figure 4.8(b) as well. As we can see, these reverberations are attenuated well at near offsets, and the quality of velocity analysis has also been improved. However, there is still much multiple energy left in the velocity semblance plot. This is because these multiples have no relative fixed periods at far offsets, and they can't be suppressed completely by the predictive deconvolution.

4.4.3 Application of the new demultiple filtering

The results of multiple attenuation using the proposed new demultiple filter are shown in Figure 4.8 in a window of $1.8s$ to $3.6s$. We can see that this technique performs better than the predictive deconvolution, especially for the multiples

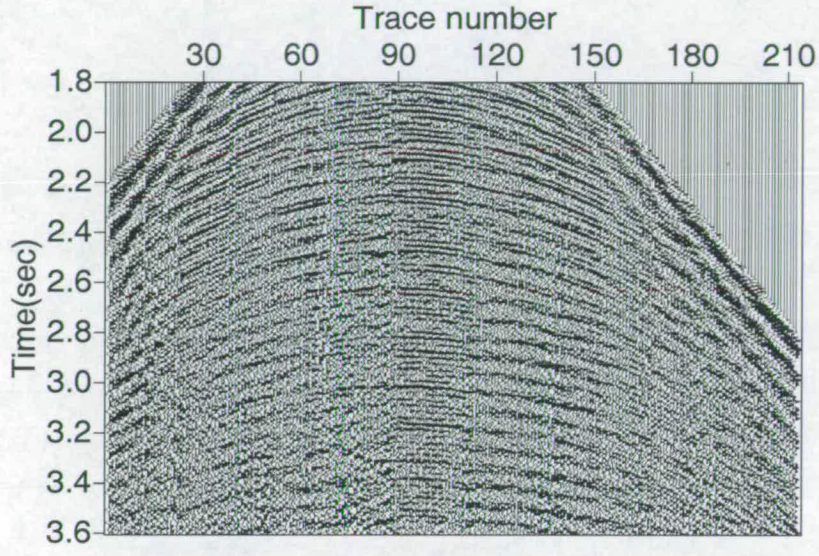
at the far offsets. The effect of multiple suppression can be demonstrated more clearly in the velocity semblance plot shown in Figure 4.8(b). This filtering greatly improves the velocity resolution, the energy of multiples is attenuated severely, and it becomes possible to derive a reasonable stacking velocity function (Figure 4.8(b)) for this common-receiver gather.

We also display two sections of the vertical cable seismic imaging by applying prestack time migration to the common-receiver gathers before and after multiple suppression using the proposed demultiple filtering in Figure 4.9. Comparison of the two plots shows that this processing scheme is effective for multiple removal in vertical cable seismic imaging; primary events at $2.18s$, $2.75s$ and $3.3s$ are obviously enhanced after the demultiple filtering (Figure 4.9b). It is hard to interpret primaries shown in Figure 4.9(a) since these events are interfered with by multiples without multiple suppression.

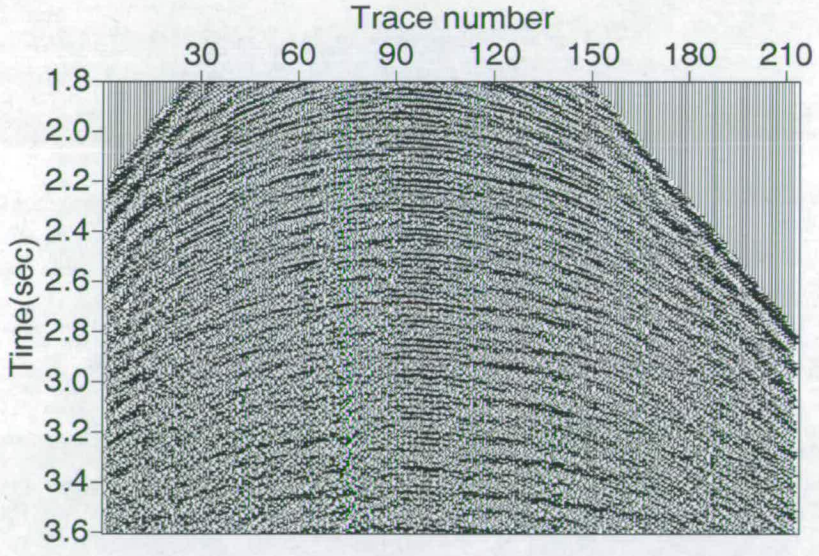
4.5 Conclusions

We have proposed a demultiple filter with a Butterworth gain function to suppress the receiver-side reverberation in vertical cable seismic data. This filtering is carried out in the $\tau - p$ domain for each common-shot VCS gather. The whole processing scheme also includes wavefield separation, forward and inverse $\tau - p$ transforms. This demultiple filter uses a different process from the common prediction and subtraction approaches for multiple suppression. It automatically defines the multiple rejection areas and tapers the rejection boundary in the $\tau - p$ domain by using the amplitude ratio of upgoing and downgoing wavefields in vertical cable seismic data. There are no requirements for any subsurface information. The synthetic and real examples show that this scheme is very effective for multiple attenuation in vertical cable seismic data processing, it gives much improvement in VCS velocity analysis and the quality of migrated section is

also enhanced. This proposed processing scheme yields much better performance on the multiple suppression compared to the predictive deconvolution.

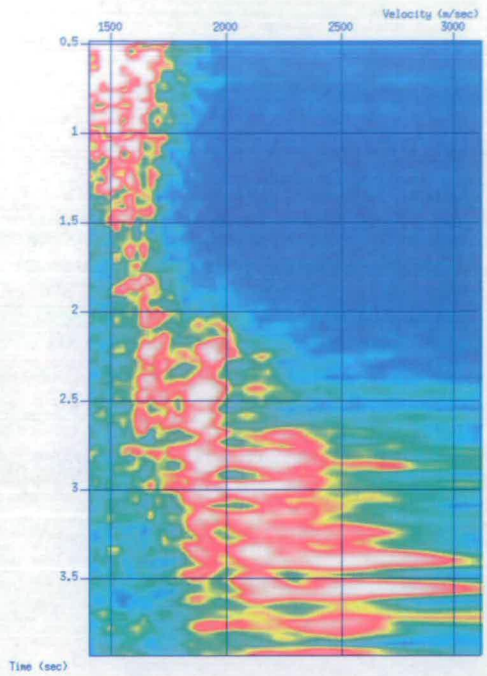


(a)

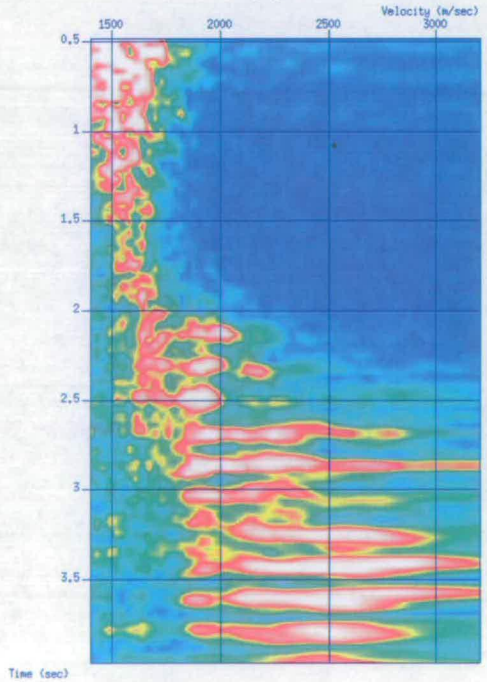


(b)

Figure 4.5: wavefield separation for a real VCS common-receiver gather along a 2-D source line at a window of $1.8s$ to $3.6s$: (a) raw data (full wavefields); (b) upgoing wavefields.

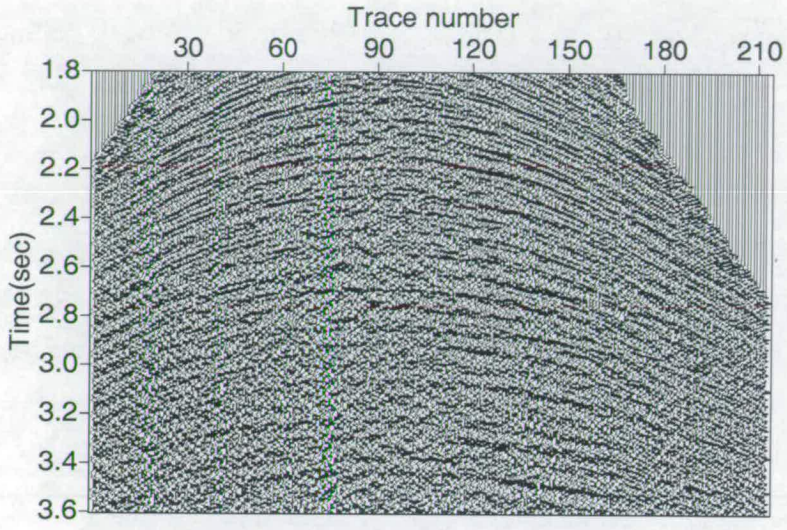


(a)

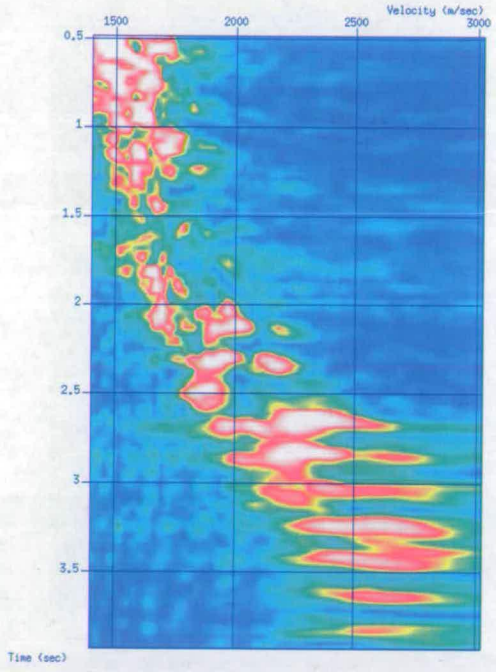


(b)

Figure 4.6: Velocity semblance plots for (a) the raw VCS common-receiver gather and (b) upgoing waves. There are strong water column and peg-leg multiples present on both sections.

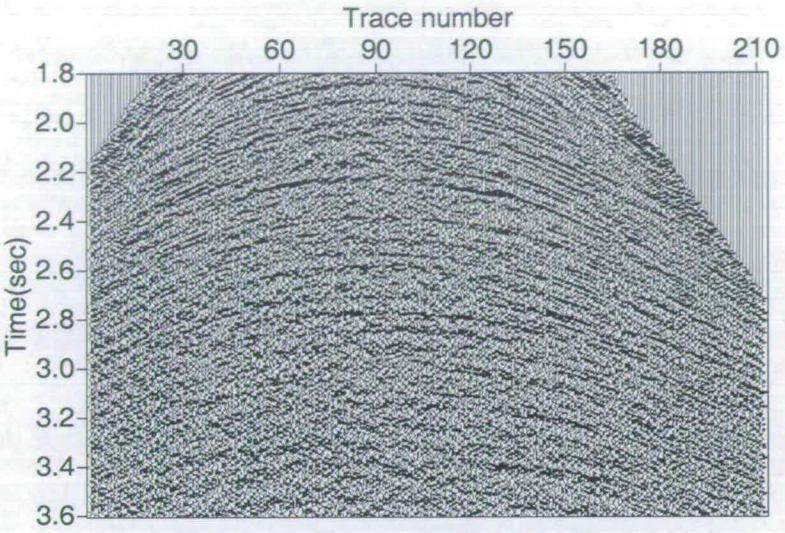


(a)

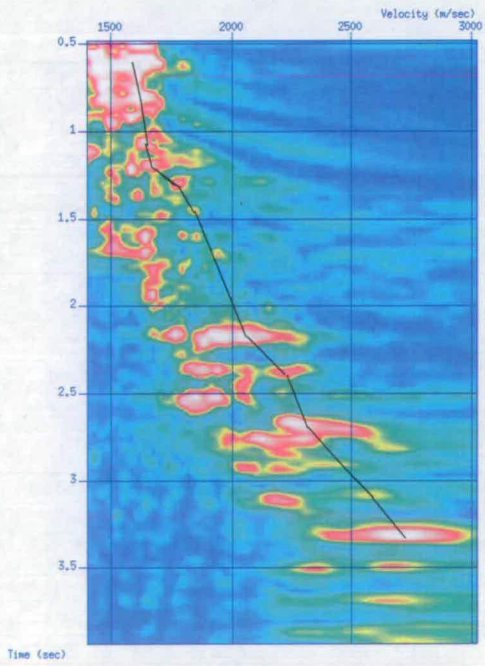


(b)

Figure 4.7: (a) Result of multiple suppression on the data set shown in Figure 4.5(b) by using the predictive deconvolution. (b) The velocity semblance plot of this common-receiver gather.

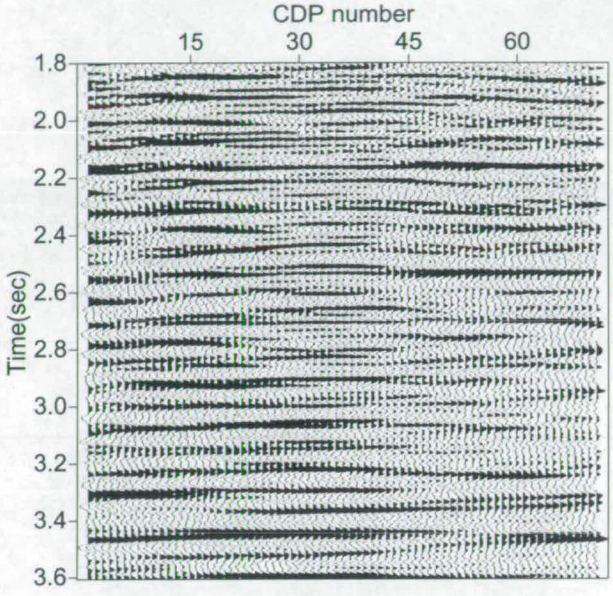


(a)

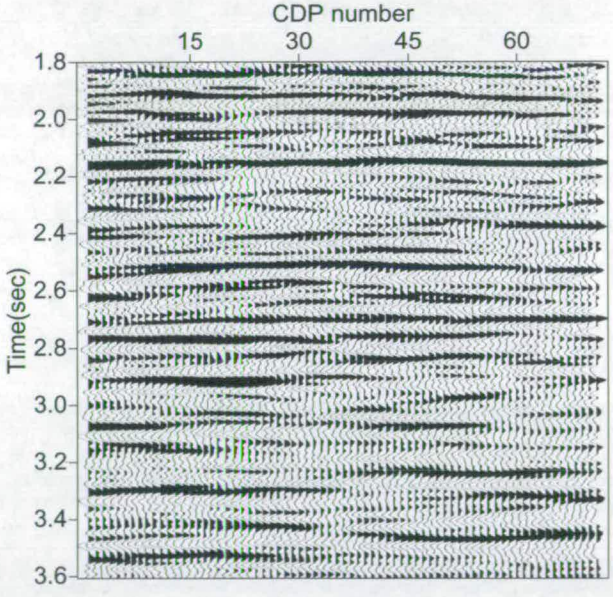


(b)

Figure 4.8: (a) Result of multiple suppression on the data set shown in Figure 4.5(b) by using the new demultiple filter. (b) The velocity semblance plot of this common-receiver gather.



(a)



(b)

Figure 4.9: Results of prestack migration applied to the upgoing wave sections: (a) without multiple suppression and (b) with the new demultiple filtering.

CHAPTER 5

Vertical cable seismic imaging

5.1 Introduction

Owing to its unique acquisition characteristics, the idea of CMP or CDP binning is not applicable to vertical cable seismic data processing, so that conventional data processing tools such as NMO correction, velocity analysis and CDP stack can not be used directly to perform processing and imaging for this kind of data. I have discussed these issues using a simple VCS example of reflection by a horizontal interface. Two case studies have been performed to show variations of residual moveouts and dispersal of reflection points with the increasing of the source-cable offset to depth ratio for two given receivers in a horizontally-layered model.

However, the concept of a point receiver can be used for this special geometry, since only a small number of fixed receivers are used in the VCS acquisition with full azimuthal coverage of sources. Alternatively, common scatter point (CSP) gathers can be constructed from a common receiver gather. This allows us to accurately process and analyze the data and it is also very suitable for performing prestack migration. This advantage has been discussed by Bancroft and Xu (1999).

In this chapter, prestack VCS migration is achieved through the wavefield extrapolation process using the classical Kirchhoff integral formula (Schneider 1978) extented to VSP imaging by Dillon (1988). Prestack Kirchhoff migration is performed on common receiver VCS gathers assuming the reciprocity principle for PP reflections. The wavefield is actually extrapolated from the source surface to the imaging point. The subsurface image is formed at the time coincidence of incident and reflected wavefields, according to Claerbout's imaging principle (Claerbout, 1971; 1985). During the wavefield extrapolation, propagation times are calculated using a novel double-square-root traveltime equation assuming an rms velocity approximation to Snell's law in a horizontally-layered medium (Kohler and Koenig, 1986). The horizontally-layered assumption is adequate for many situations, but where the known subsurface structure changes laterally and significantly, the migration is controlled through geometric ray-tracing to improve focusing.

In a real case study, we have obtained two migration results from two different common receiver gathers in the same cable. The migration velocities are taken from the residual velocity analysis on each CSP gather, and the arrival angle information is considered to remove the imaging artifacts. We also show examples of CSP gathers formed from a common receiver gather and corresponding NMO correction, velocity analysis and CSP stacking results.

5.2 Reflection from a horizontal interface

To study moveout variations between receivers at different depth levels in one cable, I derive the traveltime equation in a horizontally-layered model for VCS geometry. I also perform the residual moveout analysis and show dispersal of reflection points with variations of the source-cable offset to depth ratios in two case studies.

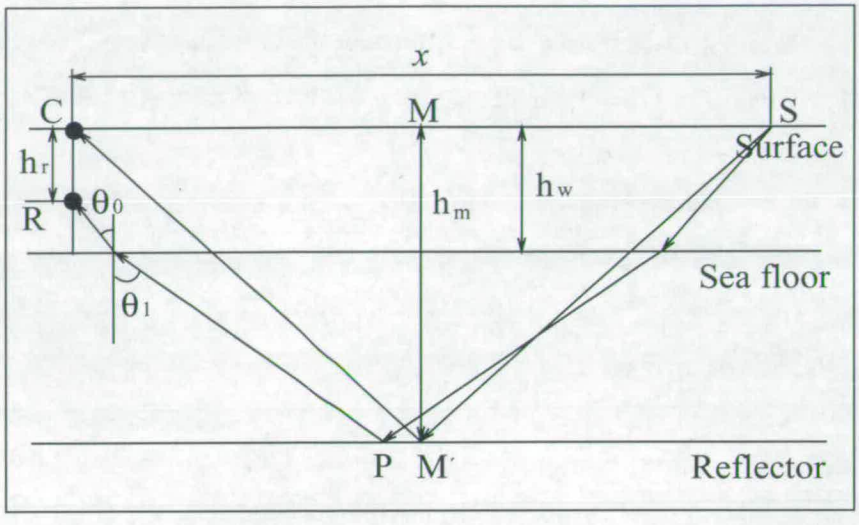


Figure 5.1: Ray path diagram for the traveltime analysis in VCS geometry. S, P and R indicate the source, reflection point and receiver locations, respectively. C and M denote the cable location and the mid-point between the cable and source. M′ is the vertical projection point of M at the target interface.

5.2.1 Traveltime

In consideration of simplicity, it is assumed that the subsurface consists of a horizontal water layer and a horizontal isotropic layer under the water which is our target reflector interface. The second layer can be considered as the equivalent of all horizontal layers under the sea-floor. The geometry and ray paths are shown in Figure 5.1. S, P and R denote the source, reflection point and receiver locations, respectively. The cable location and the mid-point between the cable and source are denoted by C and M, respectively. x is the source-cable offset. v_0 and v_1 are P wave velocities in the water and sub-water layers. h_r, h_w and h_m are depths of the receiver, sea floor and reflector, respectively. θ_1 and θ_0 are P wave incident and transmission angles from the sub-water layer to the water layer. Based on Snell's law, we have

$$\sin\theta_1 = \frac{v_1}{v_0}\sin\theta_0, \tag{5.1}$$

and

$$(h_m - h_w)\tan\theta_1 + h_w\tan\theta_0 = \frac{1}{2}(x + h_r\tan\theta_0). \tag{5.2}$$

Combining these two equations, we can obtain the solutions for the angles of θ_0 and θ_1. The reflection traveltime of the target interface from the source S to the receiver R can be expressed as

$$t_{SPR} = \frac{2}{v_1 \cos\theta_1}(h_m - h_w) + \frac{1}{v_0 \cos\theta_0}(2h_w - h_r). \tag{5.3}$$

5.2.2 Residual moveout

In conventional seismic data processing, we use Dix's (1955) traveltime equation for horizontally layered media. Referring to Figure 5.1, if the receiver is at the surface level (location C), the reflection traveltime from the source S to the receiver C via reflection point M′ can be approximated as

$$t_{SM'C} = \sqrt{t_0^2 + \frac{x^2}{V_{rms}^2}}, \tag{5.4}$$

where

$$t_0 = \frac{2h_w}{v_0} + \frac{2(h_m - hw)}{v_1}, \tag{5.5}$$

which is the two-way vertical traveltime from the surface to the reflector, V_{rms} is the root-mean-square velocity, and

$$V_{rms} = \sqrt{\frac{v_0^2 \Delta t_1 + v_1^2 \Delta t_2}{\Delta t_1 + \Delta t_2}}, \tag{5.6}$$

with

$$\begin{aligned} \Delta t_1 &= \frac{2h_w}{v_0}, \\ \Delta t_2 &= \frac{2(h_m - h_w)}{v_1}. \end{aligned} \tag{5.7}$$

To perform conventional CDP stack as in surface data processing, I introduce statics corrections to ensure receivers are at the same depth level, and then make NMO corrections. The statics corrections are achieved by a one-way vertical traveltime shift for each receiver from the receiver level to the surface. I use the

hyperbolic traveltime equation (5.4) for NMO corrections. After these corrections, the residual moveout of the receiver at the location R can be expressed as

$$\Delta t_R = t_{SPR} + \frac{h_r}{v_0} - t_{SM'C}. \tag{5.8}$$

5.2.3 *Dispersal of reflection points*

Since receivers are at different depth levels, another problem for the CDP stack of vertical cable seismic data is the dispersal of reflection points. Referring to Figure 5.1, the reflection point P is not at the vertical projection point M′ of the midpoint M between the source S and receiver R, even if the model is a horizontally-layered media. The horizontal distance between the cable and the reflection point P can be expressed as

$$x_{cp} = (h_w - h_r)\tan\theta_0 + (h_m - h_w)\tan\theta_1, \tag{5.9}$$

where θ_0 and θ_1 are taken from the solution of equations (5.1) and (5.2). Thus, the dispersal of the reflection point P, measured by the horizontal distance between the reflection point P and the point M, can be expressed as

$$x_{pm'} = \frac{1}{2}x - x_{cp}, \tag{5.10}$$

where x is the source-cable offset.

5.2.4 *Case studies*

I consider two examples to analyze variations of residual moveouts and dispersal of reflection points versus the source-cable offset to depth ratios. Case 1 is a shallow water case, in which the water layer is defined as $150m$ thick. The depth

of the target interface is $1500m$, and the maximum source-cable offset is up to 4000m. P wave velocities $v_0 = 1500m/s$ and $v_1 = 2100m/s$. I assume there are 16 receivers in one cable with an interval of $8m$, the uppermost receiver (Receiver 1) is at $8m$ below the surface. Two residual moveout curves shown in Figure 5.2 refer to Receiver 1 and Receiver 16, respectively. As we can see, the residual moveout of Receiver 16 rises with the initial increase of the offset to depth ratio. When the offset to depth ratio is over 2.2, it starts to decrease. The curve of Receiver 1 increases sharply in a negative direction when the offset to depth ratio is more than 1.0. This is because the residual moveout include two portions, one of which results from the static time shift and this part is positive. The other is caused by the hyperbolic approximation of traveltime, however, this one is negative. The difference of residual moveouts between two receivers depends only on the former portion, since all receivers with the same source-cable offset have been given the same moveout corrections. This difference increases with the increase of the offset to depth ratio, and it is up to $15ms$ when the offset to depth ratio is 2.5.

In case 2, I set the water layer to be $500m$ thick. Receiver 1 is at a depth of $360m$, and Receiver 16 is at a depth of $480m$. Other geometry parameters are the same as those of case 1. Figure 5.3 shows that the residual moveouts of Receiver 1 and Receiver 16 are up to $29ms$ and $44ms$, respectively. The difference of residual moveouts between these two receivers is up to $18ms$ when the offset to depth ratio is 2.5. We can see that this amount of difference in case 2 is always bigger than that in case 1 by comparison of the two cases.

The dispersal of reflection points for case 1 and case 2 are shown in Figure 5.4 and Figure 5.5, respectively. In both cases, the larger the offset to depth ratio, the larger the shift of the reflection point. For Receiver 16, the dispersal of the reflection point is up to $45m$ at an offset to depth ratio of 2.5 in case 1, and it is over $180m$ in case 2. The dispersal difference of reflection points between two

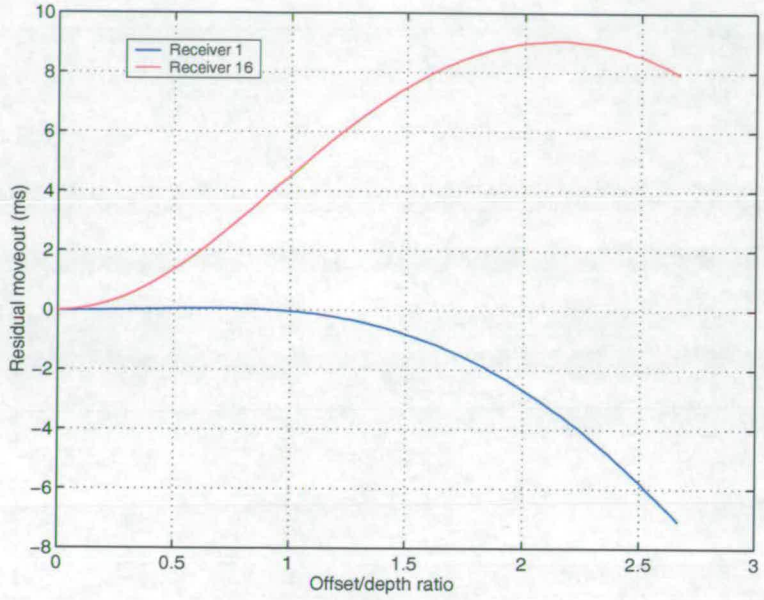


Figure 5.2: Variation of residual moveouts versus the source-cable offset to depth ratios in case 1.

receivers also increases with the increasing of the offset to depth ratio in both cases. These differences are over $40m$ when the offset to depth ratio is 2.5 in both cases.

As a result, these differences in residual moveouts and dispersal of reflection points among receivers in a single cable will degrade the CDP stack when performing conventional statics and NMO corrections.

5.3 Prestack migration

In migrating a common receiver VCS gather, the concept of shot-record migration could be applied by assuming the reciprocity of sources and receiver. As in migrating walkaway VSPs, and the data are processed as the response of a surface array of receivers to a downhole source (Dillon, 1988).

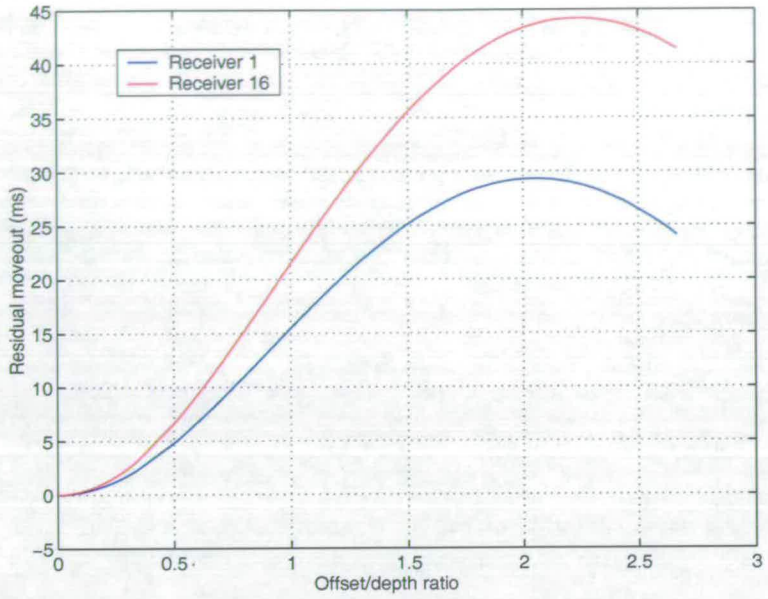


Figure 5.3: Variation of residual moveouts versus the source-cable offset to depth ratios in case 2.

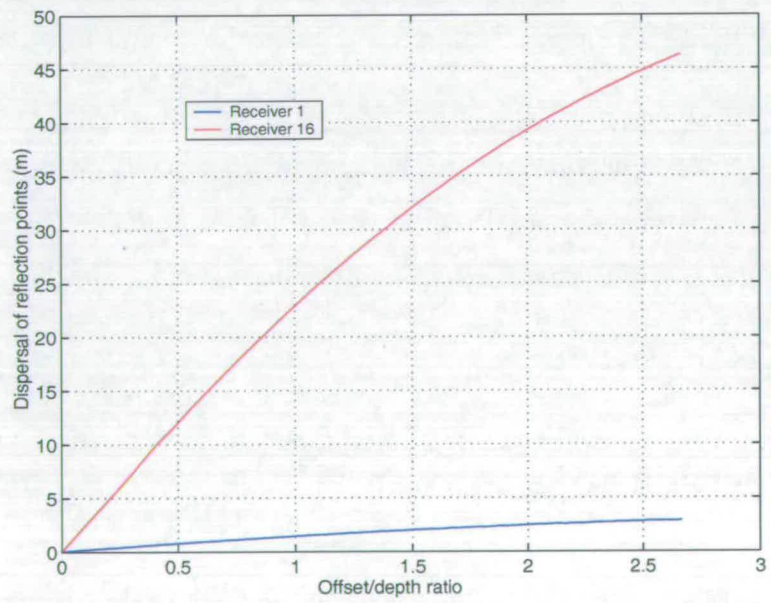


Figure 5.4: Variation of dispersal of reflection points versus the source-cable offset to depth ratios in case 1.

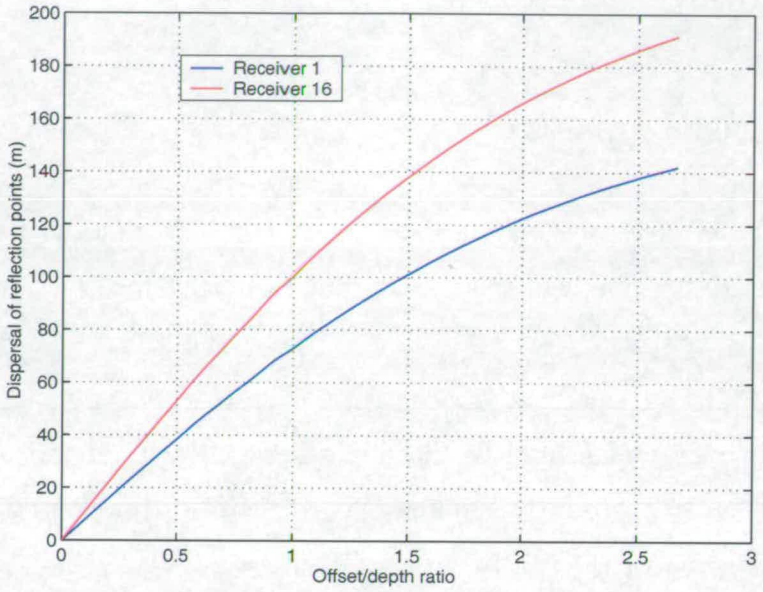


Figure 5.5: Variation of dispersal of reflection points versus the source-cable offset to depth ratios in case 2.

5.3.1 Wavefield extrapolation

Following Schneider's (1978) equation (4), the Kirchhoff wavefield extrapolation integral for predicting the wavefield at any depth of the subsurface due to the wavefield measured at the surface, in the vertical cable seismic geometry shown in Figure 5.6, can be written

$$U(\mathbf{r},t) = \frac{1}{2\pi}\int dS_0 \frac{\partial}{\partial z}\left[\frac{U(\mathbf{r}_0, t+R/v)}{R}\right], \tag{5.11}$$

where $R = |\mathbf{r} - \mathbf{r}_0|$, represents the distance between the source location $S(\mathbf{r}_0)$ and the scatter point $D(\mathbf{r})$. $U(\mathbf{r},t)$ is the wavefield to be calculated at the scatter point $D(\mathbf{r})$, and $U(\mathbf{r}_0,t)$ is the wavefield measured at a receiver deployed on the vertical cable with the source $S(\mathbf{r}_0)$ by assuming the reciprocity of source and receiver. S_0 indicates the source surface which can be considered as a horizontal plane in the VCS geometry, and the z-axis is perpendicular to this surface. v is P-wave velocity and, hence, R/v is the traveltime of P-wave from $D(\mathbf{r})$ to $S(\mathbf{r}_0)$. The above integral expresses Schneider's equation (4) as a downward continuation,

with the derivative in z direction.

5.3.2 Imaging principle

Equation (5.11) gives the wavefield at point $D(\mathbf{r})$ for all time. According to Claerbout's (1971) imaging principle, an image of the subsurface can be formed from this wavefield at $t = tr$, the time at which the source energy excites the diffractor at $D(\mathbf{r})$. Making the substitution for tr and expressing the normal derivative in terms of R and θ, the angle between the vertical axis ($z-$axis) and the the ray path from the source $S(\mathbf{r_0})$ to the scatter point $D(\mathbf{r})$, the 3-D migration integral for the source surface becomes

$$U(\mathbf{r}, tr) = \frac{1}{2\pi} \int \int dxdy \cos\theta \frac{\partial}{\partial R} \left[\frac{U(\mathbf{r}_0, tr + R/v)}{R} \right]. \tag{5.12}$$

Substituting $t = tr + R/v$ into the above equation leads to

$$U(\mathbf{r}, tr) = \frac{1}{2\pi} \int \int dxdy \frac{\cos\theta}{Rv} \left[\frac{\partial U(\mathbf{r}_0, tr + R/v)}{\partial t} - \frac{v}{R} U(\mathbf{r}_0, tr + R/v) \right]. \tag{5.13}$$

As we can see, it is the far-field term that makes the greatest contribution to the summation that is used in the practical implementation of Kirchhoff migration. If we take the far-field approximation of equation (5.13), the output image can be expressed as

$$U(\mathbf{r}, tr) = \frac{1}{2\pi} \frac{\partial}{\partial t} [\int \int \frac{\cos\theta}{Rv} U(\mathbf{r}_0, tr + R/v) dxdy]. \tag{5.14}$$

Performing the surface integration in the $y-$axis direction yields a 2-D migration integral formulation as

$$U(\mathbf{r}, tr) = \frac{1}{\sqrt{2\pi}} \frac{\partial^{1/2}}{\partial t} [\int \frac{\cos\theta}{\sqrt{Rv}} U(\mathbf{r}_0, tr + R/v) dx]. \tag{5.15}$$

This transformation has been discussed by French (1975), Schneider(1978), Wiggins (1984) and Gazdag (1984), and two assumptions have been made by implication: (1) Subsurface structure is invariant in the $y-$axis direction, and (2)

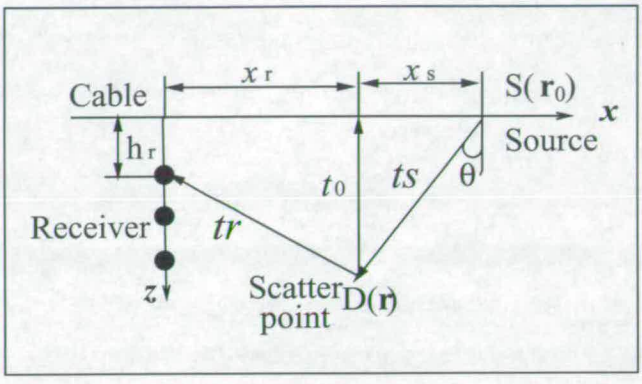


Figure 5.6: Ray path diagram showing the traveltime of ts and tr in vertical cable seismic geometry. The vertical zero-offset traveltime t_0 at the scatter point $D(\mathbf{r})$ is also shown.

Infinite line source(s) and infinite line receivers in the $y-$axis direction are used to acquire the data.

5.3.3 Traveltime calculation

The Kirchhoff integral is the most cost-effective prestack migration method. It can be described kinematically as creating the output at each point from a sum of all the input data points that satisfy the double-square-root (DSR) traveltime equation

$$\begin{aligned} t &= ts + tr, \\ &= \sqrt{\frac{t_0^2}{4} + \frac{x_s^2}{V_s^2}} + \sqrt{\frac{(t_0 - t_{rv})^2}{4} + \frac{x_r^2}{V_r^2}}, \end{aligned} \tag{5.16}$$

where ts and tr are traveltimes along the source and receiver ray paths illustrated in Figure 5.6; x_s is the horizontal distance between the source $S(\mathbf{r_0})$ and the scatter point $D(\mathbf{r})$, and x_r is the horizontal distance between the scatter point $D(\mathbf{r})$ and the receiver R; t_0 is the two-way vertical traveltime at the scatter point; $t_{rv} = 2h_r/v_0$ is the two-way vertical traveltime from the receiver level to the surface datum; h_r is the depth of the receiver; v_0 is the acoustic velocity of the water layer; and V_s is the conventional rms velocity which is defined at the

scatter point for rays that travel to the surface. The receiver ray, however, does not travel to the surface and requires a new rms velocity to be calculated for the time ranging from t_0 to t_{rv},

$$V_r^2 = \frac{t_0 V_s^2(t_0) - t_{rv} v_0^2(t_{rv})}{t_0 - t_{rv}}. \tag{5.17}$$

This traveltime equation is based on a horizontal layered hyperbolic model, whereas, a more accurate traveltime would require some form of ray tracing for complex structure imaging with velocity changing laterally and significantly. For a common receiver gather, the component of traveltime t_r is a constant for the same scatter point, hence we only need to calculate the component of traveltime t_s along paths from different sources to the common scatter point. Further migration velocity analysis can be performed on the CSP gather using the conventional velocity analysis approach.

5.3.4 Arrival angle weight

When the prestack migration is applied to field data obtained with limited observation geometry or with strong multiples, the artifacts or false images usually appear in the image. According to Takahashi (1995) and Druzhinin (1998), such false images can be removed by using arrival angle (slope) information which can be obtained by ray tracing in a background medium. To do so, we introduce the following migration weight

$$\cos^n(\theta_S - \theta_{S0}), \tag{5.18}$$

where θ_S is the arrival angle corresponding to the ray path DS shown in Figure 5.7, θ_{S0} is the slope angle associated with the specular ray path DS_0. For a given scatting point D and a given receiver R, there are a range of potential rays, where DS_0 is the expected polarization direction of scattering waves. The integer parameter $n = 0 \sim 8$ is taken in order to enhance the contribution of the specular ray and to suppress the contributions of any other potential rays during

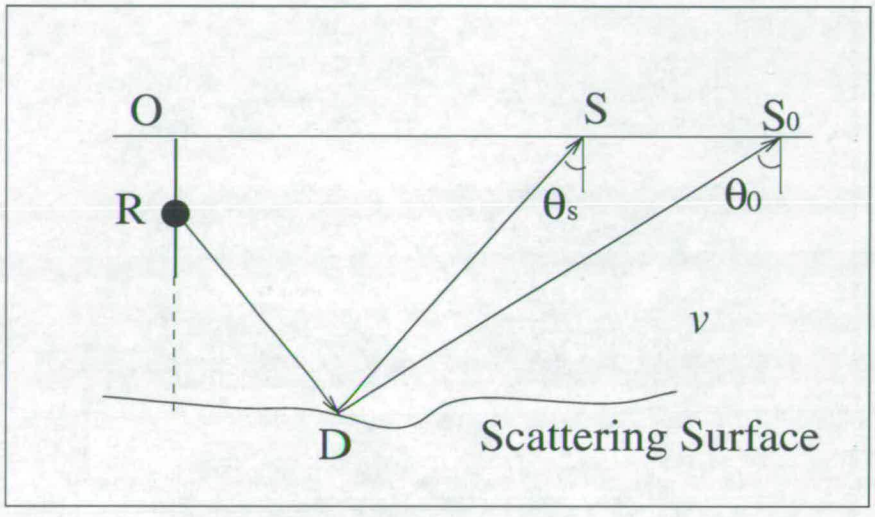


Figure 5.7: Sketch of the VCS geometry for demonstration of arrival angle weight in migration. S and S_0 indicate the source locations, D is a scatter point, R and C denote the receiver and cable locations, respectively. θ_S and θ_{S0} are defined as arrival angles corresponding to ray path DS and DS_0, respectively. Note that the reciprocity of sources and receiver is assumed.

migration process. The weight (5.18) can be considered as a polarization filter (Takahashi, 1995) that can suppress the projection of the observed wavefield onto unwanted directions of wave propagation.

5.4 CSP stack

Although alternatives to towed streamer acquisition look promising, the vast infrastructure for processing streamer data is not completely suited to handling VCS data. The first step required is to separate upgoing and downgoing wavefields in this processing, we have discussed the related techniques in Chapter 2. In this section, we propose a processing scheme of CSP stack for vertical cable seismic imaging. The key steps are to generate CSP gathers from a common receiver gather, and perform residual velocity analysis to obtain more accurate migration velocities in each CSP gather. Then we can make NMO correction and CSP stack in a CSP gather instead of a CDP gather. These steps have the same procedures

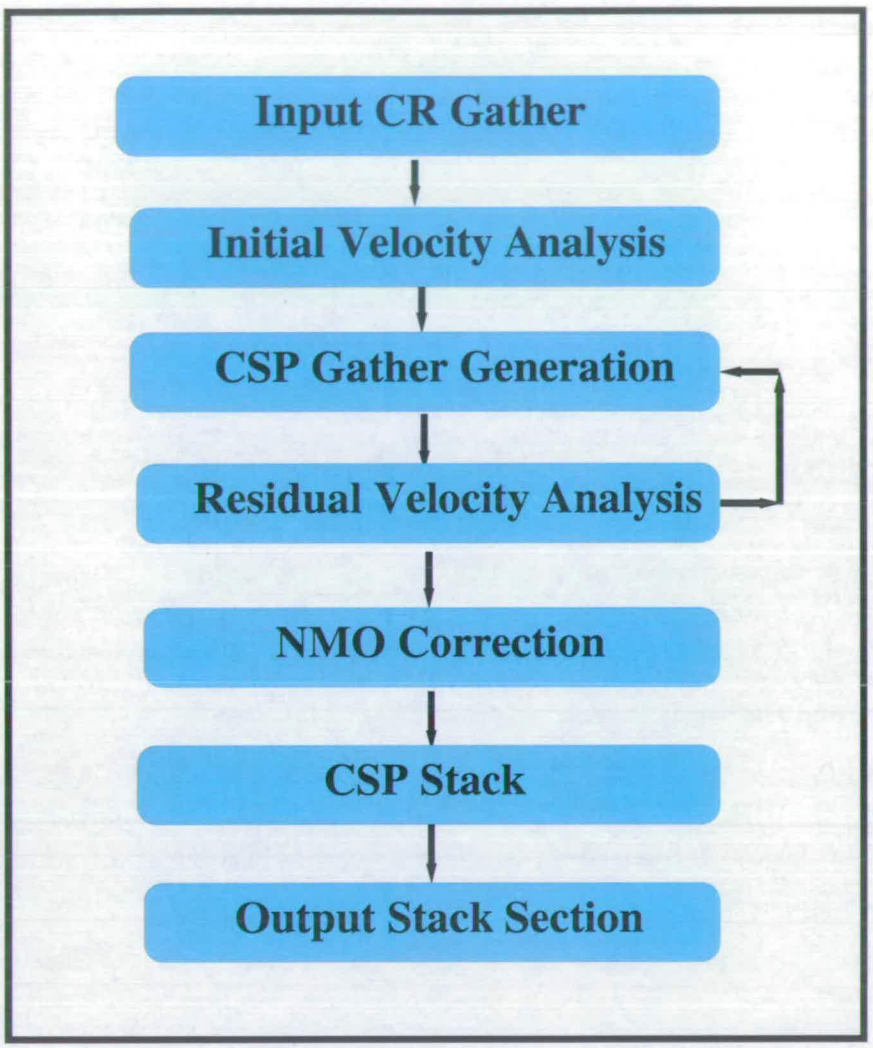


Figure 5.8: The flowchart of CSP stack processing for vertical cable seismic data. CR denotes common receiver.

as the conventional NMO velocity analysis, NMO correction and CDP stack in a CDP gather. The flowchart for this processing scheme is shown in Figure 5.8.

5.4.1 Initial velocity analysis

Owing to its unique acquisition characteristics, vertical cable seismic makes velocity analysis difficult, and the common tools for 2-D and 3-D seismic data may

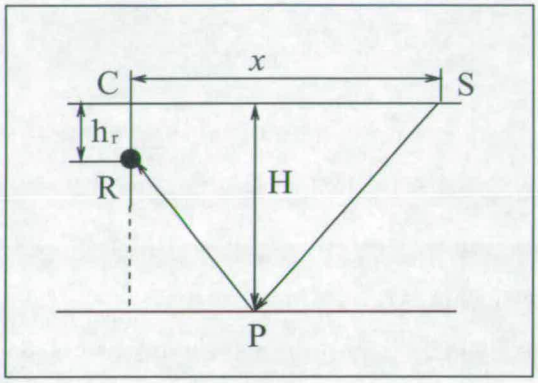


Figure 5.9: Ray path diagram for the initial velocity analysis. S, P and R indicate the source, reflection point and receiver locations, respectively. C denotes the cable location.

prove to be ineffective for VCS data, especially for complex structures (O'Brien and Etgen, 1998). Referring to Figure 5.9, we consider the source S and the receiver R at the cable C over a single interface. The reflection traveltime is expressed in terms of the offset x and velocity v as follows:

$$\begin{aligned} t &= \frac{1}{v}\sqrt{x^2 + (2H - h_r)^2} \\ &= \sqrt{t_0^2 - \frac{h_r t_0}{v} + \frac{x^2 + h_r^2}{v^2}}, \end{aligned} \tag{5.19}$$

where $t_0 = 2H/v$ is the two-way vertical traveltime, H is the depth of the reflector, and h_r is the depth of the receiver. I perform initial velocity analysis using the equation (5.19) on the common receiver gather. If the chosen receiver is located at the near surface, this equation is similar to the standard hyperbolic traveltime equation for the surface data. However, this single velocity function is not adequate to perform vertical cable seismic imaging in the presence of dip in the subsurface. The initial velocity model will be updated by the residual velocity analysis on the CSP gather described below.

5.4.2 *Generation of CSP gather*

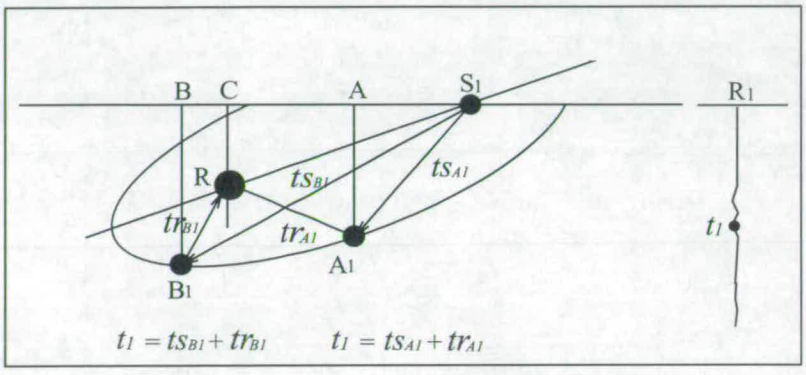
The full Kirchhoff approach to prestack migration is based on a model of scatter points, which scatter energy from any source to all receivers. The migration velocity is defined at the scatter point, regardless of the spatial or temporal extent of the scattered energy. I form a CSP gather by collecting and binning all input traces with offset in a common receiver gather as the DSR traveltime equation (5.16) and transmitting to the new traveltime t_{CSP} and offset x_{CSP}, which are given by

$$\begin{aligned} t_{CSP} = & \quad 2ts \quad , \\ = & \sqrt{t_0^2 + \frac{x_{CSP}^2}{V_s^2}} \quad , \end{aligned} \tag{5.20}$$

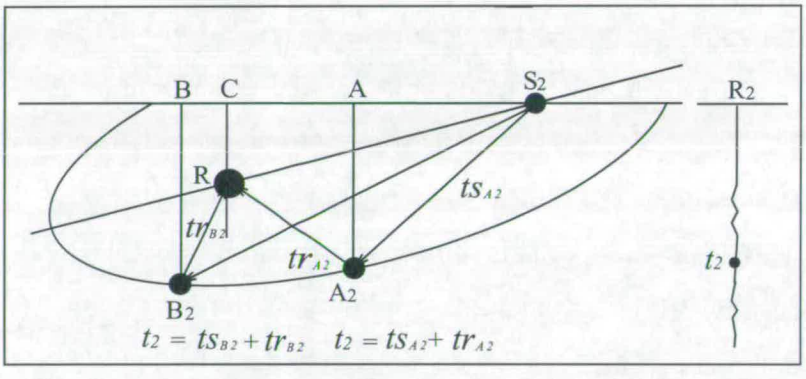
and

$$x_{CSP} = 2x_s. \tag{5.21}$$

This mapping process is shown in Figure 5.10, where traces R_1 and R_2 are taken from a common receiver gather R with sources S_1 and S_2, respectively. The mapping results are shown in Figure 5.11. The sample in the trace $R_1$with the traveltime t_1 will map into points on the tilting elliptic curve shown in Figure 5.10a, where each point on the curve belongs to a different CSP. In CSP A, this sample will map into scattering point A_1 with traveltime ts_{A1} along the ray path at the source side and tr_{A1} along at the receiver side, and $t_1 = ts_{A1} + tr_{A1}$. The traveltime of this simple in the new gather becomes $2ts_{A1}$, and the absolute offset is $2AS_1$, where AS_1 indicates the distance between the source S_1 and the common scattering point A. In the meantime, this sample will also map into scattering point B_1 in CSP B with traveltime ts_{B1} along the ray path at the source side and tr_{B1} along at the receiver side, and $t_1 = ts_{B1} + tr_{B1}$. The traveltime of this simple in the new gather becomes $2ts_{B1}$, and the absolute offset is $2BS_1$, where BS_1 indicates the distance between the source S_1 and the common scattering point B.



(a)



(b)

Figure 5.10: Generation of CSP gathers from a common receiver gather, where (a) trace R_1 corresponds to source S_1 and (b) trace R_2 corresponds to source S_2 with the same receiver R. A, B and C indicate locations of common scattering points A and B, and the cable position at the surface, respectively. A_1 and A_2, B_1 and B_2 are scattering points with the same surface projection position A and B, respectively.

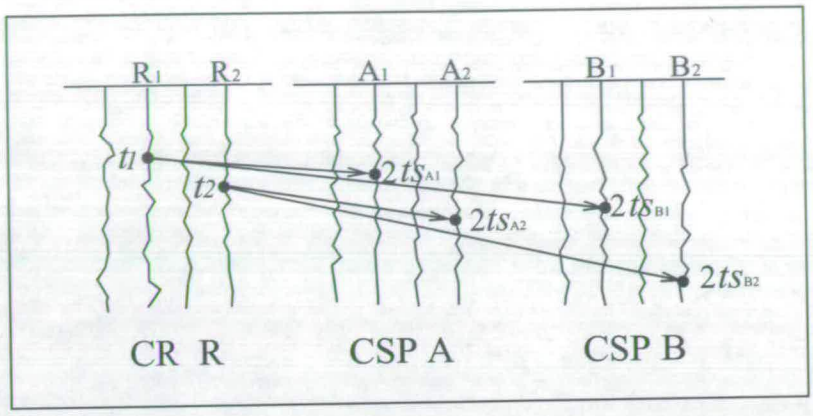


Figure 5.11: Referring to Figure 5.10, a schematic diagram showing the mapping result from a CR gather to CSP gathers.

In the same way, the sample in the trace R_2 with the traveltime t_2 will be mapped to points on the tilting elliptic curve shown in Figure 5.10b. In the CSP A, this sample will be mapped to scattering point A_2 with traveltime tS_{A2} along the ray path at the source side and tr_{A2} along at the receiver side, and $t_2 = ts_{A2} + t_{A2}$. The traveltime of this simple in the new gather becomes $2ts_{A2}$, and the absolute offset is $2AS_2$, where AS_2 indicates the distance between the source S_2 and the common scattering point A. This sample will also map into scattering point B_2 in CSP B with traveltime ts_{B2} along the ray path at the source side and tr_{B2} along at the receiver side, and $t_2 = ts_{B2} + tr_{B2}$. The traveltime of this simple in the new gather becomes $2ts_{B2}$, and the absolute offset is $2BS_2$, where BS_2 indicates the distance between the source S_2 and the common scattering point B.

This mapping procedure can be described as a process of time shift ($ts = t - tr$) with coordinate scaling ($t_{CSP} = 2ts$ and $x_{CSP} = 2x_s$) for each input sample. Each input trace will map into many CSP gathers, and each CSP gather contains all traces within the migration aperture. In contrast, if we form a CDP gather in a vertical cable seismic data set, it will be sparsely populated in offset and low in fold, since there are only a few receivers for a source in a VCS geometry. The new traveltime equation for the CSP gather is the same as the conventional hyperbolic

equation used for velocity analysis, NMO correction and stack. Therefore, we can use conventional processing tools to process VCS data by generating CSP gathers. In particular, CSP gathers can be created at any arbitrary location within a 2-D line or 3-D volume for velocity analysis, and the high fold and large offsets enable accurate velocity analysis at each migrated position.

5.5 Case study

I examine the proposed prestack migration method and the processing scheme of CSP stack in a field vertical cable seismic dataset from the North Sea (courtesy of Texaco). The acquisition geometry is given in Chapter 2.

5.5.1 Generation of CSP gather

Figure 5.12 shows two common receiver gathers along a selected 2-D source line. The first one is at the first depth level and the second one is at the sixteenth depth level. The distance between the two receivers is 120m. These gathers are due to wavefield separation using a differential-equation-based filter (see Chapter 3), only the upgoing waves are preserved for imaging in the test, and some of them are water column multiples.

I perform initial velocity analysis on the first receiver gather shown in Figure 5.12a. Since the depth of the receiver is only 6m, the equation (5.19) is near hyperbolic, the same as the equation used in the conventional velocity analysis. The velocity semblance is shown in Figure 5.13, in which I pick a rms velocity curve to produce CSP gathers although there are strong multiples presented as well. The interval of CSP is defined as $12.5m$. Three CSP gathers made from the first receiver gather are displayed in Figures 5.14, 5.15 and 5.16, respectively. The CSP 41 is located at the same surface position as the cable. We find that

some primary events are clearer in the CSP gathers than those in the common receiver gather. This is because CSP gathers are reconstructed by only using primary velocities and hence multiples are not coherent in these gathers.

5.5.2 *CSP stack*

To obtain more accurate velocities for performing VCS imaging, I apply the residual velocity analysis to each CSP gather. Figures 5.17, 5.18 and 5.19 show the velocity semblance made from CSP21, CSP41 and CSP61, respectively. The primary energy is much better focused than that in the initial velocity analysis shown in Figure 5.13. On the other hand, the energy of multiples is greatly reduced in these figures because I produce these gathers using only primary velocities.

In order to examine the accuracy of velocity analysis, I also display the corresponding NMO gathers in Figures 5.20, 5.21 and 5.22. Although some deep events are still hidden in the noise because of the presence of multiples, these primaries can be found clearly in the final CSP stack sections shown in Figure 5.23, in which section (a) is made from the first receiver gather, and section (b) is from the sixteenth receiver gather. Both sections are produced using the same velocity function. The consistency of events and the high signal-to-noise ratio in both sections demonstrate that the processing scheme of CSP stack is effective.

5.5.3 *Prestack migration*

Finally, I apply the prestack Kirchhoff time migration to the common receiver gathers. The velocity functions are taken from the residual velocity analysis on each CSP gather. The imaging results made from the data in Figure 5.12 are shown in Figure 5.24. As we can see, the corresponding events in both migration sections produced from the different common receiver gathers can be matched

with each other in the time domain. Therefore, a final imaging result for a whole cable data set can be obtained from the zero-moveout stack of each single receiver imaging, and the signal to noise ratio will be much improved. Compared to the CSP stack sections without amplitude scaling and phase correction, shown in Figure 5.23, the migration sections have high resolution, and the main primary events are consistent in these sections because all layers appear horizontal.

We also show the imaging results made from the same data set without using arrival angle information in Figure 5.25. Unfortunately, the imaging quality is much worse than that of the migration sections shown in Figure 5.24, since the primaries in these sections are distorted greatly by the false images which are the results of the limited observation geometry and strong water column multiples.

5.6 Conclusions

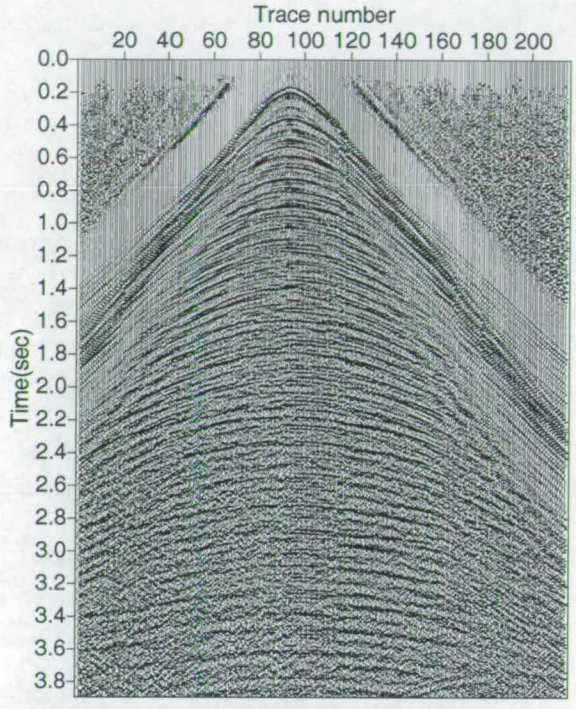
In vertical cable seismic data, the residual moveouts and dispersal of reflection points, due to the depth difference between receivers in the same cable, increase with increasing offset to depth ratios, if we make conventional statics and NMO corrections in a CDP gather. Therefore, it will degrade the quality of the conventional CDP stack, and produce mispositioning of reflectors, even if the subsurface is a horizontally-layered medium. Two examples show that the difference of residual moveouts is over $15ms$, and the dispersal difference of reflection points is over $40m$, between two given receivers with $120m$ interval, when the offset to depth ratio is 2.5.

As an alternative method to the conventional CDP stack, I have developed a processing scheme for the CSP stack. The CSP gather can be created by collecting and binning all input traces with offset in a common receiver gather according to the DSR traveltime equation, and transmitting to a new traveltime

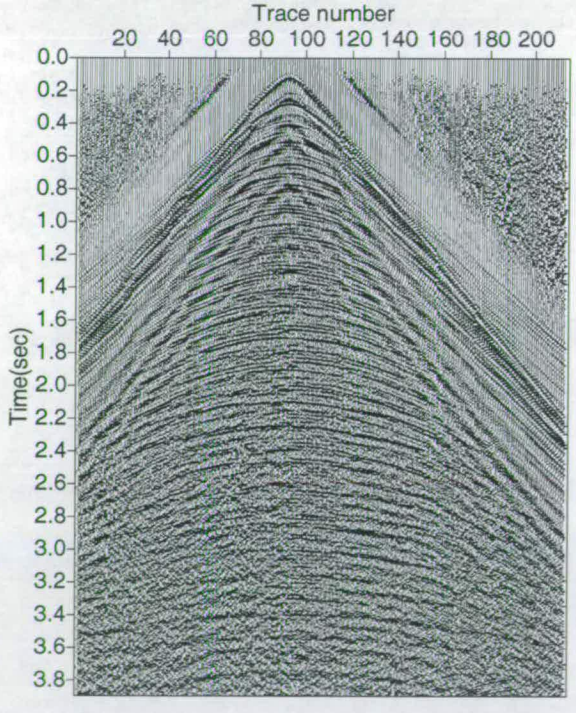
equation in terms of the new defined offset. The new traveltime equation for the CSP gather is the same as the conventional hyperbolic equation used for velocity analysis, NMO correction and stack in the surface data processing. Thus, these conventional processing tools can be used in our processing scheme of CSP stack. The high fold and large offsets in CSP gathers allow us make more accurate velocity analysis at each migrated position.

I have also proposed a prestack Kirchhoff time migration algorithm for vertical cable seismic imaging. The migration process is directly applied to each common receiver gather after the pre-processing of wavefield separation. The application of arrival angle weight in migration has much improved the imaging quality. The comparison of imaging results from the two common receiver gathers on the same cable demonstrates the efficiency of this method.

In this chapter, our imaging technique is based on the assumption that the seismic wave is propagating in an isotropic model, and the velocity is constant in the same CSP gather. In the future, we need to develop a 3-D azimuthal velocity analysis procedure to get a more accurate velocity model and to perform 3-D vertical cable seismic imaging based on the anisotropic model. So far tests have only been made on the single receiver gather which consists of a 2-D source line. For production processing, it is expected to obtain a final imaging result on the whole cable data set by stacking each single imaging achieved on the common receiver gather which consists of full 3-D sources.



(a)



(b)

Figure 5.12: Two common receiver gathers along a selected 2-D source line. (a) The receiver is at the first depth level, and (b) the receiver is at the sixteenth depth level.

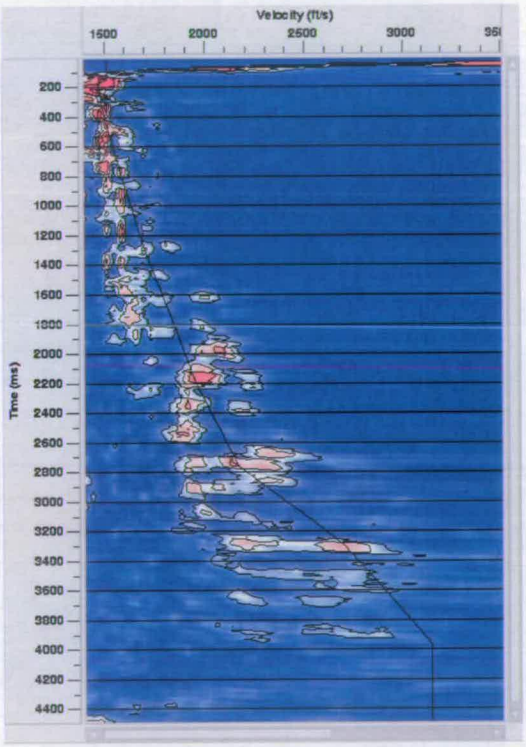


Figure 5.13: The velocity semblance of the first common receiver gather. An initial velocity function is chosen as indicated by the solid line.

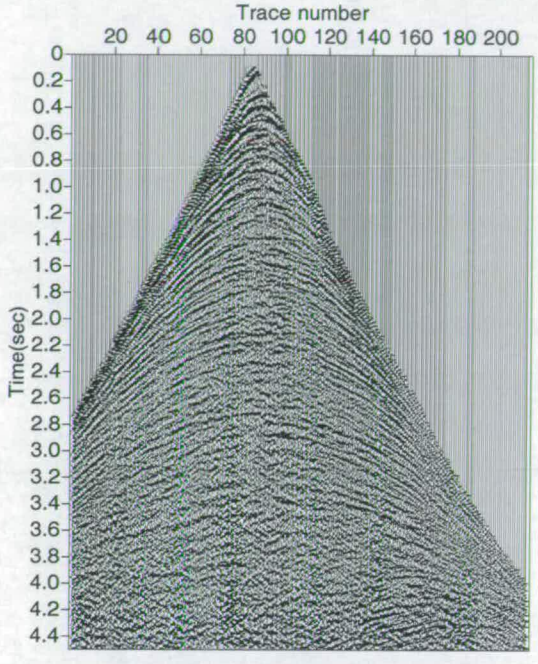


Figure 5.14: The CSP gather at CSP 21.

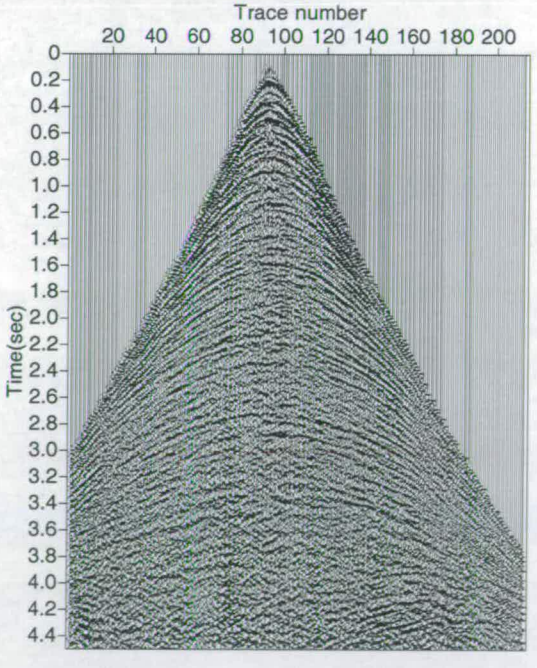


Figure 5.15: The CSP gather at CSP 41.

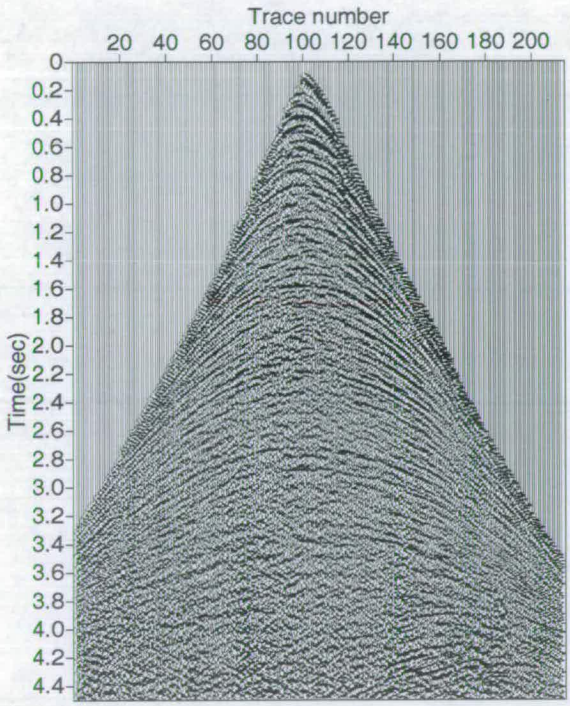


Figure 5.16: The CSP gather at CSP 61.

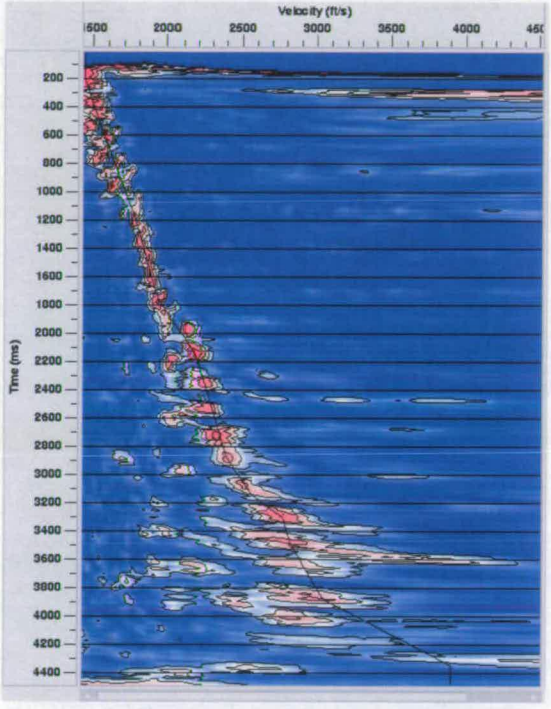


Figure 5.17: The velocity semblance of CSP 21.

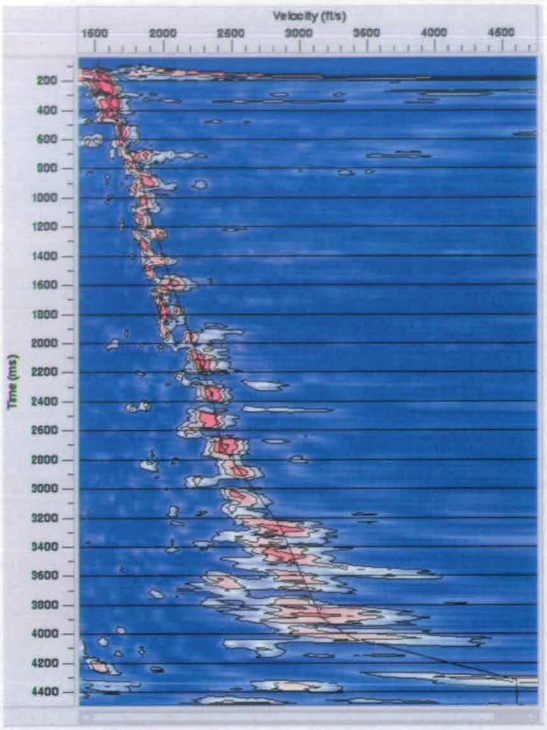


Figure 5.18: The velocity semblance of CSP 41.

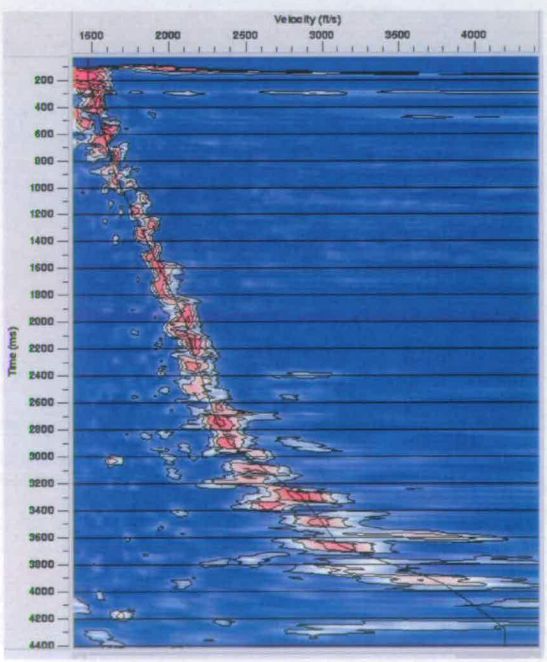


Figure 5.19: The velocity semblance of CSP 61.

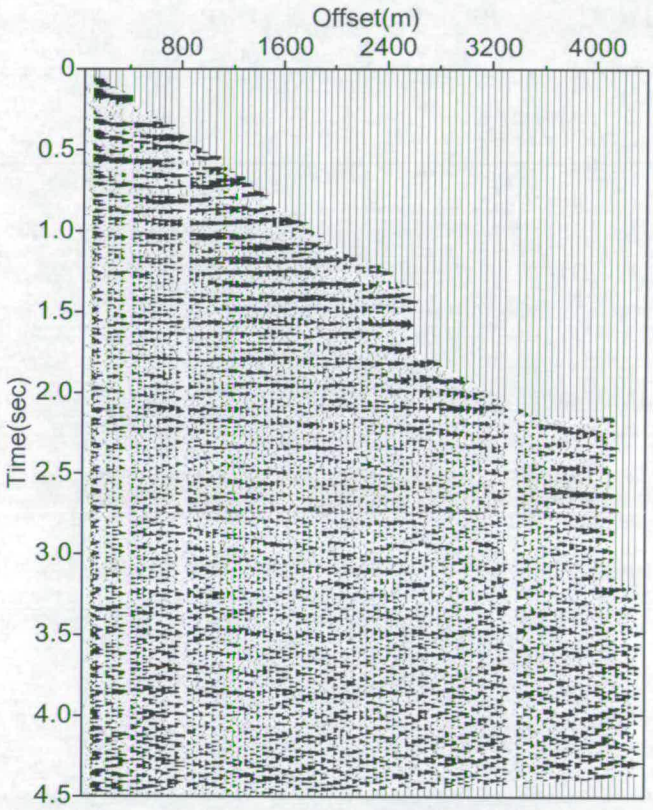


Figure 5.20: The NMO gather of CSP 21.

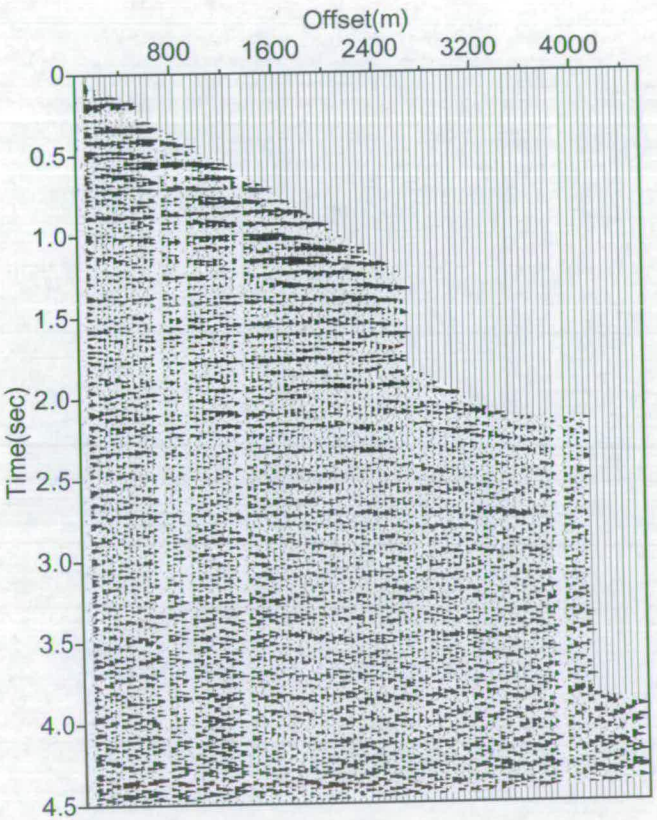


Figure 5.21: The NMO gather of CSP 41.

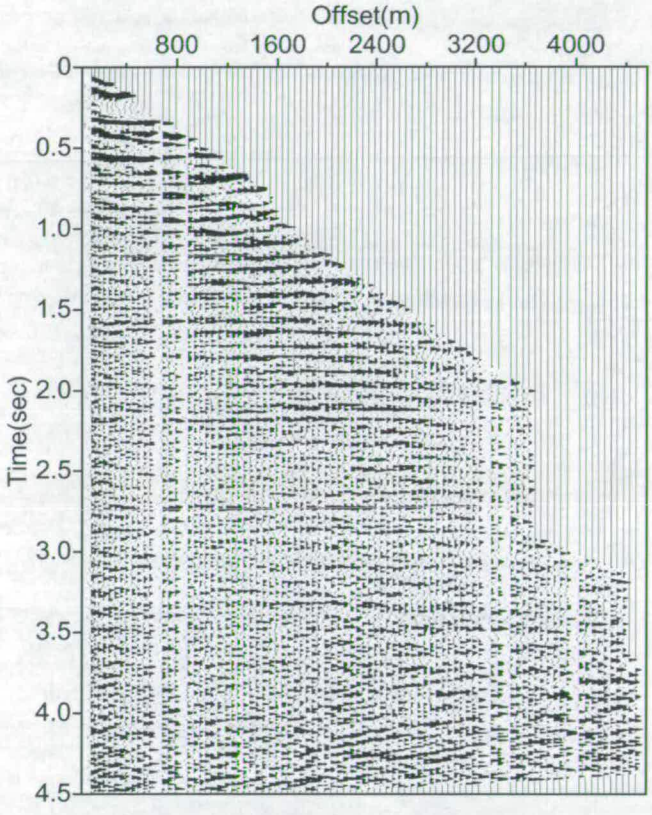
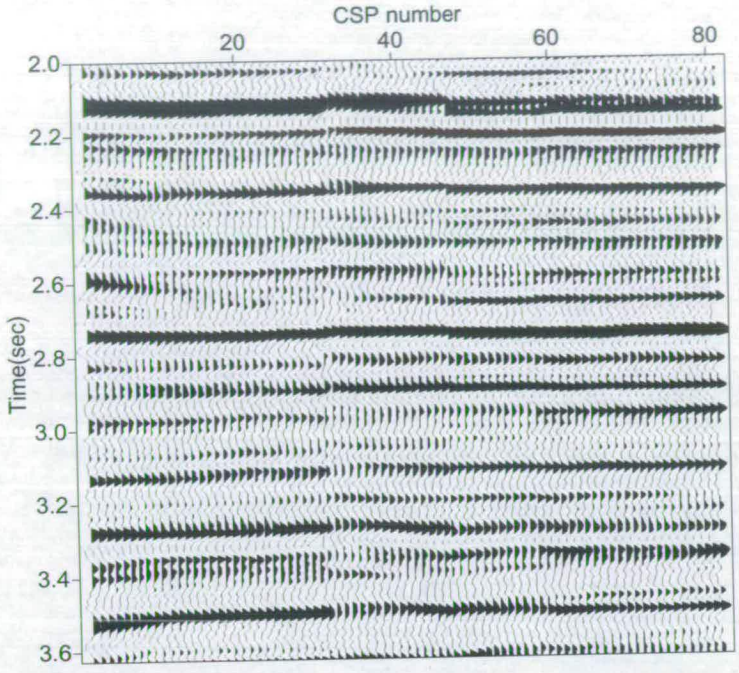
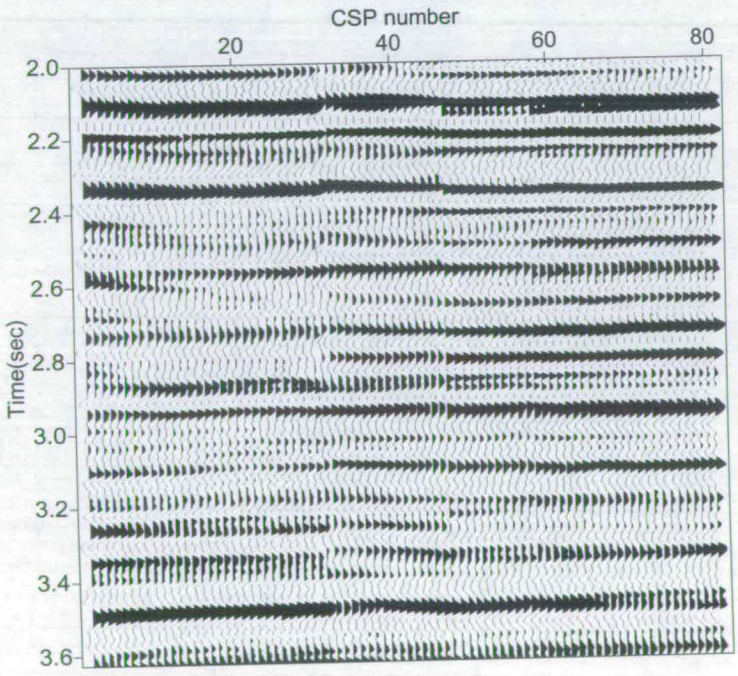


Figure 5.22: The NMO gather of CSP 61.

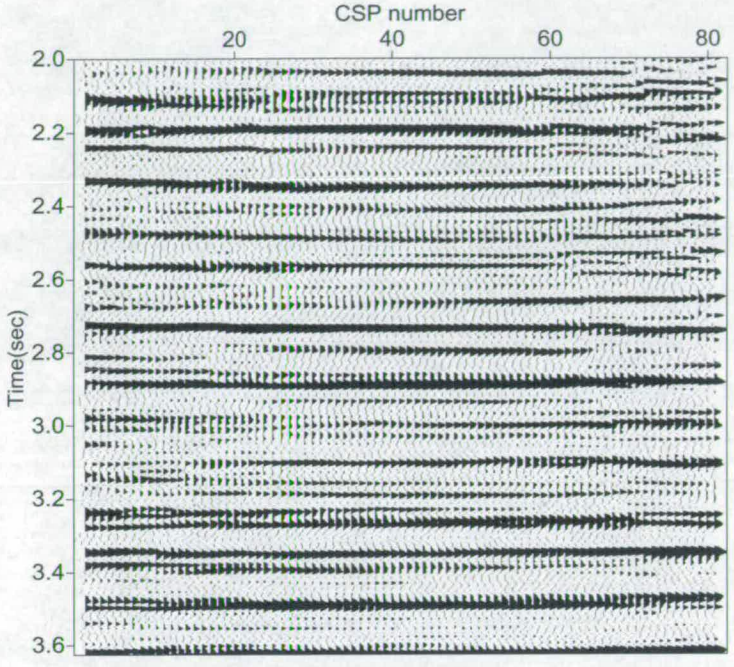


(a)

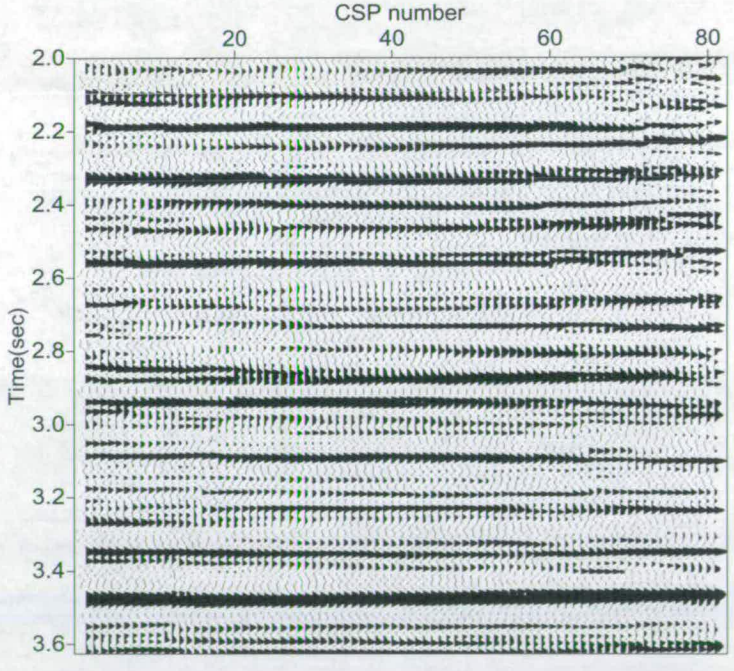


(b)

Figure 5.23: The CSP stack sections. The original data are from (a) the first receiver, and (b) the last receiver (sixteenth).



(a)



(b)

Figure 5.24: The imaging results of the data from Figure 5.12. (a) The first receiver, and (b) the last receiver (sixteenth).

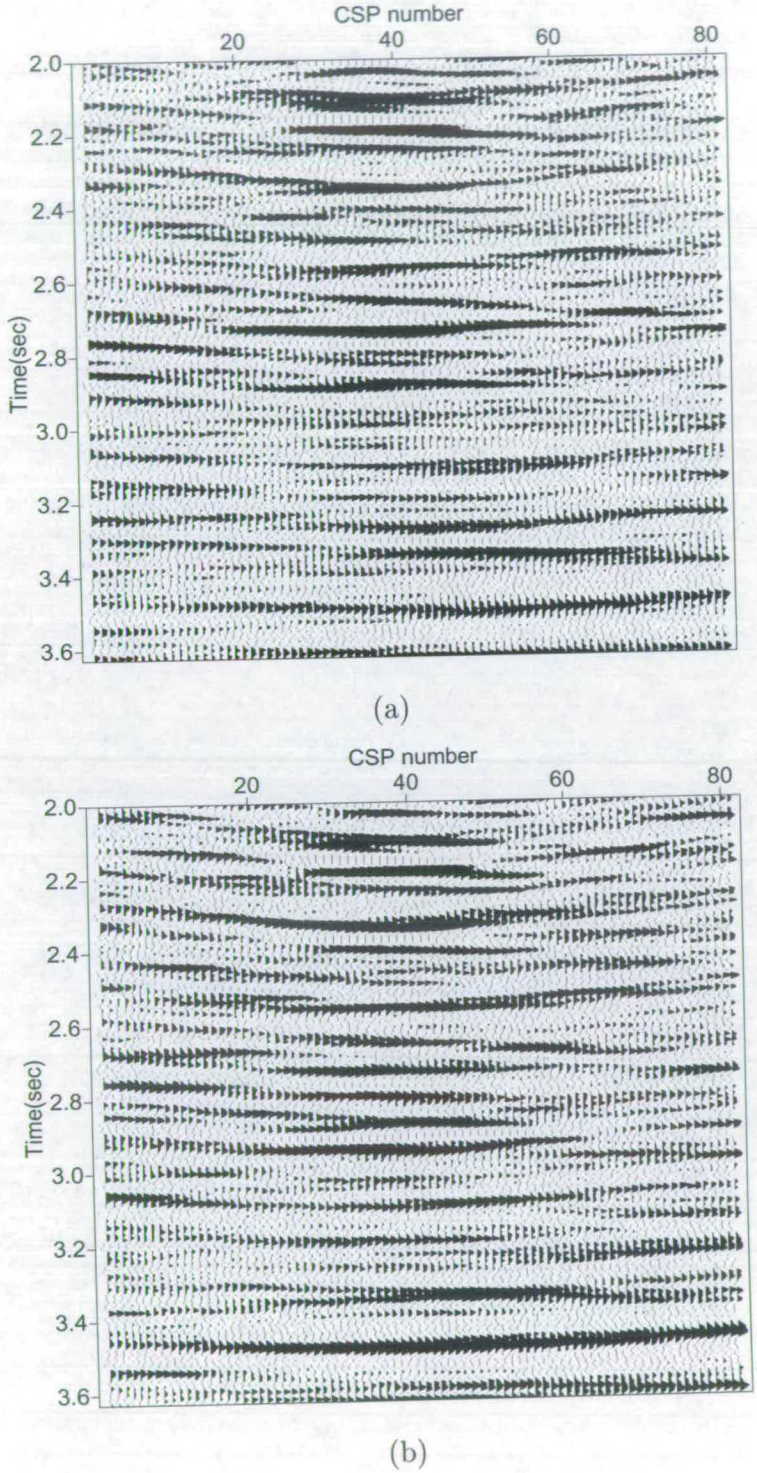


Figure 5.25: The imaging results of the data from Figure 5.12 without arrival angle weight. (a) The first receiver, and (b) the last receiver (sixteenth).

CHAPTER 6

Feasibility study of anisotropic traveltime inversion using VCS data

6.1 Introduction

Numerous investigations during the past decade have proved the presence of seismic anisotropy in different geological settings and on various scales. The existence of anisotropy may seriously affect the results of most basic processing and interpretation steps, such as NMO correction, velocity analysis, migration, dip moveout removal and AVO, while conventional processing of reflection $P-$wave data is still based on the assumption of isotropy. In order to properly account for anisotropy in the data processing, the anisotropic parameters of the rocks involved must be known. This chapter aims to investigate the feasibility of $P-$wave traveltime inversion for the estimation of anisotropic parameters using VCS data.

First, I introduced the transverse isotropic (TI) and orthorhombic media which are commonly used to describe the seismic anisotropy due to fine layering or aligned vertical fractures, or combinations of them, in exploration geophysics. Then, the slowness variations in these anisotropic media are discussed by solving the dispersion relation equations. After giving a review of anisotropic traveltime inversion methods used in walkaway VSP, reflection and refraction survey data,

I discuss the possibilities of VCS traveltime inversion by using direct, reflected and refracted arrivals in anisotropic media.

Finally, I propose a VCS refraction traveltime inversion procedure for the dip and ray-slowness estimation of the marine sediments, which is based on derivations of the traveltime equations for the refracted arrivals in a single refractor and multi-layered azimuthally anisotropic or isotropic media with parallel interfaces under VCS configuration. In order to correct the effects of dip, I obtain the horizontal and vertical ray-slownesses from the observed apparent slownesses in the up- and down-dip direction using a sum or difference at each measured azimuth. The multiple azimuths generated by a vertical cable geometry permit the ray-slowness distribution of the marine sediments to be determined. A least-squares procedure is used for inversion of the real dip and dip azimuth.

6.2 Common anisotropic media and parameters

With the increased use of multicomponent seismology, anisotropy measurements have become more quantitative. To describe a general anisotropic medium in the absence of any symmetry requires 21 independent elastic constants. In exploration geophysics, seismic anisotropy in sedimentary basins seems to be well modelled by hexagonal or orthorhombic symmetries. The hexagonal materials consist of a single symmetry axis so that the material properties appear directionally invariant in any direction perpendicular to this axis (Helbig 1994). These materials are commonly described in term of transverse isotropy (TI). Three types of TI media are introduced in this section with different directions of symmetry axes.

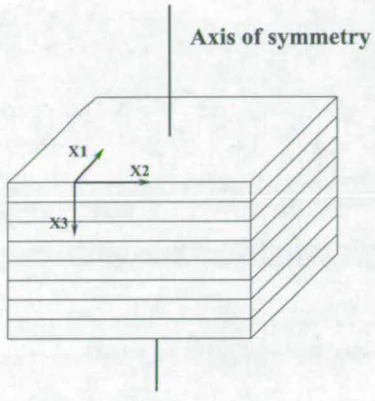


Figure 6.1: Model of a VTI medium

6.2.1 Transverse isotropic with a vertical axis of symmetry (VTI)

VTI represents a transverse isotropic medium corresponding to horizontal grain alignment or thin layering. The symmetry axis is usually orientated in a direction perpendicular to the layering shown in Figure 6.1. Any non-fractured horizontal sedimentary sequence like shales could have this type of anisotropy. VTI has been studied extensively due to its effect on velocities with consequences to traveltime calculations, normal moveouts, migration procedures and depth conversions. In the natural coordinate system (**X1-X2-X3**), 5 elastic constants are sufficient to describe the material, and the elements of the elastic tensor are distributed as

$$[C] = \begin{bmatrix} C_{11} & C_{12} & C_{13} & 0 & 0 & 0 \\ C_{12} & C_{11} & C_{13} & 0 & 0 & 0 \\ C_{13} & C_{13} & C_{33} & 0 & 0 & 0 \\ 0 & 0 & 0 & C_{44} & 0 & 0 \\ 0 & 0 & 0 & 0 & C_{44} & 0 \\ 0 & 0 & 0 & 0 & 0 & C_{66} \end{bmatrix}, \tag{6.1}$$

where

$$C_{12} = C_{11} - 2C_{66}. \tag{6.2}$$

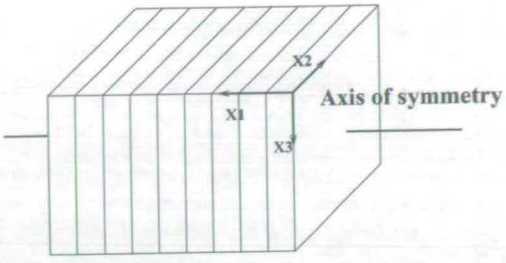


Figure 6.2: Model of an HTI medium

6.2.2 Transverse isotropic with a horizontal axis of symmetry (HTI)

HTI is the simplest type of azimuthally anisotropic media associated with a system of parallel, vertical cracks, microcracks, and preferentially orientated pore space embedded in an isotropic matrix (Crampin 1985; Thomsen 1988). HTI has attracted great interest due to its potential to hydrocarbon reservoir development. Figure 6.2 shows a model of an HTI medium. The number of independent elastic constants is exactly the same as in the VTI case. The elastic tensor of HTI media can be expressed as (see Appendix A)

$$[C] = \begin{bmatrix} C_{33} & C_{13} & C_{13} & 0 & 0 & 0 \\ C_{13} & C_{11} & C_{12} & 0 & 0 & 0 \\ C_{13} & C_{12} & C_{11} & 0 & 0 & 0 \\ 0 & 0 & 0 & C_{66} & 0 & 0 \\ 0 & 0 & 0 & 0 & C_{44} & 0 \\ 0 & 0 & 0 & 0 & 0 & C_{44} \end{bmatrix}, \tag{6.3}$$

where

$$C_{12} = C_{11} - 2C_{66}. \tag{6.4}$$

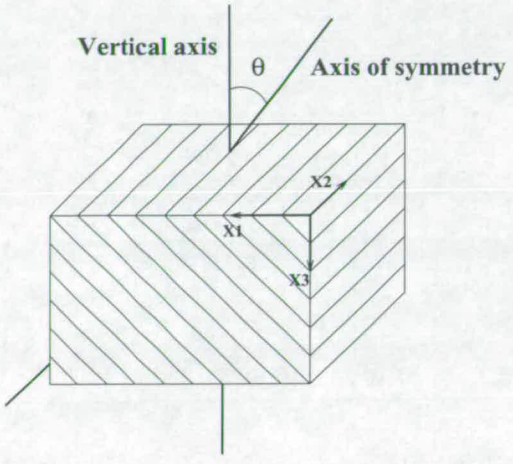


Figure 6.3: Model of a TTI medium

6.2.3 Transverse isotropic with a tilted axis of symmetry (TTI)

This type of anisotropy is associated with dipping beds, fractures, and grain orientation, with arbitrary dips of anisotropy axes. TTI is a general case of transverse isotropy with 5 independent elastic constants. Figure 6.3 shows a model of a VTI medium, where there is an angle θ between the axis of symmetry and the vertical axis. Under the coordinate system (**X1-X2-X3**), there are 13 non-zero elements in the elastic tensor of VTI shown in equation (6.5). Each element can be expressed as a function of the 5 independent elastic constants in VTI medium; the derivation of these expressions is shown in Appendix A.

$$[C'] = \begin{bmatrix} C'_{11} & C'_{12} & C'_{13} & 0 & C'_{15} & 0 \\ C'_{12} & C'_{22} & C'_{23} & 0 & C'_{25} & 0 \\ C'_{13} & C'_{23} & C'_{33} & 0 & C'_{35} & 0 \\ 0 & 0 & 0 & C'_{44} & 0 & C'_{46} \\ C'_{15} & C'_{25} & C'_{35} & 0 & C'_{55} & 0 \\ 0 & 0 & 0 & C'_{46} & 0 & C'_{66} \end{bmatrix}, \tag{6.5}$$

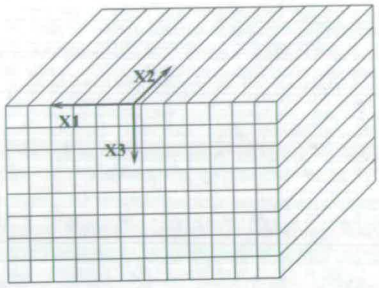


Figure 6.4: Model of an orthorhombic medium

6.2.4 Orthorhombic

The combinations of horizontal fine layering (VTI) and vertically aligned fractures (HTI) lead to a long-wavelength equivalent orthorhombic symmetry shown in Figure 6.4. The number of elastic constants that are required to describe such a material has risen to nine shown in equation (6.6). The elastic stiffness of this medium can be further expressed in terms of the VTI background moduli and the excess compliance caused by the fractures (Schoenberg and Helbig 1997).

$$[C] = \begin{bmatrix} C_{11} & C_{12} & C_{13} & 0 & 0 & 0 \\ C_{12} & C_{22} & C_{23} & 0 & 0 & 0 \\ C_{13} & C_{23} & C_{33} & 0 & 0 & 0 \\ 0 & 0 & 0 & C_{44} & 0 & 0 \\ 0 & 0 & 0 & 0 & C_{55} & 0 \\ 0 & 0 & 0 & 0 & 0 & C_{66} \end{bmatrix}. \tag{6.6}$$

6.3 Analysis of slowness variations

In this section, I will now derive the solutions for the cubic equation of the characteristic equation by which the slowness surfaces of three plane waves are determined in general anisotropic media, then discuss the slowness variations of

these waves propagating within the coordinate planes for TI and orthorhombic media.

6.3.1 Slowness surface

The Christoffel equations (Winterstein 1990), commonly used for calculating velocity and slowness surfaces, and dispersion relations of plane waves, may be written as

$$(k^2\mathbf{\Gamma} - \rho\omega^2\mathbf{I})\mathbf{u} = 0, \tag{6.7}$$

where

$$\mathbf{I} = \begin{bmatrix} 1 & 0 & 0 \\ 0 & 1 & 0 \\ 0 & 0 & 1 \end{bmatrix}, \tag{6.8}$$

k is wavenumber, ρ the density, ω the angular frequency, $\mathbf{u}$ the particle displacement vector, and the Christoffel matrix $\mathbf{\Gamma}$ can be further expressed as

$$\mathbf{\Gamma} = \mathbf{l}\mathbf{C}\mathbf{l}^T, \tag{6.9}$$

a 3×3 symmetric matrix, where $\mathbf{C}$ is the 6×6 stiffness matrix, $\mathbf{l}$ is the direction cosine matrix, and $\mathbf{l}^T$ is its transpose. Under the coordinate frame (**X-Y-Z**), $\mathbf{l}$ has the form

$$\mathbf{l} = \begin{bmatrix} l_x & 0 & 0 & 0 & l_z & l_y \\ 0 & l_y & 0 & l_z & 0 & l_x \\ 0 & 0 & l_z & l_y & l_x & 0 \end{bmatrix}. \tag{6.10}$$

Non-trivial solutions of the Christoffel equations exist if and only if the determinate of the coefficients vanishes. This condition can be expressed as

$$|k^2\mathbf{\Gamma} - \rho\omega^2\mathbf{I}| = 0. \tag{6.11}$$

This is the characteristic equation, sometimes called the dispersion relation or slowness relation, of the anisotropic medium. This equation can be further expressed as a cubic equation with respect to the square slowness, which is written as

$$x^3 + bx^2 + cx + d = 0, \tag{6.12}$$

where $x = \rho S^{-2}$, $S = k/\omega$ represents slowness, and

$$\begin{aligned} b &= -\Gamma_{11} - \Gamma_{22} - \Gamma_{33}, \\ c &= \Gamma_{11}\Gamma_{22} + \Gamma_{11}\Gamma_{33} + \Gamma_{22}\Gamma_{33} - \Gamma_{13}^2 - \Gamma_{23}^2 - \Gamma_{12}^2, \\ d &= \Gamma_{13}^2\Gamma_{22} + \Gamma_{23}^2\Gamma_{11} + \Gamma_{12}^2\Gamma_{33} - 2\Gamma_{12}\Gamma_{13}\Gamma_{23} - \Gamma_{11}\Gamma_{22}\Gamma_{33}. \end{aligned} \tag{6.13}$$

The substitution $x = y - b/3$ reduces equation (6.12) to a cubic equation in y without a quadratic term, which is written as

$$y^3 + py + q = 0, \tag{6.14}$$

where

$$\begin{aligned} p &= c - \frac{b^2}{3}, \\ q &= \frac{2b^3}{27} - \frac{bc}{3} + d. \end{aligned} \tag{6.15}$$

The discriminant of equation (6.14) can be written as

$$D = \frac{q^2}{4} + \frac{p^3}{27}. \tag{6.16}$$

If and only if $D \leq 0$, equation (6.14) has real roots. From the expression of p in equation (6.15), one can see that $p < 0$ in any direction of slowness. If $D = 0$,

$$q^2 = -\frac{4p^3}{27}, \tag{6.17}$$

then two of the three real roots of equation (6.14) are equal. The single root is $-\sqrt[3]{4q}$, and the repeated root is $\sqrt[3]{q/2}$. For $D < 0$, the roots are distinct and are

given by

$$\begin{aligned} y_1 &= 2\sqrt[3]{r}\cos\zeta, \\ y_2 &= 2\sqrt[3]{r}\cos(\zeta + 120°), \\ y_3 &= 2\sqrt[3]{r}\cos(\zeta + 240°), \end{aligned} \tag{6.18}$$

with

$$\begin{aligned} r &= \sqrt{-(\frac{p}{3})^3}, \\ \zeta &= \frac{1}{3}arc\cos(-\frac{q}{2r}). \end{aligned} \tag{6.19}$$

Finally, the slowness surfaces of three plane waves can be obtained by

$$\begin{aligned} S_1 &= \sqrt{\frac{3\rho}{3y_1 - b}}, \\ S_2 &= \sqrt{\frac{3\rho}{3y_2 - b}}, \\ S_3 &= \sqrt{\frac{3\rho}{3y_3 - b}}. \end{aligned} \tag{6.20}$$

6.3.2 VTI medium

Substituting equations (6.1) and (6.10) into equation (6.9), the elements of the Christoffel matrix for the VTI medium can be written as

$$\begin{aligned} \Gamma_{11} &= C_{11}l_x^2 + C_{66}l_y^2 + C_{44}l_z^2, \\ \Gamma_{12} &= (C_{12} + C_{66})l_x l_y, \\ \Gamma_{13} &= (C_{13} + C_{44})l_x l_z, \\ \Gamma_{22} &= C_{66}l_x^2 + C_{11}l_y^2 + C_{44}l_z^2, \\ \Gamma_{23} &= (C_{13} + C_{44})l_y l_z, \\ \Gamma_{33} &= C_{44}l_x^2 + C_{44}l_y^2 + C_{33}l_z^2. \end{aligned} \tag{6.21}$$

In the horizontal coordinate plane of **X-Y**, where $l_z = 0$, the characteristic equation of the VTI medium becomes

$$\begin{vmatrix} C_{11}l_x^2 + C_{66}l_y^2 - \rho S^{-2} & (C_{12} + C_{66})l_x l_y & 0 \\ (C_{12} + C_{66})l_x l_y & C_{66}l_x^2 + C_{11}l_y^2 - \rho S^{-2} & 0 \\ 0 & 0 & C_{44} - \rho S^{-2} \end{vmatrix} = 0. \quad (6.22)$$

This equation has three distinct roots corresponding to the three plane waves: $S_1 = \sqrt{\rho/C_{11}}$, which is the horizontal slowness of $P-$wave; $S_2 = \sqrt{\rho/C_{44}}$, which is the horizontal slowness of the fast shear wave; and $S_3 = \sqrt{\rho/C_{66}}$, which is the horizontal slowness of the slow shear wave. As we can see, these slownesses are all azimuthally isotropic. However, one can observe the shear wave splitting in the horizontal plane.

In the vertical coordinate plane of **X-Z**, where $l_y = 0$, the characteristic equation of the VTI medium becomes

$$\begin{vmatrix} C_{11}l_x^2 + C_{44}l_z^2 - \rho S^{-2} & 0 & (C_{13} + C_{44})l_x l_z \\ 0 & C_{66}l_x^2 + C_{44}l_z^2 - \rho S^{-2} & 0 \\ (C_{13} + C_{44})l_x l_z & 0 & C_{44}l_x^2 + C_{33}l_z^2 - \rho S^{-2} \end{vmatrix} = 0. \quad (6.23)$$

This equation can be further decomposed into two equations, which are written as

$$(C_{66}\sin^2\theta_p + C_{44}\cos^2\theta_p)S^2 = \rho, \quad (6.24)$$

and

$$aS^4 - \rho bS^2 + \rho^2 = 0, \quad (6.25)$$

with

$$\begin{aligned} a &= C_{44}(C_{33}\cos^4\theta_p + C_{11}\sin^4\theta_p) + (C_{11}C_{33} - 2C_{13}C_{44} - C_{13}^2)\sin^2\theta_p\cos^2\theta_p, \\ b &= C_{44} + C_{33}\cos^2\theta_p + C_{11}\sin^2\theta_p, \end{aligned} \quad (6.26)$$

where the phase angle θ_p is the angle between the wavefront normal and the vertical axis of symmetry. Equation (6.24) shows elliptic variations of the slowness for the pure shear (SH) wave propagating in the **X-Z** plane. The lengths of the long and short half-axes of this elliptic equation are $\sqrt{\rho/C_{44}}$ and $\sqrt{\rho/C_{66}}$. The slowness variations of quasi-P (qP) and quasi-SV (qSV) are determined by the equation (6.25). The roots for this equation can be further expressed as

$$(S^2)_P = \rho\frac{b-\sqrt{b^2-4a}}{2a}, \tag{6.27}$$

and

$$(S^2)_{SV} = \rho\frac{b+\sqrt{b^2-4a}}{2a}. \tag{6.28}$$

As a result, the slownesses of $P-$ and shear waves along the vertical axis of symmetry are $\sqrt{\rho/C_{33}}$ and $\sqrt{\rho/C_{44}}$, respectively. There is no shear wave splitting in this direction. One can see that the elastic constants C_{11}, C_{33}, C_{44} and C_{66} can be obtained by the measurement of slownesses of $P-$ and shear waves in the vertical and horizontal directions.

6.3.2.1 Thomsen anisotropy parameters

To specify anisotropy in TI media, I here introduce Thomsen's (1986) parameters which are widely used for anisotropy study,

$$v_{p0} = \sqrt{C_{33}/\rho}, \tag{6.29}$$

$$v_{s0} = \sqrt{C_{44}/\rho}, \tag{6.30}$$

$$\epsilon = \frac{C_{11}-C_{33}}{2C_{33}}, \tag{6.31}$$

$$\gamma = \frac{C_{66}-C_{44}}{2C_{44}}, \tag{6.32}$$

$$\delta = \frac{(C_{13}+C_{44})^2-(C_{33}-C_{44})^2}{2C_{33}(C_{33}-C_{44})}. \tag{6.33}$$

v_{p0} and v_{s0} are velocities for P and S waves propagating along the symmetry axis of the medium. For a VTI medium, in fact, these are vertical velocities.

ϵ is the parameter usually referred to as the anisotropy of a rock, and it can be used to measure the anisotropy strength of P wave. The parameter δ is a different combination elastic moduli without C_{11}, and it controls the near-vertical anisotropy in VTI media. For the special case of TI media, elliptical anisotropy is defined (Daley and Hron, 1979) by the condition of $\delta = \epsilon$. γ corresponds to the conventional meaning of "SH anisotropy", which indicates the anisotropy strength of shear wave.

6.3.3 HTI medium

Substituting equations (6.3) and (6.10) into equation (6.9), the elements of the Christoffel matrix for the HTI medium can be written as

$$\begin{aligned}
\Gamma_{11} &= C_{33}l_x^2 + C_{44}l_y^2 + C_{44}l_z^2, \\
\Gamma_{12} &= (C_{13} + C_{44})l_x l_y, \\
\Gamma_{13} &= (C_{13} + C_{44})l_x l_z, \\
\Gamma_{22} &= C_{44}l_x^2 + C_{11}l_y^2 + C_{66}l_z^2, \\
\Gamma_{23} &= (C_{12} + C_{66})l_y l_z, \\
\Gamma_{33} &= C_{44}l_x^2 + C_{66}l_y^2 + C_{11}l_z^2.
\end{aligned} \tag{6.34}$$

In the horizontal coordinate plane of **X-Y**, where $l_z = 0$ and the horizontal axis of symmetry is parallel to the **X**-axis, the characteristic equation of the HTI medium becomes

$$\begin{vmatrix}
C_{33}l_x^2 + C_{44}l_y^2 - \rho S^{-2} & (C_{13} + C_{44})l_x l_y & 0 \\
(C_{13} + C_{44})l_x l_y & C_{44}l_x^2 + C_{11}l_y^2 - \rho S^{-2} & 0 \\
0 & 0 & C_{44}l_x^2 + C_{66}l_y^2 - \rho S^{-2}
\end{vmatrix} = 0. \tag{6.35}$$

This equation can be further decomposed into two equations, which are written as

$$(C_{66}\sin^2\theta_p + C_{44}\cos^2\theta_p)S^2 = \rho, \tag{6.36}$$

and

$$aS^4 - \rho bS^2 + \rho^2 = 0, \tag{6.37}$$

with

$$\begin{aligned} a &= C_{44}(C_{33}\cos^4\theta_p + C_{11}\sin^4\theta_p) + (C_{11}C_{33} - 2C_{13}C_{44} - C_{13}^2)\sin^2\theta_p\cos^2\theta_p, \\ b &= C_{44} + C_{33}\cos^2\theta_p + C_{11}\sin^2\theta_p, \end{aligned} \tag{6.38}$$

where the phase angle θ_p is the angle between the wavefront normal and the horizontal axis of symmetry. As we can see, these equations are the same as those that determine the slowness variations in a vertical plane for VTI medium. Thus, in the HTI medium, the expression of the directionally dependent slowness for each wave in the horizontal plane take the same form as the one in the vertical plane for VTI medium.

In the vertical coordinate plane of **Y-Z**, which is perpendicular to the horizontal axis, one can obtain the same results as in the horizontal plane for a VTI medium. The slownesses of three waves propagating in this plane are all directionally invariant. For $P-$wave, the slowness is $\sqrt{\rho/C_{11}}$, and slownesses for two shear waves (SH and SV) are $\sqrt{\rho/C_{44}}$ and $\sqrt{\rho/C_{66}}$, respectively.

6.3.4 TTI medium

For a TTI medium, I assume that there is an angle of θ between the axis of symmetry and the vertical axis in the vertical coordinate plane of **X-Z**. Substituting equations (6.5) and (6.10) into equation (6.9), the elements of the Christoffel matrix for the TTI medium can be written as

$$\Gamma_{11} = C'_{11}l_x^2 + C'_{66}l_y^2 + C'_{55}l_z^2 + 2C'_{15}l_xl_z,$$

$$\begin{aligned}
\Gamma_{12} &= (C'_{12}+C'_{66})l_x l_y + (C'_{25}+C'_{46})l_z l_y, \\
\Gamma_{13} &= (C'_{13}+C'_{55})l_x l_z + C'_{46}l_y^2 + C'_{35}l_z^2, \\
\Gamma_{22} &= C'_{66}l_x^2 + C'_{22}l_y^2 + C'_{44}l_z^2 + 2C'_{46}l_x l_z, \\
\Gamma_{23} &= (C'_{23}+C'_{44})l_y l_z + (C'_{25}+C'_{46})l_x l_y, \\
\Gamma_{33} &= C'_{55}l_x^2 + C'_{44}l_y^2 + C'_{33}l_z^2 + 2C'_{35}l_x l_z.
\end{aligned} \tag{6.39}$$

In the horizontal coordinate plane of **X-Y**, where $l_z = 0$, the characteristic equation for the TTI medium becomes

$$\begin{vmatrix}
\Gamma_{11}-\rho S^{-2} & \Gamma_{12} & 0 \\
\Gamma_{12} & \Gamma_{22}-\rho S^{-2} & \Gamma_{23} \\
0 & \Gamma_{23} & \Gamma_{33}-\rho S^{-2}
\end{vmatrix} = 0, \tag{6.40}$$

with

$$\begin{aligned}
\Gamma_{11} &= C'_{11}l_x^2 + C'_{66}l_y^2, \\
\Gamma_{12} &= (C'_{12}+C'_{66})l_x l_y, \\
\Gamma_{22} &= C'_{66}l_x^2 + C'_{22}l_y^2, \\
\Gamma_{23} &= (C'_{25}+C'_{46})l_x l_y, \\
\Gamma_{33} &= C'_{55}l_x^2 + C'_{44}l_y^2.
\end{aligned} \tag{6.41}$$

Since it is difficult to decompose this equation, I write it as a general cubic equation with respect to the square slowness as

$$x^3 + bx^2 + cx + d = 0, \tag{6.42}$$

where $x = \rho S^{-2}$, and

$$\begin{aligned}
b &= -\Gamma_{11} - \Gamma_{22} - \Gamma_{33}, \\
c &= \Gamma_{11}\Gamma_{22} + \Gamma_{11}\Gamma_{33} + \Gamma_{22}\Gamma_{33} - \Gamma_{23}^2 - \Gamma_{12}^2,
\end{aligned} \tag{6.43}$$

$$d = \Gamma_{23}^2\Gamma_{11} + \Gamma_{12}^2\Gamma_{33} - \Gamma_{11}\Gamma_{22}\Gamma_{33}.$$

The solutions for this equation can be obtained using equations (6.18) to (6.20). It is so complicated that we can not directly analyse the slowness variations from these solutions.

In the vertical coordinate plane of **X-Z**, where $l_y = 0$, the characteristic equation of the TTI medium becomes

$$\begin{vmatrix} \Gamma_{11} - \rho S^{-2} & 0 & \Gamma_{13} \\ 0 & \Gamma_{22} - \rho S^{-2} & 0 \\ \Gamma_{13} & 0 & \Gamma_{33} - \rho S^{-2} \end{vmatrix} = 0, \tag{6.44}$$

with

$$\begin{aligned} \Gamma_{11} &= C'_{11}l_x^2 + C'_{55}l_z^2 + 2C'_{15}l_xl_z, \\ \Gamma_{13} &= (C'_{13} + C'_{55})l_xl_z + C'_{35}l_z^2, \\ \Gamma_{22} &= C'_{66}l_x^2 + C'_{44}l_z^2 + 2C'_{46}l_xl_z, \\ \Gamma_{33} &= C'_{55}l_x^2 + C'_{33}l_z^2 + 2C'_{35}l_xl_z. \end{aligned} \tag{6.45}$$

This equation can be further decomposed into two equations, which are written as

$$(C'_{66}l_x^2 + C'_{44}l_z^2 + 2C'_{46}l_xl_z)S^2 = \rho, \tag{6.46}$$

and

$$aS^4 - \rho bS^2 + \rho^2 = 0, \tag{6.47}$$

with

$$\begin{aligned} a &= \Gamma_{11}\Gamma_{33} - \Gamma_{13}^2, \\ b &= \Gamma_{11} + \Gamma_{33}. \end{aligned} \tag{6.48}$$

Substitution of equation (A.6) into equation (6.46) yields

$$(C_{66}\sin^2\theta_p + C_{44}\cos^2\theta_p)S^2 = \rho, \tag{6.49}$$

where θ_p is the phase angle defined by the angle between the wavefront normal and the tilted axis of symmetry. The elliptic equation (6.49) shows slowness variations of the pure shear (SH) wave propagating in the **X-Z** plane. The length of the long and short half-axes for this elliptic equation are $\sqrt{\rho/C_{44}}$ and $\sqrt{\rho/C_{66}}$, and the short axis is parallel to the tilted axis of symmetry. In the same way, equation (6.48) can be further expressed as

$$\begin{aligned} a &= C_{44}(C_{33}\cos^4\theta_p + C_{11}\sin^4\theta_p) + (C_{11}C_{33} - 2C_{13}C_{44} - C_{13}^2)\sin^2\theta_p\cos^2\theta_p, \\ b &= C_{44} + C_{33}\cos^2\theta_p + C_{11}\sin^2\theta_p. \end{aligned} \tag{6.50}$$

The slowness variations of qP and qSV are determined by the equation (6.47). The roots for this equation can be written as

$$(S^2)_P = \rho\frac{b - \sqrt{b^2 - 4a}}{2a}, \tag{6.51}$$

and

$$(S^2)_{SV} = \rho\frac{b + \sqrt{b^2 - 4a}}{2a}. \tag{6.52}$$

As we can see, the slowness expressions for three waves are the same as those in VTI and HTI media in the plane with the axis of symmetry. These slownesses in TI media can be expressed as functions of the five independent elastic constants and the phase angle measured by the angle between the wavefront normal and the axis of symmetry.

6.3.5 Orthorhombic medium

For an orthorhombic medium, the non-zero elements of the Christoffel matrix can be written as

$$\begin{aligned} \Gamma_{11} &= C_{11}l_x^2 + C_{66}l_y^2 + C_{55}l_z^2, \\ \Gamma_{12} &= (C_{12} + C_{66})l_x l_y, \end{aligned}$$

$$\begin{aligned}
\Gamma_{13} &= (C_{13}+C_{55})l_x l_z, \\
\Gamma_{22} &= C_{66}l_x^2 + C_{22}l_y^2 + C_{44}l_z^2, \\
\Gamma_{23} &= (C_{23}+C_{44})l_y l_z, \\
\Gamma_{33} &= C_{55}l_x^2 + C_{44}l_y^2 + C_{33}l_z^2.
\end{aligned} \tag{6.53}$$

In the horizontal coordinate plane of **X-Y**, where I set $l_x = \cos\theta_p$, $l_y = \sin\theta_p$ and $l_z = 0$, θ_p is the phase angle defined as the angle between the wavefront normal and the **X**-axis, the characteristic equation for the orthorhombic medium becomes

$$\begin{vmatrix}
\Gamma_{11} - \rho S^{-2} & \Gamma_{12} & 0 \\
\Gamma_{12} & \Gamma_{22} - \rho S^{-2} & 0 \\
0 & 0 & \Gamma_{33} - \rho S^{-2}
\end{vmatrix} = 0, \tag{6.54}$$

where

$$\begin{aligned}
\Gamma_{11} &= C_{11}\cos^2\theta_p + C_{66}\sin^2\theta_p, \\
\Gamma_{12} &= (C_{12}+C_{66})\cos\theta_p \sin\theta_p, \\
\Gamma_{22} &= C_{66}\cos^2\theta_p + C_{22}\sin^2\theta_p, \\
\Gamma_{33} &= C_{55}\cos^2\theta_p + C_{44}\sin^2\theta_p.
\end{aligned} \tag{6.55}$$

This equation can be further decomposed into two equations, which are written as

$$(C_{55}\sin^2\theta_p + C_{44}\sin^2\theta_p)S^2 = \rho, \tag{6.56}$$

and

$$aS^4 - \rho b S^2 + \rho^2 = 0, \tag{6.57}$$

with

$$\begin{aligned}
a &= C_{66}(C_{11}\cos^4\theta_p + C_{22}\sin^4\theta_p) + (C_{11}C_{22} - 2C_{12}C_{66} - C_{12}^2)\sin^2\theta_p\cos^2\theta_p, \\
b &= C_{66} + C_{11}\cos^2\theta_p + C_{22}\sin^2\theta_p.
\end{aligned} \tag{6.58}$$

Equation (6.56) shows elliptic variations of slownesses for the SH wave in the horizontal plane. The lengths of two half-axes for this ellipse are $\sqrt{\rho/C_{55}}$ and $\sqrt{\rho/C_{44}}$. The square slownesses for qP and qSV waves are obtained by solving the equation (6.57), whose roots can be expressed as

$$(S^2)_P = \rho\frac{b - \sqrt{b^2 - 4a}}{2a}, \tag{6.59}$$

and

$$(S^2)_{SV} = \rho\frac{b + \sqrt{b^2 - 4a}}{2a}. \tag{6.60}$$

In the two special directions, **X** and **Y** axes, slownesses of the qP wave are $\sqrt{\rho/C_{11}}$ and $\sqrt{\rho/C_{22}}$, the SH wave are $\sqrt{\rho/C_{55}}$ and $\sqrt{\rho/C_{44}}$, and the qSV wave are all $\sqrt{\rho/C_{66}}$. As we can see, the slowness solutions for three waves have the same forms as an HTI medium in the horizontal plane. This is because the slownesses in the VTI background of an orthorhombic medium reveal azimuthal isotropic features.

In the vertical coordinate plane of **X-Z**, where I set $l_x = \sin\theta_p$, $l_z = \cos\theta_p$ and $l_y = 0$, θ_p is the phase angle defined as the angle between the wavefront normal and the **Z**-axis, the characteristic equation for the orthorhombic medium becomes

$$\begin{vmatrix} \Gamma_{11} - \rho S^{-2} & 0 & \Gamma_{13} \\ 0 & \Gamma_{22} - \rho S^{-2} & 0 \\ \Gamma_{13} & 0 & \Gamma_{33} - \rho S^{-2} \end{vmatrix} = 0, \tag{6.61}$$

where

$$\begin{aligned} \Gamma_{11} &= C_{11}\sin^2\theta_p + C_{55}\cos^2\theta_p, \\ \Gamma_{13} &= (C_{13} + C_{55})\cos\theta_p\sin\theta_p, \\ \Gamma_{22} &= C_{66}\sin^2\theta_p + C_{44}\cos^2\theta_p, \\ \Gamma_{33} &= C_{55}\sin^2\theta_p + C_{33}\cos^2\theta_p. \end{aligned} \tag{6.62}$$

This equation can also be decomposed into two equations, which are written as

$$(C_{66}\sin^2\theta_p + C_{44}\cos^2\theta_p)S^2 = \rho, \tag{6.63}$$

and

$$aS^4 - \rho bS^2 + \rho^2 = 0, \tag{6.64}$$

with

$$\begin{aligned} a &= C_{55}(C_{11}\sin^4\theta_p + C_{33}\cos^4\theta_p) + (C_{11}C_{33} - 2C_{13}C_{55} - C_{13}^2)\sin^2\theta_p\cos^2\theta_p, \\ b &= C_{55} + C_{11}\sin^2\theta_p + C_{33}\cos^2\theta_p. \end{aligned} \tag{6.65}$$

Equation (6.63) shows elliptic variations of slownesses for the SH wave in the vertical plane of **X-Z**. The lengths of two half-axes for this ellipse are $\sqrt{\rho/C_{66}}$ and $\sqrt{\rho/C_{44}}$. The square slownesses for qP and qSV waves are obtained by solving the equation (6.64), and the roots can be expressed as

$$(S^2)_P = \rho\frac{b - \sqrt{b^2 - 4a}}{2a}, \tag{6.66}$$

and

$$(S^2)_{SV} = \rho\frac{b + \sqrt{b^2 - 4a}}{2a}. \tag{6.67}$$

In the vertical direction (**Z**-axis), slownesses of the quasi-P, SH and quasi-SV waves are $\sqrt{\rho/C_{33}}$, $\sqrt{\rho/C_{44}}$, and $\sqrt{\rho/C_{55}}$, respectively.

6.4 Anisotropic traveltime inversion methods

Over the past decades, much effort has been focused on the $P-$ wave traveltime inversion for investigating seismic anisotropy. The direct, refracted and reflected arrivals are used for phase slowness, headwave velocity and reflection moveout inversions, respectively, according to its corresponding acquisition geometry.

6.4.1 *Walkaway VSPs*

Gaiser (1990) has shown that a wide aperture walkaway VSP can be used to describe the qP phase slowness surface related to the localized region around a borehole receiver array. The method relies upon independent estimation of the vertical and horizontal phase slownesses from the gradient of the traveltimes across both the receiver tool and the array of source points respectively. This technique requires the assumption of a horizontally layered medium above the receiver array so that the horizontal slowness observed at a source point on a common receiver gather is the same as the horizontal slowness at the depth of the receiver. Sayers (1997) suggested the averaging of the slownesses for positive and negative offsets to correct for the effects of dip. The functional relationship between the vertical and horizontal slownesses may then be used to invert for the density-weighted stiffnesses.

For a TI medium, (Miller and Spencer, 1994), the $qP - qSV$ dispersion relation (6.25) can be rewritten as

$$A_{11}[A_{44}X^2 - X] + A_{33}[A_{44}Z^2 - Z] + A[XZ] = [A_{44}(X + Z) - 1], \qquad (6.68)$$

with

$$A = A_{11}A_{33} + A_{44}^2 - (A_{13} + A_{44})^2, \qquad (6.69)$$

where $A_{ij} = C_{ij}/\rho$, $X = S_h^2$, $Z = S_z^2$, and S_h and S_z are horizontal and vertical slownesses for qP or qSV waves. Given (squared) phase data points $(X_i, Z_i) : i = 1, n$ and a value for A_{44}, each of the bracketed quantities becomes a data vector and equation (6.68) becomes a linear system. The scalar coefficients A_{11}, A_{33} and A can then be obtained by a least squares inversion. The only requirement for the applicability of this approach is a prior estimate of A_{44}.

Under the assumption of a weak TI medium, Ohlsen and MacBeth (1998) reformulated Thomsen's (1986) first order approximation for qP velocity to obtain

three coefficients for the least squares inversion in terms of combinations of the horizontal and vertical slownesses S_h and S_z, given by

$$(1+\epsilon+\delta')S_h^2 + (\epsilon-\delta')\frac{S_h^4}{S_h^2+S_z^2} - \frac{1}{v_{p0}^2} = -S_z^2, \tag{6.70}$$

where ϵ and v_{p0} are Thomsen's original parameters whilst δ' is a slightly modified form of δ, given by

$$\delta = \frac{\epsilon+\delta'}{2}. \tag{6.71}$$

This method can also be extended to include fracture-related anisotropy. This is achieved by developing a factorized slowness equation for an orthorhombic medium created by embedding a dilute crack/fracture distribution in a VTI background (MacBeth 1998). Inspection of the equations suggests that walkaway lines along three different azimuths could prove satisfactory for determining vertical fracture strike and help contribute towards an understanding of fracture characteristics.

6.4.2 Reflection survey

The shape of the moveout curves for reflected waves is of primary importance to most processing and interpretation algorithms. The presence of anisotropy causes two principal distortions of reflection moveouts. First, the short-spread moveout velocity in the presence of anisotropy is not equal to the rms vertical velocity, even for horizontal layers (Thomsen 1986). The difference between vertical rms and moveout velocities, ignored by conventional techniques, may lead to unacceptable errors in interval velocities and in time-to-depth conversion, even for weak anisotropy (Banik 1984; Winterstein 1986). Second, anisotropy leads to nonhyperbolic moveout, even in a homogeneous layer. If not properly corrected for, nonhyperbolic moveout causes distortions in velocity estimation, and degrades the quality of stacked sections.

Sena (1991) derived analytical expressions giving traveltime-offset curves for multi-layered weakly azimuthally isotropic and anisotropic media in terms of the elastic properties of each layer. For a given layer with a depth of H, the traveltime equation can be expressed as

$$t^2 = \frac{4H^2}{V_v^2} + \frac{x^2}{V_\gamma^2} + \frac{x^4}{4H^2}\left(\frac{1}{V_h^2} - \frac{1}{V_\gamma^2}\right), \tag{6.72}$$

where x is the offset, V_v is the average vertical velocity, V_h and V_γ are defined as the horizontal and skew moveout velocities. For a multi-layered medium, the interval properties V_{v_k}, V_{h_k} and V_{γ_k} for every layer k above such a reflector can be obtained from these bulk velocities measured from the traveltime curves. Based on this equation, a traveltime inversion approach has been developed to estimate the five elastic constants together with the orientation of the axis of symmetry for each layer.

However, Tsvankin and Thomsen (1994) show that the domain of validity of that formalism is rather limited. In principle, if the vertical velocities (or layer thicknesses) are known, the anisotropic coefficients may be determined from short-spread moveouts (P, SV and SH) alone. They examined the feasibility of inverting reflection traveltimes from horizontal interfaces for the parameters of a VTI model, in the case when vertical velocities are unknown. The results show that conventional hyperbolic moveout analysis on short-spread gathers does not provide enough information to solve this problem, even if all three waves (P, SV and SH) are recorded. They also introduced a better nonhyperbolic moveout approximation for a VTI medium:

$$t^2 = t_0^2 + A_2 x^2 + \frac{A_4 x^4}{1 + A x^2}, \tag{6.73}$$

with

$$A = \frac{A_4 V_h^2}{1 - A_2 V_h^2}, \tag{6.74}$$

where t_0 is the vertical arrival time. For a $P-$wave, parameters A_2 and A_4 for a

single layer may be written as

$$A_2 = \frac{1}{v_{p0}^2(1+2\delta)}, \tag{6.75}$$

$$A_4 = \frac{-2(\epsilon-\delta)}{t_0^2 v_{p0}^4(1+2\delta)^4}(1+\frac{2\delta}{1-v_{s0}^2/v_{p0}^2}), \tag{6.76}$$

where v_{p0}, v_{s0}, ϵ and δ are Thomsen's parameters.

To determine the degree of ambiguity and find out what kind of data are necessary for unambiguous inversion, Tsvankin and Thomsen (1995) have carried out numerical analysis of the objective function (rms time residuals) for the inversion of $P-$ and $SV-$wave reflection traveltimes. The results show that $P-$wave data alone are insufficient for accurate determination of vertical velocity, even if long spreads are used ($x_{max} = 2z$). The degree of nonuniqueness may be significantly reduced by combining long-spread $P-$ and $SV-$wave data. There is no doubt that for more complicated azimuthally anisotropic models the degree of nonuniqueness in the traveltime inversion is even greater.

6.4.3 Refraction survey

Two $P-$wave refraction seismic field studies were undertaken by Leslie and Lawton (1999), in areas of steeply dipping marine shales of the Wapiabi Formation to determine the anisotropic parameters of these shales *in situ*. This structural geometry is relatively common in fold-thrust belts. In these studies, seismic lines were laid out parallel, perpendicular, and at 45° to the local strike directions. For vertically dipping strata, the measured velocities along the local strike and dip directions are the bedding-normal and bedding-parallel velocities, equivalent to the vertical and horizontal velocities described by Thomsen (1986). These parameters are obtained by measurement of headwave velocities along the seismic lines which need to be of sufficient length to ensure that the refractor velocities measured are from rocks that are below the near-surface weathered layer.

The anisotropic parameters δ and ϵ for these deeper shales are calculated by

$$\delta = 4\left[\frac{v_{45}}{v_0} - 1\right] - \left[\frac{v_{90}}{v_0} - 1\right], \tag{6.77}$$

and

$$\epsilon = \frac{v_{90} - v_0}{v_0}, \tag{6.78}$$

where v_0, v_{45}, v_{90} are the bedding-normal, 45° azimuth, and bedding-parallel velocities, respectively. Note also that the phase and ray velocities are equal in both the bedding-normal and bedding-parallel directions. Furthermore, the small error in the 45° azimuth velocity, due to the difference between the phase and group angles, is well within the calculated error in δ. A similar, successful study was undertaken by Gendzwill (1993) to investigate the effect of fractures on seismic properties of limestones in Manitoba.

6.5 Viability of VCS traveltime inversion

Past work has shown that direct P arrivals in walkaway VSPs and refracted P arrivals in refraction surveys can be successfully applied to investigate seismic anisotropy by using traveltime inversion algorithms. In this section, I discuss the usage of direct, reflected and refracted arrivals in vertical cable seismic data for anisotropic inversion.

6.5.1 Direct arrival

In marine VCS acquisition, the ray-paths of direct arrivals are all in the water column for vertical cable seismic data. It means that we can not use these waves to estimate rock properties in the subsurface with traveltime information. However, the multi-offset and multi-azimuth VCS technique provides us with the best way to obtain the $P-$wave velocity distributions in the water layer by seismic

tomography using direct arrivals. This is essential for carrying out accurate depth imaging and time-lapse seismic data processing. In general, the vertical variations of $P-$wave velocities may lead to errors in time-to-depth conversion when one use a constant velocity for the water layer. In particular, the velocity changes in the water layer between different surveys will significantly reduce the acquisition repeatability in time-lapse seismic. In order to obtain a true 4-D difference related to reservoir changes within the production, the effects of velocity changes in the water layer have to be accounted for.

6.5.2 Reflected arrival

The work of Alkhalifah and Tsvankin (1995) showed that $P-$wave reflection moveout is largely controlled by just two parameter combinations–the NMO velocity from a horizontal reflector (V_{nmo}) responsible for short-spread moveout and the anisotropic coefficient η, which determines the nonhyperbolic portion of the moveout curve, and is given by

$$\eta = \frac{1}{2}\left(\frac{V_h^2}{V_{nmo}^2} - 1\right) = \frac{\epsilon - \delta}{1 + 2\delta}, \tag{6.79}$$

where

$$V_h = V_{nmo}\sqrt{1 + 2\eta} \tag{6.80}$$

is the horizontal velocity, and

$$V_{nmo} = v_{p0}\sqrt{1 + 2\delta}. \tag{6.81}$$

As a result, in a single horizontal VTI layer, the $P-$wave nonhyperbolic moveout equation (6.73) can be rewritten as

$$t^2(x) = t_0^2 + \frac{x^2}{V_{nmo}^2} - \frac{2\eta x^4}{V_{nmo}^2[t_0^2 V_{nmo}^2 + (1 + 2\eta)x^2]}. \tag{6.82}$$

Alkhalifah (1997) suggested estimating V_{nmo} and η by a 2-D semblance scan based on this nohyperbolic moveout equation. He showed that this inversion procedure

could give reasonably accurate results for data acquired over a horizontally homogeneous VTI layer. However, he also found that the extracted values of η are sensitive to small errors in V_{nmo}, even if the spread-length is twice as large as the reflection depth.

A further study on the feasibility of nonhyperbolic moveout inversion in TI media was made by Grechkka and Tsvankin (1998). The results show that there is certain degree of tradeoff between V_h and V_{nmo} caused by the interplay between the quadratic and quartic term of the moveout series. Since the errors in V_h and V_{nmo} have opposite signs, the absolute error in the parameter η turns to be at least two times bigger than the percentage error in V_h. Therefore, the inverted value of η is highly sensitive to small correlated errors in reflection traveltimes, with moveout distortions of the order of $3-4ms$ leading to errors in η up to ± 0.1, even in the simplest model of a single VTI layer. Furthermore, the recent work of Traub and Li (2002) also shows that small η values can not be resolved using double-scanning semblance analysis of $P-$wave nonhyperbolic moveout in 4C data application.

Generally speaking, the $P-$wave alone is insufficient for accurate determination of vertical velocity v_{p0}, and anisotropic coefficients η and ϵ in anisotropic media (VTI), even if long spreads are used ($x_{max} = 2z$). There is no doubt that there will be more challenges in the practical application of VCS reflection traveltime inversion for the investigation of seismic anisotropy, even if vertical cable seismic can provide multi-azimuth long-spread data. This is because we had to perform this inversion procedure in a VCS common receiver gather instead of a CMP gather in the surface data, the inhomogeneous overburden will produce bigger errors in VCS traveltime inversion, and we also need to make a wave-field datuming from the source level to the receiver level in the common receiver gather before carrying out the inversion. Therefore, anisotropic inversion of VCS reflection traveltimes require separated studies and is beyond the scope of this thesis.

6.5.3 Refracted arrival

The concept of vertical array acquisition can provide a novel approach to seismic refraction surveying of sea-bed sediments (Hunter and Pullan, 1990). Indeed, refraction traveltimes of sea-bed sediments can be obtained from VCS acquisition at any azimuths. This full azimuthal coverage of information is essential for the investigation of near-surface anisotropy, which leads to azimuth dependent velocities and arrival-times of refracted waves, and the application of anisotropic statics may improve the structural interpretation quality (Milligan, 1998). In the remaining sections of this Chapter and in Chapter 7, I will focus on the usage of refracted arrivals.

6.6 Refracted traveltime equations

In this section, I will now derive refracted traveltime-offset equations in VCS geometry.

6.6.1 Refracted traveltime equation in a single refractor

In vertical cable seismic, the refraction at a single refractor of the marine sediments is illustrated in Figure 6.5. For the cable located at O, $SABR$ indicates the refracted path from the source S to the receiver R. Assuming a dipping anisotropic sea-bed, our objectives are to invert the dip and the anisotropy parameters of the sea-bed from the refracted arrival $SABR$.

For a homogeneous sea-bed, the travel time $t_{SABR}(\phi)$ along the path $SABR$ can be expressed as

$$t_{SABR}(\phi) = \frac{SA}{V_0} + \frac{BR}{V_0} + \frac{AB}{V_1(\phi)}, \tag{6.83}$$

where V_0 is the $P-$wave velocity in the water layer, and $V_1(\phi)$ is the $P-$wave

ray velocity of the sea-bed refractor along the source-cable azimuth ϕ, which is measured from the source-cable direction to $X-$axis in the natural coordinate system. Denoting the critical angle by θ_C, and apparent dip by α along azimuth ϕ, gives

$$\begin{aligned} SA &= \frac{AC}{\cos(\theta_C - \alpha)} \\ &= \frac{OD - AD\sin\alpha}{\cos(\theta_C - \alpha)}, \qquad (6.84) \\ BR &= \frac{RD\cos\alpha}{\cos\theta_C}, \qquad (6.85) \\ AB &= AD - BD \\ &= AD - RD\,(\sin\alpha + \cos\alpha\tan\theta_C)\,. \qquad (6.86) \end{aligned}$$

In terms of the source-cable offset x, the receiver-to-sea-bed distance h_R (receiver height), and the depth of the sea-bed at the cable location h_O, one can write

$$\begin{aligned} x &= AD\cos\alpha + AC\tan(\theta_C - \alpha) \\ &= AD\cos\alpha + (h_O - AD\sin\alpha), \qquad (6.87) \end{aligned}$$

hence,

$$\begin{aligned} AD &= \frac{x\cos(\theta_C - \alpha) - h_O\sin(\theta_C - \alpha)}{\cos\theta_C}, \qquad (6.88) \\ SA &= \frac{h_O}{\cos(\theta_C - \alpha)} - \frac{x\sin\alpha - h_O\tan(\theta_C - \alpha)\sin\alpha}{\cos\theta_C}, \qquad (6.89) \\ BR &= \frac{h_R\cos\alpha}{\cos\theta_C}, \qquad (6.90) \\ AB &= \frac{x\cos(\theta_C - \alpha) - h_O\sin(\theta_C - \alpha) - h_R\sin(\theta_C + \alpha)}{\cos\theta_C}. \qquad (6.91) \end{aligned}$$

Substituting equations (6.89), (6.90) and (6.91) in equation (6.83), the traveltime $t_{SABR}(\phi)$ can be written as

$$\begin{aligned} t_{SABR}(\phi) &= \left[\frac{\cos\alpha + \tan\theta_C\sin\alpha}{V_1(\phi)} - \frac{\sin\alpha}{V_0\cos\theta_C}\right]x \\ &\quad + \left[\frac{\cos\alpha}{V_0} - \frac{\sin(\theta_C + \alpha)}{V_1(\phi)}\right]\frac{h_R}{\cos\theta_C} \end{aligned}$$

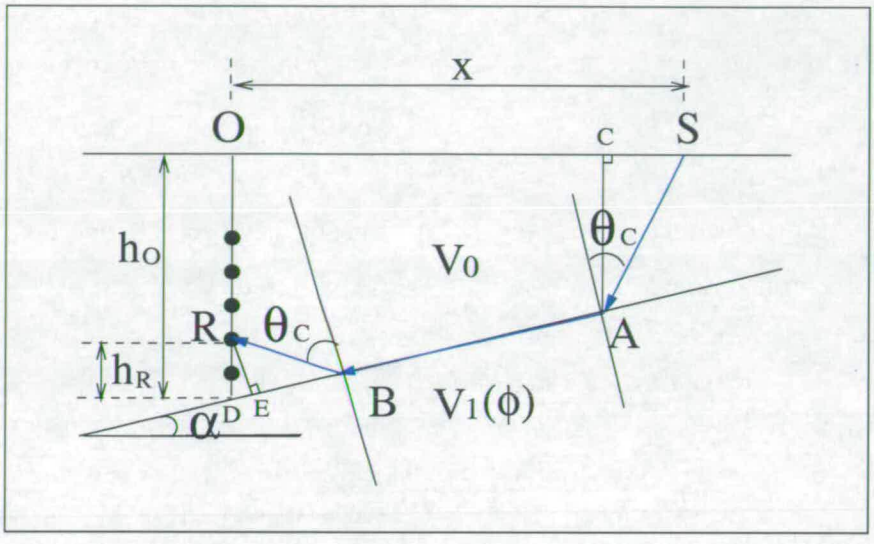


Figure 6.5: The refraction at the sea-bed in vertical cable seismic. O, S and R indicate the location of a cable, source and receiver, respectively. The ray $SABR$ shows one refraction path from source S to receiver R. α is the apparent dip of the sea-bed at the source-cable direction.

$$+\frac{h_O(\cos\theta_C + \sin(\theta_C - \alpha)\sin\alpha)}{V_0\cos\theta_C\cos(\theta_C - \alpha)}$$
$$-\frac{h_O\sin(\theta_C - \alpha)}{V_1(\phi)\cos\theta_C}. \tag{6.92}$$

Assuming the real dip and dip azimuth of the sea-bed are β and φ_d, respectively, one has the following relation between α and β:

$$\tan\alpha = \tan\beta\cos(\phi - \varphi_d). \tag{6.93}$$

Therefore, for a fixed source-cable azimuth ϕ, the traveltime $t_{SABR}(\phi)$ based on the equation (6.92) is a linear function relating to the offset x as well as the receiver height h_R.

6.6.2 Refracted traveltime equation in multi-layered media

In marine sediments, I also consider $n-$layered azimuthally anisotropic or isotropic media whose symmetry is parallel or perpendicular to the layer in-

terface. Each layer has the same dip and dip azimuth. A ray geometry for refraction in vertical cable seismic is shown in Figure 6.6. In terms of source-cable offset x, receiver height h_R, sea-bed depth h_O and vertical layer thickness z_k $(k = 1, 2, \cdots, n-1)$ at the cable location, the traveltime of a refracted wave created at the top interface of layer n from the source S to the receiver R, at the measured azimuth ϕ, can be written as (see Appendix B)

$$\begin{aligned} t_n(\phi) &= \left[\frac{\cos\alpha + \tan\theta_0 \sin\alpha}{V_n(\phi)} - \frac{\sin\alpha}{V_0 \cos\theta_0}\right] x \\ &+ \left[\frac{\cos\alpha}{V_0} - \frac{\sin(\theta_0+\alpha)}{V_n(\phi)}\right] \frac{h_R}{\cos\theta_0} \\ &+ \left[\frac{\cos\theta_0 + \sin(\theta_0-\alpha)\sin\alpha}{V_0\cos(\theta_0-\alpha)} - \frac{\sin(\theta_0-\alpha)}{V_n(\phi)}\right] \frac{h_O}{\cos\theta_0} \\ &+ 2\cos\alpha \sum_{k=1}^{n-1} \frac{z_k}{\cos\theta_k V_k(\theta_k,\phi)} - \frac{2\cos\alpha}{V_n(\phi)} \sum_{k=1}^{n-1} z_k \tan\theta_k, \end{aligned} \tag{6.94}$$

where $V_k(\theta_k, \phi)$ are $P-$wave ray velocities at given ray paths (θ_k, ϕ), θ_k $(k = 1, 2, \cdots, n-1)$ are angles of incidence, and V_0 and $V_n(\phi)$ are $P-$wave ray velocities in the water and at the top interface of layer n, respectively. Assuming $n = 1$ in equation (6.94), one can obtain the same formula as equation (6.92) for the refracted traveltime in a single refractor.

6.7 Dip and ray-slowness calculation from refracted arrivals

In order to obtain the dip and anisotropy of marine sediments, the azimuthal variations of apparent slownesses are estimated first. I can then obtain the horizontal and vertical ray-slownesses along the interface based on the relevant apparent slownesses, and I also find these attributes are all layer invariant.

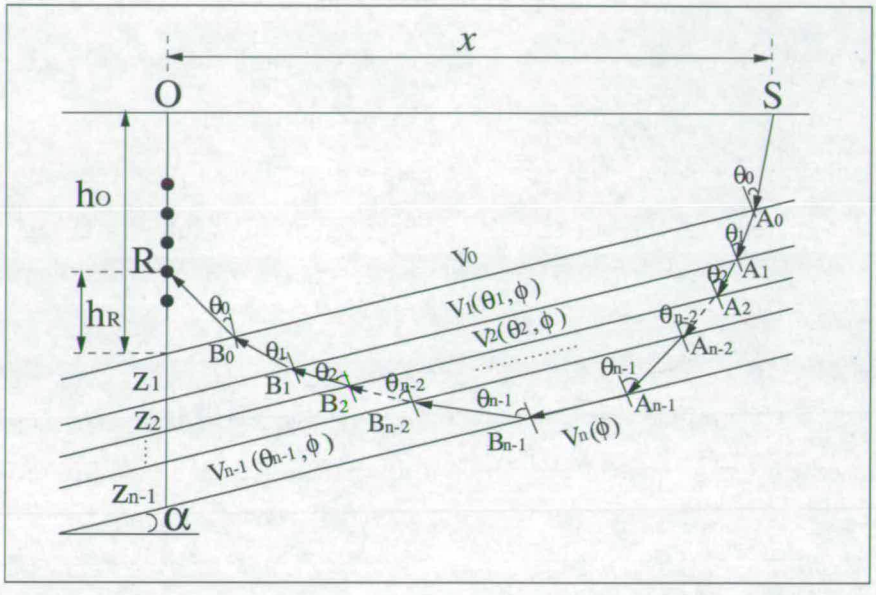


Figure 6.6: Ray geometry for refractions in layered marine sediments in vertical cable seismic.

6.7.1 Horizontal apparent and ray-slownesses

Following equation (6.94), the gradient of traveltime along the source-cable offset direction for a given receiver can be expressed as

$$\begin{aligned} S_{nx}(\phi) &= \frac{\partial t_n(\phi)}{\partial x} \\ &= \frac{\cos\alpha + \tan\theta_0 \sin\alpha}{V_n(\phi)} - \frac{\sin\alpha}{V_0 \cos\theta_0}. \end{aligned} \tag{6.95}$$

where $S_{nx}(\phi)$ is the horizontal apparent slowness from refracted arrivals at the azimuth ϕ for layer n, and it is independent of the overburden velocities. Assuming the subsurface consists of horizontal layers, it is used as horizontal slowness in the phase-slowness method for anisotropic inversion (Gaiser, 1990; Miller and Spencer, 1994; Sayers, 1997), and can be obtained from the traveltime differences of direct waves between adjacent sources for a given receiver in walkaway VSPs. Setting $\alpha = 0$ in equation (6.95), gives

$$S_{nx}(\phi) = \frac{1}{V_n(\phi)}. \tag{6.96}$$

This simple case applies only for horizontal-layered media, where the horizontal apparent slowness equals the ray-slowness of a seismic wave propagating along the refractor. In other situations, the horizontal apparent slowness $S_{nx}(\phi)$ is not only a function of velocities $V_n(\phi)$, but also a function of apparent dip angle α. In order to correct the effects of dip, I define a new function $S_{nh}(\phi)$ as

$$S_{nh}(\phi) = \frac{1}{2}\left(S_{nx}(\phi) + S_{nx}(\phi + \pi)\right). \tag{6.97}$$

Assuming the apparent dip is α at the azimuth ϕ, it will be $-\alpha$ at the azimuth $\phi + \pi$ based on equation (6.93). Thus, substituting equation (6.95) in equation (6.97) gives

$$S_{nh}(\phi) = \frac{\cos\alpha}{V_n(\phi)}. \tag{6.98}$$

Equation (6.98) indicates that $S_{nh}(\phi)$ is the horizontal component of the ray-slowness along the top interface of layer n at azimuth ϕ, which results from the sum of horizontal apparent slownesses at up- and down-dip directions for a given azimuth and source-cable offset.

To discuss the azimuthal variation of $S_{nh}(\phi)$, I give its expression with the azimuth ϕ by linearizing equation (6.93) and only keeping the first order approximation of $S_{nh}(\phi)$ for the small quantity $\tan^2\beta$. That leads to

$$S_{nh}(\phi) = \frac{1}{V_n(\phi)}\left[1 - \frac{1}{4}\tan^2\beta\left(1 + \cos 2\left(\phi - \varphi_d\right)\right)\right]. \tag{6.99}$$

Thus, the horizontal ray slowness shows $\cos 2\phi$ variations with azimuth ϕ due to the presence of dip, regardless of whether the marine sediments are azimuthally isotropic or not.

6.7.2 Vertical apparent and ray-slownesses

For a given source, one can also estimate the gradient of refracted travel time along the vertical array. Following equation (6.94), its expression can be written

as

$$\begin{aligned} S_{nz}(\phi) &= \frac{\partial t_n(\phi)}{\partial h_R} \\ &= \frac{\cos\alpha}{V_0\cos\theta_0} - \frac{\sin\alpha + \tan\theta_0\cos\alpha}{V_n(\phi)}. \end{aligned} \tag{6.100}$$

where $S_{nz}(\phi)$ is the vertical apparent slowness at the azimuth ϕ for layer n, and it is also independent of the overburden velocities. One can estimate $S_{nz}(\phi)$ from the differences of refracted travel times between adjacent receivers for a given source in vertical arrays. Equation (6.100) also shows the azimuthal variation of $S_{nz}(\phi)$ depending on the apparent dip angle α. For the simplest situation, $\alpha = 0$,

$$S_{nz}(\phi) = \frac{\sqrt{V_n^2(\phi) - V_0^2}}{V_n(\phi)V_0}. \tag{6.101}$$

In a similar way to the estimation of the horizontal ray-slowness, the vertical ray slowness of the refractor can also be estimated from the differences of vertical apparent slownesses between the up- and down-dip source directions at a given azimuth. It can be defined as

$$S_{nv}(\phi) = \frac{1}{2}\left(S_{nz}(\phi + \pi) - S_{nz}(\phi)\right). \tag{6.102}$$

Following equations (6.93) and (6.100), equation (6.102) gives

$$S_{nv}(\phi) = \frac{\sin\alpha}{V_n(\phi)}. \tag{6.103}$$

Based on equation (6.93), for the small dip β, $S_{nv}(\phi)$ can be approximated as

$$S_{nv}(\phi) \approx \frac{\tan\beta}{V_n(\phi)}\cos(\phi - \varphi_d). \tag{6.104}$$

Thus, the vertical ray slowness shows cosine variations with azimuth ϕ due to the presence of dip without considering azimuthal anisotropy.

6.7.3 Determination of dip and ray-slowness

Since there is full azimuthal coverage of sources in vertical cable seismic, the horizontal and vertical apparent slownesses can be estimated in each direction.

By integrating the horizontal and vertical apparent slownesses, one can obtain the ray slowness distribution $S_n(\phi)$ along the refractor without the effects of dip. Following equations (6.98) and (6.103), gives

$$\begin{aligned} S_n(\phi) &= \frac{1}{V_n(\phi)} \\ &= \sqrt{S_{nh}^2(\phi) + S_{nv}^2(\phi)}, \end{aligned} \tag{6.105}$$

and the tangent of apparent dip α can also be given as

$$\tan\alpha = \frac{S_{nv}(\phi)}{S_{nh}(\phi)}. \tag{6.106}$$

Furthermore, a least-squares (LSQ) procedure is used for inversion of the real dip and dip azimuth. From equation (6.93), I realize that the azimuthal variation of $\tan\alpha$ can be described by a cosine function as

$$f(A, \phi, \varphi) = A\cos(\phi - \varphi), \tag{6.107}$$

where $A = \tan\beta$ and $\varphi = \varphi_d$. In principle, it should be possible to estimate the two unknown variables (A and φ) from two given points. To reduce observing errors, a unique solution can be obtained from best fitting the function (6.107) to all measured data points by an LSQ procedure (see Appendix D). Hence, the real dip β and dip azimuth φ_d can be determined from the estimation of A and φ.

6.8 Conclusions

The existence of anisotropy causes a difference between the vertical and horizontal $P-$ and $S-$wave velocities as well as azimuthal changes. Based on a derivation for the general expressions of slowness surfaces in anisotropic media, I have discussed the slowness distributions in coordinate planes for TI including VTI, HTI and TTI, and orthorhombic media. In the symmetry-axis plane, the slowness for each

of three waves in a TI medium can be expressed as a function of five independent elastic constants and the phase angle, which is defined as the angle between the wavefront normal and the axis of symmetry. In the horizontal plane, the slownesses for orthorhombic media have the same forms as those in HTI media.

I have discussed the possibility of VCS traveltime inversion using direct, reflected and refracted arrivals in anisotropic media. The reflected $P-$waves alone in VCS data are insufficient for accurate determination of the vertical velocity and anisotropic parameters, even if long-spread data are used. The direct arrivals in VCS data can be used for inverting $P-$ velocities in the water layer. This is essential in performing accurate depth imaging and time-lapse seismic data processing.

A refraction method has been presented for determining the dip and ray-slowness along the refractor of marine sediments using vertical cable seismic data in the presence of dip. The development of this technique is based on the deviation of the refracted traveltime equation in multi-layered azimuthally isotropic or anisotropic media with an assumption that the layers are parallel to each other and the symmetry axes are perpendicular or parallel to the layer surface. This makes it possible to estimate anisotropy properties of the near-surface from the measured refracted traveltimes using a slowness-based inversion procedure which will be discussed in the next chapter.

The expressions of horizontal and vertical apparent slownesses show that each of them is not only a function of ray-velocity along the refractor, but also a function of apparent dip angle at the source-cable azimuth, however, they are independent of the overburden velocities. For a given azimuth and source-cable offset, the horizontal ray-slowness can be obtained from the sum of horizontal apparent slownesses in up- and down-dip directions, on the other hand, the vertical ray-slowness can be taken from the difference of the vertical apparent slownesses

between up- and down-dip directions. Therefore, the ray-slowness and tangent of apparent dip can be determined at any measured azimuth. Furthermore, the real dip and dip azimuth are estimated using an LSQ inversion approach from multi-azimuth VCS data.

CHAPTER 7

Applications of refracted traveltime inversion to VCS data

7.1 Introduction

The aim of this chapter is to develop a slowness-based inversion procedure to estimate marine sediment anisotropy using the refraction traveltimes measured in multi-azimuth vertical cable seismic data. For simplicity but without loss of the generality of the inversion, I consider that marine sediments are transversely isotropic (TI) media with a symmetry axis parallel to the dipping layer interfaces. Marine sediment cores routinely show transverse isotropy with a vertical symmetry axis (VTI) which results primarily from bedding, i.e. the interleaving of isotropic layers much thinner than a seismic wavelength (Backus, 1962; Bachman, 1979; 1983; Carlson et al., 1984). In practice, marine sediments may also possesses a component of transverse isotropy with a horizontal symmetry axis (HTI). This is a consequence of forces such as sea bottom currents acting on the sediments during deposition to create unidirectional flow patterns. Such HTI anisotropy has been observed in the past for the upper few hundred metres of marine sediments by Stoneley wave analysis (MacBeth,1991).

I first introduce the ray-slowness approximations in a weak TI medium for the

anisotropic inversion. The azimuthal variations in apparent and ray slownesses are shown with two sets of TI models. In the first set, I fix the anisotropic parameters of the models but vary the dip (0°, 5°, and 10°) to test the effects of the presence of dip. In the second set, I vary the $P-$wave anisotropy strength (5.2%, 10.3%, 15.8%, and 22.0%) to examine the sensitivity and accuracy of ray-slowness approximations which are independent of dip. I then test the proposed inversion procedure on synthetic $P-$wave VCS data calculated for six different models by a finite difference method. The results of inversion from a real VCS data set demonstrate the existence of azimuthal anisotropy in marine sediments as well.

7.2 Azimuthal variations of ray-slownesses

With the assumption of the weak TI medium, I make an approximation for the ray-slowness in the plane which is parallel to the axis of symmetry. Azimuthal variations of horizontal and vertical ray-slownesses measured by VCS geometry are then discussed in this section.

7.2.1 Ray-slowness approximation

Assuming a weak TI medium with a horizontal symmetry axis (HTI medium), the $P-$wave ray velocity in the survey frame has the following expression (Sena, 1991; Li, 1997):

$$V^{-2}(\phi,\theta) = a_0 + a_1 \sin^2\theta + a_2 \sin^4\theta, \tag{7.1}$$

and

$$\begin{aligned} a_0 &= v_{p0}^{-2}(1-2\epsilon), \\ a_1 &= 2v_{p0}^{-2}(2\epsilon-\delta)\cos^2(\phi-\varphi_a), \end{aligned} \tag{7.2}$$

$$a_2 = 2v_{p0}^{-2}(\delta - \epsilon)\cos^4(\phi - \varphi_a),$$

where ϕ and φ_a are the azimuths of the observation point and of the horizontal axis of symmetry, respectively, with respect to the $X-$ axis in the natural coordinate system. θ is the ray angle in the survey frame, with respect to the vertical axis. Thus, the square-ray-velocity in any plane with the symmetry axis, where $\theta = 90°$, can be expressed as

$$\begin{aligned} V^2(\phi) &= \frac{1}{a_0 + a_1 + a_2} \\ &= v_{p0}^2\left[1 + 2\delta\sin^2(\phi - \varphi_a)\cos^2(\phi - \varphi_a)\right. \\ &\quad \left. +2\epsilon\sin^4(\phi - \varphi_a)\right] \\ &= A_0 + B_0\cos 2(\phi - \varphi_a) + C_0\cos 4(\phi - \varphi_a), \end{aligned} \tag{7.3}$$

where

$$\begin{aligned} A_0 &= v_{p0}^2\left[1 + \frac{1}{4}(\delta + 3\epsilon)\right], \\ B_0 &= -v_{p0}^2\epsilon, \\ C_0 &= -\frac{1}{4}v_{p0}^2(\delta - \epsilon). \end{aligned} \tag{7.4}$$

This is a three-term approximation with the same form as the phase-velocity (Crampin, 1981). More details of ray-velocity variation in TI media are given in Appendix C.

Under the weak anisotropy approximation, further linearity of equation (7.3) yields ray-slowness, given by

$$\begin{aligned} \frac{1}{V(\phi)} &\approx \frac{1}{v_{p0}}\left[1 - \frac{1}{8}(\delta + 3\epsilon) + \frac{1}{2}\epsilon\cos 2(\phi - \varphi_a)\right. \\ &\quad \left. + \frac{1}{8}(\delta - \epsilon)\cos 4(\phi - \varphi_a)\right]. \end{aligned} \tag{7.5}$$

The first two terms in equations (7.3) and (7.5) are called elliptical approximations. These are accurate for a nearly elliptically anisotropic media.

7.2.2 Horizontal ray-slowness

Azimuthal variations of horizontal and vertical ray-slownesses due to the presence of dip along the dipping interface, are described in equations (6.17) and (6.22), assuming marine sediments are TI media with a symmetry axis parallel to the dipping interfaces. In this case, the ray-velocities along the interface are equivalent to the horizontal ray velocities in an HTI medium. Substituting equation (7.5) in (6.99) and only keeping the first two terms, the approximation of $S_{nh}(\phi)$ is given by

$$S_{nh}(\phi) \approx \frac{1}{v_{p0}} \left[a + b\cos 2(\phi - \varphi_a) + c\cos 2(\phi - \varphi_d) \right], \tag{7.6}$$

where

$$a = 1 - \frac{1}{8}(3\epsilon + \delta) - \frac{1}{4}\tan^2\beta + \frac{1}{32}(3\epsilon + \delta)\tan^2\beta, \tag{7.7}$$

$$b = \frac{1}{2}(1 - \frac{1}{4}\tan^2\beta)\epsilon, \tag{7.8}$$

$$c = -\frac{1}{4}\left[1 - \frac{1}{32}(3\epsilon + \delta)\right]\tan^2\beta. \tag{7.9}$$

Equation (7.6) can further be written as

$$S_{nh}(\phi) = \frac{1}{v_{p0}} \left[a + \frac{1}{\sqrt{b^2 + c^2 + 2bc\cos(\varphi_a - \varphi_d)}} \cos 2(\phi - \gamma) \right], \tag{7.10}$$

where

$$\tan\gamma = \frac{b\sin 2\varphi_a + c\sin 2\varphi_d}{b\cos 2\varphi_a + c\cos 2\varphi_d}. \tag{7.11}$$

Equation (7.10) describes the elliptical approximation of azimuthal variations of the horizontal slowness in weak TI media along a dipping refractor, but the effects of dip and anisotropy are, in fact, coupled together. Therefore, it would be difficult to implement the inversion from just the azimuthal distribution of the horizontal ray-slowness or apparent slowness. However, for small dips, $c \ll b$, which suggests that the effects of anisotropy on the azimuthal variation of $S_{nh}(\phi)$ are much more significant than the effects of dip. In the section on synthetic data analysis, I will discuss the effects of dip in detail using numerical solutions.

7.2.3 Vertical ray-slowness

Based on equations (7.5) and (6.104), the vertical ray slowness $S_{nv}(\phi)$ can also be approximated as

$$S_{nv}(\phi) \approx d\cos(\phi - \varphi_d), \tag{7.12}$$

where

$$d = \frac{1}{v_{p0}}\left[1 - \frac{1}{8}(3\epsilon + \delta)\right]\tan\beta. \tag{7.13}$$

Although the approximation of equation (7.12) is obtained under an assumption of small dip, the azimuthal variation of $S_{nv}(\phi)$ still depends only on the dip azimuth rather than the azimuth of the symmetry axis.

7.3 Inversion procedure

For a weak TI medium, I have introduced approximation expressions for the square-ray-velocity in equation (7.3) and ray-slowness in equation (7.5). After estimation of ray-slowness $S_n(\phi)$, a two-step LSQ procedure is used to implement anisotropy parameter inversion. Firstly, I apply the elliptical approximation of ray-slowness $S_n(\phi)$, described by

$$f(A, \phi, \varphi, y_0) = A\cos 2(\phi - \varphi) + y_0, \tag{7.14}$$

where

$$\begin{aligned} A &= \frac{\epsilon}{2v_{p0}}, \\ \varphi &= \varphi_a, \\ y_0 &= \frac{8 - (\delta + 3\epsilon)}{8v_{p0}}, \end{aligned} \tag{7.15}$$

to fit azimuthal variations of $S_n(\phi)$ (see Appendix D), the result providing a accurate solution for the direction of the symmetry axis φ_a.

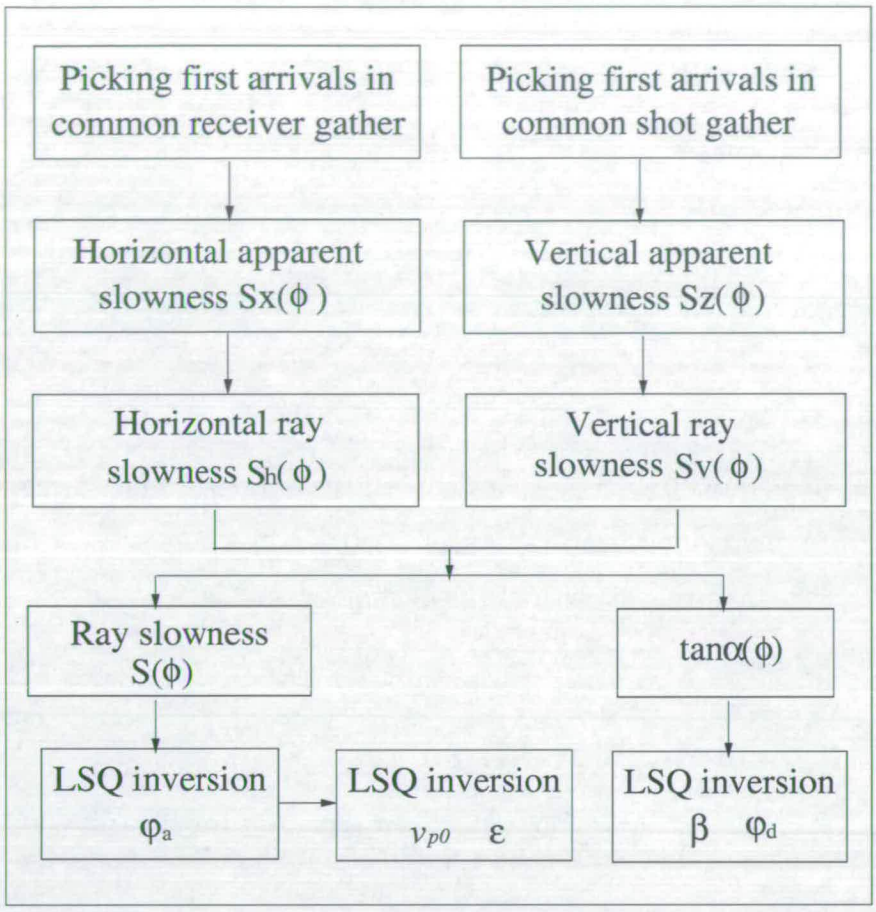


Figure 7.1: Processing sequence for inverting dip and anisotropic parameters of marine sediments using the refractions in vertical cable seismic.

A three-term fit to the square-ray-velocities is then used to estimate parameters A_0, B_0 and C_0 in equation (7.3), and corresponding Thomsen's parameters for $P-$waves are obtained as

$$v_{p0} = \sqrt{A_0 + B_0 + C_0}, \tag{7.16}$$

$$\epsilon = -\frac{B_0}{A_0 + B_0 + C_0}, \tag{7.17}$$

$$\delta = \frac{4C_0 + B_0}{A_0 + B_0 + C_0}. \tag{7.18}$$

Figure 7.1 summaries the processing sequence for inverting dip and anisotropic parameters of marine sediments from refracted arrivals in vertical cable seismic.

Table 7.1: Model parameters in anisotropic media

No.	$v_{p0}(m/s)$	$v_{s0}(m/s)$	ϵ	γ	δ	φ_a
1	2869	1508	0.052	0.345	−0.001	30°
2	2745	1508	0.103	0.345	−0.001	30°
3	2627	1508	0.158	0.345	−0.001	30°
4	2512	1508	0.220	0.345	−0.001	30°

7.4 Analysis of inversion accuracy

To examine the feasibility of inversion, I chose the set of models shown in Table 7.1 for traveltime analysis. The anisotropy parameters are taken from the anisotropic shale (Thomsen, 1986); I modify only the parameter ϵ corresponding to the anisotropy strength of $P-$waves among these models. Figure 7.2 shows the azimuthal variations of exact ray-slownesses (see Appendix C), its three-term approximation (equation (7.3)) and an elliptical fit (equation (7.14)). The solid line shows exact values, the dashed line shows the three-term approximation and the cross-marked line shows the elliptical fit. As can be seen, the three-term approximation is very accurate for anisotropy strengths up to 22%, and is much better than the elliptical fit, especially at or near the directions parallel and perpendicular to the symmetry axis. However, one can estimate accurately the direction of the symmetry axis φ_a from the elliptical fit. The results of estimation from the first step in an LSQ procedure are shown in Table 7.2.

Figure 7.3 shows azimuthal variations of the exact square-ray-velocities in the horizontal plane for HTI media and best fits based on the three-term approximation for all models shown in Table 7.1. I find that the three-term approximation provides an excellent fit to the exact square-ray-velocities. The results of estimation for anisotropy parameters are shown in Table 7.3. The comparison of

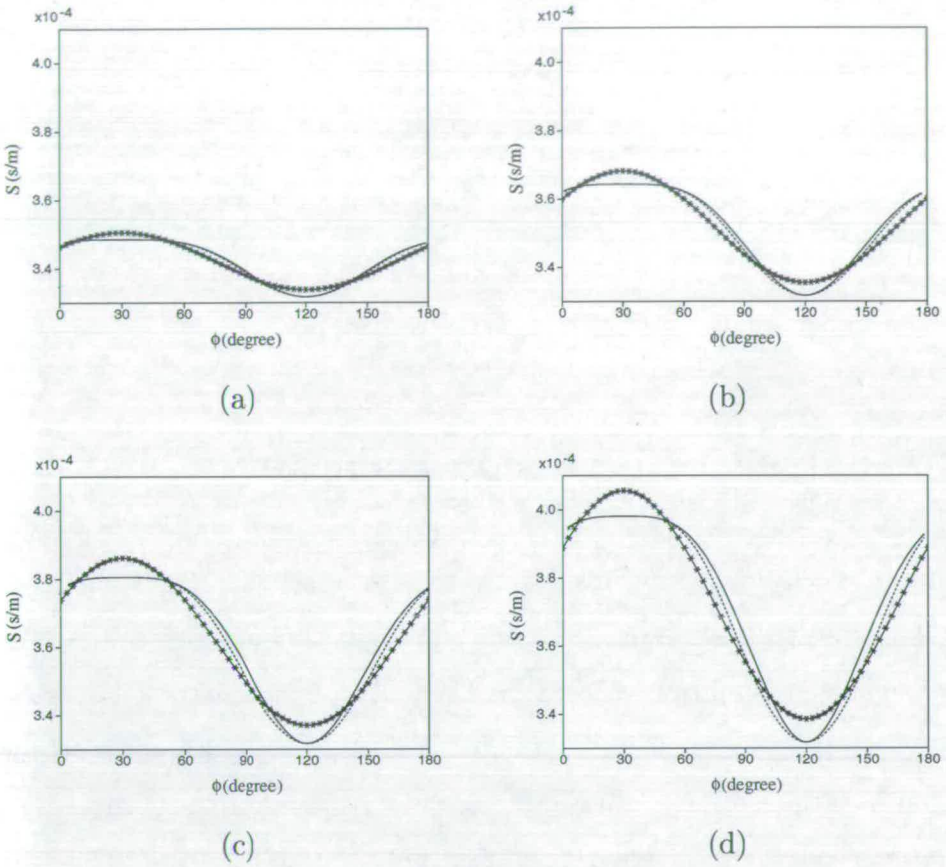


Figure 7.2: Ray slowness versus azimuth for (a) model 1, (b) model 2, (c) model 3, and (d) model 4. The solid line shows exact values, the dashed line shows the three-term approximation and the cross-marked line shows the elliptical fit.

Table 7.2: Results of estimation by using the elliptical fit

Model	A	y_0	φ_a
1	$8.3889E-06$	$3.4219E-04$	30.0°
2	$1.6316E-05$	$3.5181E-04$	30.0°
3	$2.4567E-05$	$3.616E-04$	30.0°
4	$3.3532E-05$	$3.7204E-4$	30.0°

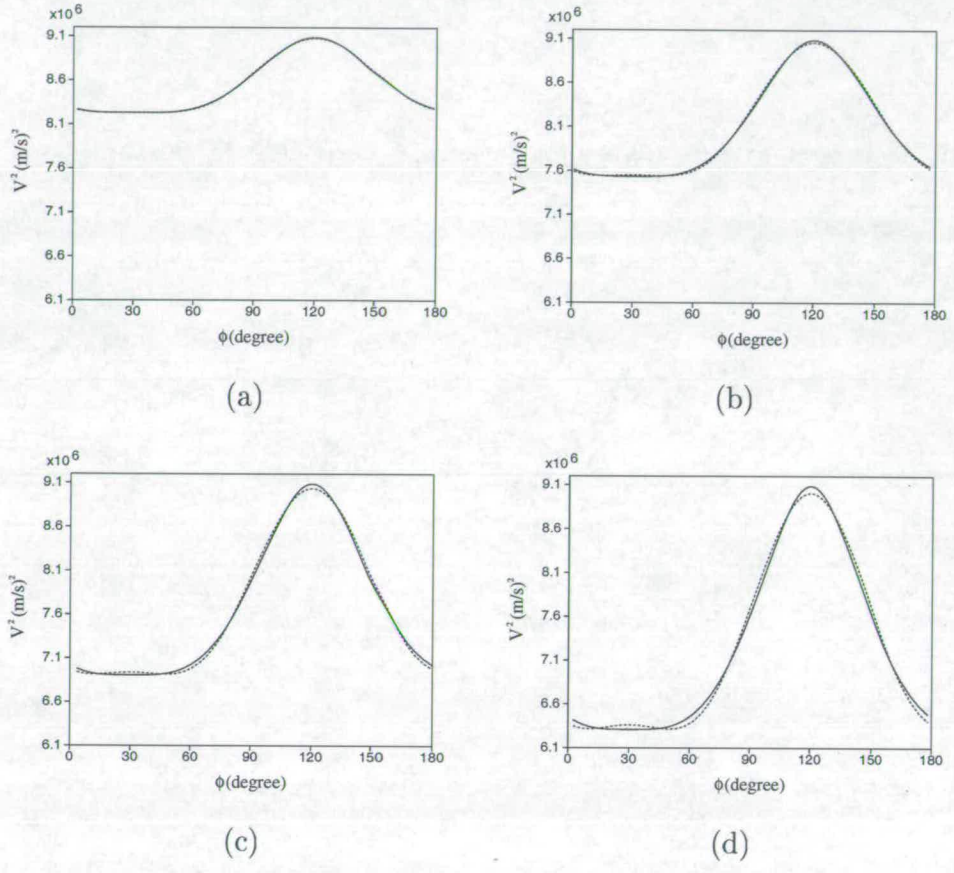


Figure 7.3: Azimuthal variations of the exact square-ray-velocities (solid line) and the three-term fits (dashed line) for (a) model 1, (b) model 2, (c) model 3, and (d) model 4.

estimated and original values for these parameters shows that parameter δ can not be estimated correctly by this procedure, because it is not only relevant to $P-$waves but also to $S-$waves. The relative errors for inverted parameters v_{p0} and ϵ shown in Table 7.4 are less than 0.4% and 6.0%, respectively, when the anisotropy strength for $P-$wave is up to 22%. This confirms that it is feasible to invert anisotropy parameters using the procedure shown in Figure 7.1.

Table 7.3: Results of estimation for anisotropy parameters by the three-term fit.

Model	$v_{p0}(m/s)$	ϵ	δ
1	2869	0.051	−0.005
2	2747	0.100	−0.016
3	2633	0.152	−0.035
4	2522	0.208	−0.063

Table 7.4: Relative errors (%) for inverted anisotropy parameters v_{p0} and ϵ.

Model	v_{p0}	ϵ
1	0	1.9
2	0.07	2.9
3	0.19	3.8
4	0.39	5.5

7.5 Applications to synthetic data

In order to evaluate the methodology further, I analyze the effects of dip and anisotropy on different models. The accuracy and feasibility of parameter inversion are further tested by synthetic full-waveform vertical cable seismic data.

7.5.1 Effects of dip

To illustrate the effects of dip, three models with dips of 0°, 5°, and 10° are examined, assuming that the $P-$wave velocity in the water layer $V_0 = 1475m/s$, the dip azimuth $\varphi_d = 30°$, and the marine sediments are TI media with parameters $v_{p0} = 2000m/s$, $\delta = 0.09$, $\epsilon = 0.11$, and $\varphi_a = 60°$, whose symmetry axis is parallel to the sea-bed surface. The azimuthal variations in horizontal and vertical apparent slownesses, and horizontal and vertical ray-slownesses are shown in Figure 7.4. It can be seen that the dip has a significant effect on both apparent slownesses and vertical ray-slowness. The shapes of apparent slowness curves change greatly for dips up to 5°. Thus, we can not ignore these changes, induced by the presence of dip in the apparent slowness if the sea-bed is not horizontal. However, the azimuthal variation of horizontal ray-slowness depends mainly on anisotropy rather than dip.

7.5.2 Numerical modelling

$P-$wave synthetic vertical cable seismic modelling is performed on six sets of models, which include single and two dipping refractors shown in Figure 7.5. The geometry parameters are given in Table 7.5, where h_{R1} is the height of the first receiver, and dh_R is the receiver interval in the vertical direction. For each source, 16 receivers are deployed vertically on the cable. The model parameters are shown in Table 7.6. The first layer in all models is water, the second and

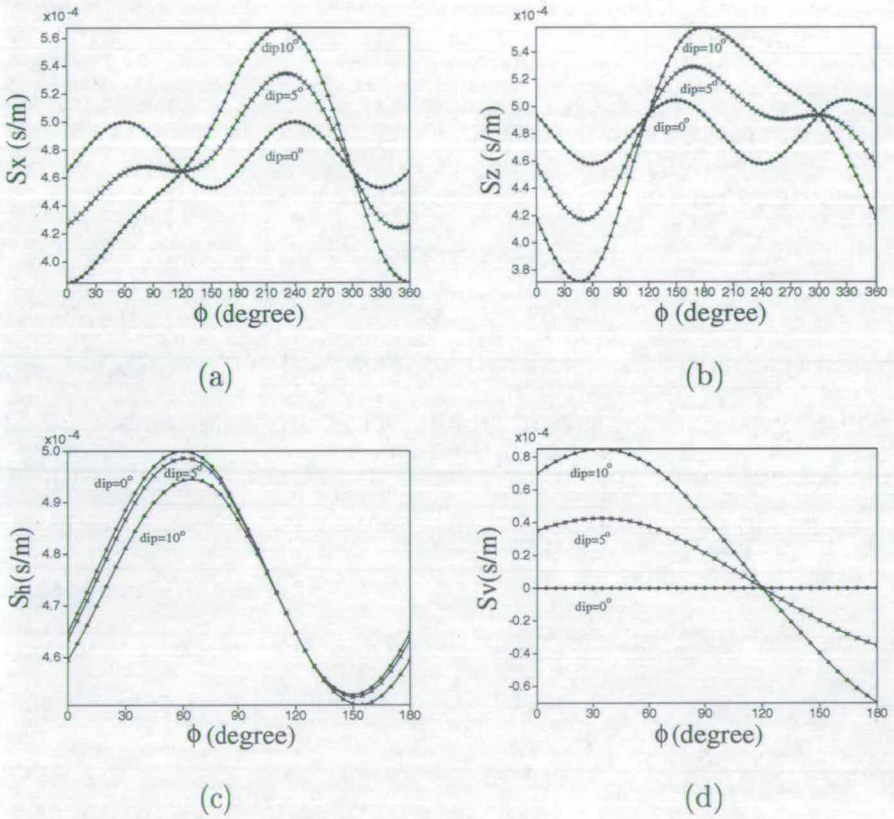


Figure 7.4: Plots of (a) horizontal apparent slowness, (b) vertical apparent slowness, (c) horizontal ray-slowness, and (d) vertical ray-slowness versus azimuth ϕ for dips of $0°$, $5°$ and $10°$, respectively.

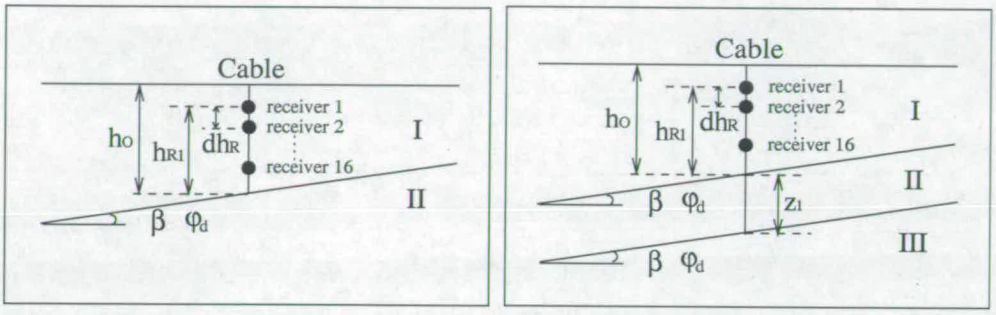


Figure 7.5: Geological models and geometry for making synthetic VCS data. (a) Single refractor; (b) two refractors.

Table 7.5: Geometry parameters in synthetic VCS data.

h_O	h_{R1}	dh_R	z_1	β	φ_d
$200m$	$64m$	$8m$	$120m$	$10°$	$30°$

third layers are isotropic or azimuthally anisotropic media, whose symmetry axes are parallel to the layer interface. The anisotropy parameters for these models are taken from Thomsen (1986) and are listed in Table 7.7.

The synthetic vertical cable seismic profiles are calculated using a finite difference method to model the elastic wave propagation in TI media (Wang and Dong, 1993; 1994). Three typical shot gathers for each model are shown in Figures 7.6 - 7.8. These VCS gathers are obtained from three typical azimuthal directions which include (a) up-dip ($\phi = \varphi_d$), (b) strike of the layer ($\phi = \varphi_d + 90°$) and (c) down-dip ($\phi = \varphi_d + 180°$) directions.

The first arrivals in Figure 7.6 are refracted waves from the first refractor (the interface between water and the second layer) for models A and B (see Table 7.6), in which the source-cable offsets are designed as $800m$. For other models, offsets are $1000m$, and first arrivals are from the second refractor (interface between the second and third layer).

Table 7.6: The model structures and velocities (m/s)

Model	layer 1	layer 2	layer 3
A	water	isotropic layer	
	$V_0 = 1475$	$V_p = 3014, V_s = 1960$	
B	water	anisotropic shale	
	$V_0 = 1475$	$\varphi_a = 45°$	
C	water	isotropic layer	isotropic layer
	$V_0 = 1475$	$V_p = 3014, V_s = 1960$	$V_p = 3720, V_s = 2248$
D	water	isotropic layer	Taylor sandstone
	$V_0 = 1475$	$V_p = 3014, V_s = 1960$	$\varphi_a = 60°$
E	water	anisotropic shale	isotropic layer
	$V_0 = 1475$	$\varphi_a = 45°$	$V_p = 3720, V_s = 2248$
F	water	anisotropic shale	Taylor sandstone
	$V_0 = 1475$	$\varphi_a = 45°$	$\varphi_a = 60°$

Table 7.7: The anisotropic parameters for shale and Taylor sandstone.

Representative material	$v_{p0}(m/s)$	$v_{s0}(m/s)$	ϵ	δ	γ
anisotropic shale	2745	1508	0.103	−0.001	0.345
Taylor sandstone	3368	1829	0.110	−0.035	0.255

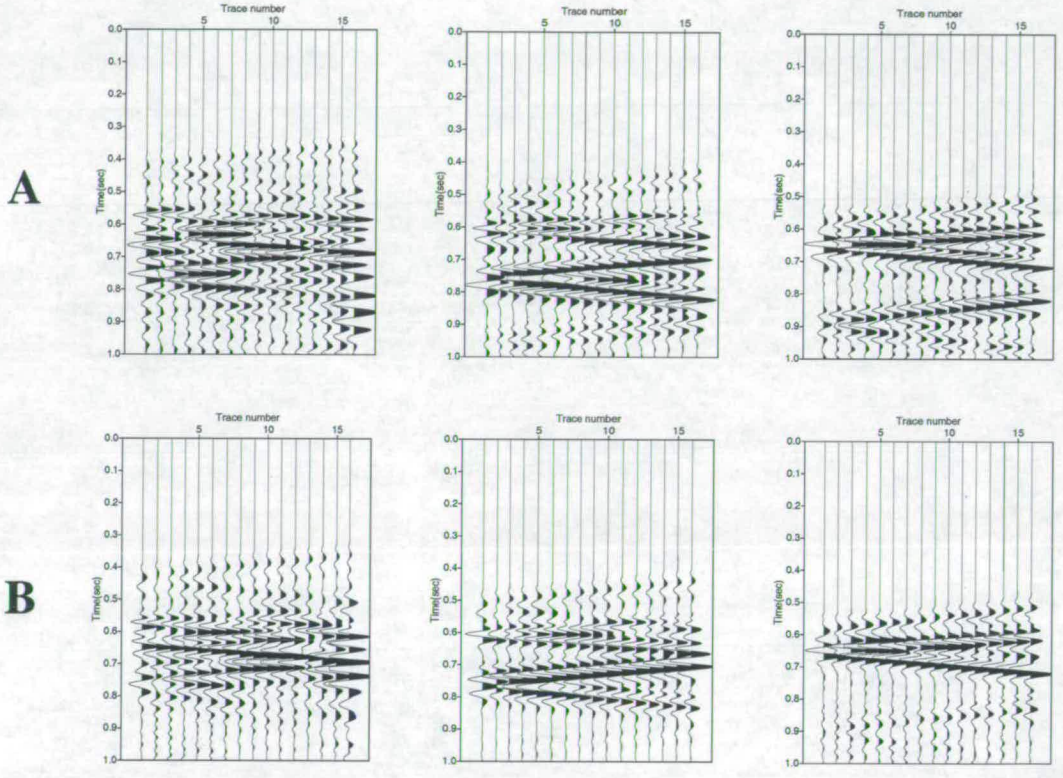


Figure 7.6: Rows: synthetic VCS shot gathers for models A and B. Columns: (a) in up-dip ($\phi = \varphi_d$), (b) along strike of the layer ($\phi = \varphi_d + 90°$) and (c) in down-dip ($\phi = \varphi_d + 180°$) directions. The source-cable offset is $800m$.

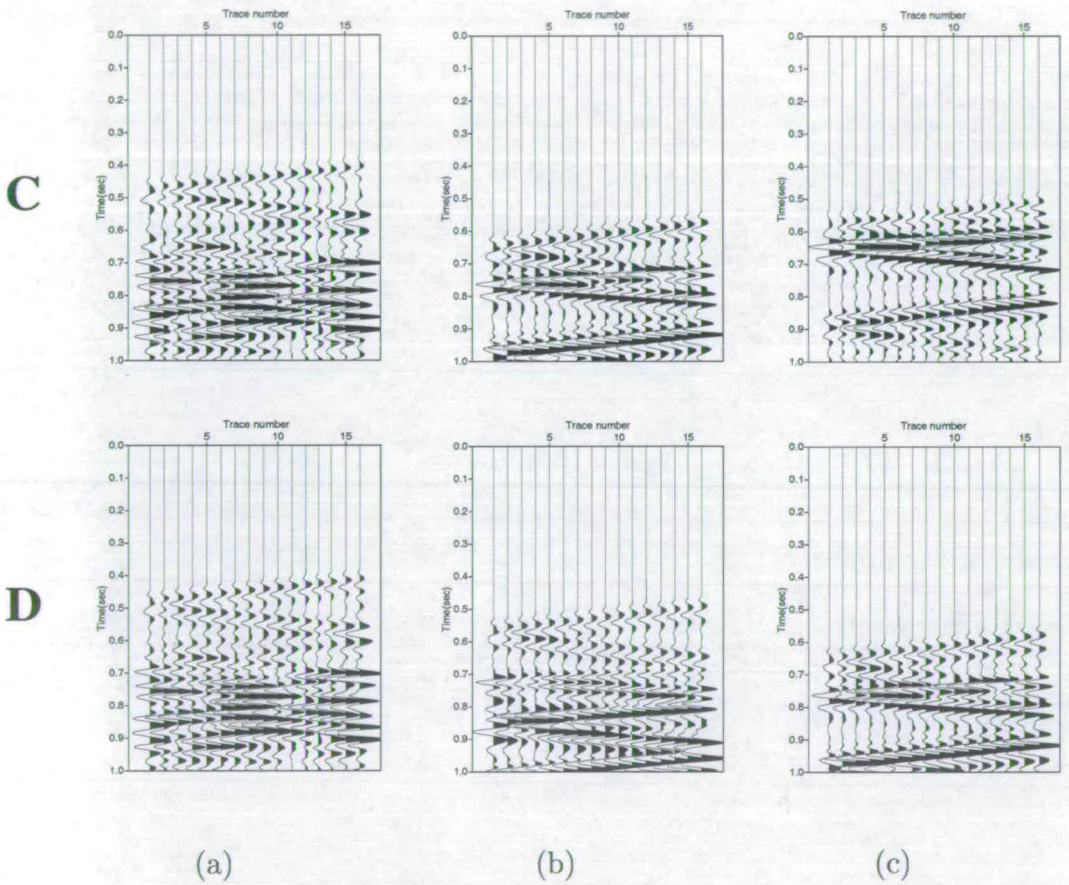


Figure 7.7: As Figure 7.6, for models C and D. The source-cable offset is $1000m$.

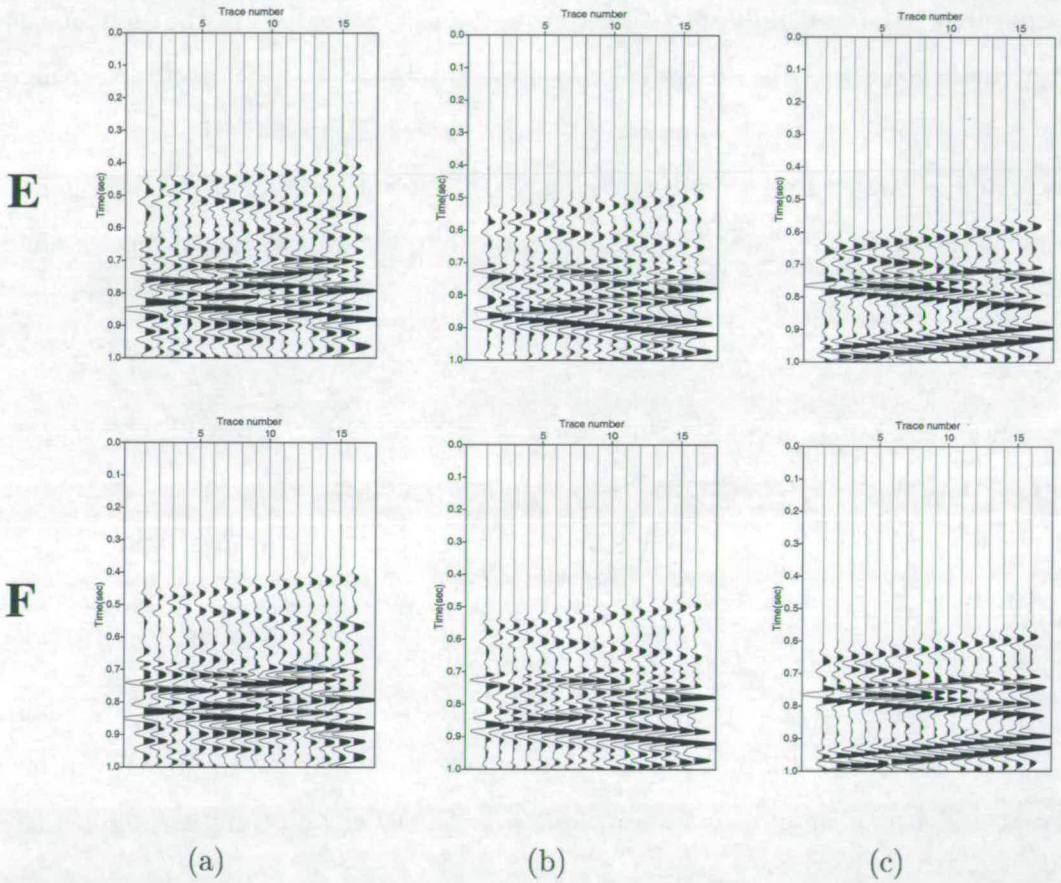


Figure 7.8: As Figure 7.6, for models E and F. The source-cable offset is $1000m$.

7.5.3 Azimuthal variations

Firstly, I obtain refracted traveltimes for each model at every 5° by picking first arrivals. For each azimuth, five shot gathers are calculated with $20m$ source intervals. The middle offset is $800m$ in models A and B, and $1000m$ is used in other models. To compare the difference between anisotropy and isotropy, I separate the six models into three groups with the same overburden of the refractor in each group: group 1 consists of models A and B, group 2 consists of models C and D, and group 3 consists of models E and F. Figure 7.9 shows the azimuthal variations in refraction traveltimes for receiver No.8. The trend of azimuthal variations among the three groups is very similar. This indicates that these changes are mainly due to the presence of dip, and the azimuthal variations caused by anisotropy are small.

Secondly, the horizontal apparent slowness is estimated by a local linear regression of the refracted traveltimes for a common receiver gather as a function of offset along each direction, and is shown in Figures 7.10(a), 7.11(a) and 7.12(a). The vertical apparent slowness is estimated by a linear regression of the refracted travel times along the vertical array, for a common source offset as a function of receiver height, and is shown in Figures 7.10(b), 7.11(b) and 7.12(b). Similarly, the variations of apparent slownesses are controlled mainly by dip rather than anisotropy although there is over 10% $P-$wave velocity anisotropy in each refractor.

Thirdly, the horizontal ray-slowness is computed by equation (6.97), and shown in Figure 7.10(c), 7.11(c) and 7.12(c) with an elliptical fit (equation (7.14)) for the anisotropy case in each figure. In these figures, the azimuthal variations in the horizontal slownesses for isotropic refractors are very small, whilst those for anisotropic refractors are very significant, and there are clear differences between anisotropic and isotropic refractors. The results of fitting show that the directions

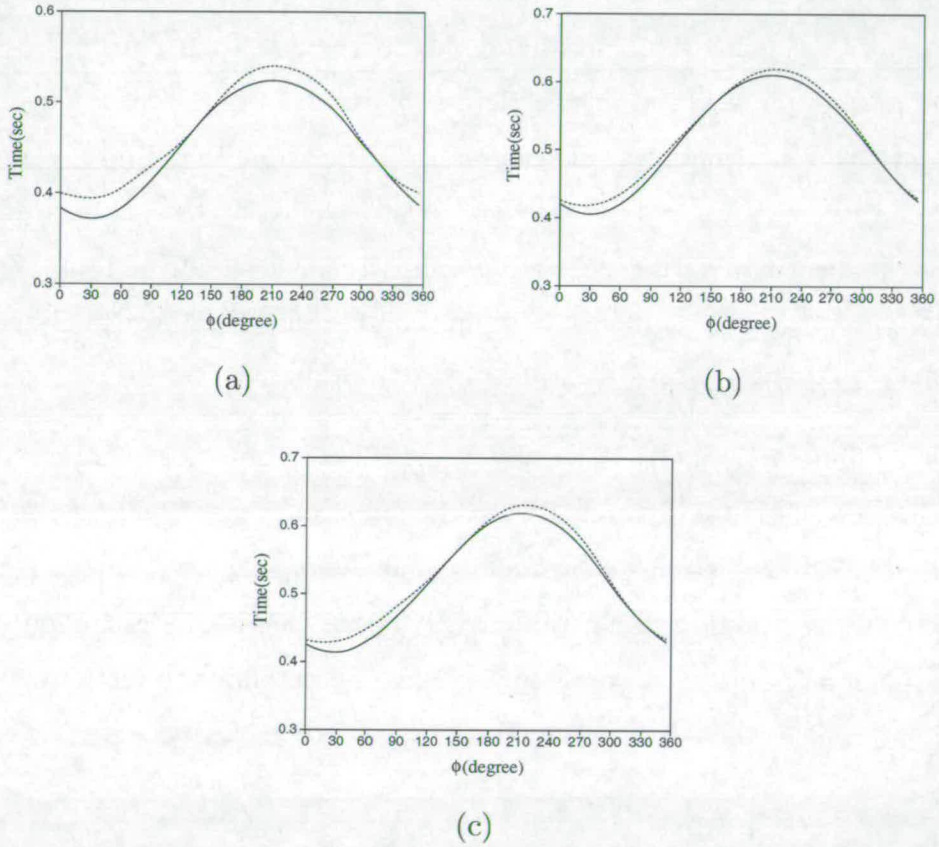


Figure 7.9: Azimuthal variations of refraction traveltimes for a given receiver (No.8) for (a) models A (solid line) and B (dashed line), (b) models C (solid line) and D (dashed line), and (c) models E (solid line) and F (dashed line).

of elliptical symmetry axes for anisotropic refractors are 47.4°, 63.5° and 63.4°, which are very near the directions of the anisotropy symmetry axes, 45° for the first refractor and 60° for the second refractor. I also display the azimuthal variations in vertical ray-slownesses estimated from equation (6.102) and the best fits of cosine function (6.107) in Figure 7.10(d), 7.11(d) and 7.12(d). One can see that the best-fitting curves agree well with exact values for all models. The initial guesses φ of the cosine functions (6.25) are 30.6°, 31.2° and 31.2°, which are very near the azimuth of real dip $\varphi_d = 30°$. There are only small differences between anisotropic and isotropic refractors for vertical ray-slowness. Therefore, the variations of horizontal ray slownesses are mainly due to anisotropy; on the other hand, those in vertical ray slowness are controlled by the presence of dip, and these also agree well with the previous numerical analysis. In addition, Figure 7.11 is almost the same as Figure 7.12, and implies that the above analysis also holds for multi-layered media regardless of the overburden.

Finally, Figure 7.13 shows the ray-slowness distributions for refractors after correcting the effects for dip and the variations in tangent α for all models. The best elliptical fits to slowness curves and cosine fits to tangent α curves are also displayed. I find that three tangent α curves overlap together for each group, and there are no variations in slowness for isotropic refractors. The real dip and its direction can be estimated accurately as 30.0° and 10.0°, respectively.

7.5.4 Results of estimation for anisotropy

Table 7.8 shows the results of estimation by an elliptical (two-term) fit to the calculated slowness shown in Figure 7.13 for each anisotropic model. Compared with the exact values given in Table 7.6, I find that the symmetry axis azimuth φ_a can be accurately estimated by this elliptical fit.

The anisotropic parameters v_{p0} and ϵ are obtained by the three-term fit to the

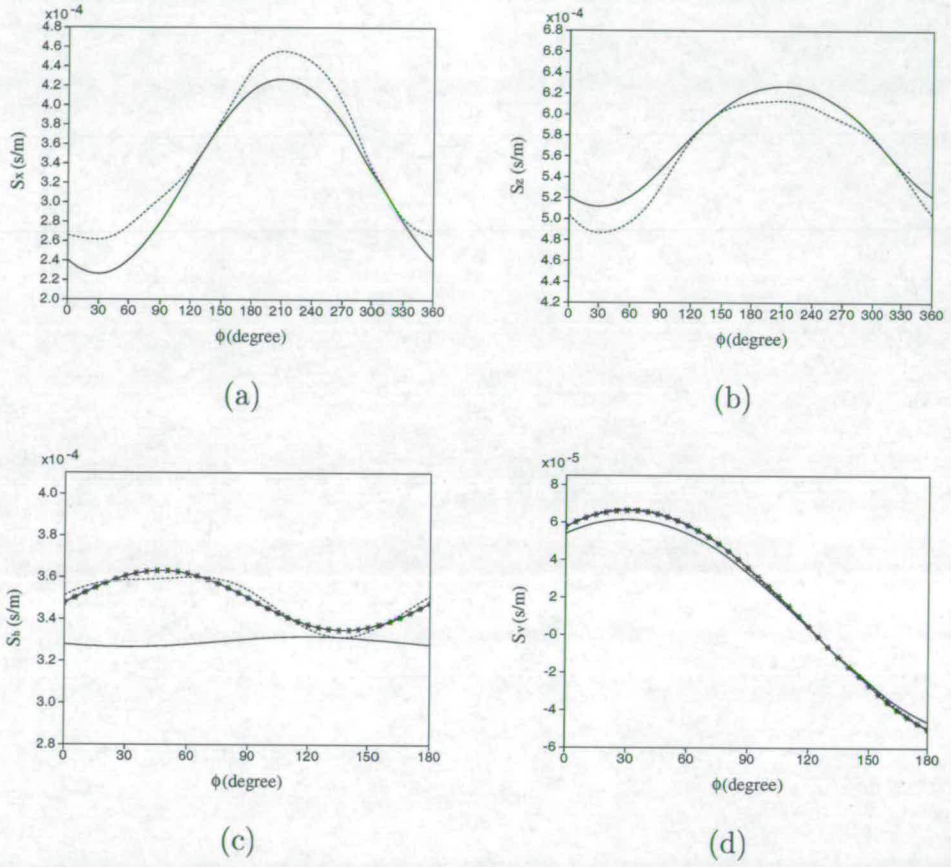


Figure 7.10: Plots of (a) horizontal apparent slowness, (b) vertical apparent slowness, (c) horizontal ray-slowness, and (d) vertical ray-slowness versus azimuth ϕ for model A (solid line) and model B (dashed line). Also shown are a best-fit (cross-marked line) of the elliptical approximation to the variations in horizontal ray-slowness on model B in (c), and a best-fit (cross-marked line) of the cosine function to variations in vertical ray-slowness on model B in (d).

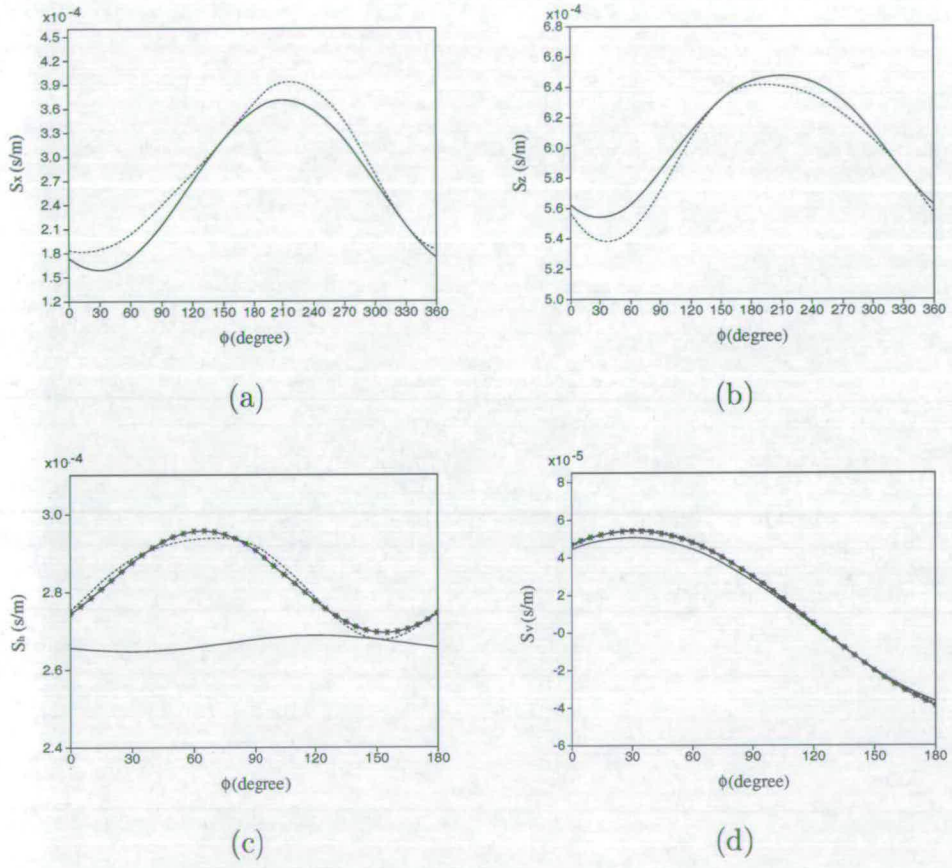


Figure 7.11: As Figure 7.10, for model C (solid line) and model D (dashed line). Also shown are a best fit (cross-marked line) of the elliptical approximation to variations in horizontal ray-slowness for model D in (c), and a best-fit (cross-marked line) of the cosine function to variations in vertical ray-slowness for model D in (d).

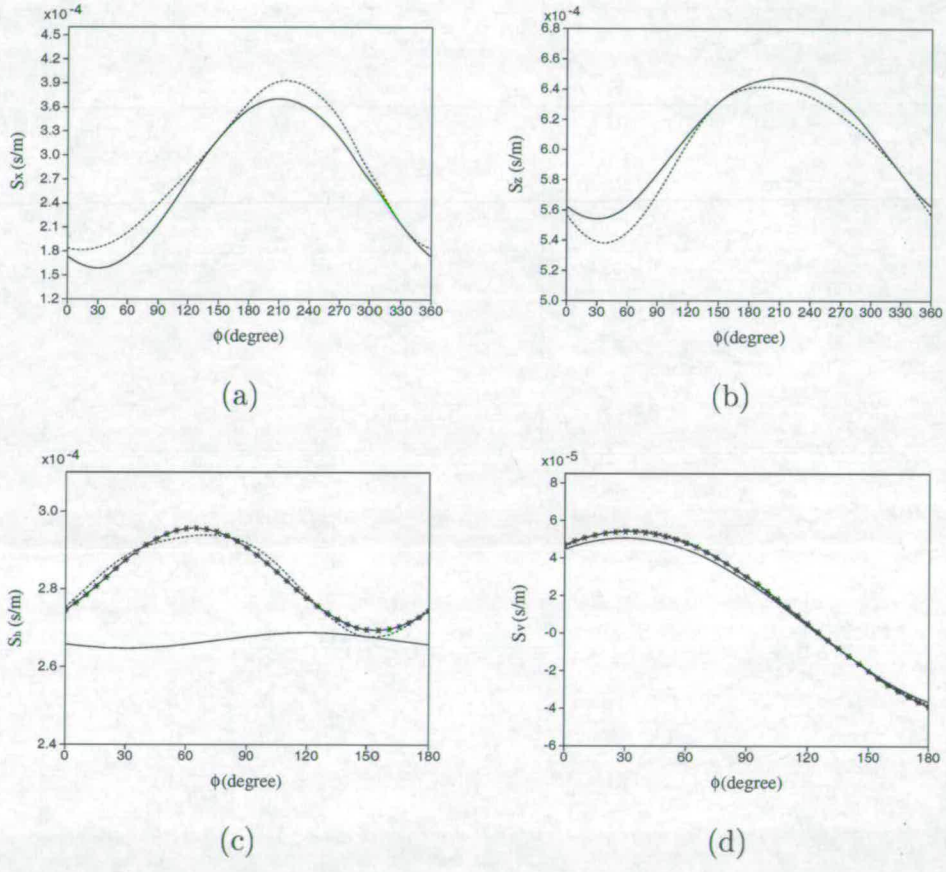


Figure 7.12: As Figure 7.10, for model E (solid line) and model F (dashed line). Also shown are a best-fit (cross-marked line) of the elliptical approximation to variations in horizontal ray-slowness for model F in (c), and a best-fit (cross-marked line) of the cosine function to variations in vertical ray-slowness for model F in (d).

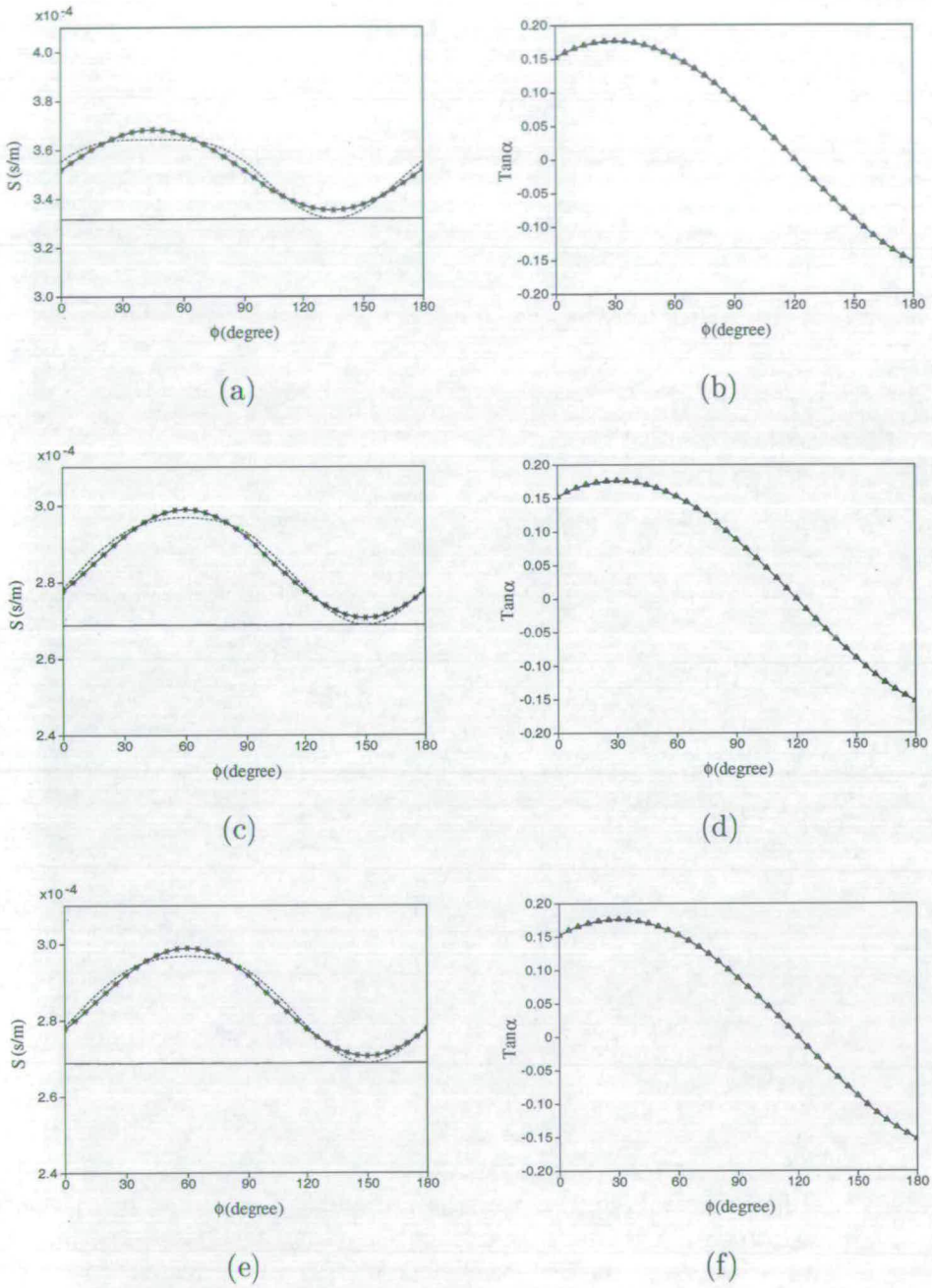


Figure 7.13: Ray slowness distributions of refractors without effects of dip for (a) models A (solid line) and B (dashed line), (c) models C (solid line) and D (dashed line) and (e) models E (solid line) and F (dashed line), and azimuthal variations in tangent α for (b) models A (solid line) and B (dashed line), (d) models C (solid line) and D (dashed line) and (f) models E (solid line) and F (dashed line). Also shown are the best elliptical fits to slowness curves and cosine fits to tangent α curves (cross-marked and triangle-marked lines).

Table 7.8: Results of estimation by an elliptical fit to the calculated slowness for each anisotropic model.

Model	A	y_0	φ_a
B	$1.6565E-05$	$3.5176E-04$	$44.67°$
D	$1.4194E-05$	$2.8480E-04$	$59.95°$
F	$1.4188E-05$	$2.8479E-04$	$59.94°$

Table 7.9: Inversion results and relative errors ($E_{v_{p0}}$ and E_ϵ) for anisotropy parameters obtained with the three-term fit to the calculated square-ray-velocities for each anisotropic model.

Model	Representative material	$v_{p0}(m/s)$	ϵ	$E_{v_{p0}}$	E_ϵ
B	anisotropic shale	$2748m/s$	0.100	0.11%	2.9%
D	Taylor sandstone	3372	0.106	0.12%	3.6%
F	Taylor sandstone	3372	0.106	0.12%	3.6%

calculated square-ray-velocity shown in Figure 7.14. The inversion results for all anisotropic models are shown in Table 7.9, which also includes the relative errors for the estimated values as compared with the exact values given in Table 7.7. One can see that the relative errors for v_{p0} and ϵ are less than 0.2% and 4%, respectively. The overburden has no effect on the anisotropy estimation of the refractor.

These results have shown the feasibility of inversion for anisotropy and dip parameters in multi-layered azimuthally anisotropic media in the presence of dip from vertical cable seismic refractions.

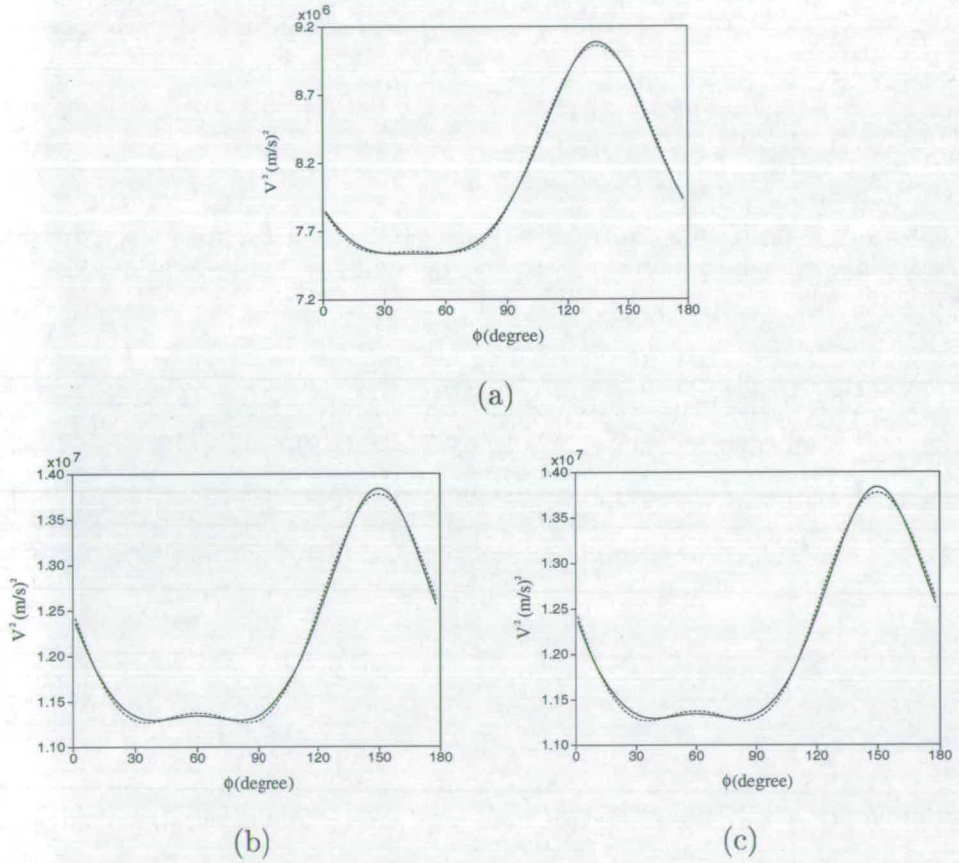


Figure 7.14: Azimuthal variations in the calculated square-ray-velocities (solid line) and their three-term approximation fits on (a) model B, (b) model D, and (c) model F.

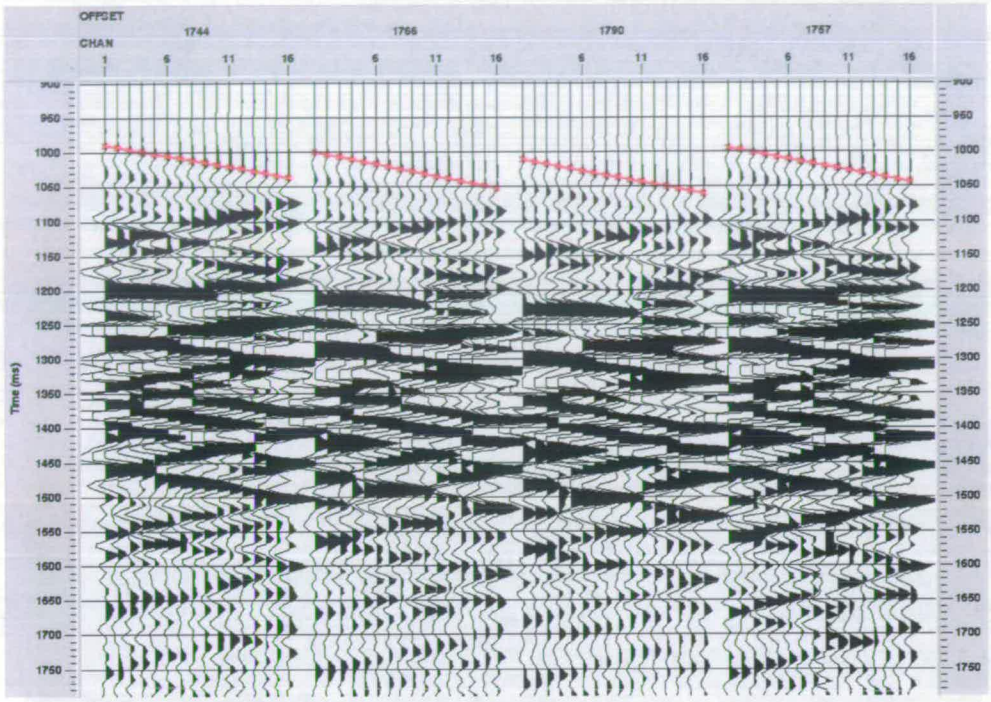
7.6 Field data example

I apply the inversion procedure to field VCS data obtained from the North Sea. The data are acquired by 12 cables, each of which has 16 hydrophones distributed vertically at 25 ft intervals. There is almost full azimuthal source coverage and also offsets ranging from 0 to 4000 metres. Figure 7.15 shows an example of first arrival picking on common source gathers and a common receiver (channel 5) gather from a selected 2-D source line. The depth of the sea floor at the cable location is about $136m$. One can see that the first arrivals are refracted waves (upgoing waves) not direct waves (downgoing waves). The picked traveltimes for the common receiver (channel 5) at offsets ranging from $800m$ to $2000m$ are shown in Figure 7.16.

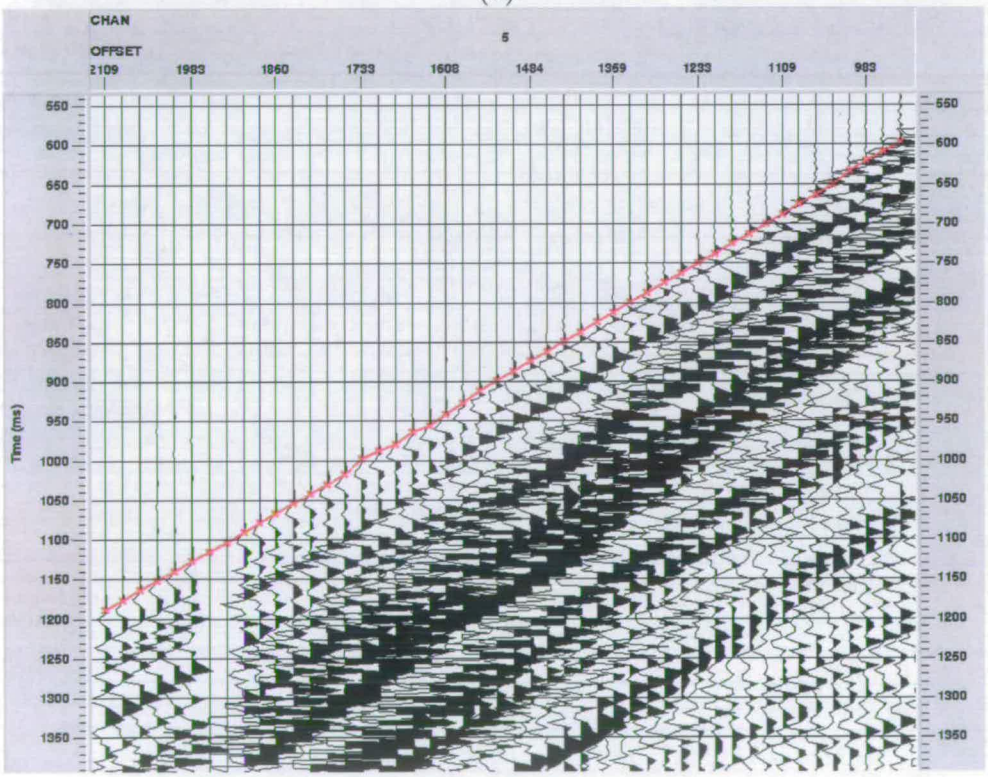
7.6.1 Azimuthal variations

Figure 7.17 illustrates the azimuthal variations in horizontal apparent slowness, vertical apparent slowness, and horizontal and vertical ray-slownesses for the sea-floor. There are 348 azimuths ranging from 0° to 360° to be measured for apparent slowness estimation. At each azimuth, five adjacent sources are used to estimate the horizontal apparent slowness for the same receiver. The middle offset is $1200m$.

Figure 7.18 shows the ray-slowness and square ray-velocity versus azimuth for the sea-floor. I also show a best elliptical fit to the calculated slowness and a fit of the three-term approximation to the calculated square-ray-velocity. The azimuthal variations in $\tan\alpha$ are illustrated in Figure 7.19. To estimate the dip of the sea-floor, a best-fit of the cosine function to the calculated data is also shown in Figure 7.19.



(a)



(b)

Figure 7.15: First-arrival picking on (a) common-source gathers and (b) one common-receiver gather from a selected 2-D source line of the VCS data.

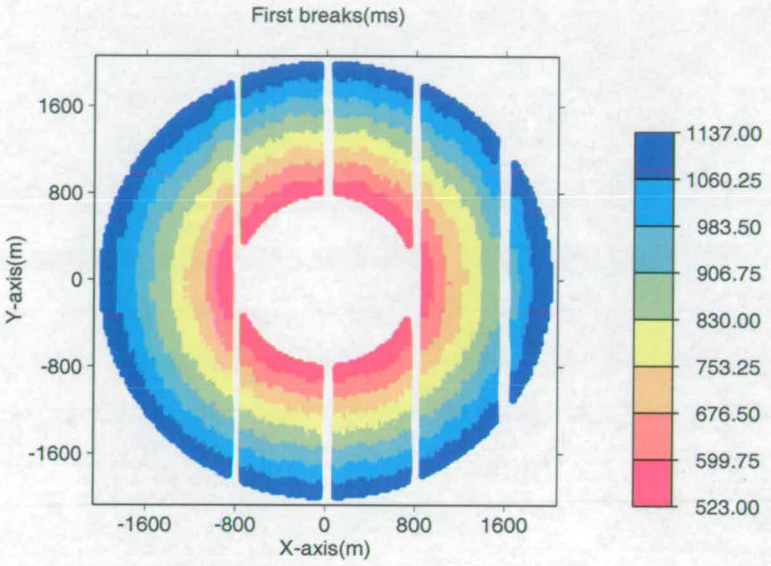


Figure 7.16: First arrivals for one common receiver (channel 5) at offsets ranging from 800m to 2000m.

Table 7.10: Inversion results for dip and anisotropic parameters from the field VCS data

φ_d	β	φ_a	v_{p0}	ϵ
23.0°	1.0°	134°	$1850m/s$	0.047

7.6.2 Inversion results

Assuming marine sediments are TI media with a symmetry axis parallel to layer interface, the inversion results for dip and anisotropic parameters from this real VCS data set are indicated in Table 7.10. One can see that the real dip β is about 1° for the sea-floor and the dip azimuth is 23.0° with respect to the $X-$axis in the natural coordinate system, and there is about 5% $P-$wave azimuthal anisotropy in this area.

The accuracy of inversion for a real data set is affected not only by the approximation used but also by errors in the traveltime picking. Since we can not

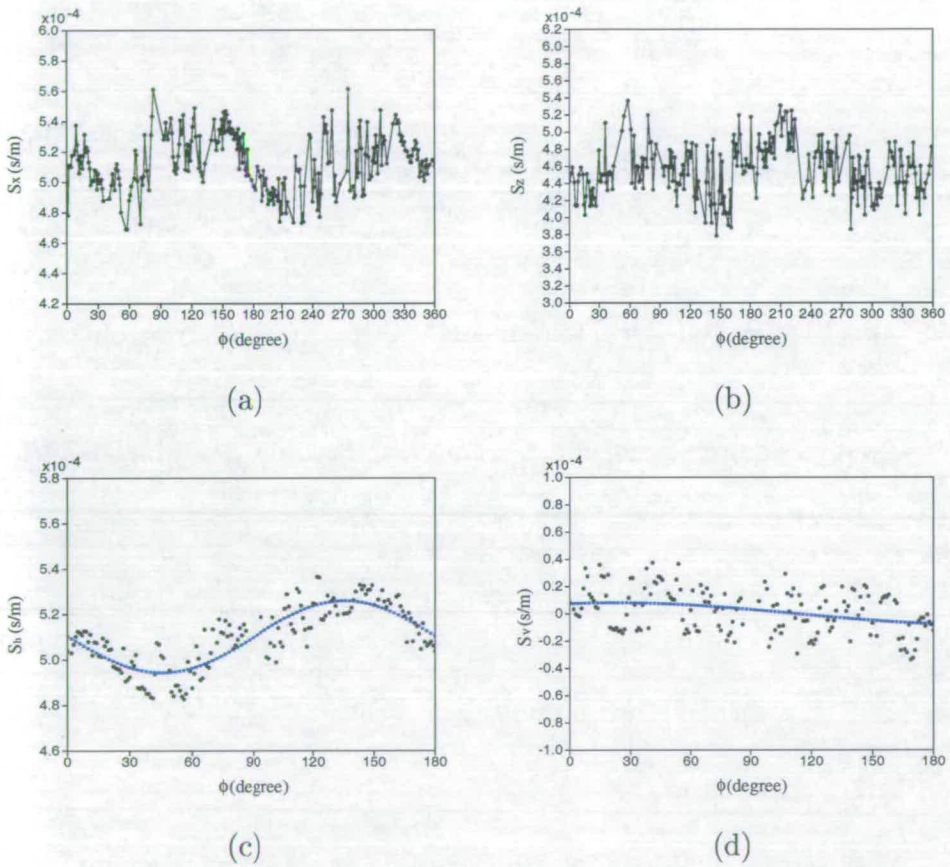
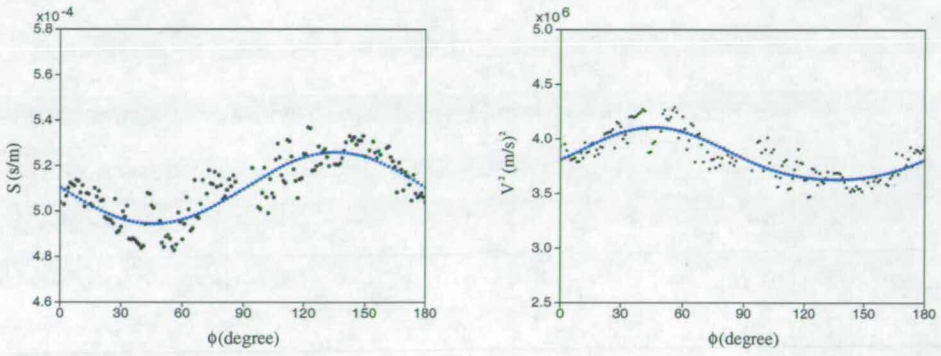


Figure 7.17: Plots of (a) horizontal apparent slowness, (b) vertical apparent slowness, (c) horizontal ray-slowness, and (d) vertical ray-slowness versus azimuth ϕ for the sea-floor. Also shown are the best-fits of elliptical approximation (blue line) in (c) and cosine function (blue line) in (d) to the calculated data.



(a) (b)

Figure 7.18: (a) Ray-slowness versus azimuth and a best-fit of elliptical approximation (blue line), and (b) square-ray-velocity versus azimuth and a best-fit of the three-term approximation (7.3) (blue line) to the calculated data for the sea-floor.

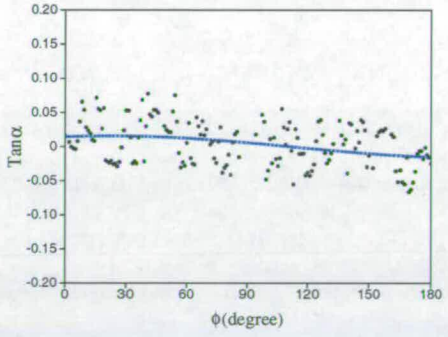


Figure 7.19: Tangentα versus azimuth ϕ for the sea-floor. Also shown is the best-fit of cosine function (blue line) to the calculated data.

calculate the relative errors of the inverted parameters in the real data inversion, a new relative estimation error S_e, defined by the following equation, is used to perform the error analysis in an LSQ procedure,

$$S_e = \sqrt{\frac{1}{N}\sum_{i=1}^{N}\left(\frac{y_i - \widehat{y}_i}{\widehat{y}_i}\right)^2}, \tag{7.19}$$

where N is the number of azimuths measured, y_i and $\widehat{y}_i$ are the measured value and fitting value, respectively, at the same azimuth i. S_e indicates the relative accuracy of regression for the real data. The error analysis shows that the relative estimation error of our data set, using a fit of the three-term approximation to the calculated square-ray-velocities, is 2.8%.

7.7 Conclusions

I have presented a refraction method for determining the anisotropy properties of marine sediments from vertical cable seismic data in the presence of dip. A slowness-based inversion procedure has been established to estimate the dip and anisotropy parameters for the refractor from the measured refracted traveltimes. The inversion feasibility has been examined by the theoretical calculations and synthetic $P-$wave vertical cable seismic data using a set of models.

Numerical tests show that the azimuthal variations in apparent slownesses are mainly due to effects of dip rather than anisotropy. When dips exceed 5°, significant errors may occur in the use of the phase-slowness approach based solely on horizontal layers. However, for azimuthal variations of horizontal ray-slowness, the influence of anisotropy is more significant than that of dip. This method yields a ray-slowness distribution independent of dips for a range of azimuths using refracted waves from VCS data. Also, the azimuthal variations of the tangents of apparent dips ($\tan\alpha$) are obtained.

The inversion results for the synthetic $P-$wave VCS data demonstrate that this

technique can provide an accurate and quantitative description of the anisotropic parameters v_{p0}, ϵ, the symmetry axis azimuth φ_a, layer parameters β and φ_d in multi-layered azimuthally anisotropic media. The relative errors for inverted parameters v_{p0} and ϵ are less than 0.4% and 6.0%, respectively, when the anisotropy strength for $P-$wave is up to 22%. Unfortunately, the estimation for the anisotropy parameter δ based solely on $P-$waves is not reliable. In addition, the overburden has no effect on the inversion results for the refractor in our case. Although this inversion procedure is based on the weak TI approximation, it can be easily extended to orthorhombic media, since both HTI and orthorhombic media may have the same form of the slowness approximation in the horizontal plane.

In the application to the field vertical cable seismic data, first arrivals along 348 azimuths were picked and used for dip and anisotropic inversions. The final results show that the near-surface sediments in this area have 1° dip with a dip azimuth of 23°, and there is about 5.0% $P-$wave azimuthal anisotropy, with the symmetry axis at 134° from the $X-$axis in the natural coordinate system. The relative estimation error of our data set, using a fit of the three-term approximation to the calculated square ray-velocities, is 2.8%.

CHAPTER 8

Summary

I have set up a special processing scheme for vertical cable seismic imaging and developed relevant techniques which involve wavefield separation, multiple suppression, CSP stack and prestack migration. Also, a traveltime inversion method has been developed to investigate seismic anisotropy in the presence of dip using refracted waves in vertical cable seismic data.

8.1 VCS processing techniques

The separation of upgoing and downgoing wavefields is an important and essential step in vertical cable seismic data processing. I have presented a zero-phase DEB filtering approach to perform this processing. Unlike conventional filtering techniques, which use convolution operations or mathematical transforms, the DEB filter is actually a dip filter using a finite-difference algorithm to solve differential equations in the time and space domain. The design of filtering parameters is quite flexible and it also can be adapted to vertical cable seismic data with nonuniform spatial sampling. This filtering is accomplished in the time-space domain by solving a diagonally dominant tridiagonal system of equations, thus it has quite high computational efficiency. In particular, this filter does not require a large number of traces and it can also overcome the undesirable artifacts re-

lated to spatial aliasing and side effects in the $f-k$ filtering. Synthetic tests show that compared to the median filtering, or $f-k$ filtering approach, this method obtains the best result. This technique is also successfully applied to perform the wavefield separation in real vertical cable seismic data.

Attenuation of water-column multiples is another challenge in vertical cable seismic data processing. The commonly-used techniques in the surface data processing, such as moveout-based and wave-equation-based methods, can not be directly applied to VCS data processing. I have proposed a demultiple filter with a Butterworth gain function to suppress the receiver-side reverberation in vertical cable seismic data. The filtering is carried out in the $\tau-p$ domain for each VCS common-shot gather. The whole processing scheme also includes wavefield separation, forward and inverse $\tau-p$ transforms. This demultiple filter use a different process from the common prediction and subtraction approaches for multiple suppression. It automatically defines the multiple rejection areas and tapers the rejection boundary in the $\tau-p$ domain by using the amplitude ratio of upgoing and downgoing wavefields in vertical cable seismic data. This filter makes no assumption on periodicity or moveout patterns of multiples, nor does it require any knowledge of the subsurface. Synthetic and field data examples demonstrate the efficiency of the procedure. Compared to predictive deconvolution, this proposed processing scheme yields much better performance in multiple suppression.

8.2 VCS imaging techniques

The analysis of a horizontal interface reflection in VCS geometry has shown that the residual moveouts and dispersal of reflection points in vertical cable seismic data, due to the depth difference between receivers in the same cable, increase with increasing offset to depth ratios in performing the conventional horizontal

stack. The difference of residual moveouts is over $15ms$, and the dispersal difference of the reflection point is over $40m$, between two given receivers with $120m$ interval, when the offset to depth ratio is 2.5. As a result, it will degrade the data quality of conventional CDP stack, and produce mispositioning of reflectors, even if the subsurface is a horizontally-layered media.

Alternatively, a CSP stacking technique has been developed for vertical cable seismic imaging. CSP gathers can be constructed by collecting and binning all input traces with offset in each common receiver gather using the DSR traveltime equation. The traveltime in a CSP gather is recalculated using a new traveltime equation in terms of new defined offsets. This new traveltime equation for the CSP gather is the conventional hyperbolic equation used for velocity analysis, NMO correction and CDP stack in surface data processing. Thus, these conventional processing tools can be used in the CSP stack processing. The high fold and large offsets in CSP gathers allow us to make a more accurate velocity analysis at each migrated position.

I have also proposed a prestack Kirchhoff time migration algorithm for vertical cable seismic imaging. The migration process is directly applied to each common receiver gather after the pre-processing of upgoing and downgoing wave separation. The migration velocities are taken from the residual velocity analysis on each CSP gather. The application of arrival angle weight in migration has much improved the imaging quality. The comparison of imaging results from the two common receiver gathers on the same cable demonstrates the efficiency of this method in real data applications.

8.3 Anisotropic inversion

Based on a derivation for the general expressions of slowness surfaces in anisotropic media, I have discussed the slowness distributions in coordinate planes for TI and orthorhombic media. In the symmetry-axis plane, the slowness for each of three waves in a TI medium can be expressed as a function of five independent elastic constants and the phase angle, which is defined as the angle between the wavefront normal and the axis of symmetry. In the horizontal plane, the slownesses for orthorhombic media have the same forms as those in HTI media.

I have also investigated the possibility of VCS traveltime inversion using direct, reflected and refracted arrivals in anisotropic media. The reflected $P-$waves alone in VCS data are insufficient for accurate determination of the vertical velocity and anisotropic parameters, even if the long-spread data are used. The direct arrivals in VCS data can be used for inverting $P-$ velocities in the water layer. This is essential in performing accurate depth imaging and time-lapse seismic data processing.

Refracted arrivals are analyzed to investigate the near-surface anisotropy of marine sediments using a VCS configuration in the presence of dip. The development of this technique is based on a multi-layered azimuthally isotropic or anisotropic model with an assumption that the layers are parallel to each other and the symmetry axes are perpendicular or parallel to the layer surface. For a given azimuth and source-cable offset, the horizontal ray-slowness can be obtained from the sum of horizontal apparent slownesses in up- and down-dip directions, on the other hand, the vertical ray-slowness can be taken from the difference of the vertical apparent slownesses between up- and down-dip directions. The multiple azimuths generated by a VCS geometry permit the ray-slowness and the tangent of apparent dip ($\tan\alpha$) to be determined at any measured azimuth.

A slowness-based anisotropic inversion procedure has then been established to

estimate the dip and anisotropy parameters for the refractor from the measured refracted traveltimes. The inversion feasibility has been examined by theoretical calculations and synthetic $P-$wave vertical cable seismic data with a set of models. Numerical tests show that the azimuthal variations in apparent slownesses are mainly due to effects of dip rather than anisotropy. When dips exceed 5°, significant errors may occur in the use of the phase-slowness approach based solely on horizontal layers. However, for azimuthal variations of horizontal ray-slowness, the influence of anisotropy is more significant than that of dip.

The inversion results for the synthetic $P-$wave VCS data demonstrate that this technique can provide an accurate and quantitative description of the anisotropic parameters v_{p0} and ϵ, the symmetry axis azimuth φ_a, and layer parameters β and φ_d in multi-layered azimuthally anisotropic media. The relative errors for inverted parameters v_{p0} and ϵ are less than 0.4% and 6.0%, respectively, when the $P-$wave anisotropy is up to 22%. Unfortunately, the estimation for the anisotropy parameter δ based solely on $P-$waves is not reliable. In addition, the overburden has no effect on the inversion results for the refractor in our case. Although this inversion procedure is based on the weak TI approximation, it can be easily extended to orthorhombic media, since both HTI and orthorhombic media may have the same form of the slowness approximation in the horizontal plane.

In the application to the field vertical cable seismic data, first arrivals along 348 azimuths were picked and used for dip and anisotropic inversions. The final results show that the near-surface sediments in this area have 1° dip with a dip azimuth of 23°, and there is about 5.0% $P-$wave azimuthal anisotropy, with the symmetry axis at 134° from the $X-$axis in the natural coordinate system. The relative estimation error of our data set, using a fit of the three-term approximation to the calculated square ray-velocities, is 2.8%.

8.4 Suggestions for future work

In this thesis, the imaging technique is based on the assumption that the seismic wave is propagating in an isotropic model, and the velocity is constant in each CSP gather. In the future, we need to develop a 3-D azimuthal velocity analysis procedure to obtain a more accurate velocity model to perform 3-D vertical cable seismic depth migration based on an anisotropic model. The multiple-azimuth vertical cable seismic data provide opportunities to estimate the azimuthal anisotropy in the subsurface and perform azimuthal CSP stack. In order to investigate such anisotropy in the subsurface, the study of the integration of traveltime and amplitude inversions using VCS reflected waves in anisotropic media will be an interesting topic.

Another potential application of vertical cable seismic is land time-lapse reservoir monitoring using the permanent multi-component VCS acquisition system. By locating the receivers in an underground environment, it may significantly improve land data quality by reducing the effects of ground roll and statics, which result from the near surface low-velocity layer. The high repeatability of this system may reduce the uncertainties in 4-D data interpretation, and obtain more accurate information for reservoir changes. Therefore, another target in the future is to undertake an 4-D multi-component vertical cable seismic modelling to investigate the feasibility of this application. In the meantime, a set of multi-component vertical cable seismic processing techniques must be developed to handle these data, and tested using synthetic data.

References

Alkhalifah, T., 1997, Velocity analysis using nonhyperbolic moveout in transversely isotropic media: Geophysics, 62, 1839-1854.

Alkhalifah, T. and Tsvankin, I., 1995, Velocity analysis in transversely isotropic media: Geophysics, 54, 1550-1566.

Anderson, J., and I., Cai, W., Delome, H., Sukup, D., and Boyd, S., 1997, 3-D vertical cable processing to obtain a pre-stack depth-migrated image: 67th Annual Internat. Mtg.-SEG, Expanded Abstracts, 1399-1401.

Araujo, F.V., Weglein, A.B., Carvalho, P.M. and Stolt, R.H., 1994, Inverse scattering series for multiple attenuation: An example with surface and internal multiples, 64th Ann. Internat. Mtg: Soc. of Expl. Geophys., 1039-1041.

Arce, G.R. and McLaughlin, M.P., 1987, Theoretical analysis of the max/median filter: IEEE Transactions on Acoustics, Speech, and Signal Processing ASSP-35(1), 60-69.

Bachman, R.T., 1979, Acoustic anisotropy in marine sediments and sedimentary rocks: J. Geophys. Res., 84, 7661-7663.

Bachman, R.T., 1983, Elastic anisotropy in marine sedimentary rocks,: J. Geophys. Res. 88, 539-545.

Backus, G.E., 1962, Long-wave elastic anisotropy produced by horizontal lay-

ering: J. Geophys. Res., 67, 4427-4440.

Backus, M.M., 1959, Water reverberations their nature and elimination: Geophysics 24, 233-261.

Bancroft, J.C., and Xu, Y., 1999, Equivalent offset migration for vertical receiver arrays: SEG 1999 Expanded Abstracts, P.1279-1282.

Berryman, J.G., 1979, Long-wave elastic anisotropy in transversely isotropic media: Geophysics, 44, 896-917.

Banik, N.C., 1984, velocity anisotropy of shales and depth estimation in the North Sea basin: Geophysics, 49, 1411-1419.

Boelle, J.-L., Canadas, G., and Hugonnet, P., 1998, Wavefield separation in borehole seismic by Linear Radon Decomposition: 68th Annual Internat. Mtg., Soc. Expl. Geophys., Expanded Abstracts, 272-275.

Buttkus, B., 1979, Coherency weighing - an effective approach to the suppression of long leg multiples: Geophys. Prosp., 27, 29-39.

Byun, B.S., 1982, Seismic parameters for media with elliptical velocity dependence: Geophysics, 47, 1621-1626.

Carlson, R.L., Schaftenaar, C.H. and Moore, R.P., 1984, Causes of compressional-wave anisotropy in carbonate-bearing, deep-sea sediments: Geophysics 49, 525-532.

Christie, P.A.F., Hughes,V.J. and Kennett, B.L.N., 1983, Velocity filtering of seismic reflection data: First Break, 1 (3), 9-24.

Claerbout, J.F., 1971, Towards a unified theory of reflector mapping: Geophysics, 36, 467-481.

Claerbout, J.F., 1985, Imaging the earth's interior: Blackwell Scientific Publications.

Cohen, J.K. and Stockwell, Jr.J.W., 2000, CWP/SU: Seismic Unix Release 34: a free package for seismic research and processing, Center for Wave Phenomena, Colorado School of Mines.

Crampin, S., 1981, A review of wave motion in anisotropic and cracked elastic media: Wave motion 3, 343-391.

Crampin, S., 1985, Evidence for aligned cracks in the earth's crust: First Break, 3, no.3, 12-15.

Daley, P.F., and Hron, F., 1979, Reflection and transmission coefficients for seismic waves in ellipsoidally anisotropic media: Geophysics, 44, 27-38.

Dillon, P.B., 1988, Vertical seismic profile migration using the Kirchhoff integral: Geophysics, Vol. 53, P. 786-799.

Dix, C.H., 1955, Seismic velocities from surface measurements: Geophysics, 20, 68-86.

Dragoset, W., and Jericevic, Z., 1998, Some remarks on surface multiple attenuation: Geophysics, 63, 772-789.

Druzhinin, A., 1998, Prestack imaging with ray constraints-simple sea-floor examples: 60th EAGE meeting, Expanded Abstracts, P092.

Esmersoy, C., 1990, Inversion of P and SV waves from multicomponent offset vertical seismic profiles: Geophysics, 55, 39-50.

French, W.S., 1975, Computer migration of oblique seismic reflection profiles: Geophysics, 40, 961-980.

Fokkema, J., and Van den Berg, P., 1990, Removal of surface-related wave phenomena: The marine case: 60th Ann. Internat Mtg., Soc. Expl. Geophys., Expanded Abstracts, 1689-1692.

Foster, D.J., and Mosher, C.C., 1992, Suppression of multiple reflections using

the Radon transform: Geophysics, 57, 386-395.

Fryer, G.J. and Miller, D.J., 1986, Effects and consequences of transverse isotropy in the sea floor, in T. Akal and J. M. Berkson (eds.), Ocean Seismo-Acoustics, Low-Frequency Underwater Acoustics, NATO Conference Series IV: Marine Science 16, Plenum Press, New York, p.589-597.

Fryer, G.J., Miller, D.J., and Berge, P.A., 1989, Seismic anisotropy and age-dependent structure of the upper oceanic crust, in J. M. Sinton (ed.), Evolution of Mid Ocean Ridges, Geophysical Monograph 57, IUGG 8, Am. Geophys. Union, Washington, D. C., p.1-8.

Gaiser, J.E., 1990, Transversely isotropic phase velocity analysis from slowness estimates: J. Geophys. Res., 95, 11241-11254.

Gaiser, J.E. and DiSiena, J.P., 1982, VSP fundamentals that improve CDP data interpretation: 52nd Annual Internat. Mtg. -SEG, Expanded Abstracts, 154-156.

Gallagher, N.C. and Wise, G.L., 1981, A theoretical analysis of properties of median filters: IEEE Transactions on Acoustics, Speech, and Signal Processing ASSP-29(6), 1136-1141.

Gazdag, J., 1984, Migration of seismic data: Proceedings of IEEE.

Gendzwill, D.J., 1993, Seismic velocity, fracture density and anisotropy of some Manitoba limestones: Can. J. Expl. Geophys., 29, 153-162.

Grechka, V. and Tsvankin, I., 1998, Feasibility of nonhyperbolic moveout inversion in transversely isotropic media: Geophysics, 63, 957-969.

Guimarães, M.G., Sekharan, K.K., Sukup, D., Krail, P., 1998, 3-D Pre-stack depth migration of vertical cable data over SEG/EAGE physical model: 68th Annual Internat. Mtg. -SEG, Expanded Abstracts, 1182-1185.

Haldorsen, J.B.U. and Farmer, P.A., 1989, Suppression of high-energy noise

using an alternative stacking procedure: Geophysics, 54, 181-190.

Hale, D., and Claerbout, J.F., 1983, Butterworth dip filters: Geophysics, 48, 1033-1038.

Hampson, D., 1986, Inverse velocity stacking for multiple elimination: J. Can. Soc. Expl. Geophys., 22, 44-45.

Hanselman, D., and Littlefield B., 2001, Mastering MATLAB 6: a comprehensive tutorial and reference: Prentice Hall, Inc.

Hardage, B.A., 1983, Vertical Seismic Profiling, Part A: Principles: Geophysical Press.

Hardy, R.J.J. and Hobbs, R.W., 1991, A strategy for multiple suppression: First Break, 9, 139-144.

Havig, S.O., and Krail, P.M., 1996, Vertical cable seismic applications: World Oil, May 1996, p.72.

Helbig, K., 1994, Foundation of anisotropy for exploration seismics: Handbook of geophysical exploration, 22.

Hunter, J.A. and Pullan, S.E., 1990, A vertical array method for shallow seismic refraction surveying of the sea floor: Geophysics, 55, 92-96.

Ikelle, L., 2001, Attenuating primaries and free-surface multiples of vertical cable (VC) data while preserving receiver ghosts of primaries: Geophysics, 66, 953-963.

Ikelle, L. and Yoo, S., 2000, An analysis of 2-D and 3-D inverse scattering multiple attenuation: 70th Ann. Internat. Mtg. Soc. of Expl. Geophys., 1973-1976.

Ikelle, L., and Wilson, R.J., 1999, Potential impacts of vertical cable (VC): The Leading Edge, 18(10), 1154-1157.

Kohler, K., and Koenig, M., 1986, Reconstruction of reflecting structures from vertical seismic profiles with a moving source: Geophysics, Vol. 51, P. 1923-1938.

Kommedal J.H. and Tjøstheim B.A.,1989, Tutorial: A study of different methods of wavefield separation for application to VSP data: Geophysical Prospecting 37, 117-142, 1989.

Krail, P.M., 1991, Case history: vertical cable 3-D acquisition: 53rd Mtg. Eur. Assoc. Expl. Geophys., Abstracts, 91, 204.

Krail, P.M., 1993, Sub-salt acquisition with vertical cable: 63rd EAGE meeting, Expanded Abstracts, P1376.

Krail, P.M., 1994, Vertical cable as a subsalt imaging tool: The Leading Edge, 46, 885-887.

Landa, E., Belfer, I., and Keydr, S., 1999, Multiple attenuation in the parabolic $\tau - p$ domain using wavefront characteristics of multiple generating primaries: Geophysics, 64, 1806-1815.

Leach, P., 1997, Strathspey vertical-cable seismic survey: a North Sea first: SPE Abstracts, P333-347.

Leslie, J.M., and Lawton, D.C., 1999, A refraction-seismic field study to determine the anisotropic parameters of shales: Geophysics, 64, 1247-1251.

Levin, F.K., 1978, The reflection, refraction, and diffraction of waves in media with an elliptical velocity dependence: Geophysics, 43, 528-537.

Li, Jianchao and Larner, K., 1993, Differential-equation-based seismic data filtering: Geophysics, 58, 1809-1819.

Li, X.-Y., 1997, Viability of azimuthal variation in $P-$ wave moveout for fracture detection: 67th Annual Internat. Mtg. -SEG, Expanded Abstracts, 1555-1558.

MacBeth, C., 1991, Share-wave anisotropy in marine sediments around Britain from surface sources, J. M. Hovem et al. (eds), Shear-waves in marine sediments 13-20, Kluwer Academic Publishers, The Netherlands.

MacBeth, C., 1998, Vertical fracture estimation using walk-away VSP: 68th Annual Internat. Mtg. -SEG, Expanded Abstracts, 304-307.

March, D.W. and Bailey, A.D., 1983, A review of the two-dimensional transform and its use in seismic processing: First Break, 1(1), 9-21.

Maroof, S.I. and Gravely, C.J., 1984, Aliasing and $\tau - p$: 54th SEG meeting, Atlanta, Expanded Abstracts, 623-625.

Meunier, J. and Huguet, F., 2000, Reservoir Monitoring using permanent sources and vertical receiver antennae: 70th Annual Internat. Mtg. -SEG, Expanded Abstracts, 1619-1622.

Miller, D. E., and Spencer, C., 1994, An exact inversion for anisotropic moduli from phase slowness data: J. Geophys. Res., 99, 21651-21657.

Milligan, P.A., 1998, Anisotropic statics for a 2D line over a mountainous overthrust belt in Bolivia: Annual Meeting Abstracts, Society Of Exploration Geophysicists, 1413-1416.

Moon, W., Carswell, A., Tang, R. and Dilliston, C., 1986, Radon transform wavefield separation for vertical seismic profiling: Geophysics 4, 940-947.

Nodes, T.A. and Gallagher, N.C., 1982, Median filters: some modifications and their properties: IEEE Transactions on Acoustics, Speech, and Signal Processing ASSP-30(5), 739-746.

O'Brien, M.J. and Etgen, J.T., 1998, Wavefield imaging of complex structures with sparse, point-receiver data: Annual Meeting Abstracts, Society Of Exploration Geophysicists, 49-76.

Ohlsen, F. and MacBeth, C., 1998, Anisotropy estimates from a North Sea

VSP: 68th Annual Internat. Mtg. -SEG, Expanded Abstracts, 280-283.

Peacock, K. L., and Treitel, S., 1969, Predictive deconvolution-Theory and practice: Geophysics, 34, 155-169.

Postma, G.W., 1955, Wave propagation in a stratified medium: Geophysics, 20, 780-806.

Ryu, J.V., 1982, Decomposition (DECOM) approach applied to wave-field analysis with seismic reflection records: Geophysics, 47, 869-883.

Sayers, C.M., 1997, Determination of anisotropic velocity models from walkaway VSP data acquired in the presence of dip: Geophysics, 62, 723-729.

Schneider, W.A., 1978, Integral formulation for migration in two and three dimensions: Geophysics, 43, 1133-1149.

Schoenberg, M. and Helbig, K., 1997, Orthorhombic media: Modeling elastic wave behavior in a vertically fractured earth: Geophysics, 62, 1954-1974.

Scott, W., Leaney, P. and Esmersoy, Cengiz, 1989, Parametric decomposition of offset VSP wave fields: 59th Annual Internat. Mtg., Soc. Expl. Geophys., Expanded Abstracts, 26-29.

Seeman, B. and Horowicz, L., 1983, Vertical seismic profiling: separation of upgoing and downgoing acoustic waves in a stratified medium: Geophysics 48, 555-568.

Sena, A.G., 1991, Seismic traveltime equations for azimuthally anisotropic and isotropic media: Estimation of interval elastic properties: Geophysics, 56, 2090-2101.

Simaan, M. and Love, P.L., 1984, Optimum suppression of coherent signals with linear moveout in seismic data: Geophysics 49, 215-226.

Sun, Chuanwen, 1997, Separation of vertical cable up-going and down-going

waves fields: 67th Annual Internat. Mtg. -SEG, Expanded Abstracts, 1131-1134.

Suprajitno, M. and Greenhalgh, S.A., 1985, Separation of upgoing and downgoing waves in vertical seismic profiling by contour-slice filtering: Geophysics 50, 950-962.

Takahashi, T., 1995, Prestack migration using arrival angle information. Geophysics, 60, 154-163.

Taner, M. T., 1980, Long-period sea-floor multiples and their suppression: Geophys. Prosp., 28, 30-48.

Thomsen, L., 1986, Weak elastic anisotropy: Geophysics, 51, 1954-1966.

Thomsen, L., 1988, Reflection seismology over azimuthally anisotropic media: Geophysics, 53, 304-313.

Thorsen, J.R. and Claerbout, J.F., 1985, Velocity stack and slant stochastic inversion: Geophysics, 50, 2727-2741.

Tjåland, E., 1986, Sepasjon av seismiske bølgefelt ved hjelp av Radontransformasjonen: Unpublished thesis, Norwegian Institute of Technology, University of Trondheim.

Traub, B. and Li, X.-Y., 2002, Sensitivity of anisotropic parameter estimation from 4c data - modelling and case studes: 64th EAGE meeting, Expanded Abstracts, F-18.

Tsvankin, I. and Thomsen, L., 1995, Inversion of reflection traveltimes for transverse isotropy: Geophysics, 60, 1095-1107.

Tsvankin, I. and Thomsen, L., 1994, Nonhyperbolic reflection moveout in anisotropic media: Geophysics, 59, 1290-1304.

Verschuur, D., Berkhout, A., and Wapenaar, C., 1992, Adaptive surface-

related multiple elimination: Geophysics, 57, 1166-1177.

Wang, H. and Dong, M., 1993, VSP modelling in EDA media and shear wave splitting analysis: Oil Geophysical Prospecting, 28(2), 63-71.

Wang, H. and Dong, M., 1994, Elastic waves in EDA media: Oil Geophysical Prospecting, 29 (6),

Ward, J.A., 1997, Towed streamer and vertical cable: Offshore, Vol 57, 3, p40-43.

Weglein, A.B., 1999, Multiple attenuation: an overview of recent advances and the road ahead: The leading edge, 18, no. 1, 40-44.

Weglein, A.B., Gasparotto, F., Carvalho, P., and Stolt, R., 1997, An inverse-scattering series method for attenuating multiples in seismic reflection data: Geophysics, 57, 386-395.

Wiggins, J.W., 1984, Kirchhoff integral extrapolation and migration of non-planar data: Geophysics, 49, 1939-1248.

Wiggins, J.W., 1988, Attenuation of complex water-bottom multiples by wave equation-based prediction and subtraction: Geophysics, 53, 1527-1539.

Winterstein, D.F., 1986, Anisotropy effects in $P-$wave and $S-$wave stacking velocity contain information on lithology: Geophysics, 51, 661-672.

Winterstein, D.F., 1990, Velocity anisotropy terminology for geophysicists: Geophysics, 55, 1070-1088.

Yilmaz, O., 1987, Seismic data processing, Investigations in Geophysics 2, Society of Exploration Geophysicists, Tulsa, OK.

Yilmaz, O., 1989, Velocity stack processing: Geophys. Prosp., 37, 357-382.

Zhou, B., and Greenhalgh, S.A., 1991, Multiple suppression by a wave-equation extrapolation method: Exploration Geophysics, 22, 481-484.

Zhou B., and Greenhalgh, S.A., 1996, Multiple suppression by 2D filtering in the parabolic $\tau - p$ domain: a wave-equation-based method: Geophys. Prosp., 44, 375-401.

Ziolkowski, A.M., Taylor, D.B. and Johnston, R.G.K., 1999, Marine seismic wavefield measurement to remove sea-surface multiples: Geophysical Prospecting, 47, 841-870.

Appendix A

Elastic tensor for TI media with a non-vertical axis of symmetry

In the natural coordinate system (X-Y-Z) shown in Figure A.1, the stiffness tensor of a transverse isotropic medium with a vertical axis of symmetry (VTI) can be written as,

$$[C] = \begin{bmatrix} C_{11} & C_{12} & C_{13} & 0 & 0 & 0 \\ C_{12} & C_{11} & C_{13} & 0 & 0 & 0 \\ C_{13} & C_{13} & C_{33} & 0 & 0 & 0 \\ 0 & 0 & 0 & C_{44} & 0 & 0 \\ 0 & 0 & 0 & 0 & C_{44} & 0 \\ 0 & 0 & 0 & 0 & 0 & C_{66} \end{bmatrix}, \tag{A.1}$$

where

$$C_{12} = C_{11} - 2C_{66}. \tag{A.2}$$

For a general case of a transverse isotropic medium with a non-vertical axis of symmetry, I assume that the symmetry axis of this medium has an angle of θ with the vertical axis. The stiffness tensor of this medium under the natural coordinate system is equivalent to that of a VTI medium in the new coordinate system by rotating the natural coordinate system clockwise about the Y-axis with angle θ,

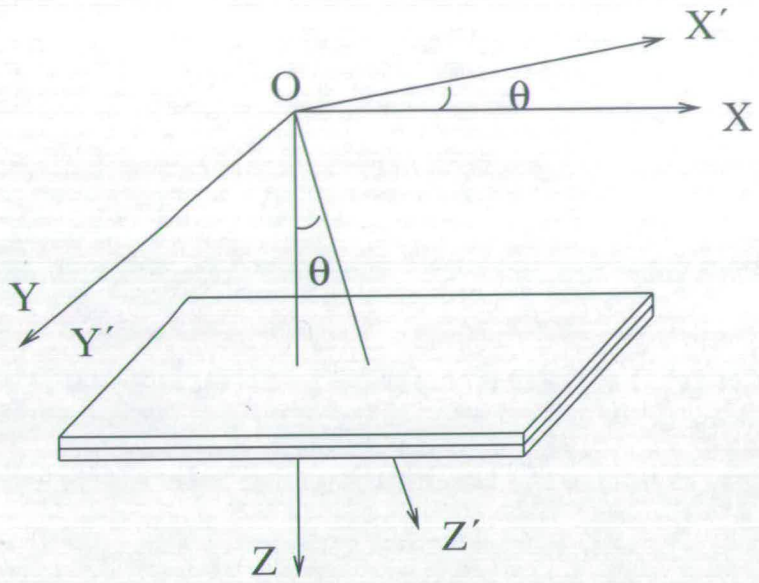


Figure A.1: A TI medium with a vertical symmetry axis in the natural coordinate system (X-Y-Z) and a new coordinate system (X'-Y'-Z') by a clockwise rotation with angle θ about the Y-axis.

which is shown in Figure A.1. The rotation matrix

$$[a] = \begin{bmatrix} \cos\theta & 0 & -\sin\theta \\ 0 & 1 & 0 \\ \sin\theta & 0 & \cos\theta \end{bmatrix}. \tag{A.3}$$

Using the Bond transform (Winterstein 1990), the stiffness can be expressed as

$$[C'] = [M][C][M]^T = \begin{bmatrix} C'_{11} & C'_{12} & C'_{13} & 0 & C'_{15} & 0 \\ C'_{21} & C'_{22} & C'_{23} & 0 & C'_{25} & 0 \\ C'_{31} & C'_{32} & C'_{33} & 0 & C'_{35} & 0 \\ 0 & 0 & 0 & C'_{44} & 0 & C'_{46} \\ C'_{51} & C'_{52} & C'_{53} & 0 & C'_{55} & 0 \\ 0 & 0 & 0 & C'_{64} & 0 & C'_{66} \end{bmatrix}, \tag{A.4}$$

where $[M]$ is a Bond transpose matrix,

$$[M] = \begin{bmatrix} a_{11}^2 & a_{12}^2 & a_{13}^2 & 2a_{12}a_{13} & 2a_{11}a_{13} & 2a_{11}a_{12} \\ a_{21}^2 & a_{22}^2 & a_{23}^2 & 2a_{22}a_{23} & 2a_{21}a_{23} & 2a_{21}a_{22} \\ a_{31}^2 & a_{32}^2 & a_{33}^2 & 2a_{32}a_{33} & 2a_{31}a_{33} & 2a_{31}a_{32} \\ a_{21}a_{31} & a_{22}a_{32} & a_{23}a_{33} & a_{22}a_{33}+a_{23}a_{32} & a_{21}a_{33}+a_{23}a_{31} & a_{21}a_{32}+a_{22}a_{31} \\ a_{11}a_{31} & a_{12}a_{32} & a_{13}a_{33} & a_{12}a_{33}+a_{13}a_{32} & a_{11}a_{33}+a_{13}a_{31} & a_{11}a_{32}+a_{12}a_{31} \\ a_{11}a_{21} & a_{12}a_{22} & a_{13}a_{23} & a_{12}a_{23}+a_{22}a_{13} & a_{11}a_{23}+a_{13}a_{21} & a_{11}a_{22}+a_{12}a_{21} \end{bmatrix}, \tag{A.5}$$

where $a_{ij}, (i = 1,2,3 \text{ and } j = 1,2,3)$ are elements of the rotation matrix $[a]$. Substitution of equation (A.3) into equation (A.5), gives

$$[M] = \begin{bmatrix} \cos^2\theta & 0 & \sin^2\theta & 0 & -\sin 2\theta & 0 \\ 0 & 1 & 0 & 0 & 0 & 0 \\ \sin^2\theta & 0 & \cos^2\theta & 0 & \sin 2\theta & 0 \\ 0 & 0 & 0 & \cos\theta & 0 & \sin\theta \\ \frac{\sin 2\theta}{2} & 0 & \frac{-\sin 2\theta}{2} & 0 & \cos 2\theta & 0 \\ 0 & 0 & 0 & -\sin\theta & 0 & \cos\theta \end{bmatrix}. \tag{A.6}$$

$[M]^T$ is the transposition of $[M]$, and the non-zero elements of the stiffness tensor $[C']$ can be expressed as

$$\begin{aligned} C'_{11} &= \cos^2\theta[C_{11}\cos^2\theta + C_{13}\sin^2\theta] + \sin^2\theta[C_{13}\cos^2\theta + C_{33}\sin^2\theta] + C_{44}\sin^2 2\theta, \\ C'_{12} &= C_{12}\cos^2\theta + C_{13}\sin^2\theta, \\ C'_{13} &= \sin^2\theta[C_{11}\cos^2\theta + C_{13}\sin^2\theta] + \cos^2\theta[C_{13}\cos^2\theta + C_{33}\sin^2\theta] - C_{44}\sin^2 2\theta, \\ C'_{15} &= \frac{\sin 2\theta}{2}[C_{11}\cos^2\theta + C_{13}\sin^2\theta] - \frac{\sin 2\theta}{2}[C_{13}\cos^2\theta + C_{33}\sin^2\theta] \\ &\quad -C_{44}\sin 2\theta\cos 2\theta, \\ C'_{21} &= C'_{12}, \\ C'_{22} &= C_{11}, \\ C'_{23} &= C_{12}\sin^2\theta + C_{13}\cos^2\theta, \end{aligned} \tag{A.7}$$

$$
\begin{aligned}
C'_{25} &= [C_{12} - C_{13}]\frac{\sin 2\theta}{2}, \\
C'_{31} &= C'_{13}, \\
C'_{32} &= C'_{23}, \\
C'_{33} &= \sin^2\theta[C_{11}\sin^2\theta + C_{13}\cos^2\theta] + \cos^2\theta[C_{13}\sin^2\theta + C_{33}\cos^2\theta] + C_{44}\sin^2 2\theta, \\
C'_{35} &= \frac{\sin 2\theta}{2}[C_{11}\sin^2\theta + C_{13}\cos 2\theta - C_{33}\cos^2\theta] + C_{44}\sin 2\theta\cos 2\theta, \\
C'_{44} &= C_{44}\cos^2\theta + C_{66}\sin^2\theta, \\
C'_{46} &= \sin\theta\cos\theta(C_{66} - C_{44}), \\
C'_{51} &= C'_{15}, \\
C'_{52} &= C'_{25}, \\
C'_{53} &= C'_{35}, \\
C'_{55} &= \frac{\sin^2 2\theta}{4}[C_{11} - 2C_{13} + C_{33}] + C_{44}\cos^2 2\theta, \\
C'_{64} &= C'_{46}, \\
C'_{66} &= C_{44}\sin^2\theta + C_{66}\cos^2\theta.
\end{aligned}
$$

If $\theta = 90°$, the stiffness tensor $[C']$ becomes

$$
\begin{bmatrix}
C_{33} & C_{13} & C_{13} & 0 & 0 & 0 \\
C_{13} & C_{11} & C_{12} & 0 & 0 & 0 \\
C_{13} & C_{12} & C_{11} & 0 & 0 & 0 \\
0 & 0 & 0 & C_{66} & 0 & 0 \\
0 & 0 & 0 & 0 & C_{44} & 0 \\
0 & 0 & 0 & 0 & 0 & C_{44}
\end{bmatrix}. \tag{A.8}
$$

This represents a transverse isotropic medium with a horizontal axis, which is the simplest form of azimuthal anisotropy with only five elastic constants.

Appendix B

Refracted traveltime equation in multilayered media

I derive a formula for the refraction travel-time of multi-layered azimuthally anisotropic or isotropic media in the presence of dip. In Figure 6.2, I considered $n-$layered transversely isotropic media with a symmetry axis parallel or perpendicular to layer interface. Each layer has the same dip and dip azimuth, and is specified by its vertical depth z_k at the cable location O and its ray velocities $V_k(\theta_k, \phi)$, $(k = 1, 2, \cdots, n-1)$, where θ_k is the angle of incidence at each layer for a given ray path. $P-$wave velocities in the water and at the nth refractor are V_0 and $V_n(\phi)$, respectively, for a given measured azimuth ϕ. The travel-time for a refracted wave of layer n from source S to receiver R can be expressed as

$$t_n(\phi) = \frac{SA_0}{V_0} + 2\sum_{k=1}^{n-1} \frac{A_{k-1}A_k}{V_k(\theta_k, \phi)} + \frac{A_{n-1}B_{n-1}}{V_n(\phi)} + \frac{B_0R}{V_0}. \tag{B.1}$$

Similar to the derivation of the traveltime equation for a single refractor, I can write

$$SA_0 = \frac{h_O}{\cos(\theta_0 - \alpha)} - \frac{x\sin\alpha - h_O\tan(\theta_0 - \alpha)\sin\alpha}{\cos\theta_0}, \tag{B.2}$$

$$BR = \frac{h_R\cos\alpha}{\cos\theta_0}, \tag{B.3}$$

$$A_0B_0 = \frac{x\cos(\theta_0 - \alpha) - h_O\sin(\theta_0 - \alpha) - h_R\sin(\theta_0 + \alpha)}{\cos\theta_0}, \tag{B.4}$$

where α is the apparent dip of each layer at the measured azimuth ϕ. In Figure 6.2, I also have

$$A_k A_{k-1} = \frac{z_k \cos\alpha}{\cos\theta_k}, \tag{B.5}$$

$$\begin{aligned} A_1 B_1 &= A_0 B_0 - 2z_1 \cos\alpha \tan\theta_1, \\ A_2 B_2 &= A_1 B_1 - 2z_2 \cos\alpha \tan\theta_2, \\ &\cdots \quad \cdots \quad \cdots \\ A_{n-1} B_{n-1} &= A_{n-2} B_{n-2} - 2z_{n-1} \cos\alpha \tan\theta_{n-1}. \end{aligned} \tag{B.6}$$

Hence,

$$A_{n-1} B_{n-1} = A_0 B_0 - 2\cos\alpha \sum_{k=1}^{n-1} z_k \tan\theta_k. \tag{B.7}$$

Based on the above expressions, the travel time $t_n(\phi)$ can be finally written as

$$\begin{aligned} t_n(\phi) &= \left[\frac{\cos\alpha + \tan\theta_0 \sin\alpha}{V_n(\phi)} - \frac{\sin\alpha}{V_0 \cos\theta_0}\right] x \\ &+ \left[\frac{\cos\alpha}{V_0} - \frac{\sin(\theta_0+\alpha)}{V_n(\phi)}\right] \frac{h_R}{\cos\theta_0} \\ &+ \left[\frac{\cos\theta_0 + \sin(\theta_0-\alpha)\sin\alpha}{V_0 \cos(\theta_0-\alpha)} - \frac{\sin(\theta_0-\alpha)}{V_n(\phi)}\right] \frac{h_O}{\cos\theta_0} \\ &+ 2\cos\alpha \sum_{k=1}^{n-1} \frac{z_k}{\cos\theta_k V_k(\theta_k,\phi)} - \frac{2\cos\alpha}{V_n(\phi)} \sum_{k=1}^{n-1} z_k \tan\theta_k. \end{aligned} \tag{B.8}$$

Appendix C

Ray velocities in transversely isotropic media

I have made derivations of the the directional dependence of the phase slownesses in Chapter 6. For TI media, the square slowness of the $P-$wave in the plane with the axis of symmetry can be expressed as

$$S_P^2(\theta_p) = \rho \frac{b - \sqrt{b^2 - 4a}}{2a}, \tag{C.1}$$

with

$$\begin{aligned} a &= C_{44}(C_{33}\cos^4\theta_p + C_{11}\sin^4\theta_p) + (C_{11}C_{33} - 2C_{13}C_{44} - C_{13}^2)\sin^2\theta_p\cos^2\theta_p, \\ b &= C_{44} + C_{33}\cos^2\theta_p + C_{11}\sin^2\theta_p, \end{aligned} \tag{C.2}$$

where ρ is the density, the phase angle θ_p is an angle between the wavefront normal and symmetry axis, and C_{11}, C_{13}, C_{33}, and C_{44} are elastic constants. Thus, the square phase velocities for the $P-$wave can be achieved as

$$v_P^2(\theta_p) = \frac{1}{2\rho}\left[C_{33} + C_{44} + (C_{11} - C_{33})\sin^2\theta_p + D(\theta_p)\right], \tag{C.3}$$

where $D(\theta_p)$ is compact notation for the quadratic combination, which is given by

$$D(\theta_p) = \left\{(C_{33} - C_{44})^2\right.$$

$$+2\left[2(C_{13}+C_{44})^2-(C_{33}-C_{44})(C_{11}+C_{33}-2C_{44})\right]\sin^2\theta_p$$
$$+\left[(C_{11}+C_{33}-2C_{44})^2-4(C_{13}+C_{44})^2\right]\sin^4\theta_p\Big\}^{1/2}. \qquad \text{(C.4)}$$

In any plane which contains the symmetry axis, the ray velocity and ray angle can be expressed in terms of the phase velocity and phase angle (e.g., Postma, 1955; Levin, 1978; Byun, 1982). A simple relationship between the two velocities is (Berryman, 1979)

$$V_P^2(\phi(\theta_p)) = v_P^2(\theta_p) + (\frac{dv_P}{d\theta_p})^2, \qquad \text{(C.5)}$$

where $V(\phi(\theta_p))$ is the ray velocity as a function of ray angle $\phi(\theta_p)$ from the symmetry axis. $\phi(\theta_p)$ is given by

$$\tan(\phi(\theta_p)) = (\tan\theta_p + \frac{1}{v_P}\frac{dv_P}{d\theta_p})/(1-\frac{\tan\theta_p}{v_P}\frac{dv_P}{d\theta_p}). \qquad \text{(C.6)}$$

From equations (C.3) and (C.4), I have

$$\frac{dv_P}{d\theta_p} = \frac{1}{4}v_P^{-1}\left[2(C_{11}-C_{33})\sin\theta_p\cos\theta_p + \frac{dD(\theta_p)}{d\theta_p}\right], \qquad \text{(C.7)}$$

and

$$\frac{dD(\theta_p)}{d\theta_p} = 2D^{-1}(\theta_p)\left\{\left[2(C_{13}+C_{44})^2-(C_{33}-C_{44})(C_{11}+C_{33}-2C_{44})\right]\sin\theta_p\cos\theta_p\right.$$
$$\left.+\left[(C_{11}+C_{33}-2C_{44})^2-4(C_{13}+C_{44})^2\right]\sin^3\theta_p\cos\theta_p\right\}. \qquad \text{(C.8)}$$

When $\theta_p = 0°$ or $90°$, ray angle $\phi(\theta_p)$ equals phase angle θ_p, and ray velocity equals phase velocity.

Therefore, for HTI media, the ray velocity distribution in the horizontal plane can be expressed as

$$V_P(\phi-\varphi_a) = \left[v_P^2(\theta_p) + (\frac{dv_P}{d\theta_p})^2\right]^{1/2}, \qquad \text{(C.9)}$$

where ϕ and φ_a are the azimuths of the observation point and the horizontal axis of symmetry, respectively, with respect to the $X-$axis in the survey coordinates, and $\phi-\varphi_a = \phi(\theta_p)$.

Appendix D

The LSQ solution for a cosine function

In this appendix, I derive a formula for the estimation of the coefficients of a cosine function with arbitrary frequency from observed data using an LSQ method. Assuming that a variable y is a cosine function with respect to variable x,

$$y = A\cos(x+\phi) + y_0, \tag{D.1}$$

and that there are pairs of measured data $((x_i, y_i),\ i = 1, 2, \ldots N)$, the objection function $Q(A, \phi, y_0)$ for the LSQ inversion can be expressed as

$$Q(A, \phi, y_0) = \sum_{i=1}^{N} (y_i - (A\cos(x_i+\phi) + y_0))^2. \tag{D.2}$$

The partial derivatives of the variable $Q(A, \phi, y_0)$ with respect to the variable A, ϕ and y_0 may be written as

$$\begin{aligned}
\frac{\partial Q}{\partial A} &= -2\sum_{i=1}^{N}(y_i - A\cos(x_i+\phi) - y_0)\cos(x_i+\phi) \\
&= -2a\cos\phi + 2b\sin\phi + 2cy_0\cos\phi - 2dy_0\sin\phi + 2eA\cos^2\phi \\
&\quad -2gA\sin 2\phi + 2fA\sin^2\phi,
\end{aligned} \tag{D.3}$$

$$\begin{aligned}
\frac{\partial Q}{\partial \phi} &= 2A\sum_{i=1}^{N}(y_i - A\cos(x_i+\phi) - y_0)\sin(x_i+\phi) \\
&= 2bA\cos\phi + 2aA\sin\phi - eA^2\sin 2\phi + fA^2\sin 2\phi \\
&\quad -2cAy_0\sin\phi - 2dAy_0\cos\phi - 2gA^2\cos^2\phi + 2gA^2\sin^2\phi,
\end{aligned} \tag{D.4}$$

and

$$\begin{aligned}\frac{\partial Q}{\partial y_0} &= -2\sum_{i=1}^{N}(y_i - A\cos(x_i+\phi) - y_0) \\ &= -2h + 2cA\cos\phi - 2dA\sin\phi + 2Ny_0, \end{aligned} \tag{D.5}$$

where

$$\begin{aligned} a &= \sum_{i=1}^{N} y_i \cos x_i, & b &= \sum_{i=1}^{N} y_i \sin x_i, \\ c &= \sum_{i=1}^{N} \cos x_i, & d &= \sum_{i=1}^{N} \sin x_i, \\ e &= \sum_{i=1}^{N} \cos x_i^2, & f &= \sum_{i=1}^{N} \sin x_i^2, \\ g &= \sum_{i=1}^{N} \sin x_i \cos x_i, & h &= \sum_{i=1}^{N} y_i. \end{aligned} \tag{D.6}$$

To minimize the function $Q(A, \phi, y_0)$ with respect to variables A, ϕ and y_0, I set the partial derivatives ((D.3)-(D.5)) to zero, which leads to

$$\begin{aligned} 0 &= b\sin\phi - a\cos\phi + cy_0\cos\phi - dy_0\sin\phi + eA\cos^2\phi \\ &\quad -2gA\sin\phi\cos\phi + fA\sin^2\phi, \end{aligned} \tag{D.7}$$

$$\begin{aligned} 0 &= a\sin\phi + b\cos\phi - dy_0\cos\phi - cy_0\sin\phi - gA\cos^2\phi \\ &\quad +(fA - eA)\sin\phi\cos\phi + gA\sin^2\phi, \end{aligned} \tag{D.8}$$

$$0 = cA\cos\phi - dA\sin\phi + Ny_0 - h. \tag{D.9}$$

From the equation (D.9), I can obtain the expression for y_0,

$$y_0 = \frac{d}{N}A\sin\phi - \frac{c}{N}A\cos\phi + \frac{h}{N}. \tag{D.10}$$

Substituting the expression (D.10) into equation (D.7) yields

$$A = \frac{(Nb - dh)\sin\phi + (ch - Na)\cos\phi}{(c^2 - eN)\cos^2\phi + 2(Ng - cd)\sin\phi\cos\phi + (d^2 - Nf)\sin^2\phi}. \tag{D.11}$$

Now inserting equation (D.11) into equation (D.10) gives a new expression for y_0 with respect only to the variable ϕ. Then the substitution of these new expressions for y_0 and A into equation (D.8) yields

$$\begin{aligned} 0 &= (bc^2 - Nbe + dhe - chg + Nag - adc)\cos\phi \\ &\quad +(ad^2 - Naf + hcf - bdc + Ngb - gdh)\sin\phi. \end{aligned} \tag{D.12}$$

This equation contains only the variable ϕ as a parameter. Therefore, the final solution of ϕ is achieved by

$$\phi = -\arctan\left(\frac{bc^2 - Nbe + dhe - chg + Nag - adc}{ad^2 - Naf + hcf - bdc + Ngb - gdh}\right), \tag{D.13}$$

where $-\pi/2 \leq \phi \leq \pi/2$. The solutions of A and y_0 can then be obtained by substituting the solution of ϕ into equations (D.11) and (D.10).

Appendix E

List of publications

1. Wang, H. and Li, X.-Y., 2002, Anisotropic inversion of refracted waves in vertical cable data in the presence of dip: Geophysical Prospecting, 50, 259-280.

2. Wang, H. and Li, X.-Y., 2001, Application of Prestack Kirchhoff Time Migration to Vertical Cable Seismic Data, 63rd Mtg.: Eur. Assn. of Expl. Geophys., Session: P072.

3. Wang, H., Druzhinin, A. and Li, X.-Y., 2000, Multiple suppression in vertical cable seismic, 62nd Mtg.: Eur. Assn. Geosci. Eng., Session:P0129.

4. Wang, H., Druzhinin, A. and Li, X.-Y., 2000, The impact of multiple suppression on vertical cable data imaging, 70th Ann. Internat. Mtg: Soc. of Expl. Geophys., 2173-2176.

5. Wang, H., Li, X.-Y. and MacBeth, C., 1999, Estimation of seabed sediment anisotropy using vertical cable seismic, 69th Ann. Internat. Mtg: Soc. of Expl. Geophys., 1963-1966.

6. Wang, H., MacBeth, C. and Li, X.-Y., 1999, Separation of up and down-going wave fields in vertical cable seismic, 61st Mtg.: Eur. Assn. Geosci. Eng., Session: P6-08.

Appendix F

A paper published on Geophysical Prospecting 50, 2002

Wang, H. and Li, X.-Y., 2002, Anisotropic inversion of refracted waves in vertical cable data in the presence of dip: Geophysical Prospecting, 50, 259-280.

Geophysical Prospecting, 2002, 50, 259–280

Anisotropic inversion of refracted waves in vertical cable data in the presence of dip

Hejie Wang[1,2*] and Xiang-Yang Li[2]

[1]*Department of Geology and Geophysics, University of Edinburgh, and* [2]*British Geological Survey, Murchison House, West Mains Road, Edinburgh EH9 3LA, UK*

Received October 2000, revision accepted July 2001

ABSTRACT

Refracted arrivals are analysed to estimate the near-surface anisotropy of marine sediments using a vertical-cable (VC) configuration. In the presence of dip, the horizontal and vertical ray-slownesses are obtained from the observed apparent slownesses in the up- and downdip directions using a sum or difference at each azimuth. The multiple azimuths generated by a VC geometry permit the ray-slowness distribution of the marine sediments to be determined.

An inversion procedure is developed to provide dip and anisotropy parameters for refractive layers from the measured refraction traveltimes in multilayered azimuthally isotropic and anisotropic media. Two sets of transversely isotropic models are used to analyse the azimuthal variations of apparent and ray slownesses. In the first set, we fix the anisotropic parameters of the models but vary the dip (0°, 5° and 10°) to test the effects of the presence of dip. In the second set, we vary the P-wave anisotropy strength (5.2%, 10.3%, 15.8% and 22.0%) to examine the sensitivity and accuracy of ray-slowness approximations which are independent of dip. We test this inversion procedure on synthetic P-wave VC data calculated for six different models by a finite-difference method. The results of applications to real VC data acquired from the North Sea are also presented.

INTRODUCTION

Sea-bed properties play an important role in marine seismics, particularly for multicomponent sea-bed seismics, because they influence significantly the amplitudes, phases and traveltimes of seismic waves. As a potential exploration technique, vertical-cable (VC) seismic uses vertical arrays of hydrophones deployed in the water column and a conventional airgun array source to acquire 3D marine data (Krail 1991; Havig and Krail 1996). The concept can also provide a novel approach to seismic refraction surveying of sea-bed sediments (Hunter and Pullan 1990). Indeed, refraction traveltimes of sea-bed sediments can be obtained from this acquisition at any azimuth. This full azimuthal coverage of information is essential for the investigation of near-surface anisotropy, which leads to azimuth-dependent velocities and arrival times of refracted waves. In addition, application of anisotropic statics may improve the structural interpretation quality (Milligan 1998).

Two P-wave refraction seismic field studies were undertaken by Leslie and Lawton (1999), in areas of steeply dipping marine shales of the Wapiabi Formation, to determine the anisotropic parameters of these shales *in situ*. In these studies, seismic lines were laid out parallel, perpendicular and at 45° to the local strike directions. The Thomsen (1986) parameters were obtained by measurement of headwave velocities along the seismic lines. A similar, successful study was undertaken by Gendzwill (1993) to investigate the effect of fractures on seismic properties of limestones in Manitoba.

*E-mail: hejiew@zpt.ntnu.no

© 2002 European Association of Geoscientists & Engineers

The technique used here is analogous to the local phase-slowness method in vertical seismic profiles (VSP). In the VSP case, the anisotropic phase-slowness surface local to a receiver array is determined by arrival times measured from a wide-aperture walkaway shot spread (Gaiser 1990; Miller and Spencer 1994; MacBeth 1998; Ohlsen and MacBeth 1998). The technique requires the assumption of a horizontally layered medium, but may be adapted to accommodate small overburden dips (Sayers 1997). In the present case, the ray-slowness distributions along the refractors can be determined using a surface shot spread and it is independent of dip (Wang, Li and MacBeth 1999). The dip and anisotropy parameters of marine sediments are then estimated by an inversion algorithm.

We first analyse the azimuthal variations of apparent and ray slownesses obtained from refracted arrivals, then present an inversion procedure of refraction for transversely isotropic (TI) media. Marine sediment cores routinely show transverse isotropy with a vertical symmetry axis (VTI) which results primarily from bedding, i.e. the interleaving of isotropic layers much thinner than a seismic wavelength (Backus 1962; Bachman 1979, 1983; Carlson, Schaftenaar and Moore 1984). In practice, marine sediments may also possess a component of transverse isotropy with a horizontal symmetry axis (HTI). This is a consequence of forces such as sea-bottom currents acting on the sediments during deposition to create unidirectional flow patterns. Such HTI anisotropy has been observed in the past for the upper few hundred metres of marine sediments by Stoneley-wave analysis (MacBeth 1991). We present the results of inversion from a real VC data set which demonstrate the existence of azimuthal anisotropy in marine sediments as well.

REFRACTED TRAVELTIME ANALYSIS

This section introduces the traveltime equations for the refracted arrivals in a single refractor and multilayered media under VC configuration, then gives the description of the layer-invariant attributes of apparent and ray slownesses.

Refracted traveltime equation in a single refractor

In vertical-cable seismics, the refraction at a single refractor of the marine sediments is illustrated in Fig. 1. For the cable located at O, $SABR$ indicates the refracted path from source S to receiver R. Assuming a dipping anisotropic sea-bed, the aims of this paper are to invert the dip and the anisotropy parameters of the sea-bed from the refracted arrival $SABR$.

For a homogeneous sea-bed, the traveltime $t_{SABR}(\phi)$ along $SABR$ can be expressed as

$$t_{SABR}(\phi) = \frac{SA}{V_0} + \frac{BR}{V_0} + \frac{AB}{V_1(\phi)}, \tag{1}$$

where V_0 is the water velocity, and $V_1(\phi)$ is the P-wave ray velocity of the sea-bed refractor along the source–cable azimuth ϕ (measured from the source–cable direction to the X-axis in the natural coordinate system). Denoting the critical angle by θ and the apparent dip by α along azimuth ϕ, we have

$$\begin{aligned} SA &= \frac{AC}{\cos(\theta-\alpha)} \\ &= \frac{OD - AD\sin\alpha}{\cos(\theta-\alpha)}, \end{aligned} \tag{2}$$

$$BR = \frac{RD\cos\alpha}{\cos\theta}, \tag{3}$$

$$\begin{aligned} AB &= AD - BD \\ &= AD - RD(\sin\alpha + \cos\alpha\tan\theta). \end{aligned} \tag{4}$$

In terms of the source-to-cable offset x, the receiver-to-sea-bed distance h_R (receiver height) and the depth of the sea-bed at the cable location h_O, we can write

$$\begin{aligned} x &= AD\cos\alpha + AC\tan(\theta-\alpha) \\ &= AD\cos\alpha + (h_O - AD\sin\alpha), \end{aligned} \tag{5}$$

and hence,

$$AD = \frac{x\cos(\theta-\alpha) - h_O\sin(\theta-\alpha)}{\cos\theta}, \tag{6}$$

$$SA = \frac{h_O}{\cos(\theta-\alpha)} - \frac{x\sin\alpha - h_O\tan(\theta-\alpha)\sin\alpha}{\cos\theta}, \tag{7}$$

$$BR = \frac{h_R\cos\alpha}{\cos\theta}, \tag{8}$$

$$AB = \frac{x\cos(\theta-\alpha) - h_O\sin(\theta-\alpha) - h_R\sin(\theta+\alpha)}{\cos\theta}. \tag{9}$$

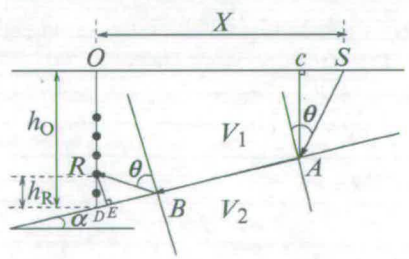


Figure 1 The refraction at the sea-bed in VC seismics. O, S and R indicate the locations of a cable, source and receiver, respectively. The ray $SABR$ shows one refraction path from source S to receiver R. α is the apparent dip of the sea-bed in the source–cable direction.

Substituting (7), (8) and (9) in (1), the traveltime $t_{SABR}(\phi)$ can be written as

$$t_{SABR}(\phi) = \left[\frac{\cos\alpha + \tan\theta\sin\alpha}{V_1(\phi)} - \frac{\sin\alpha}{V_0\cos\theta}\right]x + \left[\frac{\cos\alpha}{V_0} - \frac{\sin(\theta+\alpha)}{V_1(\phi)}\right]\frac{h_R}{\cos\theta} + \frac{h_O(\cos\theta + \sin(\theta-\alpha)\sin\alpha)}{V_0\cos\theta\cos(\theta-\alpha)} - \frac{h_O\sin(\theta-\alpha)}{V_1(\phi)\cos\theta}. \quad (10)$$

Assuming the real dip and dip azimuth of the sea-bed are β and φ_d, respectively, we have the following relationship between α and β:

$$\tan\alpha = \tan\beta\cos(\phi - \varphi_d). \quad (11)$$

Therefore, for a fixed source–cable azimuth ϕ, the traveltime $t_{SABR}(\phi)$ based on (10) is a linear function relating to the offset x as well as the receiver height h_R.

Refracted traveltime equation in multilayered media

In marine sediments, we also consider n-layered azimuthally anisotropic or isotropic media whose symmetry is parallel or perpendicular to the layer interface. Each layer has the same dip and dip azimuth. A ray geometry for refraction in VC seismic is shown in Fig. 2. In terms of source–cable offset x, receiver height h_R, sea-bed depth h_O and vertical layer thickness z_k $(k = 1, 2, \cdots, n-1)$ at the cable location, the traveltime of a wave refracted from layer n from source S to receiver R, at measured azimuth ϕ, can be written as (see Appendix A)

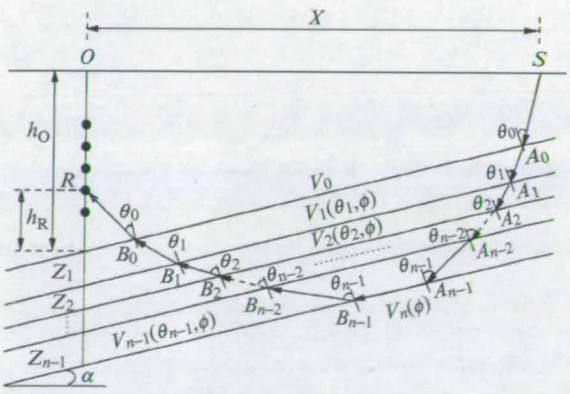


Figure 2 Ray geometry for refractions in layered marine sediments in VC seismics.

$$t_n(\phi) = \left[\frac{\cos\alpha + \tan\theta_0\sin\alpha}{V_n(\phi)} - \frac{\sin\alpha}{V_0\cos\theta_0}\right]x + \left[\frac{\cos\alpha}{V_0} - \frac{\sin(\theta_0+\alpha)}{V_n(\phi)}\right]\frac{h_R}{\cos\theta_0} + \left[\frac{\cos\theta_0 + \sin(\theta_0-\alpha)\sin\alpha}{V_0\cos(\theta_0-\alpha)} - \frac{\sin(\theta_0-\alpha)}{V_n(\phi)}\right]\frac{h_O}{\cos\theta_0} + 2\cos\alpha\sum_{k=1}^{n-1}\frac{z_k}{\cos\theta_k V_k(\theta_k,\phi)} - \frac{2\cos\alpha}{V_n(\phi)}\sum_{k=1}^{n-1} z_k\tan\theta_k, \quad (12)$$

where $V_k(\theta_k, \phi)$ are P-wave ray velocities at given raypaths (θ_k, ϕ), θ_k $(k = 1, 2, \cdots, n-1)$ are angles of incidence, and V_0 and $V_n(\phi)$ are P-wave ray velocities in the water and at the interface of layer n, respectively. Assuming $n = 1$ in (12), we can obtain the same formula as (10) for the refracted traveltime in a single refractor.

Layer-invariant attributes

In order to obtain the dip and anisotropy of marine sediments, the azimuthal variations of apparent slownesses are estimated first. We can then obtain the horizontal and vertical ray-slownesses along the interface based on the relevant apparent slownesses. We find these attributes are all layer invariant.

Horizontal apparent and ray slownesses

Following (12), the gradient of traveltime along the source–cable offset direction for a given receiver can be expressed as

$$S_{nx}(\phi) = \frac{\partial t_n(\phi)}{\partial x} = \frac{\cos\alpha + \tan\theta_0\sin\alpha}{V_n(\phi)} - \frac{\sin\alpha}{V_0\cos\theta_0}, \quad (13)$$

where $S_{nx}(\phi)$ is the horizontal apparent slowness from refracted arrivals at the azimuth ϕ for layer n, and it is independent of the overburden velocities. Assuming the subsurface consists of horizontal layers, it is used as horizontal slowness in the phase-slowness method for anisotropic inversion (Gaiser 1990; Miller and Spencer 1994; Sayers 1997), and can be obtained from the traveltime differences of direct waves between adjacent sources for a given receiver in walk-away VSPs. Setting $\alpha = 0$ in (13),

$$S_{nx}(\phi) = \frac{1}{V_n(\phi)}. \quad (14)$$

This simple case applies only for horizontal-layered media, where the horizontal apparent slowness equals the ray slowness of a seismic wave propagating along the refractor. In

other situations, the horizontal apparent slowness $S_{nx}(\phi)$ is not only a function of the velocities $V_n(\phi)$, but also a function of the apparent dip angle α. To correct for the effects of dip, we define a new function $S_{nh}(\phi)$ as

$$S_{nh}(\phi) = \frac{1}{2}(S_{nx}(\phi) + S_{nx}(\phi + \pi)). \tag{15}$$

Assuming the apparent dip is α at the azimuth ϕ, it will be $-\alpha$ at the azimuth $\phi + \pi$ (equation (11)). Thus, substituting (13) in (15) gives

$$S_{nh}(\phi) = \frac{\cos\alpha}{V_n(\phi)}. \tag{16}$$

Equation (16) indicates that $S_{nh}(\phi)$ is the horizontal component of the ray slowness along the interface of layer n at azimuth ϕ, which results from the sum of horizontal apparent slownesses in up- and downdip directions for a given azimuth and source–cable offset.

To discuss the azimuthal variation of $S_{nh}(\phi)$, we give its expression in terms of the azimuth ϕ by linearizing (11) and keeping only the first-order approximation of $S_{nh}(\phi)$ for the small quantity $\tan^2\beta$. This leads to

$$S_{nh}(\phi) = \frac{1}{V_n(\phi)}\left[1 - \frac{1}{4}\tan^2\beta\,(1 + \cos 2(\phi - \varphi_d))\right]. \tag{17}$$

Thus, the horizontal ray-slowness shows $\cos 2\phi$ variations with azimuth ϕ due to the presence of dip, regardless of whether the marine sediments are azimuthally isotropic or not.

Vertical apparent and ray slownesses

For a given source, we can also estimate the gradient of the refracted traveltime along the vertical array. Following (12), its expression can be written as

$$\begin{aligned} S_{nz}(\phi) &= \frac{\partial t_n(\phi)}{\partial h_R} \\ &= \frac{\cos\alpha}{V_0\cos\theta_0} - \frac{\sin\alpha + \tan\theta_0\cos\alpha}{V_n(\phi)}, \end{aligned} \tag{18}$$

where $S_{nz}(\phi)$ is the vertical apparent slowness at the azimuth ϕ for layer n, and it is also independent of the overburden velocities. We can estimate $S_{nz}(\phi)$ from the differences of refracted traveltimes between adjacent receivers for a given source in vertical arrays. Equation (18) also shows that the azimuthal variation of $S_{nz}(\phi)$ depends on the apparent dip angle α. For the simplest situation, $\alpha = 0$,

$$S_{nz}(\phi) = \frac{\sqrt{V_n^2(\phi) - V_0^2}}{V_n(\phi)V_0}. \tag{19}$$

Similarly to the estimation of the horizontal ray-slowness, the vertical ray-slowness of the refractor can also be estimated from the differences in vertical apparent slownesses between the up- and downdip source directions at a given azimuth. It can be defined as

$$S_{nv}(\phi) = \frac{1}{2}(S_{nz}(\phi + \pi) - S_{nz}(\phi)). \tag{20}$$

Following (11) and (18), (20) gives

$$S_{nv}(\phi) = \frac{\sin\alpha}{V_n(\phi)}. \tag{21}$$

Based on (11), for the small dip β, $S_{nv}(\phi)$ can be approximated as

$$S_{nv}(\phi) \approx \frac{\tan\beta}{V_n(\phi)}\cos(\phi - \varphi_d). \tag{22}$$

Thus, the vertical ray-slowness exhibits cosine variations with azimuth ϕ due to the presence of dip without considering azimuthal anisotropy.

Determination of dip and ray slowness

Since there is full azimuthal coverage of sources in VC seismic, the horizontal and vertical apparent slownesses can be estimated in each direction. By integrating the horizontal and vertical apparent slownesses, we can obtain the ray-slowness distribution $S_n(\phi)$ along the refractor without the effects of dip. Following (16) and (21), we have

$$\begin{aligned} S_n(\phi) &= \frac{1}{V_n(\phi)} \\ &= \sqrt{S_{nh}^2(\phi) + S_{nv}^2(\phi)}, \end{aligned} \tag{23}$$

and the tangent of the apparent dip α can be given as

$$\tan\alpha = \frac{S_{nv}(\phi)}{S_{nh}(\phi)}. \tag{24}$$

Furthermore, a least-squares (LSQ) procedure is used for inversion of the real dip and dip azimuth. From (11), we realize that the azimuthal variation of $\tan\alpha$ can be described by a cosine function as

$$f(A, \phi, \varphi) = A\cos(\phi - \varphi), \tag{25}$$

where $A = \tan\beta$ and $\varphi = \varphi_d$. In principle, it should be possible to estimate the two unknown variables (A and φ) from two given points. To reduce observation errors, a unique solution can be obtained from best-fitting the function (25) to all measured data points by an LSQ procedure. Hence, the

real dip β and dip azimuth φ_d can be determined from the estimation of A and φ.

SLOWNESS-BASED INVERSION FOR TI MEDIA

Here, we present a slowness-based inversion procedure to estimate marine sediment anisotropy using multi-azimuth VCS data. For simplicity, but without loss of the generality of the inversion, we consider marine sediments to be transversely isotropic (TI) media with a symmetry axis parallel to the layer interface.

TI media and parameters

For this type of medium, we need to specify the five elastic constants $C_{11}, C_{33}, C_{13}, C_{44}, C_{66}$ and the orientation of the axis of symmetry. We introduce Thomsen's (1986) notation,

$$v_{P0} = \sqrt{C_{33}/\rho}, \tag{26}$$

$$v_{S0} = \sqrt{C_{44}/\rho}, \tag{27}$$

$$\varepsilon = \frac{C_{11} - C_{33}}{2C_{33}}, \tag{28}$$

$$\gamma = \frac{C_{66} - C_{44}}{2C_{44}}, \tag{29}$$

$$\delta = \frac{(C_{13} + C_{44})^2 - (C_{33} - C_{44})^2}{2C_{33}(C_{33} - C_{44})}, \tag{30}$$

where ρ is the density.

Assuming a weak TI medium with a horizontal symmetry axis (HTI medium), the horizontal ray velocity has the following expression (Sena 1991; Li 1997):

$$\begin{aligned} V^2(\phi) &= v_{P0}^2[1 + 2\delta \sin^2(\phi - \varphi_a)\cos^2(\phi - \varphi_a) \\ &\quad + 2\varepsilon \sin^4(\phi - \varphi_a)] \\ &= A_0 + B_0 \cos 2(\phi - \varphi_a) + C_0 \cos 4(\phi - \varphi_a), \end{aligned} \tag{31}$$

where

$$\begin{aligned} A_0 &= v_{P0}^2\left[1 + \frac{1}{4}(\delta + 3\varepsilon)\right], \\ B_0 &= -v_{P0}^2\varepsilon, \\ C_0 &= -\frac{1}{4}v_{P0}^2(\delta - \varepsilon), \end{aligned} \tag{32}$$

and φ_a is the azimuth of the symmetry axis with respect to the X-axis in the natural coordinate system. This is a three-term approximation with the same form as the phase velocity (Crampin 1981). More details of ray-velocity variation in TI media are given in Appendix B.

Under the weak anisotropy approximation, further linearity of (31) yields the ray slowness, given by

$$\begin{aligned} \frac{1}{V(\phi)} \approx \frac{1}{v_{P0}}\Big[1 - \frac{1}{8}(\delta + 3\varepsilon) + \frac{1}{2}\varepsilon \cos 2(\phi - \varphi_a) \\ + \frac{1}{8}(\delta - \varepsilon)\cos 4(\phi - \varphi_a)\Big]. \end{aligned} \tag{33}$$

The first two terms in (31) and (33) are called elliptical approximations. These are accurate for nearly elliptically anisotropic media.

Azimuthal variations of horizontal and vertical ray-slownesses

In (17) and (22), we described the azimuthal variations of horizontal and vertical ray-slownesses due to the presence of dip along the dipping interface, assuming marine sediments are TI media with a symmetry axis parallel to the dipping interfaces. In this case, the ray velocities along the interface are equivalent to the horizontal ray-velocities in an HTI medium. Substituting (33) in (17) and keeping only the first two terms, the approximation of $S_{nh}(\phi)$ is given by

$$S_{nh}(\phi) \approx \frac{1}{v_{P0}}[a + b\cos 2(\phi - \varphi_a) + c\cos 2(\phi - \varphi_d)], \tag{34}$$

where

$$a = 1 - \frac{1}{8}(3\varepsilon + \delta) - \frac{1}{4}\tan^2\beta + \frac{1}{32}(3\varepsilon + \delta)\tan^2\beta, \tag{35}$$

$$b = \frac{1}{2}(1 - \frac{1}{4}\tan^2\beta)\varepsilon, \tag{36}$$

$$c = -\frac{1}{4}\left[1 - \frac{1}{32}(3\varepsilon + \delta)\right]\tan^2\beta. \tag{37}$$

Equation (34) can also be written as

$$S_{nh}(\phi) = \frac{1}{v_{P0}}\left[a + \frac{1}{\sqrt{b^2 + c^2 + 2bc\cos(\varphi_a - \varphi_d)}}\cos 2(\phi - \gamma)\right], \tag{38}$$

where

$$\tan\gamma = \frac{b\sin 2\varphi_a + c\sin 2\varphi_d}{b\cos 2\varphi_a + c\cos 2\varphi_d}. \tag{39}$$

Equation (38) describes the elliptical approximation of azimuthal variations of the horizontal slowness in weak TI media along a dipping refractor, but the effects of dip and anisotropy are, in fact, coupled together. Therefore, it would be difficult to implement the inversion from just the

azimuthal distribution of the horizontal ray-slowness or apparent slowness. However, for small dips, $c \ll b$, which suggests that the effects of anisotropy on the azimuthal variation of $S_{nh}(\phi)$ are much more significant than the effects of dip. In the section on synthetic data analysis, we discuss the effects of dip in detail using numerical solutions.

Based on (22) and (33), the vertical ray-slowness $S_{nv}(\phi)$ can also be approximated as

$$S_{nv}(\phi) \approx d\cos(\phi - \varphi_d), \tag{40}$$

where

$$d = \frac{1}{v_{P0}}\left[1 - \frac{1}{8}(3\varepsilon + \delta)\right]\tan\beta. \tag{41}$$

Although the approximation (40) is obtained under the assumption of small dip, the azimuthal variation of $S_{nv}(\phi)$ still depends only on the dip azimuth rather than the azimuth of the symmetry axis.

Inversion procedure

For a weak TI medium, we have introduced approximation expressions for the square-ray-velocity in (31) and the ray slowness in (33). After estimation of the ray slowness $S_n(\phi)$, a two-step LSQ procedure is used to implement anisotropy parameter inversion. Firstly, we apply the elliptical approximation of ray slowness $S_n(\phi)$, described by

$$f(A, \phi, \varphi, y_0) = A\cos 2(\phi - \varphi) + y_0, \tag{42}$$

where

$$\begin{aligned} A &= \frac{\varepsilon}{2\alpha_0}, \\ \varphi &= \varphi_a, \\ y_0 &= \frac{8 - (\delta + 3\varepsilon)}{8\alpha_0}, \end{aligned} \tag{43}$$

to fit azimuthal variations of $S_n(\phi)$, the result providing a steady solution for the direction of the symmetry axis φ_a.

Then a three-term fit to the square-ray-velocities is used to estimate the parameters A_0, B_0, C_0 in (31), and Thomsen's parameters for P-waves are obtained as

$$v_{P0} = \sqrt{A_0 + B_0 + C_0}, \tag{44}$$

$$\varepsilon = -\frac{B_0}{A_0 + B_0 + C_0}, \tag{45}$$

$$\delta = \frac{4C_0 + B_0}{A_0 + B_0 + C_0}. \tag{46}$$

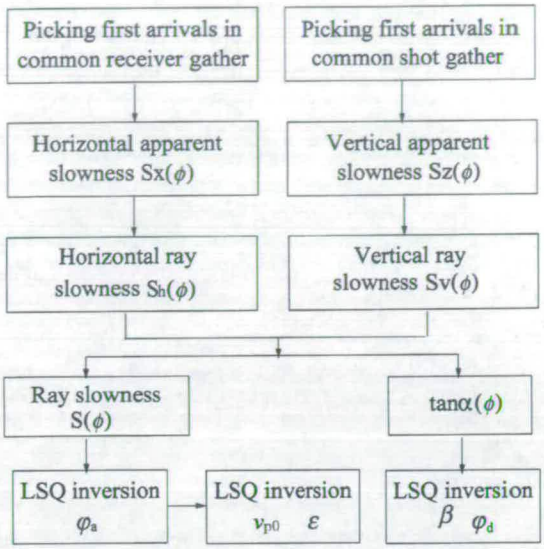


Figure 3 Processing sequence for inverting dip and anisotropic parameters of marine sediments using the refractions in VC seismics.

Figure 3 summarizes the processing sequence for inverting dip and anisotropic parameters of marine sediments from refracted arrivals in VC seismic.

Inversion feasibility

To examine the feasibility of inversion, we chose the set of models shown in Table 1 for traveltime analysis. The anisotropy parameters are taken from anisotropic shale (Thomsen 1986); we modify only the parameter ε corresponding to the anisotropy strength of P-waves among these models. Figure 4 shows the azimuthal variations of exact ray-slownesses (Appendix B), its three-term approximation (equation (31)) and an elliptical fit (equation (42)). As can be seen, the three-term approximation is very accurate for anisotropy strengths up to 22%, and is much better than the elliptical fit, especially at or near the directions parallel and perpendicular to the symmetry axis. However, we can estimate accurately the direction of the symmetry axis φ_a from the elliptical fit. The results of estimation from the first step in an LSQ procedure are shown in Table 2.

Figure 5 shows azimuthal variations of the exact square-ray-velocities in the horizontal plane for HTI media and best-fits based on the three-term approximation for all the models shown in Table 1. We find that the three-term approximation provides an excellent fit to the exact square-ray-velocities. The results of estimation for anisotropy parameters are

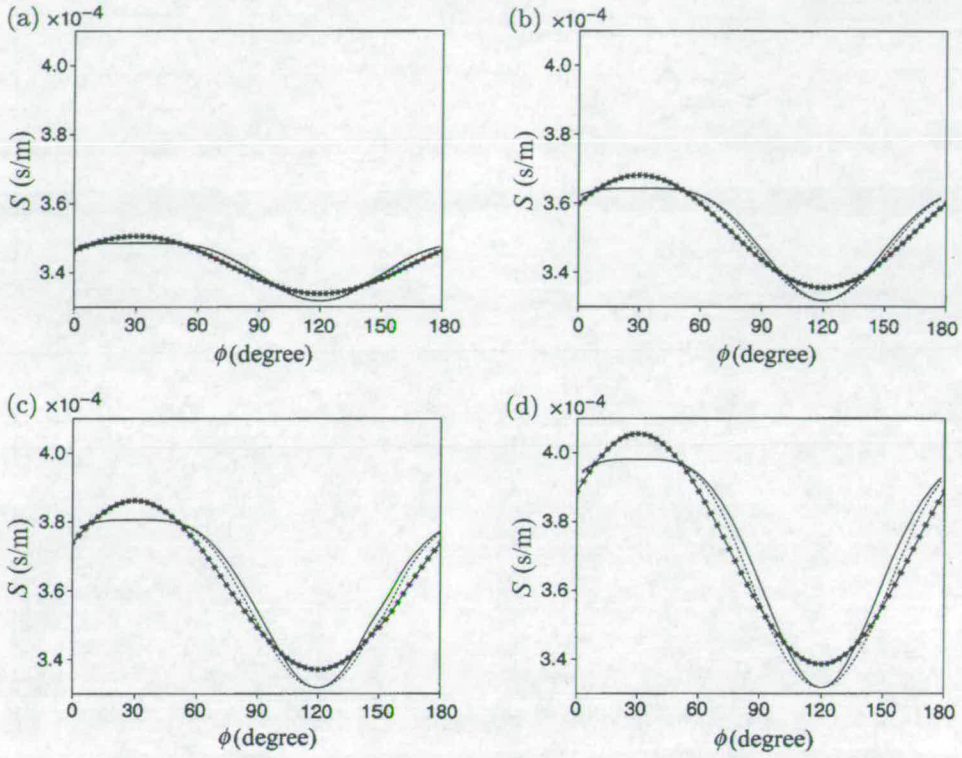


Figure 4 Ray slowness versus azimuth for (a) model 1, (b) model 2, (c) model 3 and (d) model 4. The solid line shows exact values, the dashed line shows the three-term approximation and the marked line shows the elliptical fit.

Table 1 Model parameters in anisotropic media

No.	v_{P0} (m/s)	v_{S0} (m/s)	ε	γ	δ	φ_a
1	2869	1508	0.052	0.345	−0.001	30°
2	2745	1508	0.103	0.345	−0.001	30°
3	2627	1508	0.158	0.345	−0.001	30°
4	2512	1508	0.220	0.345	−0.001	30°

Table 2 Results of estimation by using the elliptical fit

Model	A	y_0	φ_a
1	8.3889E-06	3.4219E-04	30.0
2	1.6316E-05	3.5181E-04	30.0
3	2.4567E-05	3.616E-04	30.0
4	3.3532E-05	3.7204E-04	30.0

shown in Table 3. The comparison of estimated and original values for these parameters shows that parameter δ cannot be estimated correctly by this procedure, because it is relevant not only to P-waves but also to S-waves. The relative errors for inverted parameters v_{P0} and ε shown in Table 4 are less than 0.4% and 6.0%, respectively, when the anisotropy strength for P-waves is up to 22%. This confirms that it is feasible to invert anisotropy parameters using the procedure shown in Fig. 3.

SYNTHETIC DATA ANALYSIS

To evaluate the methodology further, we analyse the effects of dip and anisotropy on different models. The accuracy and feasibility of the parameter inversion are further tested by synthetic full-waveform VCS data.

Effects of dip

To illustrate the effects of dip, three models with dips of $0°, 5°$ and $10°$ are examined, assuming that the water velocity $V_0 = 1475$ m/s, the dip azimuth $\varphi_d = 30°$, and the marine sediments are TI media, with parameters $v_{P0} = 2000$ m/s, $\delta = 0.09, \varepsilon = 0.11, \varphi_a = 60°$, whose symmetry axis is parallel to the sea-bed surface. The azimuthal variations in horizontal

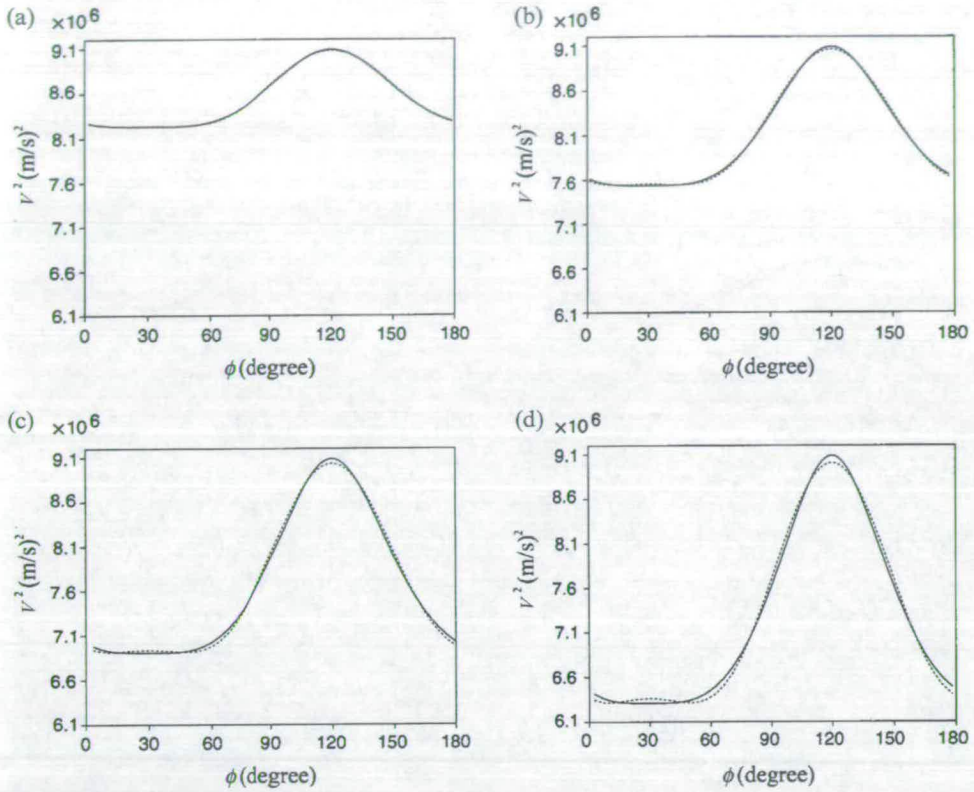


Figure 5 Azimuthal variations of the exact square-ray-velocities (solid line) and the three-term fits (dashed line) for (a) model 1, (b) model 2, (c) model 3 and (d) model 4.

Table 3 Results of estimation for anisotropy parameters by the three-term fit

Model	v_{P0} (m/s)	ε	δ
1	8869	0.051	−0.005
2	2747	0.100	−0.016
3	2633	0.152	−0.035
4	2522	0.208	−0.063

Table 4 Relative errors (%) for inverted anisotropy parameters v_{P0} and ε

Model	v_{P0}	ε
1	0	1.9
2	0.07	2.9
3	0.19	3.8
4	0.39	5.5

and vertical apparent slownesses and horizontal and vertical ray-slownesses are shown in Fig. 6. It can be seen that the dip has a significant effect on both apparent slownesses and the vertical ray-slowness. The shapes of the apparent-slowness curves change greatly for dips up to 5°. Thus, we cannot ignore these changes, induced by the presence of dip in the apparent slowness if the sea-bed is not horizontal. However, the azimuthal variation of horizontal ray-slowness depends mainly on anisotropy rather than dip.

Numerical modelling

P-wave synthetic vertical-cable seismic data modelling is performed on six sets of models, which include single and two dipping refractors (Fig. 7). The geometry parameters are given in Table 5, where h_{R1} is the height of the first receiver, and dh_R is the receiver interval in the vertical direction. For each source, 16 receivers are deployed vertically on the cable. The model parameters are shown in Table 6. The first layer in all models is water, and the second and third layers are

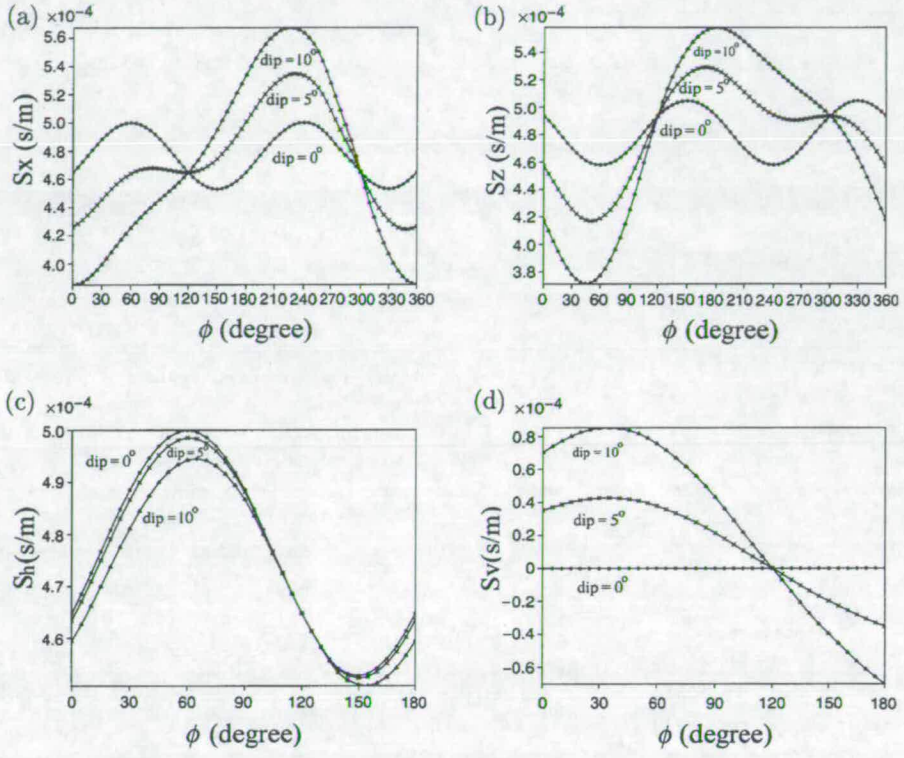


Figure 6 Plots of (a) horizontal apparent slowness, (b) vertical apparent slowness, (c) horizontal ray-slowness and (d) vertical ray-slowness versus azimuth ϕ for dips of 0°, 5° and 10°, respectively.

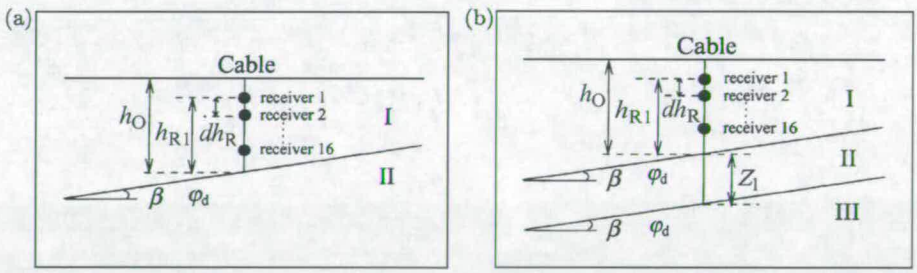


Figure 7 Geological models and geometry for synthetic VC seismics. (a) Single refractor; (b) two refractors.

Table 5 Geometry parameters in synthetic VC seismics

h_O	h_{R1}	dh_R	z_1	β	φ_d
200 m	64 m	8 m	120 m	10°	30°

isotropic or azimuthally anisotropic media, whose symmetry axis is parallel to the layer interface. The anisotropy parameters for these models are taken from Thomsen (1986) and are listed in Table 7.

The synthetic VCS profiles are calculated using a finite-difference method to model the elastic wave propagation in TI media (Wang and Dong 1993, 1994). Three typical shot gathers for each model are shown in Figs 8–10. These VCS gathers are obtained from three typical azimuthal directions which include (a) updip ($\phi = \varphi_d$), (b) strike of the layer ($\phi = \varphi_d + 90°$) and (c) downdip ($\phi = \varphi_d + 180°$) directions.

The first arrivals in Fig. 8 are refracted waves from the first refractor (the interface between water and the second layer) for models A and B (see Table 6), in which the source–cable

Table 6 The model structures and velocities (m/s)

Model	Layer 1	Layer 2	Layer 3
A	Water $V_0 = 1475$	Isotropic layer $V_P = 3014$, $V_S = 1960$	
B	Water $V_0 = 1475$	Anisotropic shale $\varphi_a = 45°$	
C	Water $V_0 = 1475$	Isotropic layer $V_P = 3014$, $V_S = 1960$	Isotropic layer $V_0 = 3720$, $V_S = 2248$
D	Water $V_0 = 1475$	Isotropic layer $V_P = 3014$, $V_S = 1960$	Taylor sandstone $\varphi_a = 60°$
E	Water $V_0 = 1475$	Anisotropic shale $\varphi_a = 45°$	Isotropic layer $V_P = 3720, V_S = 2248$
F	Water $V_0 = 1475$	Anisotropic shale $\varphi_a = 45°$	Taylor sandstone $\varphi_a = 60°$

offsets are 800 m. For the other models, the offsets are 1000 m and the first arrivals are from the second refractor (interface between the second and third layers).

Azimuthal variations

Firstly, we obtain refracted traveltimes for each model at every 5° by picking first arrivals. For each azimuth, five

Table 7 The atmospheric parameters for shale and Taylor sandstone

Representative material	v_{P0} (m/s)	v_{S0} (m/s)	ε	δ	γ
Anisotropic shale	2745	1508	0.103	−0.001	0.345
Taylor sandstone	3368	1829	0.110	−0.035	0.255

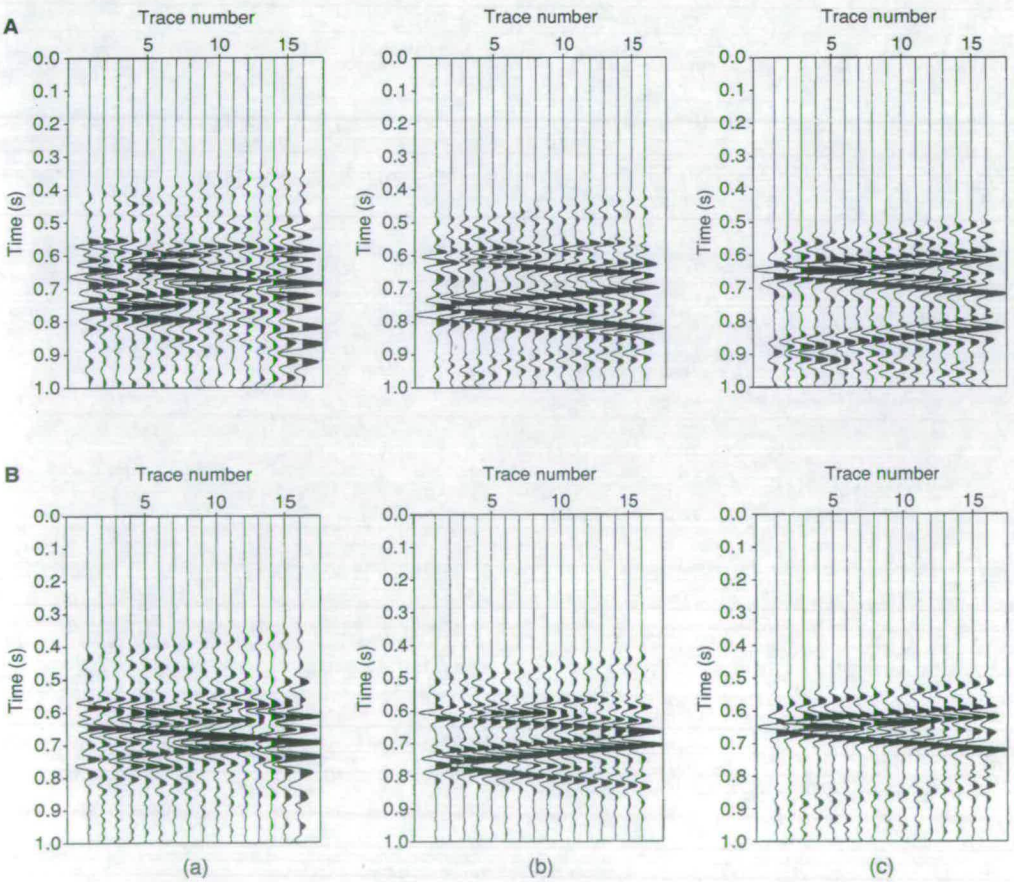


Figure 8 Rows: Synthetic VC shot gathers for models A and B. Columns: (a) at updip ($\phi = \varphi_d$), (b) at strike of the layer ($\phi = \varphi_d + 90°$) and (c) at downdip ($\phi = \varphi_d + 180°$) directions. The source–cable offset is 800 m.

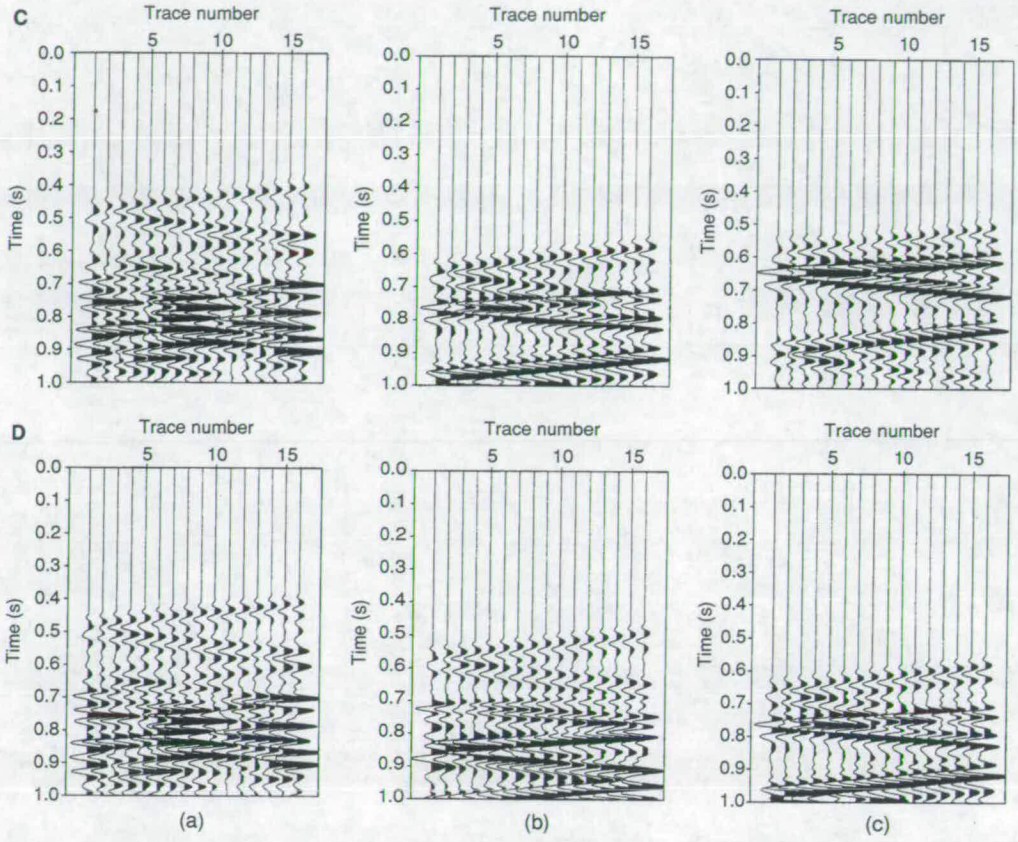


Figure 9 As Fig. 8, for models C and D. The source–cable offset is 1000 m.

shot gathers are calculated with 20 m source intervals. The middle offset is 800 m in models A and B, and 1000 m is used in the other models. To compare the difference between anisotropy and isotropy, we separate the six models into three groups with the same overburden refractor in each group: group 1 consists of models A and B, group 2 consists of models C and D and group 3 consists of models E and F. Figure 11 shows the azimuthal variations in refraction traveltimes for receiver No. 8. The trend of azimuthal variations among the three groups is very similar. This indicates that these changes are mainly due to the presence of dip, and the azimuthal variations caused by anisotropy are small.

Secondly, the horizontal apparent slowness is estimated by a local linear regression of the refracted traveltimes for a common-receiver gather as a function of offset along each direction, and is shown in Figs 12(a), 13(a) and 14(a). The vertical apparent slowness is estimated by a linear regression of the refracted traveltimes along the vertical array, for a common-source offset as a function of receiver height, and is shown in Figs 12(b), 13(b) and 14(b). Similarly, the variations in apparent slownesses are controlled mainly by dip rather than anisotropy although there is over 10% P-wave velocity anisotropy in each refractor.

Thirdly, the horizontal ray-slowness is computed using (15), and is shown in Figs 12(c), 13(c) and 14(c) with an elliptical fit (equation (42)) for the anisotropy case in each figure. In these figures, the azimuthal variations in the horizontal slownesses for isotropic refractors are very small, while those for anisotropic refractors are very significant, and there are clear differences between anisotropic and isotropic refractors. The results of fitting show that the directions of the elliptical symmetry axes for anisotropic refractors are 47.4°, 63.5° and 63.4°, which are very near the directions of the anisotropy symmetry axes, i.e. 45° for the first refractor and 60° for the second refractor. We also show the azimuthal variations in vertical slowness estimated from (20) and the best-fits of the cosine function (25) in Figs 12(d), 13(d) and 14(d). We can see that the

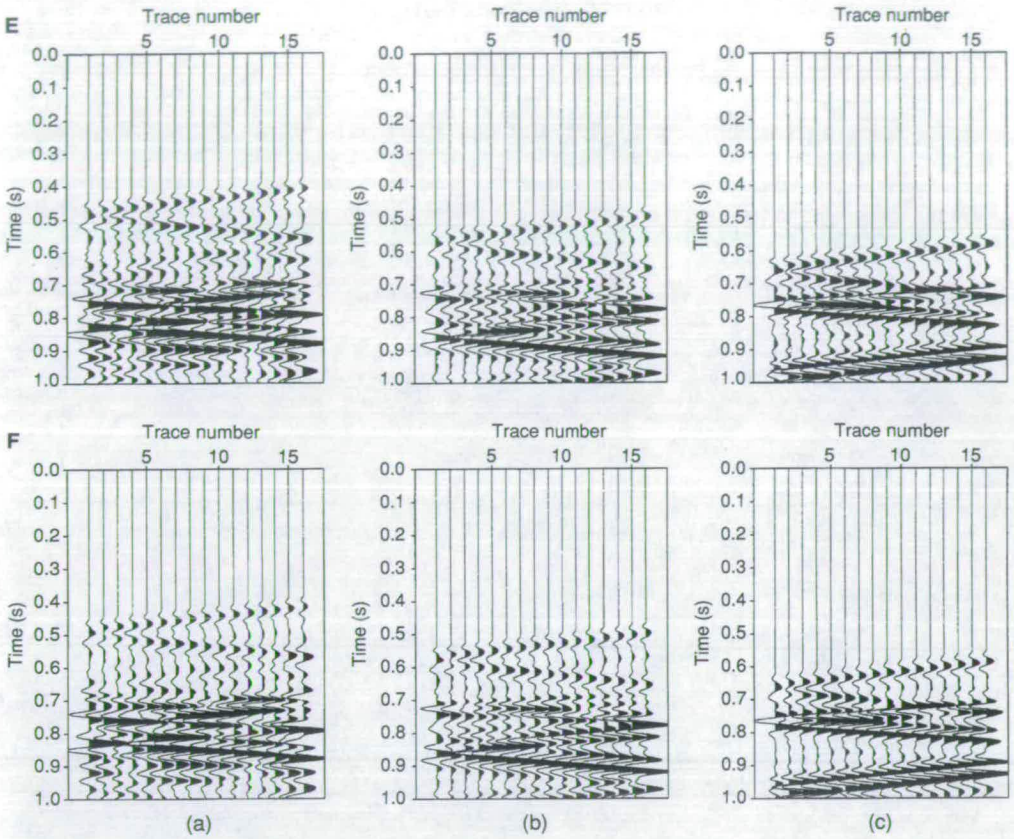


Figure 10 As Fig. 8, for models E and F. The source–cable offset is 1000 m.

best-fitting curves agree well with exact values for all models. The initial guesses φ of the cosine functions (25) are 30.6°, 31.2° and 31.2°, which are very near the azimuth of real dip $\varphi_d = 30°$. There are only small differences between anisotropic and isotropic refractors for the vertical ray-slowness. Therefore, the variations in horizontal ray-slowness are mainly due to anisotropy; on the other hand, those in vertical ray-slowness are controlled by the presence of dip, and these also agree well with the previous numerical analysis. In addition, Fig. 13 is almost the same as Fig. 14, and implies that the above analysis also holds for multi-layered media.

Finally, Fig. 15 shows the ray-slowness distributions for refractors after correcting for the effects of dip and the variations in $\tan\alpha$ for all models. The best elliptical fits to slowness curves and cosine fits to $\tan\alpha$ curves are also displayed. We find that three $\tan\alpha$ curves overlap for each group, and there are no variations in slowness for isotropic refractors. The real dip and its direction can be estimated accurately as 30.0° and 10.0°, respectively.

Table 8 Results of estimation by an elliptical fit to the calculated slowness for each anisotropic model

Model	A	y_0	φ_a
B	1.6565E-05	3.5176E-04	44.67°
D	1.4194E-05	2.8480E-04	59.95°
F	1.4188E-05	2.8479E-04	59.94°

Results of estimation for anisotropy

Table 8 shows the results of estimation by an elliptical (two-term) fit to the calculated slowness shown in Fig. 15 for each anisotropic model. Compared with the exact values given in Table 6, we find that the symmetry axis azimuth φ_a can be accurately estimated by this elliptical fit.

The anisotropic parameters v_{P0} and ε are obtained by the three-term fit to the calculated square-ray-velocity shown in Fig. 16. The inversion results for all anisotropic models are shown in Table 9, which also includes the relative errors for

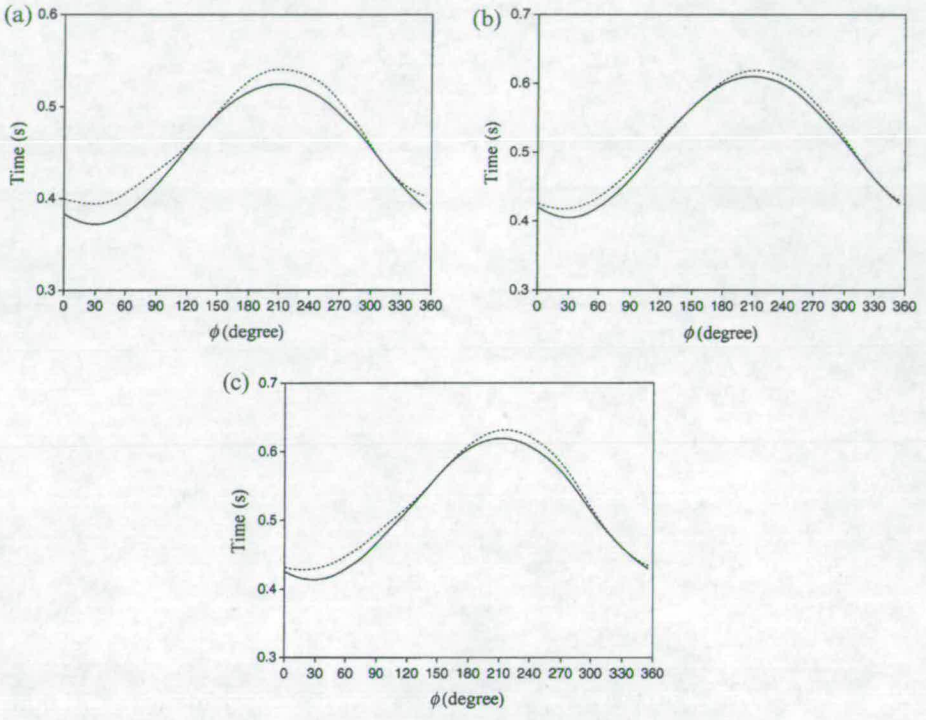


Figure 11 Azimuthal variations of refraction traveltimes for a given receiver (No. 8) for (a) models A (solid line) and B (dashed line), (b) models C (solid line) and D (dashed line) and (c) models E (solid line) and F (dashed line).

Table 9 Inversion results and relative errors (E_{vP0} and E_ε) for anisotropy parameters obtained with the three-term fit to the calculated square-ray-velocities for each anisotropic model

Model	Representative material	v_{P0} (m/s)	ε	E_{vP0} (%)	E_ε (%)
B	Anisotropic shale	2748	0.100	0.11	2.9
D	Taylor sandstone	3372	0.106	0.12	3.6
F	Taylor sandstone	3372	0.106	0.12	3.6

the estimated values compared with the exact values given in Table 7. We can see that the relative errors for v_{P0} and ε are less than 0.2% and 4%, respectively. The overburden has no effect on the anisotropy estimation of the refractor.

These results have shown the feasibility of inversion for anisotropy and dip parameters in multilayered azimuthally anisotropic media in the presence of dip from VCS refractions.

FIELD DATA EXAMPLE

We apply the inversion procedure to field VC data obtained from the North Sea. The data are acquired by 12 cables, each of which has 16 hydrophones distributed vertically at 25 ft intervals. There is almost full azimuthal source coverage and also offsets ranging from 0 to 4000 m. Figure 17 shows an example of first-arrival picking on common-source gathers and a common-receiver (channel 5) gather from a selected 2D source line. The depth of the sea-floor at the cable location is about 136 m. We can see that the first arrivals are refracted waves (upgoing waves) not direct waves (downgoing waves). The picked traveltimes for the common-receiver (channel 5) at offsets ranging from 800 m to 2000 m are shown in Fig. 18.

Figure 19 illustrates the azimuthal variations in horizontal apparent slowness, vertical apparent slowness and horizontal and vertical ray-slownesses for the sea-floor. There are 348 azimuths ranging from 0° to 360° to be measured for apparent-slowness estimation. At each azimuth, five adjacent sources are used to estimate the horizontal apparent slowness for the same receiver. The middle offset is 1200 m.

Figure 20 shows the ray slowness and square-ray-velocity versus azimuth for the sea-floor. We also show a best elliptical fit to the calculated slowness and a fit of the three-term approximation to the calculated square-ray-velocity. The azimuthal variations in tan α are illustrated in Fig. 21. To estimate the dip of the sea-floor, a best-fit of

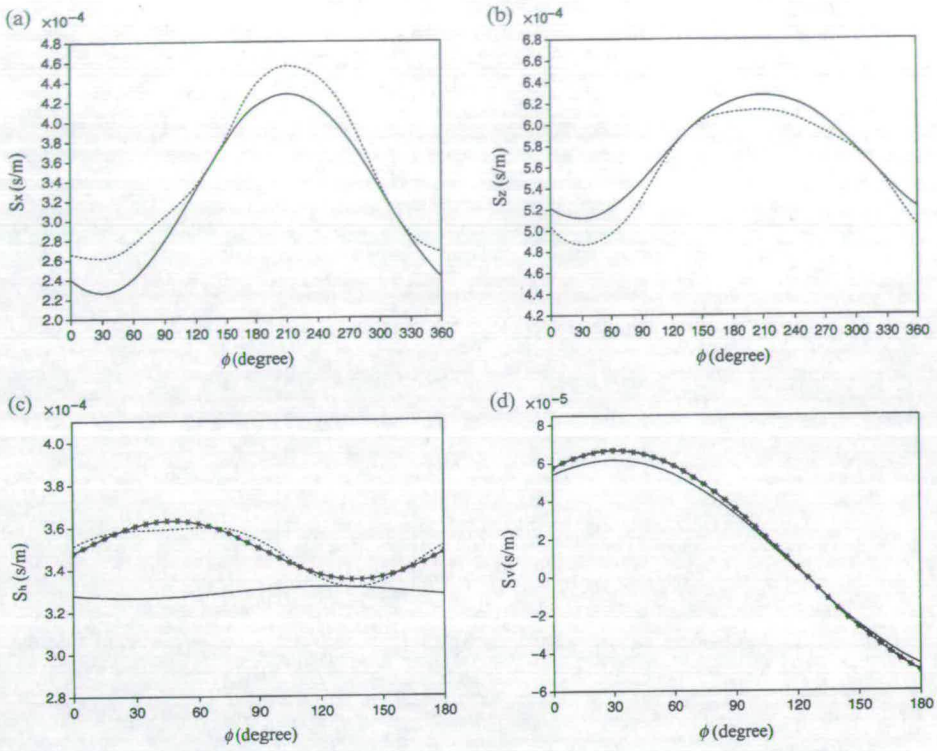


Figure 12 Plots of (a) horizontal apparent slowness, (b) vertical apparent slowness, (c) horizontal ray-slowness and (d) vertical ray-slowness versus azimuth ϕ for model A (solid line) and model B (dashed line). Also shown are a best-fit (marked line) of the elliptical approximation to the variations in horizontal ray-slowness on model B in (c), and a best-fit (marked line) of the cosine function to variations in vertical ray-slowness on model B in (d).

Table 10 Inversion results for dip and anisotropic parameters from the field VC data

φ_d	β	φ_a	v_{P0}	ε
23.0°	1.0°	134°	1850 m/s	0.047

the cosine function to the calculated data is also shown in Fig. 21.

Assuming marine sediments are TI media with a symmetry axis parallel to the layer interface, the inversion results for dip and anisotropic parameters from this real VC data set are as given in Table 10. We can see that the real dip β is about 1° for the sea-floor and the dip azimuth is 23.0° with respect to the X-axis in the natural coordinate system, and there is about 5% P-wave azimuthal anisotropy in this area. The accuracy of inversion for a real data set is affected not only by the approximation used but also by errors in the travel-time picking. Since we cannot calculate the relative errors of the inverted parameters in the real data inversion, a new relative estimation error S_e, defined by the following equation, is used to perform the error analysis in an LSQ procedure,

$$S_e = \sqrt{\frac{1}{N}\sum_{i=1}^{N}\left(\frac{y_i - \hat{y}_i}{\hat{y}_i}\right)^2}, \tag{47}$$

where N is the number of azimuths measured, and y_i and $\hat{y}_i$ are the measured value and fitting value, respectively, at the same azimuth i. S_e indicates the relative accuracy of regression for the real data. The error analysis shows that the relative estimation error of our data set using a fit of the three-term approximation to the calculated square-ray-velocities is 2.8%.

CONCLUSIONS

We have presented a refraction method for determining the anisotropy properties of marine sediments from vertical-cable

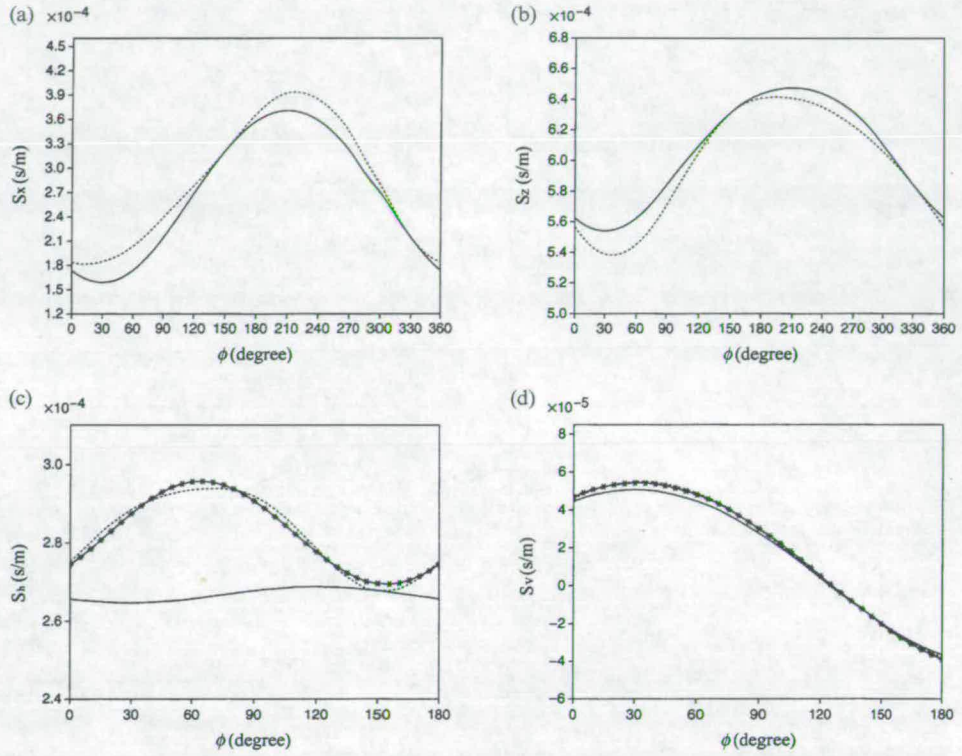


Figure 13 As Fig. 12, for model C (solid line) and model D (dashed line). Also shown are a best-fit (marked line) of the elliptical approximation to variations in horizontal ray-slowness on model D in (c), and a best-fit (marked line) of the cosine function to variations in vertical ray-slowness on model D in (d).

seismic data in the presence of dip. A slowness-based inversion procedure has been established to estimate the dip and anisotropy parameters for the refractor from the measured refracted traveltimes. The development of this technique is based on the deviation of the refracted traveltime equation in multilayered azimuthally isotropic or anisotropic media (TI) with the assumption that the layers are parallel to each other and the symmetry axes are perpendicular or parallel to the layer surface.

Numerical tests show that the azimuthal variations in apparent slowness are mainly due to effects of dip rather than anisotropy. When dips exceed 5°, significant errors may occur in the use of the phase-slowness approach based solely on horizontal layers. However, for azimuthal variations of horizontal ray-slowness, the influence of anisotropy is more significant than that of dip. This method yields a ray-slowness distribution independent of dips for a range of azimuths using refracted waves from VC data. Also, the azimuthal variations in the tangents of apparent dips ($\tan\alpha$) are obtained.

The inversion results for the synthetic P-wave VC data demonstrate that this technique can provide an accurate and quantitative description of the anisotropic parameters v_{P0}, ε, the symmetry axis azimuth φ_a, and layer parameters β and φ_d in multilayered azimuthally anisotropic media. The relative errors for the inverted parameters v_{P0} and ε are less than 0.4% and 6.0%, respectively, when the anisotropy strength for P-waves is up to 22%. Unfortunately, the estimation for the anisotropy parameter δ based solely on P-waves is not reliable. In addition, the overburden has no effect on the inversion results for the refractor in our case.

In the application to the field VCS data, first arrivals along 348 azimuths were picked and used for dip and anisotropic inversions. The final results show that the near-surface sediments in this area have 1° dip with a dip azimuth of 23°, and there is about 5.0% P-wave azimuthal anisotropy, with the symmetry axis at 134° from the X-axis in the natural coordinate system. The relative estimation error of our data set, using a fit of the three-term approximation to the calculated square-ray-velocities, is 2.8%.

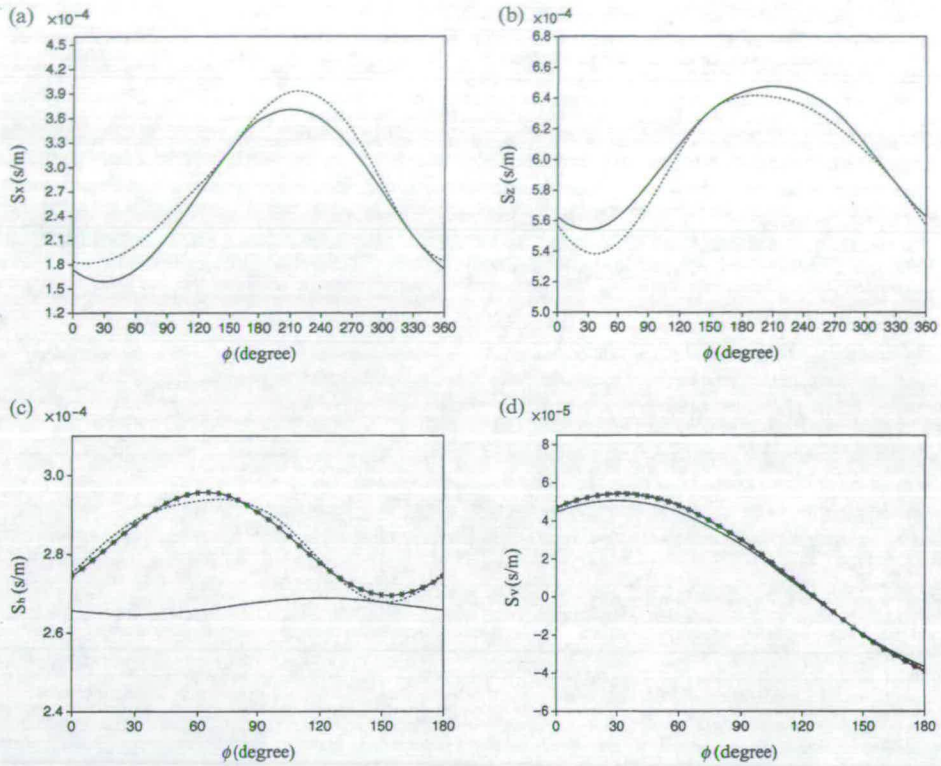


Figure 14 As Fig. 12, for model E (solid line) and model F (dashed line). Also shown are a best-fit (marked line) of the elliptical approximation to variations in horizontal ray-slowness on model F in (c), and a best-fit (marked line) of the cosine function to variations in vertical ray-slowness on model F in (d).

ACKNOWLEDGEMENTS

We thank Professor Colin MacBeth of Heriot-Watt University for his participation, guidance and valuable suggestions in early stages of this work. We also thank Texaco for providing the data and permission to publish the results. This work is funded by the Edinburgh Anisotropy Project (EAP) of the British Geological Survey, and is published by permission of the Executive Director of the British Geological Survey (NERC) and EAP sponsors: Agip, Amerada Hess, BPAmoco, Chevron, Conoco, ExxonMobil, PGS, Philips, Saga Petroleum, Schlumberger, Shell, Texaco, TotalFinaElf and Veritas DGC.

REFERENCES

Bachman R.T. 1979. Acoustic anisotropy in marine sediments and sedimentary rocks. *Journal of Geophysical Research* **84**, 7661–7663.

Bachman R.T. 1983. Elastic anisotropy in marine sedimentary rocks. *Journal of Geophysical Research* **88**, 539–545.

Backus G.E. 1962. Long-wave elastic anisotropy produced by horizontal layering. *Journal of Geophysical Research* **67**, 4427–4440.

Berryman J.G. 1979. Long-wave elastic anisotropy in transversely isotropic media. *Geophysics* **44**, 896–917.

Byun B.S. 1982. Seismic parameters for media with elliptical velocity dependence. *Geophysics* **47**, 1621–1626.

Carlson R.L., Schaftenaar C.H. and Moore R.P. 1984. Causes of compressional-wave anisotropy in carbonate-bearing, deep-sea sediments. *Geophysics* **49**, 525–532.

Crampin S. 1981. A review of wave motion in anisotropic and cracked elastic media. *Wave Motion* **3**, 343–391.

Daley P.F. and Hron F. 1977. Reflection and transmission coefficients for transversely isotropic media. *Bulletin of the Seismological Society of America* **67**, 661–675.

Gaiser J.E. 1990. Transversely isotropic phase velocity analysis from slowness estimates. *Journal of Geophysical Research* **95**, 11241–11254.

Gendzwill D.J. 1993. Seismic velocity, fracture density and anisotropy of some Manitoba limestones. *Canadian Journal of Exploration Geophysics* **29**, 153–162.

Havig S.O. and Krail P.M. 1996. Vertical cable seismic applications. *World Oil* **217**(5), 72.

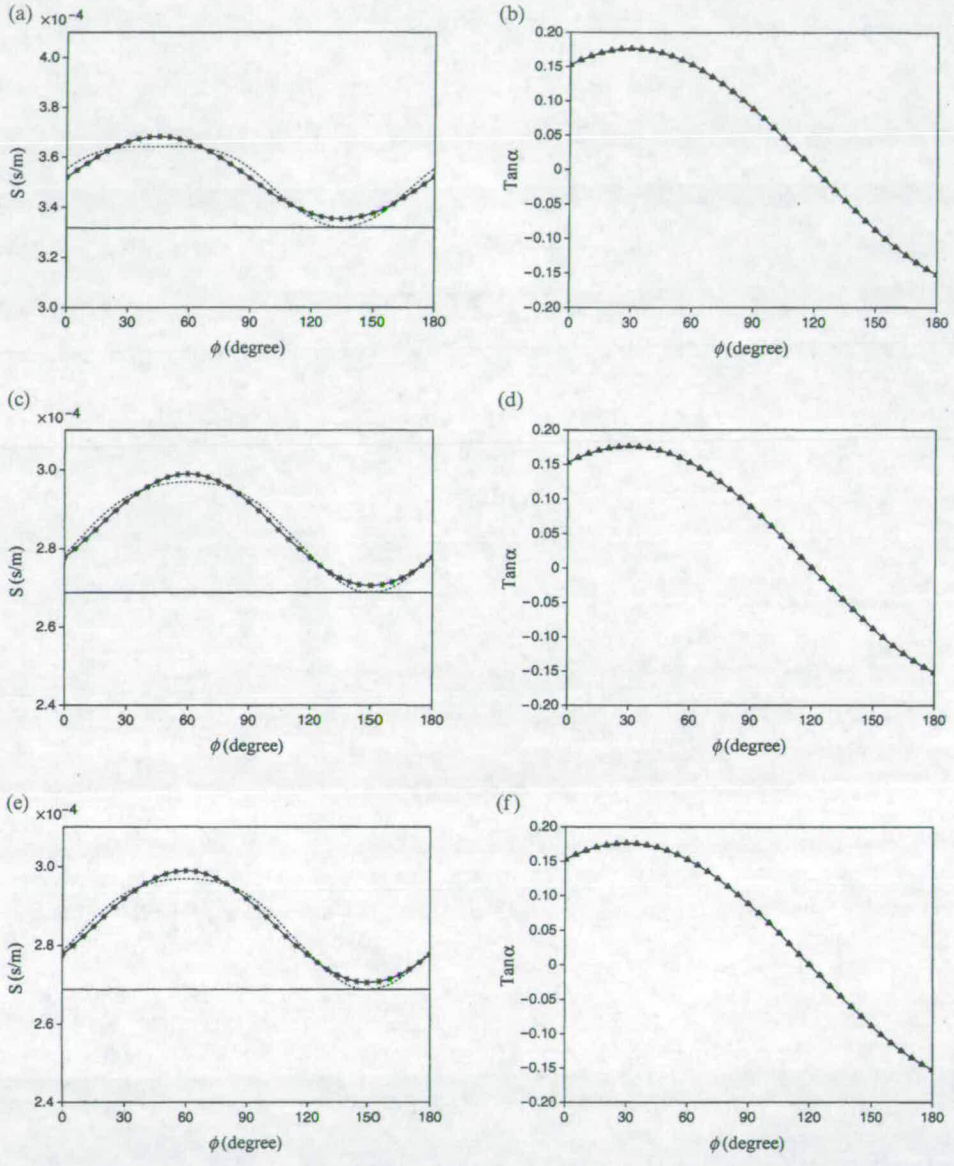


Figure 15 Ray-slowness distributions of refractors without effects of dip for (a) models A (solid line) and B (dashed line), (c) models C (solid line) and D (dashed line) and (e) models E (solid line) and F (dashed line), and azimuthal variations in tanα for (b) models A (solid line) and B (dashed line), (d) models C (solid line) and D (dashed line) and (f) models E (solid line) and F (dashed line). Also shown are the best elliptical fits to slowness curves and cosine fits to tanα curves (marked line).

Hunter J.A. and Pullan S.E. 1990. A vertical array method for shallow seismic refraction surveying of the sea floor. *Geophysics* 55, 92–96.

Krail P.M. 1991. Case history: vertical cable 3-D acquisition. 53rd EAEG meeting, Florence, Italy, Expanded Abstracts, 204.

Leslie J.M. and Lawton D.C. 1999. A refraction-seismic field study to determine the anisotropic parameters of shales. *Geophysics* 64, 1247–1251.

Levin F.K. 1978. The reflection, refraction, and diffraction of waves in media with an elliptical velocity dependence. *Geophysics* 43, 528–537.

Li X.-Y. 1997. Viability of azimuthal variation in P-wave moveout for fracture detection. 67th SEG meeting, Dallas, USA, Expanded Abstracts, 1555–1558.

MacBeth C. 1991. Shear-wave anisotropy in marine sediments around Britain from surface sources. In: *Shear-Waves in Marine*

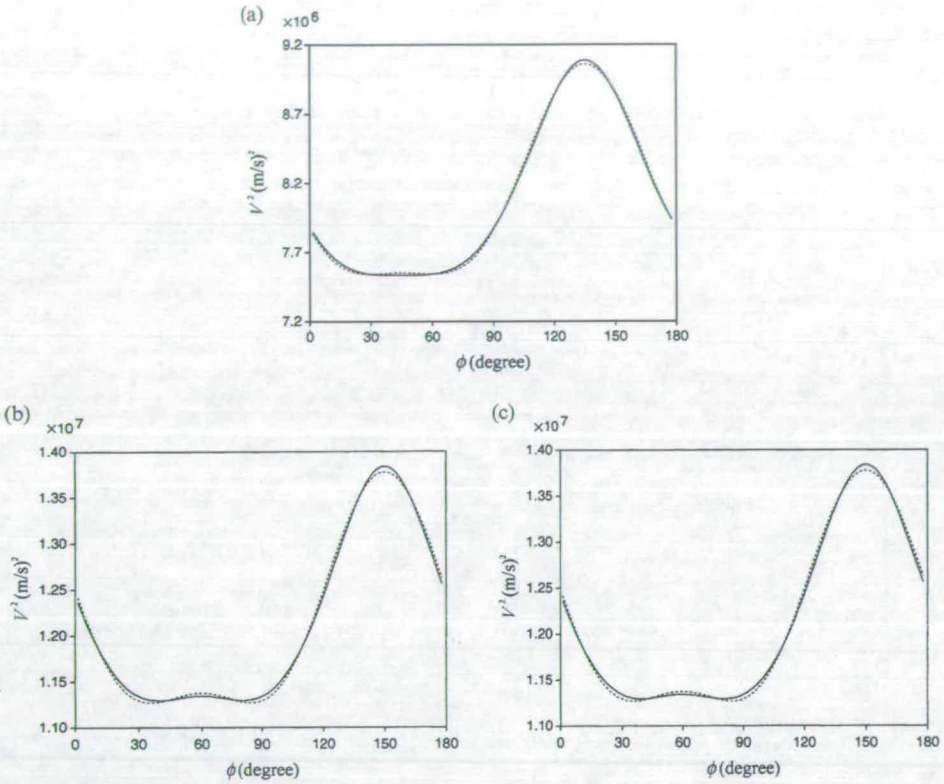


Figure 16 Azimuthal variations in the calculated square-ray-velocities (solid line) and their three-term approximation fits on (a) model B, (b) model D and (c) model F.

Sediments (eds J.M. Hovem *et al.*), pp. 13–20. Kluwer Academic Publishers, The Netherlands.

MacBeth C. 1998. Vertical fracture estimation using walk-away VSP. 68th SEG meeting, New Orleans, USA, Expanded Abstracts, 304–307.

Miller D.E. and Spencer C. 1994. An exact inversion for anisotropic moduli from phase slowness data. *Journal of Geophysical Research* **99**, 21651–21657.

Milligan P.A. 1998. Anisotropic statics for a 2D line over a mountainous overthrust belt in Bolivia. 68th SEG meeting, New Orleans, USA, Expanded Abstracts, 1413–1416.

Ohlsen F. and MacBeth C. 1998. Anisotropy estimates from a North Sea VSP. 68th SEG meeting, New Orleans, USA, Expanded Abstracts, 280–283.

Postma G.W. 1955. Wave propagation in a stratified medium. *Geophysics* **20**, 780–806.

Sayers C.M. 1997. Determination of anisotropic velocity models from walkaway VSP data acquired in the presence of dip. *Geophysics* **62**, 723–729.

Sena A.G. 1991. Seismic traveltime equations for azimuthally anisotropic and isotropic media: estimation of interval elastic properties. *Geophysics* **56**, 2090–2101.

Thomsen L. 1986. Weak elastic anisotropy. *Geophysics* **51**, 1954–1966.

Wang H. and Dong M. 1993. VSP modelling in EDA media and shear wave splitting analysis. *Oil Geophysical Prospecting* **28**(2), 63–71.

Wang H. and Dong M. 1994. Elastic waves in EDA media. *Oil Geophysical Prospecting* **29**(6), 706–712.

Wang H., Li X. and MacBeth C. 1999. Estimation of seabed sediment anisotropy using vertical cable seismics. 69th SEG meeting, Houston, USA, Expanded Abstracts, 1963–1966.

APPENDIX A

Traveltime equation for refraction of the marine sediments in vertical-cable seismic

We derive a formula for the refraction traveltime of multilayered azimuthally anisotropic or isotropic media in the presence of dip. In Fig. 2, we considered n-layered TI media with a symmetry axis parallel or perpendicular to the layer interfaces. Each layer has the same dip and dip azimuth, and is specified by its vertical depth z_k at the cable location O and its ray velocities $V_k(\theta_k, \phi)$, $(k = 1, 2, \cdots, n-1)$, where θ_k is the angle of incidence at each layer for a given raypath.

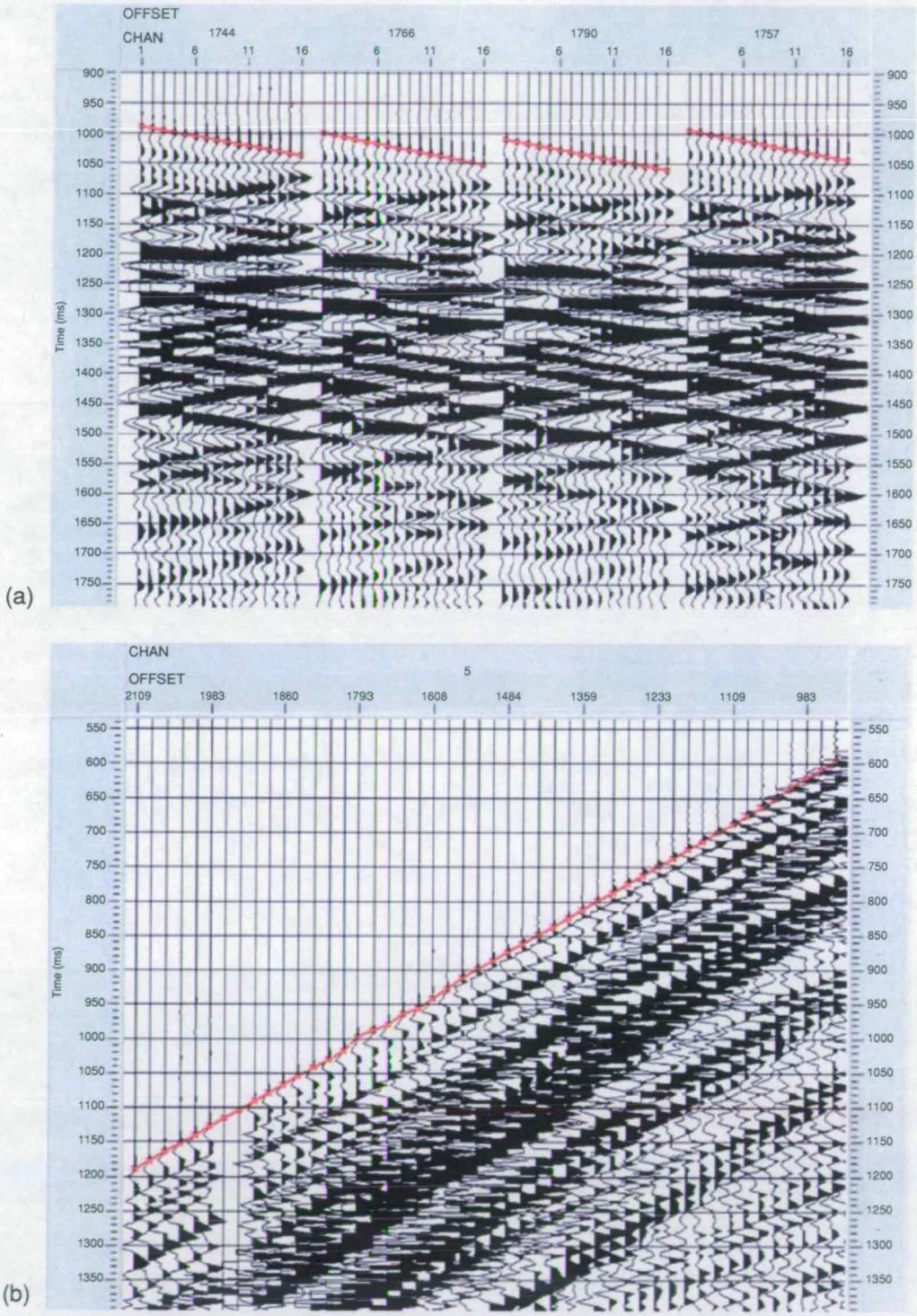


Figure 17 First-arrival picking on (a) common-source gathers and (b) one common-receiver gather from a selected 2D source line of the VC data.

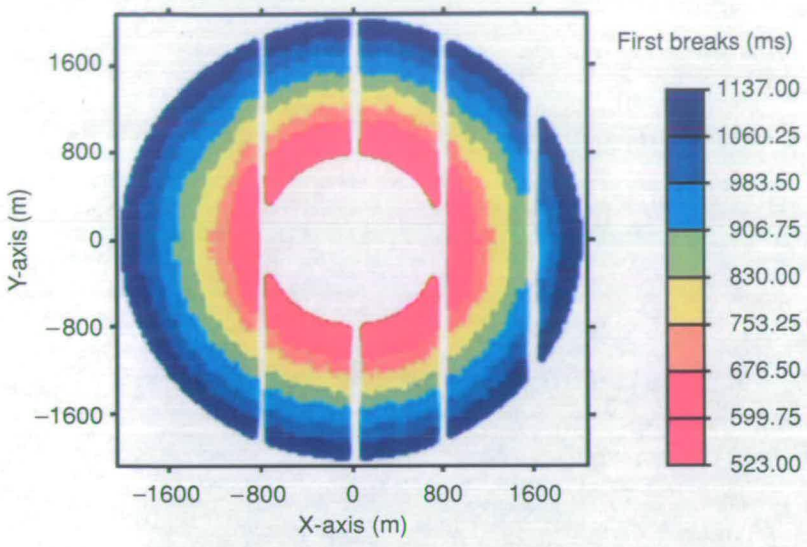


Figure 18 First arrivals for one common receiver (channel 5) at offsets ranging from 800 m to 2000 m.

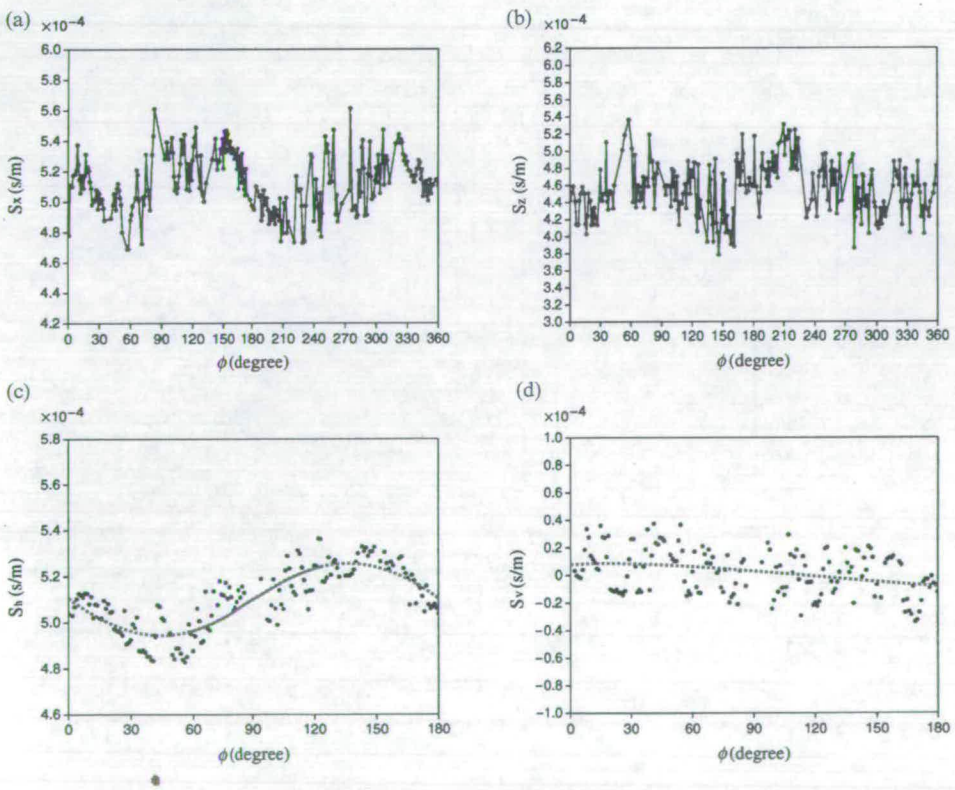


Figure 19 Plots of (a) horizontal apparent slowness, (b) vertical apparent slowness, (c) horizontal ray-slowness and (d) vertical ray-slowness versus azimuth ϕ for the sea-floor. Also shown are the best-fits of elliptical approximation in (c) and cosine function in (d) to the calculated data.

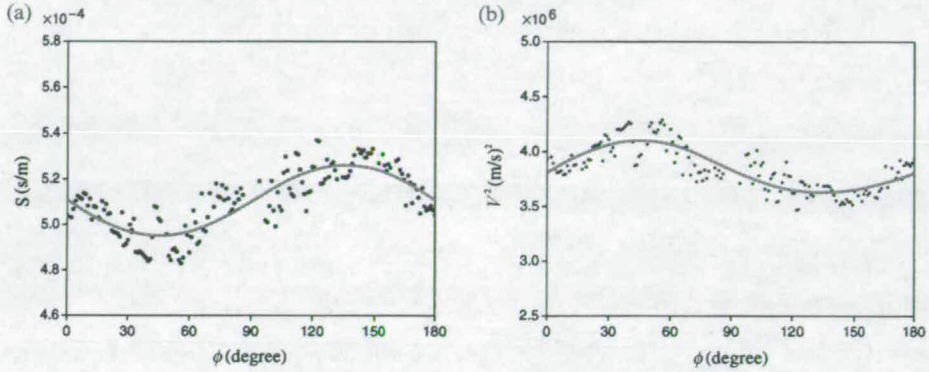


Figure 20 (a) Ray slowness versus azimuth and a best-fit of elliptical approximation, and (b) square-ray-velocity versus azimuth and a best-fit of the three-term approximation (31) to the calculated data for the sea-floor.

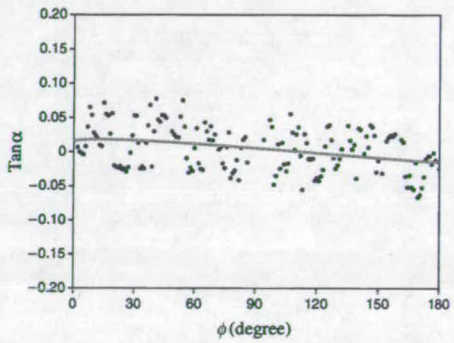


Figure 21 Tanα versus azimuth ϕ for the sea-floor. Also shown is the best-fit of the cosine function to the calculated data.

P-wave velocities in the water and at the nth refractor are V_0 and $V_n(\phi)$, respectively, for a given measured azimuth ϕ. The traveltime for a refracted wave of layer n from source S to receiver R can be expressed as

$$t_n(\phi) = \frac{SA_0}{V_0} + 2\sum_{k=1}^{n-1} \frac{A_{k-1}A_k}{V_k(\theta_k, \phi)} + \frac{A_{n-1}B_{n-1}}{V_n(\phi)} + \frac{B_0 R}{V_0}. \tag{A1}$$

As the derivation of the traveltime equation is for a single refractor, we can write

$$SA_0 = \frac{h_O}{\cos(\theta_0 - \alpha)} - \frac{x\sin\alpha - h_O\tan(\theta_0 - \alpha)\sin\alpha}{\cos\theta_0}, \tag{A2}$$

$$BR = \frac{h_R\cos\alpha}{\cos\theta_0}, \tag{A3}$$

$$A_0B_0 = \frac{x\cos(\theta_0 - \alpha) - h_O\sin(\theta_0 - \alpha) - h_R\sin(\theta_0 + \alpha)}{\cos\theta_0}, \tag{A4}$$

where α is the apparent dip of each layer at the measured azimuth ϕ. In Fig. 2, we also have

$$A_kA_{k-1} = \frac{z_k\cos\alpha}{\cos\theta_k}, \tag{A5}$$

$$\begin{aligned} A_1B_1 &= A_0B_0 - 2z_1\cos\alpha\tan\theta_1, \\ A_2B_2 &= A_1B_1 - 2z_2\cos\alpha\tan\theta_2, \\ &\cdots \quad \cdots \quad \cdots \\ A_{n-1}B_{n-1} &= A_{n-2}B_{n-2} - 2z_{n-1}\cos\alpha\tan\theta_{n-1}. \end{aligned} \tag{A6}$$

Hence,

$$A_{n-1}B_{n-1} = A_0B_0 - 2\cos\alpha\sum_{k=1}^{n-1} z_k\tan\theta_k. \tag{A7}$$

Based on the above expressions, the traveltime $t_n(\phi)$ can be finally written as

$$\begin{aligned} t_n(\phi) = &\left[\frac{\cos\alpha + \tan\theta_0\sin\alpha}{V_n(\phi)} - \frac{\sin\alpha}{V_0\cos\theta_0}\right]x \\ &+ \left[\frac{\cos\alpha}{V_0} - \frac{\sin(\theta_0 + \alpha)}{V_n(\phi)}\right]\frac{h_R}{\cos\theta_0} \\ &+ \left[\frac{\cos\theta_0 + \sin(\theta_0 - \alpha)\sin\alpha}{V_0\cos(\theta_0 - \alpha)} - \frac{\sin(\theta_0 - \alpha)}{V_n(\phi)}\right]\frac{h_O}{\cos\theta_0} \\ &+ 2\cos\alpha\sum_{k=1}^{n-1}\frac{z_k}{\cos\theta_k V_k(\theta_k, \phi)} - \frac{2\cos\alpha}{V_n(\phi)}\sum_{k=1}^{n-1} z_k\tan\theta_k. \end{aligned} \tag{A8}$$

APPENDIX B

Ray velocities in transversely isotropic media

For a P-wave, Daley and Hron (1977) gave a clear derivation of the directional dependence of the phase velocities:

$$\rho v_P^2(\theta) = \frac{1}{2}\left[C_{33} + C_{44} + (C_{11} - C_{33})\sin^2\theta + D(\theta)\right], \tag{B1}$$

where ρ is the density, θ is the phase angle between the wavefront normal and symmetry axis, and $D(\theta)$ is given by

$$D(\theta) = \{(C_{33} - C_{44})^2 + 2[2(C_{13} + C_{44})^2 - (C_{33} - C_{44})(C_{11} + C_{33} - 2C_{44})]\sin^2\theta + [(C_{11} + C_{33} - 2C_{44})^2 - 4(C_{13} + C_{44})^2]\sin^4\theta\}^{1/2} \quad \text{(B2)}$$

(Thomsen 1986), and C_{11}, C_{13}, C_{33} and C_{44} are elastic constants.

In any plane which contains the symmetry axis, the ray velocity and ray angle can be expressed in terms of the phase velocity and phase angle (e.g. Postma 1955; Levin 1978; Byun 1982). A simple relationship between the two velocities is (Berryman 1979)

$$V_P^2(\phi(\theta)) = v_P^2(\theta) + \left(\frac{dv_P}{d\theta}\right)^2, \quad \text{(B3)}$$

where $V(\phi(\theta))$ is the ray velocity as a function of ray angle $\phi(\theta)$ from the symmetry axis. $\phi(\theta)$ is given by

$$\tan(\phi(\theta)) = \left(\tan\theta + \frac{1}{v_P}\frac{dv_P}{d\theta}\right)\Big/\left(1 - \frac{\tan\theta}{v_P}\frac{dv_P}{d\theta}\right). \quad \text{(B4)}$$

From (B1) and (B2), we have

$$\frac{dv_P}{d\theta} = \frac{1}{4}v_P^{-1}\left[2(C_{11} - C_{33})\sin\theta\cos\theta + \frac{dD(\theta)}{d\theta}\right], \quad \text{(B5)}$$

and

$$\frac{dD(\theta)}{d\theta} = 2D^{-1}(\theta)\{[2(C_{13} + C_{44})^2 - (C_{33} - C_{44})(C_{11} + C_{33} - 2C_{44})]\sin\theta\cos\theta. + [(C_{11} + C_{33} - 2C_{44})^2 - 4(C_{13} + C_{44})^2]\sin^3\theta\cos\theta\}. \quad \text{(B6)}$$

When $\theta = 0°$ or $90°$, the ray angle $\phi(\theta)$ equals the phase angle θ, and the ray velocity equals the phase velocity.

Therefore, for HTI media, the ray-velocity distribution in the horizontal plane can be expressed as

$$V_P(\phi - \varphi_a) = \left[v_P^2(\theta) + \left(\frac{dv_P}{d\theta}\right)^2\right]^{1/2}, \quad \text{(B7)}$$

where ϕ and φ_a are the azimuths of the observation point and the horizontal axis of symmetry, respectively, with respect to the X-axis in the survey coordinates, and $\phi - \varphi_a = \phi(\theta)$.